Oxic-anoxic dynamics in the continental subsurface : prediction and control of rock weathering and deep biomass

Ivan-David Osorio-Leon

COLLEGE ECOLOGIE
DOCTORAL GEOSCIENCES
BRETAGNE AGRONOMIE ALIMENTATION

Université de Rennes

THÈSE DE DOCTORAT DE

L'UNIVERSITÉ DE RENNES

ÉCOLE DOCTORALE N° 600
Écologie, Géosciences, Agronomie, Alimentation
Spécialité : *Sciences de la Terre et de l'Environnement*

Par
Ivan-David OSORIO-LEON

Dynamiques oxiques-anoxiques dans la subsurface continentale :

prédiction et contrôle sur l'altération des roches et la biomasse profonde

Thèse présentée et soutenue à Rennes, le 16 Octobre 2023
Unité de recherche : Géosciences Rennes - UMR 6118

Rapporteurs avant soutenance :

Damien DAVAL Chargé de Recherche CNRS à l'ISTerre, Université Grenoble Alpes
Olivier ATTEIA Professeur à l'INP ENSEGID Bordeaux

Composition du Jury :

Président :	Jérôme GAILLARDET	Professeur à l'IPGP, Université Paris Cité
Examinateurs :	Susan BRANTLEY	Professeur à Pennsylvania State University
	Thomas STIEGLITZ	Directeur de Recherche IRD au CEREGE
Rapporteurs :	Olivier ATTEIA	Professeur à l'INP ENSEGID Bordeaux
	Damien DAVAL	Chargé de Recherche CNRS à l'ISTerre, Univ. Grenoble Alpes
Dir. de thèse :	Tanguy LE BORGNE	Physicien CNAP à l'Université de Rennes
Co-encadr. de thèse :	Camille BOUCHEZ	Physicienne-adjointe CNAP à l'Université de Rennes

Invité :

Alexis DUFRESNE Chargé de Recherche CNRS à ECOBIO, Université de Rennes

Esta tesis de doctorado, el tiempo invertido y la pasión con la que he vivido este tiempo, están dedicados a mis padres, Uriel y Clarivel. Son ellos dos los que sembraron en mí la curiosidad que me llevó hasta este punto y los que durante cada día de este doctorado me estuvieron esperando y acompañando desde la distancia. Nuestras conversaciones y disquisiciones en casa fueron la semilla que llevaría después a querer pasar 4 años de mi vida estudiando el viaje de una gota de agua.

VIAJE DE UNA GOTA DE AGUA

A mis padres...

I

Esta es una historia de manos y de agua. Está ocurriendo ahora, entre la invisibilidad del cielo y la inmensidad del suelo. Esta historia debió ser escrita hace años por las manos de mi viejo, cuando viendo caer la lluvia, supo encontrar en cada gota, páginas de historias escritas durante milenios. Casi puedo imaginar a mi joven padre, con sus ojos bien abiertos; con su cuerpo junto a la ventana, pero la mente fluyendo, lloviendo, sin pausa, como si fuera tiempo. En la lluvia los niños veían juego, los padres frío y viento, pero en los ojos de mi padre, ahí donde había agua, él veía movimiento. Tal como el agua en su eterno y cíclico destino, va y vuelve sin parar entre mar y cielo, la idea de esta historia ha dado vueltas en la mente de mi padre por mucho tiempo. A él, que hoy prefiere esculpir con sus manos las formas de las plantas, le presto mis manos para escribir "El viaje de una gota de agua".

II

Viajera del espacio, llegaste cual jinete cabalgando cuerpos rocosos que, con sus colas de hielo y polvo, iluminaban la oscuridad del vacío espacio interestelar. Llegaste para dar de beber al joven planeta, ardiente de fiebres magmáticas, y así apagarías incendios, te mezclarías en la esencia de las rocas, descansarías en los bajos del paisaje y entonces, te acumularías tanto que dominarías en un futuro la superficie de la joven tierra. Fue así como descubriste a la tierra, el gran amor de tu historia; la amante que habría de mezclarse contigo a lo largo de eras geológicas en un contacto íntimo pero indescriptible en términos de la incipiente sexualidad que emergería al otro lado de los eones. Así, llegaste desde las profundidades del cosmos para hacerte voluntariamente prisionera de un ciclo perfecto, en el que has estado recorriendo sin descanso todos los rincones de tu amante. Tú, pequeña gota de agua, que aprenderías a servirte del fuego lejano del sol para mutar y hacerte a la vez solido hielo o invisible gas, serías la teta que dio de mamar a la vida que crecería más adelante en tus entrañas.

III

Cualquier punto puede ser el inicio de un ciclo que se repite hasta la eternidad.

¿Quizás todo empieza en la evaporación que da vida a ríos voladores que llenan con su invisible presencia la transparencia de la atmósfera?

O, ¿es la condensación que forma nubes, en apariencia intangibles, pero que son cúmulos de cristales microscópicos de hielo?

¿Es acaso la lluvia el inicio? ¿Esa, en la que la obesidad de los cristales de hielo logra vencer las fuerzas descritas por Arquímedes para llevarlos al encuentro de la tierra?

¿Y si el inicio fuera la caricia? como la caricia entre el río que se desliza por los pliegues de la vieja superficie terrestre. O la caricia que acompaña y hace brotar la lágrima del ojo infantil que ha visto el alcance de la estupidez humana. O como esas caricias invisibles que ocurren en la oscuridad del subsuelo, en donde las gotas de agua se deslizan lenta y pacientemente entre los poros de las rocas hasta que, algún día lejano, movidas por la gravedad, regresan al mar después de haber sido nube, cristal, gota, lágrima.

Si cualquier punto puede ser el inicio de un ciclo que se repite hasta la eternidad, todo puede comenzar con la gota de transpiración que está colgando de la ceja de mi padre en este momento. Justo ahora, mientras él esculpe con sus manos las formas de las plantas y yo le presto mis manos para escribir “El viaje de una gota de agua”.

Ivan Osoriovich

ACKNOWLEDGEMENTS

Ce travail de thèse est la synthèse de plusieurs projets développés pendant ma thèse à l'Université de Rennes. À la fin de chaque chapitre, je mentionne les remerciements aux collaborateurs respectifs qui ont rendu possible le travail spécifique dans chaque cas. Cependant, il y a eu des personnes qui étaient transversales à l'ensemble de ces travaux et qui ont été essentielles pour la construction de mon projet de recherche. Je pense particulièrement aux membres de l'équipe de géomicrobiologie qui est née pendant le confinement lié au Covid-19 : Camille Bouchez, Tanguy Le Borgne, Alexis Dufresne, Melissa Garry et Julien Farasin. Je pense également aux membres de mon comité de suivi individuel (CSI) qui m'ont beaucoup apporté avec ces commentaires constructifs et encourageants : Julien Bouchez, Bénédicte Menez, Laurent Longuevergne et Kerry Gallagher.

Une thèse est aussi s'installer dans une autre culture :
En tant qu'étranger, cette thèse a été pour moi l'occasion de m'intégrer dans de nouvelles cultures et d'adopter des modes de pensée, de communication et de travail qui ne sont pas toujours évidents à assimiler.

Sans aucun doute, la personne à qui je serai toujours reconnaissant après mon séjour à Rennes est Camille Bouchez. Merci de m'avoir aidé, guidé et appris tant de choses pendant mes années de thèse. Grâce à toi, mon installation et mon adaptation au monde de la recherche française ont été plus simples. Merci pour ta bienveillance et ta patience inépuisables !

Merci Camille également d'avoir intégré la team de direction avec Tanguy Le Borgne. En terminant cette thèse, je suis très heureux et satisfait d'avoir pu bénéficier de conseils et des idées de vous deux. Elles ont été de grandes sources d'inspiration. J'ai grandement apprécié la liberté et l'encouragement avec lesquels vous avez toujours soutenu mon désir de découvrir et d'apprendre. Vous avez été présents non seulement sur le plan scientifique, mais aussi sur le plan personnel. Je vous remercie d'avoir été toujours arrangeants et coopératifs pour mes voyages en Colombie. Plus généralement, merci de m'avoir fait confiance pendant ces années de collaboration étroite ! J'espère que cette collaboration pourra se poursuivre encore longtemps dans le futur !

Je suis également très reconnaissant envers toute la communauté des laboratoires Géosciences Rennes et Ecobio pour leur accueil constant et pour m'avoir permis de m'intégrer à leur culture bretonne. Je peux dire que j'ai trouvé mon bonheur avec la mer bretonne et la bienveillance des Français, au point d'envisager une naturalisation. Merci du fond du cœur pour votre hospitalité et votre amitié !

Une thèse est aussi apprendre à trouver l'équilibre entre la vie et l'envie de toujours vouloir pousser plus la recherche :
Merci à tous ceux qui m'ont aidé à ne jamais oublier de trouver l'équilibre et à profiter du temps en dehors du laboratoire : l'équipe de Swingin' pour la danse, Martin pour nos balades à vélo, les collègues du labo pour les moments autour d'une bière, mes colocataires pour leur compagnie et leur soutien pendant la période du covid (Luc, Hermeline, Marion) ainsi que pendant la phase finale de ma thèse (Sabine et Nico). Un grand merci à Lina, au bbcito et à sa famille pour une amitié qui ne connaît pas le temps qui passe. À Marion et sa famille,

merci d'avoir élargi les limites de votre famille pour me faire une petite place où je me suis heureusement installé. Et *last but not least*, a mi familiecita bella que siempre ha creído en mí y me reconforta siempre con sus palabras de amor y de apoyo. Gracielitas !

Une thèse est aussi des imprévus :

Merci Barbara et Mélissa de m'avoir sauvé sur le terrain le jour de mon accident. Grâce à vous et vos services d'ambulancières j'ai encore 5 doigts à ma main ;). Également, merci à tous ceux et celles qui m'ont envoyé des mots de soutien et m'ont tant aidé pendant ce moment compliqué, particulièrement les AP Marine et Nico, l'équipe de la direction Olivier et Chantal, ainsi que mes encadrants Tanguy et Camille. Mais également le reste de mes collègues qui m'ont gentiment fait parvenir leurs mots de soutien. Et bien sûr, merci à ma famille (y compris mes gogors) qui de près ou de loin m'ont aidé à guérir plus vite avec leur amour.

Une thèse n'est pas que de la recherche :

Une des activités que j'ai le plus aimées durant ces années de thèse a été la possibilité de faire de l'enseignement. Je souhaite remercier les enseignants qui m'ont fait confiance et qui m'ont permis de participer des enseignements à différents niveaux. Merci notamment à Olivier Bour, Cécile Robin, Luc Aquilina, Tanguy Le Borgne, Florence Nicollin, Mathieu Pedrot, Virginie Vergnaud, Thierry Labasque, Cedric Wolf et Aline Le Merrer.

J'ai également eu l'opportunité de m'engager auprès de l'association Géocontact, ce qui m'a permis de renforcer mes liens avec les différents membres du laboratoire. Je tiens à remercier mes collègues du bureau pour cette expérience associative, qui était une première pour moi : Aurélie, Mara et "les Nicos", ainsi que mon cher Philippe Boulvais, qui apporte une merveilleuse vitalité au laboratoire avec sa joie de vivre. Les sorties de terrain que nous avons organisées avec Géocontact, que ce soit en Auvergne ou à Naples, resteront sans aucun doute parmi mes meilleurs souvenirs, alliant la géologie, l'histoire et l'amitié. Sans oublier le plaisir que nous avons eu à participer à des activités économiques pour récolter des fonds pour ces sorties de terrain, comme la vente de t-shirts, les soirées raclette à l'Amaryllis, la tombola, etc. Merci pour tous ces merveilleux souvenirs !

Et une thèse est aussi partager un espace...

C'est en faisant une thèse que j'ai découvert à quel point les postes des jeunes chercheurs sont éphémères. J'ai ainsi partagé mon espace de travail, le bureau, avec plusieurs collègues avec qui on a pu partager plus ou moins de moments. Je tiens à remercier d'avoir supporté mon désordre et parfois la musique qui s'échappait de mes écouteurs : les "co-bureaux" du 3ème étage Ewan, Simon, Barbara et Guillaume, et aux "co-bureaux" du 2ème Mélissa, Hugo, Pratyaksh, Satoshi, Manuel and Aleksandar.

FOREWORD

This manuscript has been adapted for its online publication. For a fully clickable version with fully resolved images, don't hesitate to contact me at the permanent email address:

idosoriole@unal.edu.co

Table of Contents

List of Figures

List of Tables

I. GENERAL CONTEXT

Contents

1 Introduction

Life on Earth depends on non-equilibrium processes of electron transfer, that is, on redox processes. In the terms of Falkowski (2006), the evolutionary pathways of life evolved to form a planetary "electron-market" where electron donors and acceptors are traded across the globe. Since the appearance of photosynthesis, that splits the water molecule and produces molecular oxygen as a by-product, oxygen levels in the atmosphere started to rise during the Great Oxidation Event (GOE) 2.5 billion years ago and changed the terms of the planetary electron market (Canfield; 2004; Petsch; 2014). The increase in atmospheric oxygen levels posed a challenge to the anaerobic life forms of that time, which had to adapt to the emergence of this new oxidant. They either had to retreat to the anaerobic side of the evolving oxic-anoxic interface, evolve to use oxygen or face the risk of perishing. This challenge led to the emergence of approximately 10^3 new oxygen-dependant metabolic pathways (Raymond and Segrè; 2006) and the emergence of complex life forms like multi-cellular organisms (Hedges et al.; 2004). As such, the role of oxygen has not only altered the redox functioning of the planet, but has also contributed to the diversification and complexification of life on Earth.

The irreversible rise in atmospheric oxygen levels during the GOE also had an effect in the mineralogical diversity of Earth. First, because the change in redox conditions enhanced oxidative weathering and favored the precipitation of water solutes such as Fe^{2+} or Mn^{2+} to form oxides [e.g. banded iron formations, BIFs (Hazen et al.; 2008)]. Second, because the increased complexification of life forms and the numerous evidence of microbial biomineralization (Weiner and Dove; 2003) or microbial weathering of minerals (Shi et al.; 2016) converged towards a co-evolution between life and minerals (Hazen et al.; 2008).

Nowadays, modern approaches in molecular ecology, such as metagenomics, reveal the molecular evidence of the co-evolution of atmospheric oxygen concentrations and life. For instance, Morris and Schmidt (2013) demonstrated that approximately 70% of bacterial and archaeal genomes, sequenced at that time, encoded the capacity for microaerobic respiration. Additionally, some microbes considered strict anaerobes, such as denitrifying bacteria or sulfate reducing bacteria, encode genes for oxygen reduction (Berg et al.; 2022).

Oxygen thus plays a central role in the evolution and interactions of life and of the Earth surface mineralogy. These interactions are especially important in environments where the presence of oxygen is limited and the capacity to use it can represent an ecological advantage. In dark environments, such as the *deep continental subsurface*[1], the absence of photosynthesis limits the production of oxygen. The present dissertation focuses on these environments.

The upcoming sections address the current state of knowledge and the primary questions surrounding the distributions and implications of Dissolved Oxygen (DO) in the continental subsurface. The chapter starts by addressing the current evidence of the presence of DO in the subsurface and how it controls the redox structure of aquifers and biogeochemical reactions. The links between DO and essential critical zone processes such as rock weathering and biomass production are introduced. The chapter concludes by presenting the current understanding of reactive-transport mechanisms controlling the transport of DO into the subsurface, and it discusses how this phenomenon can challenge our existing perceptions of deep subsurface functioning.

2 The deep continental subsurface: the underground critical zone

The *Critical Zone* (CZ) (NRC; 2001), which goes from the upper limit of vegetation down to the "base of active groundwater" systems (Anderson et al.; 2008), is the thin layer of our planet in which the water cycle transports energy and solutes which are essential for the functioning of ecosystems, the survival of all living forms and the evolution of landscapes (Brantley et al.; 2007; Singha and Navarre-Sitchler; 2022). Solar energy is the main energy source that sustains life on Earth's surface through photosynthesis, and powers the global water cycle which connects the fluxes of energy and matter between the continents and the oceans. This remarkably

[1] In this work, we adopt the definition of Whitman et al. (1998) for the deep continental subsurface as the rocky environment deeper than 8m, excluding soil.

complex web of interactions at the surface of our planet has led to the emergence of a new interdisciplinary research field known as *Critical Zone science*, integrating geology, hydrology, geochemistry, ecology among other disciplines.

Nonetheless, the continental subsurface is a particular compartment of the CZ, less studied than surface environments because the access is less straightforward, and with a particular functioning because underground ecosystems can not be powered by sun energy (Singha and Navarre-Sitchler; 2022). This *underground critical zone* hosts dark ecosystems which are, indeed, thought to be mostly sustained by chemical energy from inorganic sources (Edwards et al.; 2012) such as rock-forming minerals. Through their interaction with groundwater, those minerals provide nutrients for living forms and sustain the so-called *deep subsurface biosphere* (Edwards et al.; 2012). Furthermore, some authors suggest that the majority of the microbial biomass on our planet resides in the pore space of rocks within the continental subsurface (Whitman et al.; 1998; Edwards et al.; 2012; Bar-on et al.; 2018). **It is however poorly known at which extent the underground critical zone interacts with its surface counterpart. Is the deep continental subsurface an environment isolated from the dynamic fluxes of energy and matter from Earth's surface?**

The works presented in this dissertation take place in this particular underground compartment in which the interactions between life, water and minerals are still poorly understood.

3 Redox-powered processes in the continental subsurface

3.1 Redox reactions: the power source in the deep continental subsurface

Dark environments such as the continental subsurface are devoid of sunlight and the functioning of biogeochemical processes relies on chemical sources of energy provided by reduction/oxidation (redox) reactions (Edwards et al.; 2012; LaRowe and Amend; 2019). In a manner similar to acid/base reactions in the Brønsted-Lowry definition, which involve a proton (H^+) donor (the acid) and a proton acceptor (the base), redox reactions entail the transfer of electrons between two chemical elements, from an electron donor (the "reductant") to an electron acceptor (the "oxidant"). In a general form, a redox reaction can be seen as:

$$aA_{red} + bB_{ox} \rightleftharpoons cC_{ox} + dD_{red} \tag{I.1}$$

From a general perspective, the energy released or consumed by reaction I.1 is expressed by its thermodynamic potential, i.e. by its Gibbs free energy ΔG_r:

$$\Delta G_r = \Delta G_r^0 + RT \ln Q_r \tag{I.2}$$

$$\text{With, } Q_r = \frac{(C_{ox})^c (D_{red})^d}{(A_{red})^a (B_{ox})^b} \tag{I.3}$$

where ΔG_r^0 corresponds to the standard-state Gibbs energy of reaction, R and T are the universal gas constant and the absolute temperature, respectively. The reaction quotient, denoted as Q_r, establishes a relationship between the activities of products and reactants and their corresponding stoichiometric coefficients.

Negative values of ΔG_r indicate exergonic reactions, which are spontaneous and release energy. Conversely, reactions with $\Delta G_r > 0$ are endergonic, meaning that they need additional energy inputs to occur. However, redox reactions are commonly expressed as half-reactions for both electron donor and acceptor:

$$aA_{red} \longrightarrow cC_{ox} + ne^- \tag{I.4}$$

$$bB_{ox} \longrightarrow dD_{red} + ne^- \tag{I.5}$$

While electrons do not exist in a free form in the nature, redox half-reactions are commonly used to express

the energy potential of the electron transaction. By convention, half-reactions are coupled to the standard half-reaction of H_2 oxidation:

$$H_2 \rightleftharpoons 2\,H^+ + e^- \tag{I.6}$$

By definition, at 25°C and 1 atm, reaction I.6 is associated with both a standard Gibbs free energy change of $\Delta G_r^0 = 0$ and a redox potential of zero, denoted as $E^0 = 0$.

While the Gibbs free energy is a useful quantity to express the energy of chemical reactions, it can not be directly measured. It can be nonetheless be related to a *redox potential* (E) which is measured in Volt:

$$\Delta G = nFE \tag{I.7}$$

The redox energy potential (E) is expressed by the *Nerst* equation:

$$E = E^0 + \frac{RT}{nF} \ln Q_r \tag{I.8}$$

Where E_0 is the standard redox potential [Volt] measured at 25 °C and 1 atm for a solution with unit activities. R is the universal gas constant, T is the absolute temperature n is the number of electrons transferred in the half-reaction and F is the Faraday's constant ($96.42\ kJ/Volt - gram - equivalent$).

The redox potential for both electron donor and acceptors is expressed, in a standard form, as the voltage that results from coupling their *reduction* half-reaction to the reference oxidation reaction I.6 in a standard electrochemical cell, where $[H_2] = [H^+] = 1$ (see Figure I.1-A). In such case, the redox potential referenced to the hydrogen standard reaction, E_h, is given by:

$$Eh = E^0 + \frac{RT}{F} \ln \frac{(C_{ox})^c}{(A_{red})^a} \tag{I.9}$$

Redox half-reactions, or redox couples, can this way be classified by their redox potential in a "redox ladder" as the one presented in Figure I.1-B. Any oxidation reaction will proceed with any reduction reaction as long as the latter has a higher redox potential. The farther apart the redox half-reactions are, the greater the energy potential released from the electron transfer, making the reaction more favorable. The position of redox-couples in the redox ladder is indeed correlated with field observations in which the more reactive redox-couples are the first to be depleted (Borch et al.; 2009; Mcmahon et al.; 2011).

3.2 The redox-powered deep biosphere

The deep continental biosphere is primarily inhabited by prokaryotes, specifically bacteria and archaea (Bar-on et al.; 2018). These unicellular organisms can be classified based on their metabolic pathways for survival. They are categorized as *heterotrophs*, which obtain energy and carbon from complex organic molecules synthesized by other organisms, and *autotrophs*, which derive energy from simple inorganic molecules while utilizing CO_2 as their carbon source. Due to their ability to harness energy from simple inorganic elements, autotrophs serve as the primary producers of biomass in the continental subsurface, bridging the gap between the mineral and living worlds, connecting the geosphere and biosphere.

The electron transfer that takes place in redox reactions is used in microbial *metabolism*, which has two components: (1) *catabolism*, which mainly provides the cell with the energy required for its maintenance and (2) *anabolism* which uses part of the energy produced in catabolism to synthesize new organic molecules necessary for cell growth and reproduction. Catabolism is therefore the component of microbial metabolism that is powered by the energy flow provided by redox reactions.

The molecular machinery involved in catabolic processes in prokaryotes is complex and exceeds the scope of this work. It is however worth noting that the energetic machinery involved in catabolic processes uses the flow of electrons from redox reactions to power an *electron transport system* (ETS) which involves a different

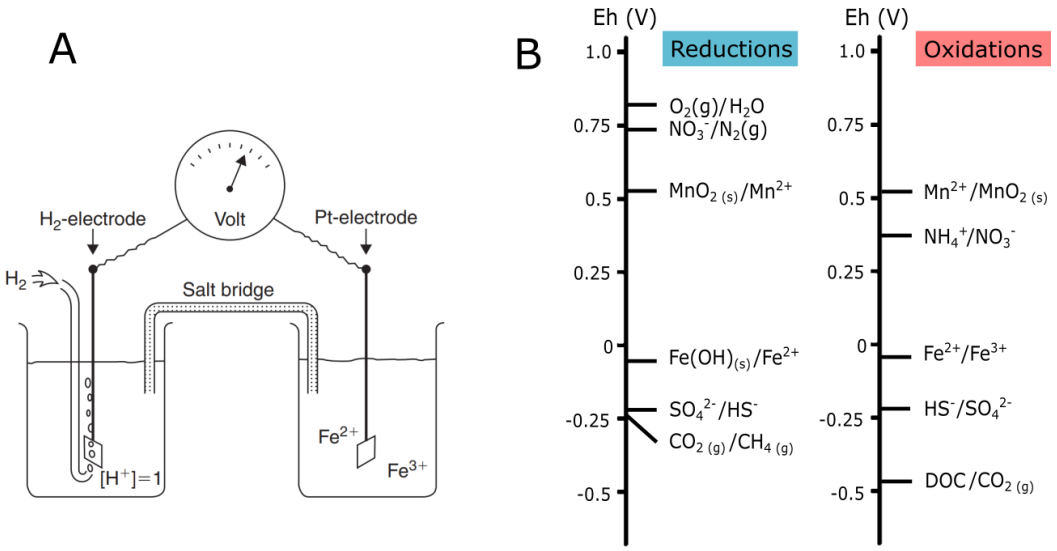

Figure I.1: **Conceptual view of the redox potential.** (A): The redox potential is measured as the voltage of the redox half-reaction (e.g. the reduction of Fe^{3+} to Fe^{2+}) coupled to the oxidation of molecular hydrogen in an electrochemical cell. The oxidation of molecular hydrogen is, by convention, the reference reaction defined with a zero standard redox potential at 25 °C and 1 atm, $E^0 = 0\,Volt$. Illustration taken from Appelo and Postma (2004). (B): Redox potentials computed for the most common redox couples involved in the redox reactions in aquatic environments [adapted from Borch et al. (2009)]. Redox couples represent reduced/oxidized species for reduction half-reactions and their opposites for reduction half-reactions.

set of molecular complexes (proteins and enzymes) present in the cell membrane. During the electron flow in the ETS, the energetic potential of redox reactions (Eh) is in part used to synthesize adenosine 5'-triphosphate (ATP), which is the universal energy carrier in cells synthesized through the *oxidative phosphorilation* process. Depending on the redox couples which provide the energy, different molecular complexes are involved and lead to different production levels of ATP (see Table I.1). Furthermore, catabolic processes are highly dependent on the presence of oxygen. Catabolism can indeed take place as aerobic or anaerobic respiration processes, that can only be performed by specific microorganisms. Indeed, prokaryotes are often classified as (1) *obligate aerobic*, organisms which use O_2 as unique final electron acceptor, (2) *obligate anaerobic*, organisms which can final electron acceptors other than O_2, (3) *microaerophilic*, organisms that require low concentrations of oxygen and (4) *facultative organisms* which can use either O_2 or other final electron acceptors. To sum it up, microbial catabolic processes, which involve cellular mechanisms that capture environmental flows of energy into ATP molecules in the cell, depend on the environmental factors such as the identity and the abundance of electron donors and acceptors, and particularly on the presence of dissolved O_2. **Although redox potentials are the primary energy source that drives microbial life in the deep continental subsurface, little is known about factors that control the redox state of natural groundwater environments.**

Table I.1: **Examples of interactions between redox reactions and microbial cells.** The electron transfer involved in the redox half-reactions Table adapted from Ehrlich et al. (2015).

Redox half-reaction	Eh	Molecular complexes involved in the ETS	ATP/2e$^-$
$Fe^{2+} \longrightarrow Fe^{3+} + e^-$	+0.77	Complex IV	1
$S^0 + 4\,H_2O \longrightarrow {SO_4}^{2-} + 8\,H^+ + 6\,e^-$	-0.20	Complex III or IV	2
$H_2S \longrightarrow S^0 + 2\,H^+ + 2\,e^-$	-0.27	Complex I or III	3
$H_2 \longrightarrow {}_2\,H^+ + 2\,e^-$	-0.42	Complex I or III	3
$Mn^{2+} + 2\,H_2O \longrightarrow MnO_2 + 4\,H^+ + 2\,e^-$	+0.46	Complex IV (?)	1

4 Dissolved oxygen: a key tracer of redox conditions in the subsurface

The previous sections highlighted the relevance of redox reactions for dark environments such as the deep continental subsurface: redox reactions are the main energy source that powers the biogeochemical processes in these environments. In groundwater systems, the redox state of groundwater is defined in terms of the availability of electron acceptors, specially in terms of the availability of dissolved O_2. In fact, DO offers the highest redox potential for oxidizing electron donors in the redox ladder (see Figure I.1-B) and imposes a limit for the catabolic processes that can take place in groundwater: its concentration determines whether aerobic, microaerobic or anaerobic metabolisms can take place. Despite the major relevance that DO can have on the redox processes, **the factors that control the formation of oxic environments in the continental subsurface are not yet well understood, nor are the potential consequences that the presence of DO may have on the types and extents of biogeochemical processes within the subsurface.** In the next sections we will present some pieces of evidence supporting the presence of oxic groundwater in the deep subsurface.

4.1 The journey from the light to the dark: how does oxygen get into the subsurface?

Molecular oxygen (O_2) is the second most important component of the atmosphere, with a concentration of 20.9 vol% that is the result of the steady-state balance between global photosynthetic production and biogeochemical respiration/consumption processes (Petsch; 2014). The dissolution of O_2 in water is explained by Henry's law, in which the equilibrium concentration of a dissolved gas is related to its partial pressure affected by the Henri's coefficient K_H. DO solubility in water is inversely proportional to temperature and water salinity variations. For instance, at constant temperature, the equilibrium concentration of dissolved O_2 is almost 25 % lower in seawater than in freshwater. At 20 °C, the solubility of O_2 in freshwater is 284 $\mu molL^{-1}$ or 8.87 $mg.L^{-1}$. This way, O_2 dissolves in rainwater and infiltrates in the unsaturated zone, provided the clay content of soils allows for water infiltration (Kim et al.; 2017).

DO is then transported by advection with water flow in the porous media. In the unsaturated zone or at the water table interface with air, oxygen can also reach groundwater by diffusion, yet this is a very slow process [oxygen diffusion in water is about 10^{-4} times smaller than in air (Refsgaard et al.; 1991)]. As illustrated in the redox ladder from Figure I.1-B, DO is the electron acceptor with the highest redox potential and therefore it can take part on redox reactions with multiple electron donors which can be present in groundwater such as DOC, H_2, H_2S, NH_4^+, Mn^{2+}, CH_4 or Fe^{2+}. In environments close to the surface such as in soils or in the unsaturated zone, organic matter is usually abundant and readily reacts with the infiltrated oxic waters in the aerobic respiration reaction, that is commonly mediated by heterotrophic organisms (Ehrlich et al.; 2015). Lasaga and Ohmoto (2002) estimated that the oxidation of soil organic matter is indeed the major O_2-sink on Earth, consuming up to 75 % of the global production of O_2.

Box I.1 - Dark oxygen: processes producing O_2 in the continental subsurface

Because of the absence of light, O_2 can not be produced by photosynthesis in the subsurface. Yet, some "dark" pathways have been reported to produce of O_2. For instance, water radiolysis by alpha emissions, a process that occurs at depths >2-3 km (Gutsalo; 1971) is an abiotic pathway for dark oxygen production. Some biological pathways rely on the use of oxidants with a more positive redox potential than the O_2/H_2O couple: chlorate and perchlorate respiring bacteria (Rikken et al.; 1996; van Ginkel et al.; 1996) and intra-aerobic denitrification performed by some methane-oxidizing bacteria (Ettwig et al.; 2010). Although demonstrated in the literature, the conditions for those O_2-producing processes require specific and restricted conditions. So far, dark oxygen production has only been reported in deep groundwater associated with carbon-rich strata (Ruff et al.; 2023).

Table I.2: **Compilation of the main microbe-mediated aqueous reactions consuming dissolved oxygen in groundwater**. Abbreviations correspond to MT: methanotrophs [e.g. Trotsenko and Murrell (2008)], FeOB: Iron oxidizing bacteria [e.g. Emerson et al. (2010)], MnOB: Manganese oxidizing bacteria [e.g. Tebo et al. (2004)], AOB: Ammonia oxidizing bacteria [e.g. Könneke et al. (2005)], SOB: Sulfur oxidizing bacteria [e.g. Ehrlich et al. (2015)], KB: Knalgass bacteria [e.g. Aragno (1992)]

e^- donor	Reaction	Related microbes	e^- donor sources
Chemo-organo-heterotrophs			
DOC	$CH_2O + O_2 \longrightarrow CO_2 + H_2O$		Surface and shallow waters
CH_4	$CH_4 + O_2 \longrightarrow CO_2 + 2H_2O$	MT	anaerobic sediments
Chemo-litho-autotrophs			
Fe^{2+}	$4Fe^{2+} + O_2 + 10H_2O \longrightarrow Fe(OH)_3 + 8H^+$	FeOB	Fe-bearing minerals[a]
Mn^{2+}	$Mn^{2+} + 0.5O_2 + H_2O \longrightarrow MnO_2 + H^+$	MnOB	Mn-bearing minerals[a]
NH_4^+	$NH_4^+ + 2O_2 \longrightarrow NO_3^- + 2H^+ + H_2O$	AOB	Sediments or fertilizers
H_2S	$H_2S + 2O_2 \longrightarrow SO_4^{2-} + 2H^+$	SOB	S-bearing minerals[a]
H^+	$2H_2 + O_2 \longrightarrow 2H_2O$	KB	Crustal processes

[a]: also produced by microbe-mediated reducing reactions transforming the oxidized species.

Due to the importance of respiration in soils, which consumes DO derived from the atmosphere, and the impossibility of producing O_2 through photosynthesis, aquifers have commonly been assumed to be anoxic environments (Winograd and Robertson; 1982; Rose and Long; 1988b; Malard and Hervant; 1999). However, in environments where DOC contents or soil thickness are small, DO can reach the saturated zone and groundwater can be oxic. In this case, the transport of DO to deep groundwater will depend on the availability of alternative electron donors that promote redox reactions which can be mediated by either heterotrophic or autotrophic microorganisms as presented in Table I.2. Most of these alternative electron donors in the subsurface are essentially originated from mineral's dissolution (see reactions in Table I.2) suggesting that the distribution of DO in the subsurface can be related to the geological setting.

In fact, a compilation of redox conditions in the main aquifers across the United States (Figure I.2) has shown that the redox conditions seem related to the geological setting. Aquifers with reducing conditions globally indicate an abundance of electron donors relative to electron acceptors. A large range of DO concentrations with depth are observed in the aquifers of the United States and a tendency towards an increase of DO with depth is observed. This increase is correlated with a decrease of DOC, highlighting that aquifers with low DOC contents are more likely to host oxic groundwater. DO concentrations are sparse and the average red line in Figure I.2-C indicates that the average concentration increases with depth. DO concentrations tend to be lower when DOC concentrations are the highest. Geological settings characterized by low DOC contents are therefore more likely to host oxic groundwater. Diagenetic changes of sedimentary rocks usually imply lower pressure (P) and temperature (T) conditions that those involved in the formation of crystalline rocks (metamorphic and igneous). Higher P and T conditions are favorable for the transformation and degradation of organic matter and as a consequence, DOC contents in crystalline rocks are usually lower than in sedimentary rocks (Ehrlich et al.; 2015). While this large spatial view is very interesting to highlight the variability of redox conditions with lithology and depth, it gives no information on how heterogeneous the distribution of oxic waters is at the watershed scale.

The DO distribution at a local scale (watershed scale) has been mostly studied in sedimentary or alluvial aquifers (Winograd and Robertson; 1982; Rose and Long; 1988a; Malard and Hervant; 1999; Chen and Liu; 2003; McMahon et al.; 2004; Chapelle et al.; 2012). Those works show that the redox state of groundwater also depends on the hydrogeological structure of aquifers (confined vs unconfined). For instance, unconfined aquifers have a uniform free boundary conditions at the interface between the water table and the unsaturated zone, in which DO can be replenished. For instance, Rose and Long (1988a) reported an increasing DO gradient with flow path distance in an unconfined aquifer within the Tucson basin, and a similar pattern was reported by Chen and Liu (2003) in a gravel aquifer. This suggests that redox gradients in unconfined aquifers

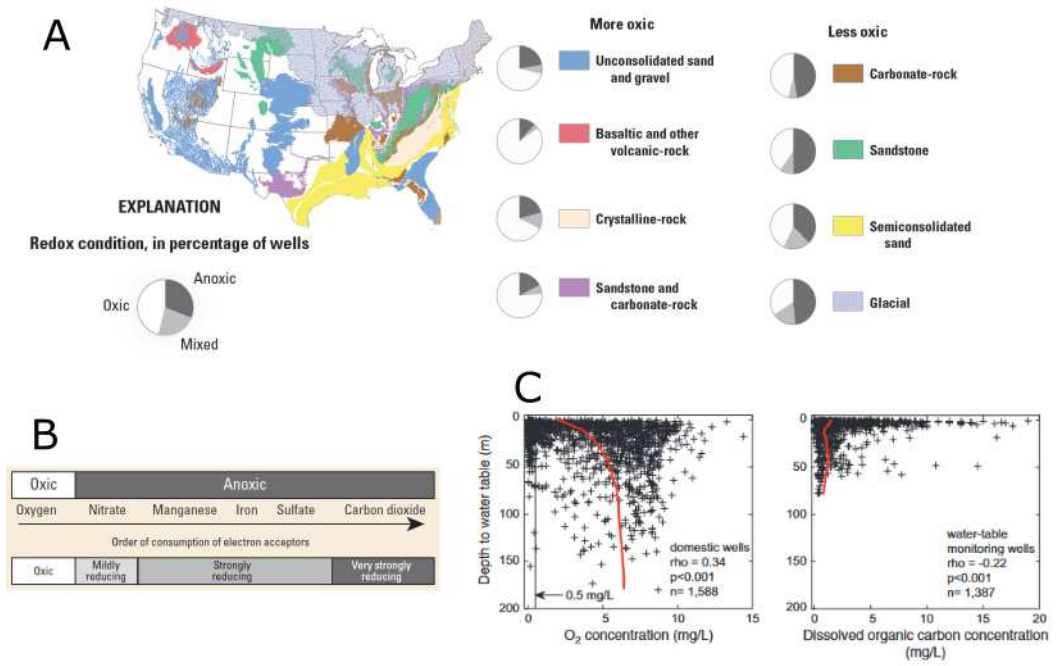

Figure I.2: **Redox landscapes in aquifer systems from USA.** A): Redox condition in main aquifers from the USA, distinguished by lithology. Data corresponds to measurements in domestic wells in selected regional aquifers. B): Corresponding redox facies definition for subfigure A. C): Depth distribution of dissolved oxygen and dissolved organic carbon. Red solid lines correspond to lowest (moving average) curve fits. Figures A and B are from (DeSimone et al.; 2014) while figure C is taken from (McMahon and Chapelle; 2008).

are more influenced by stratification with depth than by the distance along flow paths (Chen and Liu; 2003; McMahon et al.; 2011). On the other hand, in confined aquifers, groundwater is isolated from atmospheric replenishment and electron acceptors are consumed along flow paths. In this latter case, the concentrations of DO decrease with groundwater residence time and the distance in the flow path (Malard and Hervant; 1999; McMahon et al.; 2004). Overall, the observations of DO distributions in sedimentary aquifers indicate that in unconfined aquifers, DO distributions mostly present a subhorizontal stratification, while confined aquifers present a subvertical stratification. **Nevertheless, no systematic studies have been conducted to characterize the distribution of DO in heterogeneous media such as in fractured-rocks.** This leads to a key open question: **How to characterize the patterns and the factors that control DO distributions at catchment scale in heterogeneous subsurface environments?**

Box I.2 - The case of crystalline-rock aquifers

Crystalline rocks (igneous and metamorphic) represent around 35% of the exposed rocks in the continental surface (Amiotte Suchet et al.; 2003). Crystalline rocks, formed under high pressure and temperature conditions, typically contain lower amounts of organic matter compared to sedimentary rocks (Ehrlich et al.; 2015). This condition creates a more favorable environment for the persistence of oxic groundwater. Nevertheless, no systematic studies on the distribution of dissolved O_2 have been done in these environments. The data reported by McMahon and Chapelle (2008) and DeSimone et al. (2014) in Figure I.2 is indeed based on few agricultural boreholes that were accessible to the authors. In crystalline rocks, the pore space is essentially constituted by heterogeneous networks of fractures where channelized flow results in transport processes which are different from the more homogeneous flow in sedimentary aquifers (Olsson and Gale; 1995). Fracture networks can create shortcuts between flow paths, thereby promoting the mixing of groundwater with contrasting chemical compositions and redox states (Bochet et al.; 2020). These mixing zones, denominated reactive *hotspots*, exhibit high reaction rates and are energetically advantageous for microorganisms (Houghton and Seyfried Jr; 2010; Bethencourt et al.; 2020).

4.2 Coupling dissolved O_2 with geochemical cycles of elements

As a major control of the redox state of groundwater, DO significantly affects geochemical fluxes of elements. Along with pH, DO exerts a significant control over the transport, mobility, and fate of redox-sensitive elements (Nordstrom; 2011). This can be illustrated by elements such as Uranium and Iron, which solubility in water is strongly influenced by the redox and pH conditions. In the case of Uranium, its oxidized form, U(VI), is soluble, while for Iron, the oxidized form Fe(III) is insoluble. Therefore, DO concentrations can have contrasting effects on the mobility of elements, ultimately influencing water quality. In this work we focus on circum-neutral pH waters (6.5<pH<7.5) which are the most representative pH facies among the most common aquifer lithologies (DeSimone et al.; 2014).

In the continental subsurface, the oxygen cycle is coupled to biogeochemical cycles of, at least, Carbon (Petsch et al.; 2004), Iron (Melton et al.; 2014; Napieralski et al.; 2019), Manganese (Tebo et al.; 2005), Sulfur (Gu et al.; 2020) and Nitrogen (Könneke et al.; 2005) as illustrated by the main reactions in Table I.2. As discussed earlier in Section 3, redox reactions can have both chemical and biological pathways. Although these reactions are presented as independent processes, they are actually interrelated through *metabolic hand-offs*[2] (Anantharaman et al.; 2016) or *cryptic cycles*[3] of elements (Kappler and Bryce; 2017).

The network of interconnections between the underground oxygen cycle with other elements remains poorly constrained. For example, current literature on the global oxygen cycle neglects the continental subsurface compartment (Petsch; 2014). Moreover, new instrumental developments for sensing low DO concentrations as well as molecular ecology approaches have evidenced microbial aerobic respiration in processes that were historically considered as anoxic (Berg et al.; 2022). Since the continental subsurface hosts the majority of the microbial biomass on Earth (Bar-on et al.; 2018), those fluxes could be significant at a global scale. For instance, Overholt et al. (2022) found that carbon fixation in groundwater is on the same order of magnitude than carbon fixation in oceans.

[2]The term *metabolic hand-offs* refers to byproducts of a microbial metabolism that are used by other organisms either as an electron donor or acceptor.

[3]The term *cryptic cycles* refers to coupled redox processes that rapidly oxidize and reduce a same chemical species, returning it to its initial state and making difficult the identification of the intermediate steps.

Box I.3 - Links between oxygen and iron cycles in the subsurface: a key process

Among the different electron donors in Table I.2, iron is the most common element in the continental subsurface. Indeed, iron is the most abundant redox-sensitive element in the upper Earth's crust (Wedepohl; 1995) and can be a potential major sink for dissolved O_2 in the subsurface. Since the oxidation of iron by oxygen is a process commonly mediated by iron oxidizing bacteria (FeOB), this reaction could be associated with a potentially large biomass production in the subsurface, that has not yet been estimated. Moreover, the source for dissolved iron in groundwater comes from the dissolution of Fe-bearing minerals, where silicates, and in particular biotite, is the most widespread primary rock-forming mineral in the upper Earth's crust (Nanzyo and Kanno; 2018; Shu et al.; 2020). Overall, looking at the effects of dissolved O_2 on rock weathering and microbial biomass production in the continental subsurface can help to disentangle the links between the oxygen, iron and carbon cycles.

4.3 Partial conclusion: Which environments to study?

This section showed different pieces of evidence of the presence of dissolved O_2 in groundwater, in which certain geological contexts are more favorable to host oxic groundwater. Figure I.2 shows that fractured-rock aquifers are generally more oxic than porous environments, However, the mechanisms explaining higher DO contents and the consequences of oxic groundwater on subsurface reactive processes are largely unknown. We identified fractured rocks as a geological environment where the low organic carbon content makes it prone to the existence of oxic groundwater. **This makes of fractured-rocks a good case study to explore the effects O_2 has in the subsurface biogeochemical processes. Furthermore, this study will focus on the particular case of crystalline rocks (igneous and metamorphic) which represent more than 30% of the exposed rocks in the continental surface.** Table I.2 showed that dissolved O_2 can take part in a variety of aqueous reactions in which it can oxidize electron donors in microbe-mediated redox processes. Among the different electron donors, ferrous iron is the most common and abundant in Earth's crust. As we will see in the next sections, it plays a critical role in the subsurface biogeochemical processes. **Therefore, this study will particularly focus on the interaction between dissolved O_2 and ferrous iron in the subsurface.**

In the following section, we will examine in more detail the links between dissolved O_2 and the weathering of rock-forming minerals, which serve as sources of electron donors, in particular, ferrous iron that consumes DO in aquifers.

5 Dissolved O_2 and its role in water-rock interactions

In the preceding sections, we primarily discussed redox reactions taking place in the aqueous phase. However, within the continental subsurface, the majority of the volume is occupied by rocks, whose minerals are the primary source of electron donors in the subsurface. Electron donors from minerals can be either released to the aqueous phase by dissolution reactions which are promoted by the acidity of CO_2, or directly oxidized in crystalline form by the action of dissolved O_2. In either case, the weathering of rock-forming minerals is the primary process that provides the electron donors for redox reactions in the continental subsurface. While CO_2 has long been recognized as a key reactant in rock weathering by its acid character that promotes mineral dissolution (Walker et al.; 1981), the role of DO as a key reactant in mineral weathering has only been recently suggested. Fletcher et al. (2006) proposed DO as a critical reactant to explain spheroidal weathering observations[4]. Since then, several studies investigating weathering fronts development and the controls of the

[4]Spheroidal weathering, also called onion concentric or onion-skin weathering, is a process observed in almost all rock types and climates in which concentric shells of weathered rock form sequentially by fracture formation.

process known as *weathering induced fracturing* have inferred the presence of DO in crystalline aquifers (see Box I.4).

Box I.4 - DO in crystalline-rock aquifers: inferred but rarely measured?

The transport of DO with recharge water in crystalline-rock aquifers has been hypothesized by several works studying weathering profiles (Fletcher et al.; 2006; Brantley et al.; 2013; Bazilevskaya et al.; 2013; Sullivan et al.; 2016; Kim et al.; 2017; Antoniellini et al.; 2017; Krone et al.; 2021; Hampl et al.; 2022). While those works infer that DO transport in groundwater must be a common process in order to explain the presence of oxidized minerals in the first 100m below surface, only limited monitoring of DO at these depths has been conducted to support this hypothesis [e.g. (Bucher et al.; 2009; Bochet et al.; 2020; Ruff et al.; 2023)].

5.1 Drilling the bedrock or how DO opens fractures

Among the oxygen-consuming electron donors in Table I.2, iron is the most widespread element (Wedepohl; 1995). At near neutral-pH, iron is soluble in its reduced ferrous form (Fe^{2+}), which comes from the weathering of Fe(II)-bearing minerals. Fletcher et al. (2006) proposed that the reaction between DO and Fe-bearing minerals (see Equation I.10) is a process that results in a positive change in rock's volume, therefore producing Weathering Induced Fracturing (WIF):

$$FeO_{(s)} + 0.5O_2 + 1.5H_2O \longrightarrow Fe(OH)_{3(s)} \tag{I.10}$$

Here, $FeO_{(s)}$ represents a model ferrous mineral.

The high weatherability of biotite (Goldich; 1938), coupled with its widespread occurrence in various lithologies (Bisdom et al.; 1982), suggests that the weathering of this iron-bearing mineral is likely induced by the coupled action of CO_2 and DO. This mechanism is believed to contribute to the development of weathering-induced porosity (Buss et al.; 2008; Bazilevskaya et al.; 2013) and the deepening of weathering fronts (Kim et al.; 2017). Still, other Fe-bearing minerals such as pyroxene [e.g. Behrens et al. (2015)], hornblende [e.g. Fletcher et al. (2006)], chlorite [e.g. Liao et al. (2022)], and pyrite [e.g. Gu et al. (2020)] can also contribute to this process.

Biotite is a phyllosilicate from the mica family with a typical triple layer structure "TOT" (Tetrahedron-Octahedron-Tetrahedron) as illustrated in Figure I.3. The "O" sheets host octahedrally-coordinated cations like Mg^{2+}, Al^{3+}, Fe^{2+} and Fe^{3+}, while the "T" sheets host tetrahedrons of Si and Al (Stucki et al.; 2012). The TOT structure of biotite has a net negative charge that is compensated by the presence of interlayered K^+ atoms. Biotite weathers through a process known as vermiculitization (Wilson; 2004). The exact mechanism is still not clear but the common view of the process includes the action of water acidity to release cations from the octahedral sheets (Fe^{2+} and Mg^{2+}) and from interlayer space (K^+). The released iron is then oxidized by the presence of oxygen to form iron oxides in the interlayer space that gets expanded (see weathered biotite examples from Figure I.3). Because of its 2D structure, biotite dissolution is anisotropic, i.e. the dissolution rate in the edges of the sheets is more important than in the basal surface (Acker and Bricker; 1992; Malmström and Banwart; 1997).

The release of Fe^{2+} from biotite followed by its oxidation, is commonly described as a non-oxidative dissolution in two steps:

Cation release:

$$K(Mg_2Fe)(Si_3, Al)O_{10}(OH)_2 + 10H^+ \longrightarrow 2Mg^{2+} + Fe^{2+} + K^+ + Al^{3+} + 3H_4SiO_4 \tag{I.11}$$

Iron oxidation:

$$4Fe^{2+} + O_2 + 4H^+ \longrightarrow 4Fe^{3+} + 2H_2O \quad \text{(I.12)}$$

The produced ferric iron (Fe^{3+}) then forms a different variety of Fe oxyhydroxides depending on crystallisation conditions such as pH, presence of organic matter or temperature (Stucki et al.; 2012). Sung and Morgan (1980) have shown that the first mineral phase to be formed is lepidocrocite ($\gamma - FeOOH$) and it can further evolve into ferryhydrite, goethite and hematite. Moreover, the neoformed iron oxyhydroxides have an autocatalytic effect on Equation I.12 by providing adsorption sites for Fe^{2+} which lowers its activation energy and then increases the reaction rates (Tamura et al.; 1976; Sung and Morgan; 1980).

While equations I.11 and I.12 represent the commonly accepted mechanisms for non-oxidative dissolution of biotite, it has also been reported that biotite can undergo oxidative dissolution, in which iron is directly oxidized within the mineral structure (Buss et al.; 2008).

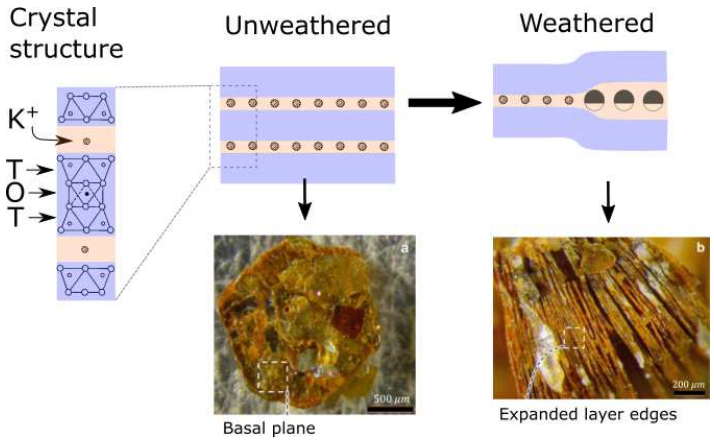

Figure I.3: **Schematics of biotite crystal structure and weathering mechanism.** Unweathered biotite is a 2D-layered mineral composed of TOT layers (i.e. an Octahedron sheet "O" sandwiched by two Tetrahedron sheets "T"). TOT layers are interlayered by K^+ atoms. During weathering, interlayer K^+ is released and substituted by secondary minerals of bigger volume. The expansion of the mineral generates weathering induced fracturing (WIF) (Fletcher et al.; 2006). Schematic figures have been adapted from (Bisdom et al.; 1982) while microscope images of weathered and unweathered biotite come from (Nanzyo and Kanno; 2018).

5.2 Microbe-mediated weathering of biotite

Microbes can mediate the biotite weathering in two different ways: (1) by chemical mechanisms that modify the physicochemical gradients or displace the chemical equilibrium of the mineral dissolution reaction or (2) by redox processes in which the structural iron of biotite is directly oxidized. In the first case, microbe-assisted dissolution of biotite has been demonstrated for different isolated species like *Bacillus subtilis, Shewanella putrefaciens, Pseudomonas putida* among others [e.g. Hopf et al. (2009); Grant et al. (2016)] and the mechanisms used by microbes to promote mineral dissolution include a variety of processes that are synthesized in Table I.3. In the second case, Bonneville et al. (2009, 2016) demonstrated that for shallow environments the capacity of mycorrhizal fungi to oxidize structural Fe(II) and found evidence for WIF in the biotite structure by the newly formed Fe(III) hydroxides. On the other hand, iron oxidizing bacteria (FeOB, described in next section) also have the capacity to oxidize structural Fe(II) from biotite (Shelobolina et al.; 2012) and this capacity of FeOB seems to extend beyond the microaerobic range (Napieralski et al.; 2019). **Nevertheless, little is known of how these microbe-mineral interactions actually operate in natural systems, where the action of isolates studied in laboratory settings can not be directly transposed to describe the action of complex microbial consortia. How are these microbe-mineral interactions affected by the compartmentalization or the variation of fluid redox conditions in the deep continental subsurface?**

Table I.3: **Microbial mechanisms that enhance mineral weathering.** References correspond to (1): (Uroz et al.; 2009), (2): (Hopf et al.; 2009), (3): (Balogh-Brunstad et al.; 2008), (4): (Ahmed and Holmström; 2015), (5): (Barker et al.; 1998), (6): (Bigham et al.; 2001), (7): (Bonneville et al.; 2016). Table based and enriched from the former review of Cuadros (2017).

Mechanism	Acting parameters	References
Chemical mechanisms		
Acid attack	Protons release; CO_2; carbonic, phosphoric, aliphatic, or aromatic acids; EPS acidic groups	e.g. (1), (2)
Chelating agents exudation	Oxalic or citric acid; siderophores and EPS that bind to Fe and displace chemical equilibrium towards mineral dissolution	e.g. (3), (4)
Cell adsorption or assimilation of dissolved ions	Displaces chemical equilibrium towards mineral dissolution	
Microenvironment creation	Biofilm around minerals creates microenvironments with aggressive pH or favorable redox and nutrient conditions	e.g. (5)
Redox mechanisms		
Structural redox reaction	Oxidation of structural elements (mainly Fe, Mn, S) promoting mineral cracking and dissolution	e.g. (6), (2), (7)

5.3 Iron oxidizing bacteria (FeOB): microbe-mediated oxidation of Fe^{2+} by DO

During the non-oxidative weathering of Fe-bearing minerals, Fe^{2+} is released into water and can be used as energy source for planktonic[5] iron-oxidizing bacteria (FeOB). FeOB are neutrophilic bacteria that form microbial mats in a variety of environments where iron-rich fluids encounter oxygenated water such as groundwater seeps (Vollrath et al.; 2012), hydrothermal vents (Edwards et al.; 2004) and fractured aquifers (Bochet et al.; 2020; Bethencourt et al.; 2020). FeOB microbial mats are built upon characteristic extracellular forms like stalks produced by *Gallionella* (Chan et al.; 2011), sheaths as produced by *Leptothrix* [e.g. (Vollrath; 2014)] or dreads produced by some *Mariprofundus sp.* (McAllister et al.; 2019). FeOB derive their metabolic energy from the electron transfer between iron and oxygen (Melton et al.; 2014). However, the rapid kinetics of Equation I.12 at near-neutral pH imply that FeOB are unable to outcompete the rapid abiotic oxidation of Fe^{2+} at high DO concentrations. As a result, FeOB preferentially grow under low DO concentrations where the half-life of Fe(II) is approximately 300 times higher than at high DO concentrations (Emerson et al.; 2010). This optimal range for FeOB growth under low DO concentrations is known as the *microaerobic range*, whose limits are between $1\mu M < [DO] < 30\mu M$ based on culture experiments of FeOB (Druschel et al.; 2008; Maisch et al.; 2019), but recent works suggest that the limits of the microaerobic range could be even lower (Berg et al.; 2022). Moreover, depending on the FeOB genus, the habitat requirements in terms of Fe^{2+} and pH ranges can be very different (Eggerichs et al.; 2014). For instance, *Gallionella* is an obligate iron-oxidizing and microaerobic genus that grows optimally at slightly acid conditions ($6.3 < pH < 6.6$) (Kucera and Wolfe; 1957). On the other hand, *Leptothrix* is a facultative FeOB that tolerates higher DO and pH levels (Zhang et al.; 2002; Vollrath; 2014). To sum it up, FeOB have been studied essentially as planktonic organisms which can thrive from the oxidation of dissolved iron in near-neutral microaerobic environments. **Nevertheless, little is known about how the activity of FeOB is actually transposed in natural environments where they form part of microbial consortia. Is the microaerobic range also relevant to explain the activity of FeOB in natural settings? How do changes in redox conditions affect the availability of dissolved iron which is essential for FeOB? How are FeOB related with mineral-attached microbial consortia, where they could access solid-supported iron sources?**

[5]The term planktonic refers to microbes which are suspended and can be advected with water flow, contrary to attached microbes which are fixed to mineral surfaces.

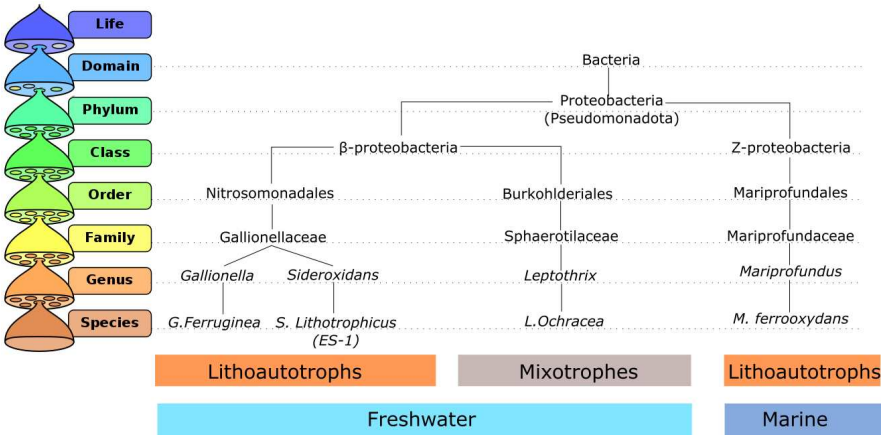

Figure I.4: **Phylogeny of the most common iron oxidizing bacteria (FeOB) reported in the literature.** Phylogenetic classification is as reported by De Vienne (2016) and has been limited to the most common proteobacteria. Nonetheless, Emerson et al. (2010) has reported 6 more phylum that include bacteria and archaea known to oxidize iron.

5.4 Partial conclusion: linking Fe and O_2 cycles in the continental subsurface

Understanding the links between rock-weathering processes and DO fate in groundwater is a key aspect since the weathering of minerals provide the electron donors that react with DO. A particularly relevant case is the one of iron because it is the most abundant electron donor in the upper Earth's crust. The figure below summarizes the reactive network of the processes presented in the previous sections. Iron-bearing minerals are the primary source of ferrous iron (structural Fe(II) or $Fe(II)_s$). **The reaction of ferrous minerals with dissolved O_2 triggers weathering**, leading to either direct oxidation of $Fe(II)_s$ or non-oxidative release of aqueous ferrous iron (Fe^{2+}). In the latter case, aqueous oxidation of iron by oxygen generates Fe(III)-oxyhydroxides, which have autocatalytic properties and increase Fe^{2+} oxidation. Microbes can thrive from the electron transfer during iron oxidation and, therefore, are common mediators of both $Fe(II)_s$ and Fe^{2+} oxidation reactions. Still, as found in laboratory experiments **microbial activity occurs preferentially at low *microaerobic* O_2 concentrations, where microbes can outcompete the abiotic oxidation reaction of iron**.

When seen in the context of natural environments, the different reactions presented in this section can be limited by an important fact: while the iron source comes from underground rock minerals, the O_2 source is in the atmosphere. Therefore, the occurrence of the reactive processes of Figure I.5 depend on whether O_2 can be delivered by groundwater flow to the subsurface, i.e. **the fate of DO in aquifers is a reactive-transport problem that is presented in the next section**.

6 Reactive transport: a dialog between hydrology and reaction kinetics

6.1 The transport vs reaction continuum

The mass conservation equation for DO in a fractured system is determined by the balance between the kinetics of DO-consuming reactions (e.g. Figure I.5) and the hydrological dynamics that transport DO with recharge water. This is expressed by the Advection-Diffusion Equation (Steefel and Lasaga; 1994) illustrated in Figure I.6. In crystalline aquifers, the solute transport can occur either by advection-dispersion in fractures or by diffusion in the matrix. Indeed, fractured-rocks are usually conceptualized as double porosity systems composed of two compartments: (1) the matrix (*primary* porosity compartment) where both porosity and transmissivity are low and (2) the fractures (*secondary* porosity compartment) where both porosity and transmissivity are high (Caine et al.; 1996; Singhal; 2008; Bense et al.; 2013). Due to the contrasted hydrodynamic properties of the matrix and fracture compartments, the transport rates in these two compartments are radically different and

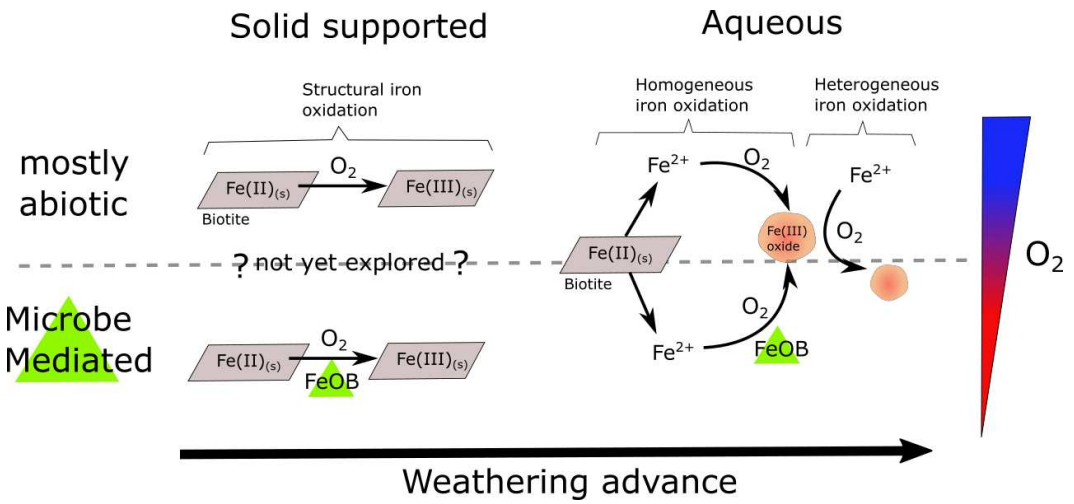

Figure I.5: **Network of reactive process relating the iron and the oxygen cycles in groundwater.** Iron oxidizing bacteria (FeOB) are involved in microbe mediated processes which are favored by low micro-aerobic DO concentrations. While researchers have demonstrated the microaerobic effect in aqueous reactions, its impact on solid supported reactions remains unexplored.

leads to characteristic transport times that are orders of magnitude longer for diffusion than advection (Grisak and Pickens; 1980). As previously shown in Figure I.5, the reaction with mineral surfaces is the triggering process of DO consumption and therefore, the ability of O_2 to reach ferrous minerals in fracture walls or in matrix pores depends on whether a hydrogeological system is transport or reaction limited. A convenient way to classify a system in this regard is the dimensionless number of Damköhler (Da), defined as the ratio of the characteristic transport and reaction timescales (Maher; 2010; Maher and Chamberlain; 2014). A system is defined as transport limited if the transport timescale is longer than the reaction timescale ($Da > 1$) or reaction limited in the opposite case ($Da < 1$). For instance, a reaction limited system favors the persistence of DO in groundwater either because the host rocks are poorly reactive (low content of ferrous minerals) or because the transport properties of the aquifer favor groundwater flow.

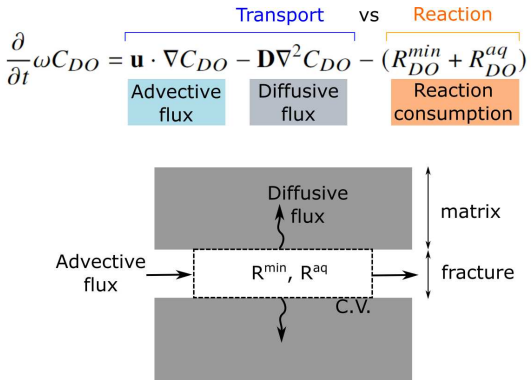

Figure I.6: **Illustration of the Advection-Diffusion Equation** adapted for the mass conservation of dissolved oxygen (DO) in a *control volume* (C.V.) in a fractured-rock system. Quantities involved in the equation are: ω is the porosity of the system, C_{DO} the DO concentration, $\mathbf{u}$ the Darcian flux, $\mathbf{D}$ the dispersion-diffusion tensor and R represents the DO consumption terms by both mineral (*min*) and aqueous (*aq*) reactions.

6.2 Feedbacks between transport and reaction processes

Depending on whether a system is transport or reaction limited affects the distribution of O_2 in the subsurface. A good illustration of this is the fact that crystalline rocks with lower contents of Fe-bearing minerals systematically

present thicker regoliths[6] (Bazilevskaya et al.; 2013). In a model aiming to predict the regolith thickness as a function of the geological context, Bazilevskaya et al. (2013) proposes that the less reactive rocks (i.e. rocks with low contents of Fe-bearing minerals like granite) allow DO to persist for longer times in the saturated zone, thus reaching deeper horizons in the aquifer. Since the presence of DO triggers regolith development and porosity creation through WIF as introduced in Section 5.1, the deeper oxic zone in low reactive rocks results in the formation of a deeper regolith (Figure I.7-A). This example illustrates a positive feedback between reactive and transport processes in poorly reactive rocks: DO facilitates new porosity formation through mineral weathering, which in turn facilitates the weathering of new minerals and creation of new porosity (Figure I.7-A). Similarly, highly reactive rocks present shallower regoliths because DO is depleted more rapidly and no WIF is produced (Figure I.7-B).

The conceptual model of Bazilevskaya et al. (2013) applies to bedrocks in which the initial state of the rocks is massive and fractures are mostly created through WIF. Nevertheless, crystalline rocks are most of the times characterized by complex fracture networks around fault zones that enhance transport and groundwater flow (Olsson and Gale; 1995; Caine et al.; 1996; Bense et al.; 2013). Thus, fractures can compensate the fast DO depletion in high reactive rocks allowing for a positive feedback between O_2 and WIF and the creation of thick regolith (Figure I.7-C). This latter case is perhaps the most relevant because bedrocks with inherited fracture networks offer strategic groundwater resources (Roques et al.; 2014, 2016), play a key role to sustain intraterrestrial life (Bochet et al.; 2020) and also threaten underground waste disposal sites, in which stable redox conditions are needed to avoid the remobilization of contaminants (Sidborn and Neretnieks; 2008).

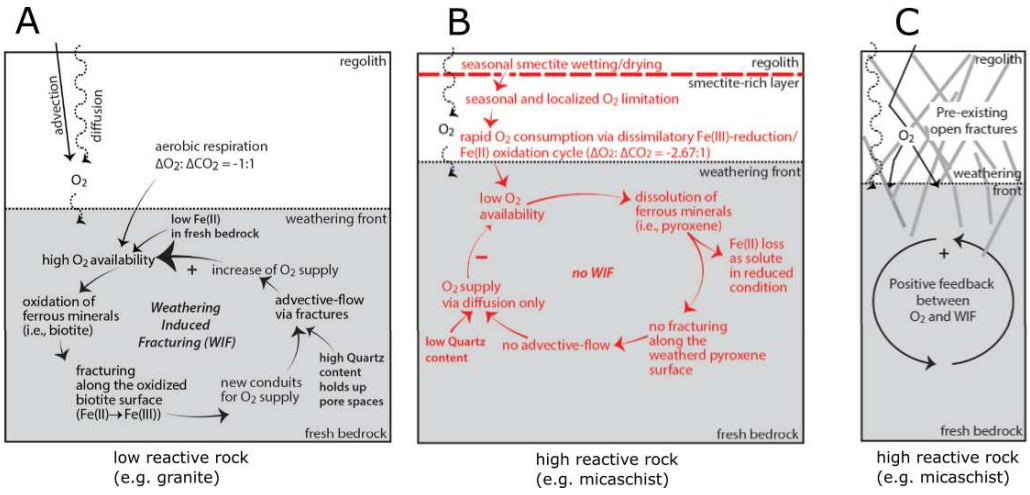

Figure I.7: **Feedbacks between regolith formation in crystalline rocks and reactive transport of DO as conceptualized by Kim et al. (2017).** A) in low reactive rocks (low content of Fe-bearing minerals), dissolved oxygen (DO) can persist in groundwater, producing weathering induced fracturing (WIF) that enhances DO transport. This creates a positive feedback that results in thick regolith. B) In high reactive rocks, DO is easily depleted, minerals dissolve in reduced conditions that do not generate WIF. The resulting negative feedback leads to thin regolith. C) The rapid depletion of DO in high reactive rocks can be counterbalanced by the presence of fractures that enhance oxic groundwater transport and DO availability. This way, a positive feedback leads to WIF and results in thick regolith formation.

6.3 Key parameters controlling reactive transport of DO in crystalline rocks

Considerable efforts have been devoted to conceptualize and model the reactive transport of DO in fractured rocks, primarily due to the oxidizing power of O_2 which poses a safety threat to future projects of nuclear waste storage in crystalline rocks. The reactive transport of DO of those systems has been modelled by following three main approaches in which the Advection-Diffusion equation is applied (Macquarrie et al.; 2010): 1)

[6]In aquifers composed of crystalline rock, the regolith refers to the portion that corresponds to weathered rocks. The regolith includes the saprolite, which represents a low state of weathering, as well as the soil horizons, which correspond to an advanced state of weathering.

equivalent porous medium (EPM) models for fracture zones, 2) discrete fracture models (DFN) with reactive infill and no interaction with the adjacent rock matrix, and 3) single fracture–matrix models in which the fracture and/or matrix may contain reactive minerals. The choice of the conceptual model, that mainly depends on the geological context and the timescales of the problem, can lead to significant differences in the predictions of DO penetration in fractured-rocks (Macquarrie et al.; 2010). For instance, whether groundwater flow can be considered to occur in a single fracture or in a fracture zone determines if the more suitable model is, respectively, a single fracture model or an EPM. Also, depending on the timescales of the reactive transport problem, the DO diffusion into the matrix can play a significant role.

Numerical studies simulating the advance of the redox front in granitic rocks (Spiessl et al.; 2008; Macquarrie et al.; 2010) have found that the main parameters that influence the penetration depth of the redox front in single fracture and EPM models are the fluid velocity in the fractures and the dissolution rate of minerals in the matrix. Simulations in more realistic domains such as DFN models (Trinchero et al.; 2017, 2018) have shown that transmissive fractures and deformation zones are preferential pathways along which dissolved O_2 reaches the subsurface. These simulations have also shown that an heterogeneous distribution of ferrous minerals in the host rock can produce a finger shaped redox front, with a deeper O_2 penetration when ferrous minerals are absent in the model domain.

Due to the nature of the nuclear waste repositories, where nuclear waste must be stored in low permeable media for several thousand years (about $10^2 ky$), most of these reactive transport models have found that diffusion into the matrix is an important control on DO penetration. Indeed, diffusion into the rock matrix gives access to a bigger amount of reactive minerals than the one that is exposed in the fracture wall (see Figure I.6), thus increasing the extent of DO consuming reactions (Spiessl et al.; 2008; Macquarrie et al.; 2010). In this context, approximate analytical solutions to model the diffusive advance of the redox front in the rock matrix have been obtained (Sidborn and Neretnieks; 2007, 2008; Rajaram and Arshadi; 2016; Antoniellini et al.; 2017) by doing some important simplifications which are relevant for slow flow systems under large timescales (thousands of years):

1. Consider instantaneous mineral dissolution reactions compared to transport, i.e. *pseudo steady state* approximation (Neretnieks; 1986).
2. Consider that diffusion timescales are comparable to advection timescales, i.e. diffusion-dominated transport.
3. Focus on abiotic processes by neglecting the contribution of microbes into DO reactivity.

6.4 DO reactive transport under short timescales: advection and reactive hotspots in fractured systems

In the context of modern groundwater systems, most of the above assumptions are not suitable. In fact, groundwater residence times in active flow catchments are generally in the order of several hundred years (Sprenger et al.; 2019). At these timescales, DO diffusion in the matrix may be assumed to be relatively small compared to advective fluxes (Grisak and Pickens; 1980) while mineral dissolution rates cannot be assumed to be fast (Maher et al.; 2006). **It is therefore necessary to establish a kinetic treatment of rock weathering reactions which are potentially impacted by the presence of O_2 in the subsurface (e.g. Figure I.5) and assess their importance with respect to advection timescales with the Advection-Diffusion Equation (Figure I.6).**

Moreover, the participation of O_2 in multiple microbe-mediated reactions (see Table I.2) implies that the microbial contribution in the reactive transport models should not be neglected. While subsurface aerobic metabolisms in deep reducing environments are supposed to be limited by the absence of DO, fractures favoring the fast infiltration of oxic groundwater can indeed deliver DO and trigger aerobic metabolisms in the subsurface (see Figure I.8). While the response rate of subsurface microbial communities to this fast-recharge events is

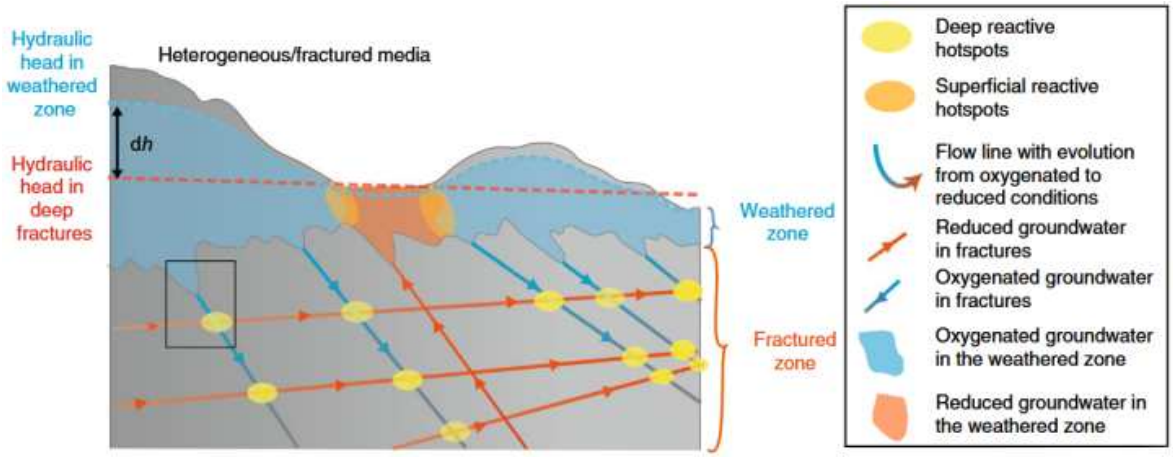

Figure I.8: **Illustration of intermittent reactive hotspots in the subsurface.** Fractures have been shown to provide a strong hydraulic connectivity between surface and subsurface environments, allowing for the deep transport of DO in the subsurface during intermittent recharge events. The mixing between oxic and reducing groundwater at the intersection of fractures triggers redox reactions that stimulate microbial activity in the so-called *deep reactive hotspots*. Figure and conceptual model by Bochet et al. (2020).

not well constrained, fractures conducting oxic groundwater have been related with more diverse and abundant microbial communities (Bethencourt et al.; 2020). **Do microbial communities have the capacity to enhance DO depletion rates in the subsurface? Can the deep biosphere thrive from these fast recharge events of oxic groundwater?**

6.5 Partial conclusion: reactive transport treatment for DO in the subsurface

This section introduced the transport vs reaction continuum that determines the redox state of groundwater in fractured-rock aquifers. This reactive transport problem has been treated by two main research communities that were reviewed in this section: (1) the *rock weathering community* for which DO is a weathering agent and its presence in the subsurface is a primer that defines the depth of weathering fronts and (2) the *nuclear waste community* for which DO is a safety threat for nuclear storage projects. In the first case, the observation that lithologies with lower proportions of ferrous minerals exhibit a deeper weathering front led to the identification of feedback mechanisms between the transport and reactive processes of dissolved oxygen (DO). Lithologies characterized by low reactivity or those containing inherited fractures promote positive feedback loops: DO persists at greater depths in groundwater, initiating the weathering of fresh minerals that leads to the opening of porosity. This subsequently facilitates the transport of DO. In contrast, high-reactive lithologies lead to a negative feedback loop: Dissolved oxygen (DO) is rapidly consumed by mineral weathering reactions, preventing the initiation of porosity creation in fresh minerals. As a result, DO transport is diminished. **These studies highlight the importance of the reactive transport approach since both reactivity and transport determine the advance of the redox front.** In the case of nuclear waste research, the reactive transport of DO has been tackled more directly. The use of a variety of numerical and analytical approaches has led to identify that O_2-rich groundwater infiltrates preferentially in transmissive fractures and deformation zones. In such pathways, the groundwater velocity and the reaction kinetics between DO and ferrous minerals are the main controls. **A common characteristic of a majority of these research works is that they are focused on very long timescales (relevant for nuclear waste storage or for rock-weathering surveys) and on environments where groundwater flow is slow. This leads to several simplifications that are unsuitable for DO reactive transport in active catchments (see Box I.5). A conceptual framework for the transport and reactive processes of DO at time-scales relevant for modern groundwater systems is still missing. What are the impacts of the presence of oxic groundwater on processes occurring at these short time-scales, such as microbial activity?**

Box I.5 - Current view of DO reactive transport: the problem of timescales

Because the rock weathering community addresses questions on a geological timescale, the reactive transport of DO is treated by a *palaeo-hydrogeological* approach, i.e. oxygenated groundwater is **inferred** through the mineralogical record rather than measured *in-situ* [e.g. (Dideriksen et al.; 2010; Bazilevskaya et al.; 2013; Antoniellini et al.; 2017; Kim et al.; 2017; Krone et al.; 2021; Hampl et al.; 2022)]. Similarly, the nuclear waste community studies the reactive transport of DO over timescales around $10^2 ky$ for which several strong hypotheses are relevant. To the best of our knowledge, those two communities cover the essential of the research that has tackled the reactive transport of DO in aquifers. It means that this reactive transport problem has not been assessed for short timescales that are relevant for groundwater residence times in modern groundwater systems (in the order of $10^2 y$). At these short timescales, some of the assumptions of the previous studies loose validity and need to be reconsidered. For instance, the timescale ratio between advective and diffusive transport or between transport and reactive processes. Likewise, microbe-mediated process which are neglected on long term models must be considered at short timescales. In fact, turnover times of microbial communities in the deep continental subsurface are compatible with timescales below $10^2 y$ (Templeton and Caro; 2023).

7 Chapter conclusion: DO at the crossroads of groundwater, microbes and mineral interactions

In the words of Brantley et al. (2011), the critical zone is described as 'the realm where rocks meet life'. Extending this assertion to the deep continental subsurface introduces the crucial role of water into the scenario (other fluids such as oil and gas are also present, but they are less prevalent than water). In fact, the deep continental subsurface primarily consists of pores and fractures saturated with water. The interface between rocks and water forms the primary nexus where the biosphere interacts with minerals. This interaction is characterized by intricate feedback loops among the three principal actors mentioned earlier: water, minerals, and microbes. This intricate interplay is illustrated in Figure I.9.

Many of the biogeochemical processes involved in Figure I.9 could be affected by the redox conditions of groundwater, but these effects are poorly constrained in the continental subsurface. In the present chapter, we have shown that dissolved O_2 is central in redox reactions in the subsurface, with major consequences on water quality, rock-weathering and micro-organism metabolism. Therefore, **understanding the factors that control its distribution is essential to better understand the biogeochemical processes than can operate in groundwater environments**.

While in surface environments the biogeochemical rates are controlled by dynamic processes that depend on daily and seasonal cycles, the deep continental subsurface is commonly viewed as a more inertial system, related to stable geological processes. Nevertheless, the examples shown throughout this chapter have presented some pieces of evidence pointing to the presence of dissolved O_2 in subsurface environments. **Since the presence of dissolved O_2 in the subsurface is closely related to variable hydrological fluxes, a potentially O_2-dependant deep biosphere challenges the view of the subsurface environment as an inertial system.** In this work we will tackle this problem by first identifying the controls and mechanisms that allow the transport of dissolved O_2 in the deep subsurface, and then exploring the potential consequences on a *dynamic* deep subsurface.

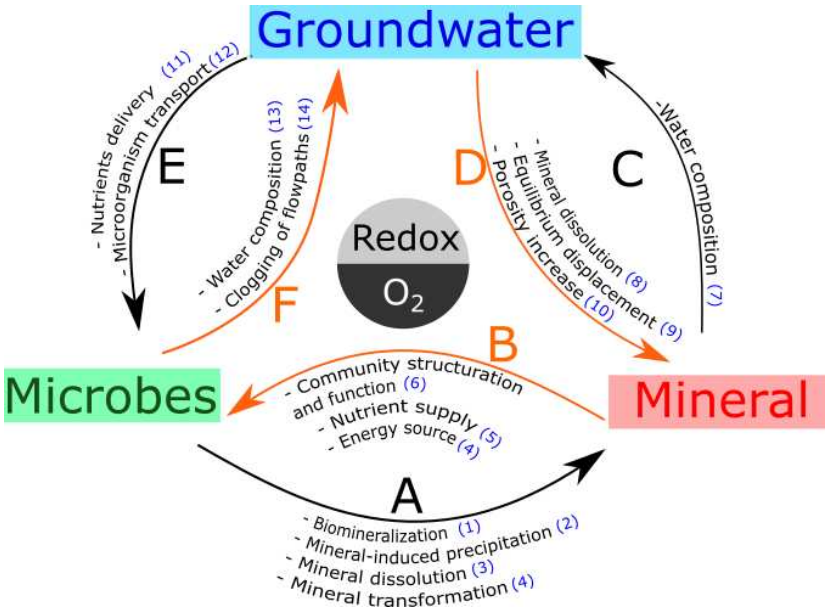

Figure I.9: **Feedbacks between minerals, water and life in the deep continental subsurface.** Most of the processes involved here are sensitive to redox conditions, which are controlled by the dissolved O_2 concentration in groundwater. References correspond to **1:** (Benzerara et al.; 2011), **2:** (Chan et al.; 2011), **3:** (Samuels et al.; 2020), **4:** (Shelobolina et al.; 2012; Napieralski et al.; 2019), **5:** (Gadd; 2010), **6:** (Uroz et al.; 2015; Jones and Bennett; 2017), **7:** (McMahon and Chapelle; 2008), **8:** (Lasaga; 1984; Brantley et al.; 2008), **9:** (Maher; 2010), **10:** (Buss et al.; 2008; Kim et al.; 2017), **11:** (Bochet et al.; 2020), **12:** (Borgonie et al.; 2019; Zhang et al.; 2022), **13:** (Bagnoud et al.; 2016), **14:** (Kurz et al.; 2022)

Bibliography

Acker, J. G. and Bricker, O. P. (1992). The influence of pH on biotite dissolution and alteration kinetics at low temperature. *Geochimica et Cosmochimica Acta*, 56(8):3073–3092.

Ahmed, E. and Holmström, S. J. M. (2015). Microbe – mineral interactions : The impact of surface attachment on mineral weathering and element selectivity by microorganisms. *Chemical Geology*, 403:13–23.

Amiotte Suchet, P., Probst, J.-L., and Ludwig, W. (2003). Worldwide distribution of continental rock lithology: Implications for the atmospheric/soil CO2 uptake by continental weathering and alkalinity river transport to the oceans. *Global Biogeochemical Cycles*, 17(2):1038.

Anantharaman, K., Brown, C. T., Hug, L. A., Sharon, I., Castelle, C. J., Probst, A. J., Thomas, B. C., Singh, A., Wilkins, M. J., Karaoz, U., Brodie, E. L., Williams, K. H., Hubbard, S. S., and Banfield, J. F. (2016). Thousands of microbial genomes shed light on interconnected biogeochemical processes in an aquifer system. *Nature Communications*, 7:1–11.

Anderson, S. P., Bales, R. C., and Duffy, J. (2008). Critical Zone Observatories : Building a network to advance interdisciplinary study of Earth surface processes. *Mineralogical Magazine*, 72(1):7–10.

Antoniellini, M., Mollema, P., and Del Sole, L. (2017). Application of analytical diffusion models to outcrop observations: Implications for mass transport by fluid flow through fractures. *Water Resources Research*, 53:5545–5566.

Appelo, C. A. J. and Postma, D. (2004). *Geochemistry, groundwater and pollution*. CRC press.

Aragno, M. (1992). Thermophilic, Aerobic, Hydrogen-Oxidizing (Knallgas) Bacteria. In Balows, A., Trüper, H. G., Dworkin, M., Harder, W., and Schleifer, K.-H., editors, *The Prokaryotes*, pages 3917–3933. Springer New York, New York, NY.

Bagnoud, A., Chourey, K., Hettich, R. L., De Bruijn, I., Andersson, A. F., Leupin, O. X., Schwyn, B., and Bernier-Latmani, R. (2016). Reconstructing a hydrogen-driven microbial metabolic network in Opalinus Clay rock. *Nature Communications*, 7:1–10.

Balogh-Brunstad, Z., Kent Keller, C., Thomas Dickinson, J., Stevens, F., Li, C. Y., and Bormann, B. T. (2008). Biotite weathering and nutrient uptake by ectomycorrhizal fungus, Suillus tomentosus, in liquid-culture experiments. *Geochimica et Cosmochimica Acta*, 72(11):2601–2618.

Bar-on, Y. M., Phillips, R., and Milo, R. (2018). The biomass distribution on Earth. *Proceedings of the National Academy of Sciences of the United States of America*, 115(25):6506–6511.

Barker, W. W., Welch, S. A., Chu, S., and Banfield, J. F. (1998). Experimental.observations of the effects of bacteria on aluminosilicate weathering. *American Mineralogist*, 83(11-12 PART 2):1551–1563.

Bazilevskaya, E., Lebedeva, M., Pavich, M., Rother, G., Parkinson, D. Y., Cole, D., and Brantley, S. L. (2013). Where fast weathering creates thin regolith and slow weathering creates thick regolith. *Earth Surface Processes and Landforms*, 38:847–858.

Behrens, R., Bouchez, J., Schuessler, J. A., Dultz, S., Hewawasam, T., and Von Blanckenburg, F. (2015). Mineralogical transformations set slow weathering rates in low-porosity metamorphic bedrock on mountain slopes in a tropical climate. *Chemical Geology*, 411:283–298.

Bense, V., Gleeson, T., Loveless, S., Bour, O., and Scibek, J. (2013). Fault zone hydrogeology. *Earth-Science Reviews*, 127:171–192.

Benzerara, K., Miot, J., Morin, G., Ona-Nguema, G., Skouri-Panet, F., and Férard, C. (2011). Significance, mechanisms and environmental implications of microbial biomineralization. *Comptes Rendus Geoscience*, 343(2):160–167.

Berg, J. S., Ahmerkamp, S., Pjevac, P., Hausmann, B., Milucka, J., and Kuypers, M. M. M. (2022). How low can they go? Aerobic respiration by microorganisms under apparent anoxia. *FEMS Microbiology Reviews*, 46(3):fuac006.

Bethencourt, L., Bochet, O., Farasin, J., Aquilina, L., Borgne, T. L., Quaiser, A., Biget, M., Michon-Coudouel, S., Labasque, T., and Dufresne, A. (2020). Genome reconstruction reveals distinct assemblages of Gallionellaceae in surface and subsurface redox transition zones. *FEMS Microbiology Ecology*, 96(5).

Bigham, J. M., Bhatti, T. M., Vuorinen, A., and Tuovinen, O. H. (2001). Dissolution and structural alteration of phlogopite mediated by proton attack and bacterial oxidation of ferrous iron. *Hydrometallurgy*, 59(2-3):301–309.

Bisdom, E., Stoops, G., Delvigne, J., Curmi, P., and Altemüller, H. (1982). Micromorphology of weathering biotite and its secondary products. *Pedologie*, 32.

Bochet, O., Bethencourt, L., Dufresne, A., Farasin, J., Pédrot, M., Labasque, T., Chatton, E., Lavenant, N., Petton, C., Abbott, B. W., Aquilina, L., and Le Borgne, T. (2020). Iron-oxidizer hotspots formed by intermittent oxic–anoxic fluid mixing in fractured rocks. *Nature Geoscience*, 13(2):149–155.

Bonneville, S., Bray, A. W., and Benning, L. G. (2016). Structural Fe(II) Oxidation in Biotite by an Ectomycorrhizal Fungi Drives Mechanical Forcing. *Environmental Science & Technology*, 50(11):5589–5596.

Bonneville, S., Smits, M. M., Brown, A., Harrington, J., Leake, J. R., Brydson, R., and Benning, L. G. (2009). Plant-driven fungal weathering: Early stages of mineral alteration at the nanometer scale. *Geology*, 37(7):615–618.

Borch, T., Kretzschmar, R., Kappler, A., Van Cappellen, P., Ginder-Vogel, M., Voegelin, A., and Campbell, K. (2009). Biogeochemical Redox Processes and their Impact on Contaminant Dynamics. *Environmental Science and Technology*, 44:15–23.

Borgonie, G., Magnabosco, C., García-Moyano, A., Linage-Alvarez, B., Ojo, A. O., Freese, L. B., Van Jaarsveld, C., Van Rooyen, C., Kuloyo, O., Cason, E. D., Vermeulen, J., Pienaar, C., Van Heerden, E., Sherwood Lollar, B., Onstott, T. C., and Mundle, S. O. (2019). New ecosystems in the deep subsurface follow the flow of water driven by geological activity. *Scientific Reports*, 9(1):1–16.

Brantley, S. L., Goldhaber, M. B., and Vala Ragnarsdottir, K. (2007). Crossing disciplines and scales to understand the critical zone. *Elements*, 3(5):307–314.

Brantley, S. L., Holleran, M. E., Jin, L., and Bazilevskaya, E. (2013). Probing deep weathering in the Shale Hills Critical Zone Observatory, Pennsylvania (USA): The hypothesis of nested chemical reaction fronts in the subsurface. *Earth Surface Processes and Landforms*, 38(11):1280–1298.

Brantley, S. L., Kubicki, J., and White, A. F. (2008). *Kinetics of Water-Rock Interaction*. Springer, New York.

Brantley, S. L., Megonigal, J. P., Scatena, F. N., Barnes, R. T., Bruns, M. A., Cappellen, P. V. A. N., Dontsova, K., Hartnett, H. E., and Hartshorn, A. S. (2011). Twelve testable hypotheses on the geobiology of weathering. *Geobiology*, 9:140–165.

Bucher, K., Zhu, Y., and Stober, I. (2009). Groundwater in fractured crystalline rocks, the Clara mine, Black Forest (Germany). *International Journal of Earth Sciences*, 98(7):1727–1739.

Buss, H. L., Sak, P. B., Webb, S. M., and Brantley, S. L. (2008). Weathering of the Rio Blanco quartz diorite , Luquillo Mountains , Puerto Rico : Coupling oxidation , dissolution , and fracturing. *Geochimica et Cosmochimica Acta*, 72:4488–4507.

Caine, J. S., Evans, J. P., and Forster, C. B. (1996). Fault zone architecture and permeability structure. *Geology*, 24(11):1025–1028.

Canfield, D. (2004). Canfield, D. E. The Early History of atmospheric oxygen: Homage to Robert M. Garrels. Annu. Rev. Earth. Planet. Sci. 33, 1-36. *Annu Rev Earth Pl Sci*, 33:1–36.

Chan, C. S., Fakra, S. C., Emerson, D., Fleming, E. J., and Edwards, K. J. (2011). Lithotrophic iron-oxidizing bacteria produce organic stalks to control mineral growth: Implications for biosignature formation. *ISME Journal*, 5(4):717–727.

Chapelle, F. H., Bradley, P. M., Mcmahon, P. B., Kaiser, K., and Benner, R. (2012). Dissolved Oxygen as an Indicator of Bioavailable Dissolved Organic Carbon in Groundwater. *Ground Water*, 50(2):230–241.

Chen, W.-F. and Liu, T.-K. (2003). Dissolved oxygen and nitrate of groundwater in Choshui Fan-Delta, western Taiwan. *Environmental Geology*, 44(6):731–737.

Cuadros, J. (2017). Clay minerals interaction with microorganisms: A review. *Clay Minerals*, 52(2):235–261.

De Vienne, D. M. (2016). Lifemap: Exploring the Entire Tree of Life. *PLOS Biology*, 14(12):e2001624.

DeSimone, L., Mcmahon, P. B., and Rosen, M. (2014). The quality of our Nation's waters - Water quality in Principal Aquifers of the United States, 1991-2010. Technical report, U.S. Geological Survey Circular 1360.

Dideriksen, K., Christiansen, B. C., Frandsen, C., Balic-Zunic, T., Mørup, S., and Stipp, S. L. S. (2010). Paleo-redox boundaries in fractured granite. *Geochimica et Cosmochimica Acta*, 74(10):2866–2880.

Druschel, G. K., Emerson, D., Sutka, R., Suchecki, P., and Luther, G. W. (2008). Low-oxygen and chemical kinetic constraints on the geochemical niche of neutrophilic iron(II) oxidizing microorganisms. *Geochimica et Cosmochimica Acta*, 72(14):3358–3370.

Edwards, K. J., Bach, W., McCollom, T. M., and Rogers, D. R. (2004). Neutrophilic iron-oxidizing bacteria in the ocean: Their habitats, diversity, and roles in mineral deposition, rock alteration, and biomass production in the deep-sea. *Geomicrobiology Journal*, 21(6):393–404.

Edwards, K. J., Becker, K., and Colwell, F. (2012). The Deep, Dark Energy Biosphere: Intraterrestrial Life on Earth. *Annual Review of Earth and Planetary Sciences*, 40(1):551–568.

Eggerichs, T., Opel, O., Otte, T., and Ruck, W. (2014). Interdependencies between Biotic and Abiotic Ferrous Iron Oxidation and Influence of pH, Oxygen and Ferric Iron Deposits. *Geomicrobiology Journal*, 31(6):461–472.

Ehrlich, H. L., Newman, D. K., and Kappler, A., editors (2015). *Ehrlich's Geomicrobiology*. CRC Press, 0 edition.

Emerson, D., Fleming, E. J., and McBeth, J. M. (2010). Iron-Oxidizing Bacteria: An Environmental and Genomic Perspective. *Annual Review of Microbiology*, 64(1):561–583.

Ettwig, K. F., Butler, M. K., Le Paslier, D., Pelletier, E., Mangenot, S., Kuypers, M. M. M., Schreiber, F., Dutilh, B. E., Zedelius, J., de Beer, D., Gloerich, J., Wessels, H. J. C. T., van Alen, T., Luesken, F., Wu, M. L., van de Pas-Schoonen, K. T., Op den Camp, H. J. M., Janssen-Megens, E. M., Francoijs, K.-J., Stunnenberg, H., Weissenbach, J., Jetten, M. S. M., and Strous, M. (2010). Nitrite-driven anaerobic methane oxidation by oxygenic bacteria. *Nature*, 464(7288):543–548.

Falkowski, P. G. (2006). Tracing Oxygen's Imprint on Earth's Metabolic Evolution. *Science*, 311(5768):1724–1725.

Fletcher, R. C., Buss, H. L., and Brantley, S. L. (2006). A spheroidal weathering model coupling porewater chemistry to soil thicknesses during steady-state denudation. *Earth and Planetary Science Letters*, 244(1-2):444–457.

Gadd, G. M. (2010). Metals, minerals and microbes: Geomicrobiology and bioremediation. *Microbiology*, 156(3):609–643.

Goldich, S. S. (1938). A Study in Rock-Weathering. *The Journal of Geology*, 46(1):17–58.

Grant, M. R., Tymon, L. S., Helms, G. L., Thomashow, L. S., Kent Keller, C., and Harsh, J. B. (2016). Biofilm adaptation to iron availability in the presence of biotite and consequences for chemical weathering. *Geobiology*, 14(6):588–598.

Grisak, G. E. and Pickens, J. F. (1980). Solute transport through fractured media: 1. The effect of matrix diffusion. *Water Resources Research*, 16(4):719–730.

Gu, X., Heaney, P. J., Reis, F. D., and Brantley, S. L. (2020). Deep abiotic weathering of pyrite. *Science*, 370(6515).

Gutsalo, L. K. (1971). Radiolysis of water as the source of free oxygen in the underground hydrosphere. *Geochem. Int.*, 8(6):897–903.

Hampl, F. J., Schiperski, F., Byrne, J. M., Schwerdhelm, C., Kappler, A., Bryce, C., von Blanckenburg, F., and Neumann, T. (2022). The role of iron-bearing minerals for the deep weathering of a hydrothermally altered plutonic rock in semi-arid climate (Chilean Coastal Cordillera). *Chemical Geology*, 604:120922.

Hazen, R. M., Papineau, D., Bleeker, W., Downs, R. T., Ferry, J. M., McCoy, T. J., Sverjensky, D. A., and Yang, H. (2008). Mineral evolution. *American Mineralogist*, 93(11-12):1693–1720.

Hedges, S. B., Blair, J. E., Venturi, M. L., and Shoe, J. L. (2004). A molecular timescale of eukaryote evolution and the rise of complex multicellular life. *BMC Evolutionary Biology*, 4(1):2.

Hopf, J., Langenhorst, F., Pollok, K., Merten, D., and Kothe, E. (2009). Influence of microorganisms on biotite dissolution: An experimental approach. *Chemie der Erde*, 69(S2):45–56.

Houghton, J. and Seyfried Jr, W. (2010). An experimental and theoretical approach to determining linkages between geochemical variability and microbial biodiversity in seafloor hydrothermal chimneys. *Geobiology*, 8(5):457–470.

Jones, A. A. and Bennett, P. C. (2017). Mineral Ecology : Surface Specific Colonization and Geochemical Drivers of Biofilm Accumulation , Composition , and Phylogeny. *Frontiers in Microbiology*, 8(March):1–14.

Kappler, A. and Bryce, C. (2017). Cryptic biogeochemical cycles: Unravelling hidden redox reactions. *Environmental Microbiology*, 19(3):842–846.

Kim, H., Stinchcomb, G., and Brantley, S. L. (2017). Feedbacks among O2 and CO2 in deep soil gas , oxidation of ferrous minerals , and fractures : A hypothesis for steady-state regolith thickness. *Earth and Planetary Science Letters*, 460:29–40.

Könneke, M., Bernhard, A. E., de la Torre, J. R., Walker, C. B., Waterbury, J. B., and Stahl, D. A. (2005). Isolation of an autotrophic ammonia-oxidizing marine archaeon. *Nature*, 437(7058):543–546.

Krone, L. V., Hampl, F. J., Schwerdhelm, C., Bryce, C., Ganzert, L., Kitte, A., Übernickel, K., Dielforder, A., Aldaz, S., Oses-Pedraza, R., Perez, J. P. H., Sanchez-Alfaro, P., Wagner, D., Weckmann, U., and von Blanckenburg, F. (2021). Deep weathering in the semi-arid Coastal Cordillera, Chile. *Scientific Reports*, 11(1):1–15.

Kucera, S. and Wolfe, R. S. (1957). A selective enrichment method for Gallionella Ferruginea. *Journal of Bacteriology*, 74(3):344–349.

Kurz, D. L., Secchi, E., Carrillo, F. J., Bourg, I. C., Stocker, R., and Jimenez-Martinez, J. (2022). Competition between growth and shear stress drives intermittency in preferential flow paths in porous medium biofilms. *Proceedings of the National Academy of Sciences*, 119(30):e2122202119.

LaRowe, D. and Amend, J. (2019). *Energy Limits for Life in the Subsurface*, volume 3.

Lasaga, A. C. (1984). Chemical kinetics of water-rock interactions. *Journal of Geophysical Research: Solid Earth*, 89(B6):4009–4025.

Lasaga, A. C. and Ohmoto, H. (2002). The oxygen geochemical cycle: Dynamics and stability. *Geochimica et Cosmochimica Acta*, 66(3):361–381.

Liao, R., Gu, X., and Brantley, S. L. (2022). Weathering of chlorite from grain to watershed: The role and distribution of oxidation reactions in the subsurface. *Geochimica et Cosmochimica Acta*, 333:284–307.

Macquarrie, K. T. B., Mayer, K. U., Jin, B., and Spiessl, S. M. (2010). The importance of conceptual models in the reactive transport simulation of oxygen ingress in sparsely fractured crystalline rock. *Journal of Contaminant Hydrology*, 112(1-4):64–76.

Maher, K. (2010). The dependence of chemical weathering rates on fluid residence time. *Earth and Planetary Science Letters*, 294(1-2):101–110.

Maher, K. and Chamberlain, C. P. (2014). Hydrologic Regulation of Chemical Weathering and the Geologic Carbon Cycle. *Science*, 343(6178):1502–1504.

Maher, K., Steefel, C. I., DePaolo, D. J., and Viani, B. E. (2006). The mineral dissolution rate conundrum: Insights from reactive transport modeling of U isotopes and pore fluid chemistry in marine sediments. *Geochimica et Cosmochimica Acta*, 70(2):337–363.

Maisch, M., Lueder, U., Laufer, K., Scholze, C., Kappler, A., and Schmidt, C. (2019). Contribution of Microaerophilic Iron(II)-Oxidizers to Iron(III) Mineral Formation. *Environmental Science and Technology*, 53(14):8197–8204.

Malard, F. and Hervant, F. (1999). Oxygen supply and the adaptations of animals in groundwater. *Freshwater Biology*, 41:1–30.

Malmström, M. and Banwart, S. (1997). Biotite dissolution at 25°C: The pH dependence of dissolution rate and stoichiometry. *Geochimica et Cosmochimica Acta*, 61(14):2779–2799.

McAllister, S. M., Moore, R. M., Gartman, A., Luther, III, G. W., Emerson, D., and Chan, C. S. (2019). The Fe(II)-oxidizing Zetaproteobacteria: Historical, ecological and genomic perspectives. *FEMS Microbiology Ecology*, 95(4):fiz015.

McMahon, P., Böhlke, J., and Christenson, S. (2004). Geochemistry, radiocarbon ages, and paleorecharge conditions along a transect in the central High Plains aquifer, southwestern Kansas, USA. *Applied Geochemistry*, 19(11):1655–1686.

McMahon, P. B. and Chapelle, F. H. (2008). Redox processes and water quality of selected principal aquifer systems. *Ground Water*, 46(2):259–271.

Mcmahon, P. B., Chapelle, F. H., and Bradley, P. M. (2011). Evolution of Redox Processes in Groundwater. In *Aquatic Redox Chemistry*, pages 581–597. ACS Symposium Series.

McMahon, P. B., Plummer, L. N., Böhlke, J. K., Shapiro, S. D., and Hinkle, S. R. (2011). A comparison of recharge rates in aquifers of the United States based on groundwater-age data. *Hydrogeology Journal*, 19(4):779–800.

Melton, E. D., Swanner, E. D., Behrens, S., Schmidt, C., and Kappler, A. (2014). The interplay of microbially mediated and abiotic reactions in the biogeochemical Fe cycle. *Nature Reviews Microbiology*, 12(12):797–808.

Morris, R. L. and Schmidt, T. M. (2013). Shallow breathing: Bacterial life at low O2. *Nature Reviews Microbiology*, 11(3):205–212.

Nanzyo, M. and Kanno, H. (2018). *Primary Minerals*, pages 11–35. Springer Singapore, Singapore.

Napieralski, S. A., Buss, H. L., Brantley, S. L., Lee, S., Xu, H., and Roden, E. E. (2019). Microbial chemolithotrophy mediates oxidative weathering of granitic bedrock. *Proceedings of the National Academy of Sciences of the United States of America*, 116(52):26394–26401.

Neretnieks, I. (1986). Some uses for natural analogues in assessing the function of a HLW repository. *Chemical Geology*, 55(3):175–188.

Nordstrom, D. K. (2011). Hydrogeochemical processes governing the origin, transport and fate of major and trace elements from mine wastes and mineralized rock to surface waters. *Applied Geochemistry*, 26(11):1777–1791.

NRC (2001). *Basic Research Opportunities in Earth Science*.

Olsson, O. and Gale, J. E. (1995). Site assessment and characterization for high-level nuclear waste disposal: Results from the Stripa Project, Sweden. *Quarterly Journal of Engineering Geology and Hydrogeology*, 28(Supplement_1):S17–S30.

Overholt, W. A., Trumbore, S., Xu, X., Bornemann, T. L. V., Probst, A. J., Krüger, M., Herrmann, M., Thamdrup, B., Bristow, L. A., Taubert, M., Schwab, V. F., Hölzer, M., Marz, M., and Küsel, K. (2022). Carbon fixation rates in groundwater similar to those in oligotrophic marine systems.

Petsch, S. T. (2014). *The Global Oxygen Cycle*, volume 10. Elsevier Ltd.

Petsch, S. T., Bolton, E., Mok, U., and Evans, B. (2004). The weathering of sedimentary organic matter as a control on athmospheric O2 : I . Analysis of a black shale. *American Journal of Science*, 304:234–249.

Rajaram, H. and Arshadi, M. (2016). A similarity solution for reaction front propagation in a fracture-matrix system. *Philosophical Transactions of the Royal Society A: Mathematical, Physical and Engineering Sciences*, 374(2078).

Raymond, J. and Segrè, D. (2006). The Effect of Oxygen on Biochemical Networks and the Evolution of Complex Life. *Science*, 311(5768):1764–1767.

Refsgaard, J. C., Christensen, T. H., and Ammentorp, H. C. (1991). A model for oxygen transport and consumption in the unsaturated zone. *Journal of Hydrology*, 129(1-4):349–369.

Rikken, G. B., Kroon, A. G. M., and van Ginkel, C. G. (1996). Transformation of (per)chlorate into chloride by a newly isolated bacterium: Reduction and dismutation. *Applied Microbiology and Biotechnology*, 45(3):420–426.

Roques, C., Bour, O., Aquilina, L., and Dewandel, B. (2016). High-yielding aquifers in crystalline basement: Insights about the role of fault zones, exemplified by Armorican Massif, France. *Hydrogeology Journal*, 24(8):2157–2170.

Roques, C., Bour, O., Aquilina, L., Dewandel, B., Leray, S., Schroetter, J. M., Longuevergne, L., Le Borgne, T., Hochreutener, R., Labasque, T., Lavenant, N., Vergnaud-Ayraud, V., and Mougin, B. (2014). Hydrological behavior of a deep sub-vertical fault in crystalline basement and relationships with surrounding reservoirs. *Journal of Hydrology*, 509:42–54.

Rose, S. and Long, A. (1988a). Dissolved oxygen systematics in the Tucson Basin Aquifer. *Water Resources Research*, 24(1):127–136.

Rose, Seth. and Long, Austin. (1988b). Monitoring Dissolved Oxygen in Ground Water : Some Basic Considerations. *Ground Water Monitoring & Remediation*, 8(1):93–97.

Ruff, S. E., Humez, P., de Angelis, I. H., Diao, M., Nightingale, M., Cho, S., Connors, L., Kuloyo, O. O., Seltzer, A., Bowman, S., Wankel, S. D., McClain, C. N., Mayer, B., and Strous, M. (2023). Hydrogen and dark oxygen drive microbial productivity in diverse groundwater ecosystems. *Nature Communications*, 14(1):3194.

Samuels, T., Bryce, C., Landenmark, H., Marie-Loudon, C., Nicholson, N., Stevens, A. H., and Cockell, C. (2020). Microbial weathering of minerals and rocks in natural environments. *Biogeochemical Cycles: Ecological Drivers and Environmental Impact*, (January 2021):59–79.

Shelobolina, E., Xu, H., Konishi, H., Kukkadapu, R., Wu, T., Blöthe, M., and Roden, E. (2012). Microbial lithotrophic oxidation of structural Fe(II) in biotite. *Applied and Environmental Microbiology*, 78(16):5746–5752.

Shi, L., Dong, H., Reguera, G., Beyenal, H., Lu, A., Liu, J., Yu, H. Q., and Fredrickson, J. K. (2016). Extracellular electron transfer mechanisms between microorganisms and minerals. *Nature Reviews Microbiology*, 14(10):651–662.

Shu, X., Liu, Y., and Li, D. (2020). Contrasting composition of two biotite generations in the Lizhuang rare-earth element deposit, Sichuan Province, Southwestern China. *Geological Journal*, 55(12):7638–7658.

Sidborn, M. and Neretnieks, I. (2007). Long term redox evolution in granitic rocks: Modelling the redox front propagation in the rock matrix. *Applied Geochemistry*, 22(11):2381–2396.

Sidborn, M. and Neretnieks, I. (2008). Long-term oxygen depletion from infiltrating groundwaters: Model development and application to intra-glaciation and glaciation conditions. *Journal of Contaminant Hydrology*, 100(1-2):72–89.

Singha, K. and Navarre-Sitchler, A. (2022). The Importance of Groundwater in Critical Zone Science. *Groundwater*, 60(1):27–34.

Singhal, B. B. S. (2008). Nature of Hard Rock Aquifers: Hydrogeological Uncertainties and Ambiguities. In Ahmed, S., Jayakumar, R., and Salih, A., editors, *Groundwater Dynamics in Hard Rock Aquifers: Sustainable Management and Optimal Monitoring Network Design*, pages 20–39. Springer Netherlands, Dordrecht.

Spiessl, S. M., Macquarrie, K. T. B., and Mayer, K. U. (2008). Identification of key parameters controlling dissolved oxygen migration and attenuation in fractured crystalline rocks. *Journal of Contaminant Hydrology*, 95:141–153.

Sprenger, M., Stumpp, C., Weiler, M., Aeschbach, W., Allen, S. T., Benettin, P., Dubbert, M., Hartmann, A., Hrachowitz, M., Kirchner, J. W., Mcdonnell, J. J., Orlowski, N., Penna, D., Pfahl, S., Rinderer, M., Rodriguez, N., Schmidt, M., and Werner, C. (2019). The demographics of water : A review of water ages in the critical zone. *Reviews of Geophysics*, 57.

Steefel, C. I. and Lasaga, A. C. (1994). A coupled model for transport of multiple chemical species and kinetic precipitation/dissolution reactions with application to reactive flow in single phase hydrothermal systems. *American Journal of Science*, 294(5):529–592.

Stucki, J. W., Goodman, B. A., and Schwertmann, U. (2012). *Iron in Soils and Clay Minerals*. Springer Science & Business Media.

Sullivan, P. L., Hynek, S. A., Gu, X., Singha, K., White, T., West, N., Kim, H., Clarke, B., Kirby, E., Duffy, C., and Brantley, S. L. (2016). Oxidative dissolution under the channel leads geomorphological evolution at the shale hills catchment. *American Journal of Science*, 316(10):981–1026.

Sung, W. and Morgan, J. J. (1980). Kinetics and Product of Ferrous Iron Oxygenation in Aqueous Systems. *Environmental Science and Technology*, 14(5):561–568.

Tamura, H., Goto, K., and Nagayama, M. (1976). The effect of ferric hydroxide on the oxygenation of ferrous ions in neutral solutions. *Corrosion Science*, 16(4):197–207.

Tebo, B. M., Bargar, J. R., Clement, B. G., Dick, G. J., Murray, K. J., Parker, D., Verity, R., and Webb, S. M. (2004). Biogenic manganese oxides: Properties and mechanisms of formation. *Annual Review of Earth and Planetary Sciences*, 32(Goldberg 1954):287–328.

Tebo, B. M., Johnson, H. A., McCarthy, J. K., and Templeton, A. S. (2005). Geomicrobiology of manganese(II) oxidation. *Trends in Microbiology*, 13(9):421–428.

Templeton, A. S. and Caro, T. A. (2023). The Rock-Hosted Biosphere. *Annual Review of Earth and Planetary Sciences*, 51(1):493–519.

Trinchero, P., Molinero, J., Ebrahimi, H., Puigdomenech, I., Gylling, B., Svensson, U., Bosbach, D., and Deissmann, G. (2018). Simulating Oxygen Intrusion into Highly Performance Computing. *Mathematical Geosciences*, pages 49–51.

Trinchero, P., Puigdomenech, I., Molinero, J., Ebrahimi, H., Gylling, B., Svensson, U., Bosbach, D., and Deissmann, G. (2017). Continuum-based DFN-consistent numerical framework for the simulation of oxygen infiltration into fractured crystalline rocks. *Journal of Contaminant Hydrology*, 200(October 2016):60–69.

Trotsenko, Y. A. and Murrell, J. C. (2008). Metabolic Aspects of Aerobic Obligate Methanotrophy⋆. In *Advances in Applied Microbiology*, volume 63, pages 183–229. Academic Press.

Uroz, S., Calvaruso, C., Turpault, M. P., and Frey-Klett, P. (2009). Mineral weathering by bacteria: Ecology, actors and mechanisms. *Trends in Microbiology*, 17(8):378–387.

Uroz, S., Kelly, L. C., Turpault, M. P., Lepleux, C., and Frey-Klett, P. (2015). The Mineralosphere Concept: Mineralogical Control of the Distribution and Function of Mineral-associated Bacterial Communities. *Trends in Microbiology*, 23(12):751–762.

van Ginkel, C. G., Rikken, G. B., Kroon, A. G. M., and Kengen, S. W. M. (1996). Purification and characterization of chlorite dismutase: A novel oxygen-generating enzyme. *Archives of Microbiology*, 166(5):321–326.

Vollrath, S. (2014). *Microbial Fe (II) Oxidation at Circumneutral pH : Reaction Kinetics , Mineral Products , and Distribution of Neutrophilic Iron Oxidizers in Wetland Soils*. Number February.

Vollrath, S., Behrends, T., and van Cappellen, P. (2012). Oxygen Dependency of Neutrophilic Fe(II) Oxidation by Leptothrix Differs from Abiotic Reaction. *Geomicrobiology Journal*, 29(6):550–560.

Walker, J. C. G., Hays, P. B., and Kasting, J. F. (1981). A negative feedback mechanism for the long-term stabilization of Earth's surface temperature. *Journal of Geophysical Research: Oceans*, 86(C10):9776–9782.

Wedepohl, K. (1995). The composition of the continental crust. *Geochimica et Cosmochimica Acta*, 59(7):1217–1232.

Weiner, S. and Dove, P. M. (2003). An Overview of Biomineralization Processes and the Problem of the Vital Effect. *Reviews in Mineralogy and Geochemistry*, 54(1):1–29.

Whitman, W. B., Coleman, D. C., and Wiebe, W. J. (1998). Prokaryotes: The unseen majority. *Proceedings of the National Academy of Sciences of the United States of America*, 95(12):6578–6583.

Wilson, M. J. (2004). Weathering of the primary rock-forming minerals: Processes, products and rates. *Clay Minerals*, 39(3):233–266.

Winograd, Isaac. and Robertson, F. (1982). Deep Oxygenated Ground Water : Anomaly or Common Occurrence? *Science*, 216(4551):1227–1230.

Zhang, J., Lion, L. W., Nelson, Y. M., Shuler, M. L., and Ghiorse, W. C. (2002). Kinetics of Mn(II) oxidation by Leptothrix discophora SS1. *Geochimica et Cosmochimica Acta*, 66(5):773–781.

Zhang, Y., Horne, R. N., Hawkins, A. J., Primo, J. C., Gorbatenko, O., and Dekas, A. E. (2022). Geological activity shapes the microbiome in deep-subsurface aquifers by advection. *Proceedings of the National Academy of Sciences*, 119(25):e2113985119.

II. QUESTIONS AND FRAMEWORK

Contents

1 Knowledge gaps

The preceding chapter established the overarching context of this dissertation, where we explored various instances that have either detected or inferred the presence of oxic groundwater within the deep continental subsurface. These findings challenged the prevailing notion of aquifers as exclusively anoxic environments and raised the question of whether oxic groundwater is "a common occurrence or an anomaly" (Winograd and Robertson; 1982). Dissolved oxygen (DO) was identified as a key biogeochemical variable of the deep continental subsurface. Moreover, we identified fractured-bedrock aquifers as environments that are favorable to the presence of oxic groundwater in the continental subsurface and thus serve as a good case study to explore: (1) the mechanisms allowing DO to persist in the subsurface and (2) the implications of the presence of oxic groundwater on the biogeochemical processes within the continental subsurface.

Oxic groundwater has been reported in some fractured-bedrock aquifers [e.g. Bucher et al. (2009); Bochet et al. (2020); Ruff et al. (2023)] **but a systematic study of the distribution of DO, and the factors that control its transport and fate in the continental subsurface, is still missing**. In the previous section we presented a series of significant advances on the conceptualization of the feedbacks between the presence of oxic groundwater and geological and biogeochemical processes in the subsurface. Notably, geological factors such as the presence of fractures and rock lithology [e.g. Kim et al. (2017); Trinchero et al. (2019)] and hydrological factors such as fast flow in preferential flow paths (Bochet et al.; 2020), have been identified to exert controls on how deep DO can persist in aquifers. These conceptualization advancements on the reactive-transport problem of DO in the continental subsurface, have, however, been essentially focused on processes that are relevant at geological timescales. In fact, **a conceptual framework to describe how oxic-anoxic interfaces are controlled in modern groundwater systems is still missing**. At these short timescales, we have highlighted the disregarded role of O_2 in biological and chemical reactions occurring in the subsurface. We have particularly noted the close links between redox reactions taking part in rock weathering processes, and the activity of the planktonic and mineral-attached microorganisms that integrate the deep continental biosphere. **The extent to which groundwater redox conditions affect the rates and fluxes of the biogeochemical processes in the deep continental subsurface is still poorly understood.**

Box II.1 - Global objective in this dissertation

Conceptualize the factors that control the occurrence of the deep oxic hydrosphere in modern groundwater systems and develop *in-situ* approaches to characterize and quantify how oxic/anoxic environments affect rock weathering reactions and the activity of the deep subsurface biosphere.

2 Questions guiding this research work

Guiding research questions

1. **Depth of the oxic hydrosphere:** how deep can oxic groundwater persist in the continental subsurface and which processes control its transport and reactivity?
2. **Dissolved O_2 impacts on biotic and abiotic processes:** how to disentangle the contribution of DO in biotic and abiotic processes in the deep continental subsurface and how to trace them in heterogeneous environments?
3. **Dynamics of redox conditions in the subsurface:** how are biogeochemical processes impacted when the transport of oxic groundwater changes the redox conditions in the subsurface?
4. **Microbe-mineral interactions under contrasting redox conditions:** how are microbe-mineral interactions affected by the existence of contrasting redox environments in the continental subsurface?

3 Rationale for the study

In Figure II.1 we present the general organization of the present work and the associated questions and studied scales. This dissertation is composed of two major parts. In a first part, composed by Chapters III to V, we tackle questions Q1 and Q2 through *monitoring* and *modeling* approaches to identify the main controls on the subsurface redox landscapes at catchment scale (Figure II.1-A). Then, in a second part integrated by chapters VI and VII, we tackle questions Q3 and Q4 to explore the consequences of groundwater redox variations on biogeochemical processes by using *in-situ experimental* approaches at smaller scales (Figure II.1-B and C). To study *in-situ* processes, we develop novel tools that enable us to decouple key variables within the complexity of natural environments.

To build our research, we exploit the capabilities of the Critical Zone Observatory (CZO) of Ploemeur (Brittany, France). This CZO, presented in detail in Chapter III, is composed of two catchments, Guidel and Kermadoye, in which more than forty boreholes offer access to the saturated zone in a fractured-bedrock aquifer. Moreover, the proximity of these two catchments and their different lithological and hydrogeological contexts offer a remarkable opportunity to decouple the influence of geological and hydrological factors on their respective redox landscapes.

In Chapter IV, we propose a conceptual framework to define the reactive-transport problem of DO in Fe-bearing silicate rocks (Figure II.1-A). From this conceptual framework, we derive analytical solutions to describe the depth distributions of both dissolved O_2 and Fe in modern groundwater systems. The analytical model is parameterized with dimensionless numbers which integrate the effects of geological and hydrological forcings and provide a synthetic interpretative tool. We validate the assumptions underlying the analytical model with a fully-resolved numerical model of water-rock interactions. Our validated analytical model is

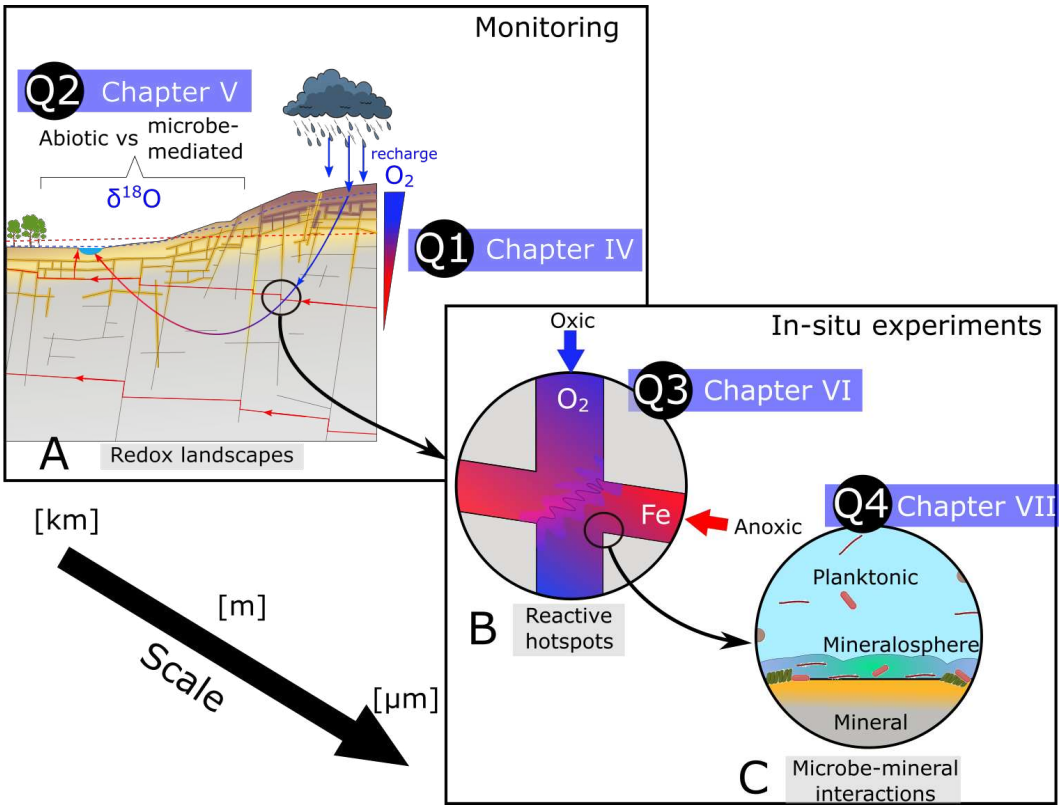

Figure II.1: **Research strategy adopted in this work.** The guiding questions (Q) and their related chapters are classified into two research approaches: *monitoring* and *in-situ experiments*. **A):** Groundwater flow paths with decreasing DO concentrations are represented in a catchment scale view. DO distributions are heterogeneous and depend on the balance between DO transport from the surface and consumption by biogeochemical reactions in the subsurface (Q1). DO consumption in the subsurface by abiotic and microbe-mediated processes can lead to DO isotope fractionation (Q2). **B):** The intersection of flow paths with redox contrasted groundwater creates intermittent reactive hotspots in the subsurface, that depend on DO transport from the surface. Changing redox conditions during reactive hotspots are potentially favorable environments for subsurface prokaryotes (Q3). **C):** Subsurface prokaryotes, both planktonic and mineral-attached, depend on redox potentials to thrive and are potentially affected by compartmentalized or changing redox conditions in the subsurface (Q4).

finally applied to the case study of the CZO of Ploemeur and allows for the identification of the controlling processes that lead to the contrasted redox landscapes that we observe in these two comparable catchments.

In Chapter V, we use the isotope composition of dissolved O_2 to decipher the reactive pathways including DO in the subsurface (Figure II.1-A). This work is the first systematic measurement of DO stable isotopes in deep subsurface environments. By coupling this isotopic information with an in-depth hydrogeochemical characterization of the Guidel catchment including groundwater residence time, the structure of flow paths and the redox distribution in the aquifer, we identify the zones in the catchment where DO concentrations are dominated either by physical or microbe-mediated processes.

In chapters VI and VII, *in-situ* experimental approaches are carried out to explore the effects that the redox state of groundwater has on biogeochemical processes, particularly on microbial biomass, both planktonic and mineral-attached, and on weathering rates of minerals.

In Chapter VI, we investigate the biogeochemical response of a fracture-hosted ecosystem under dynamic redox conditions (Figure II.1-B). For this, we perform a fracture-scale reactive-tracer test that simulates a fast recharge episode bringing oxic groundwater into a reducing fracture and monitor the biogeochemical response within it. We characterize the reactive processes in an *in-situ* reactive hotspot where we determine *in-situ* rates of DO consumption in the subsurface and reveal how fluctuating redox conditions in the subsurface promote a reorganization of the biogeochemical potentials and the activity of planktonic consortia.

Finally, in Chapter VII, we present a second *in-situ* experiment in which we study the effects that redox

conditions have on the mineral-attached communities and their reciprocal effects on mineral weathering (Figure II.1-C). Using a novel mineral-incubation device, we sampled mineral-attached microorganisms, estimated their biomass, identified their taxonomy and quantified their influence on mineral weathering rates. The study in this chapter is one among few that have quantified mineral-attached biomass and *in-situ* weathering rates of minerals. We show that redox conditions do not significantly impact the mineral-attached biomass but should impact the composition of mineral-attached consortia. On the other hand, weathering rates present strong differences depending on the redox conditions and on the action of prokaryotes in the dissolution process.

Bibliography

Bochet, O., Bethencourt, L., Dufresne, A., Farasin, J., Pédrot, M., Labasque, T., Chatton, E., Lavenant, N., Petton, C., Abbott, B. W., Aquilina, L. and Le Borgne, T. (2020). Iron-oxidizer hotspots formed by intermittent oxic–anoxic fluid mixing in fractured rocks, *Nature Geoscience* **13**(2): 149–155.

Bucher, K., Zhu, Y. and Stober, I. (2009). Groundwater in fractured crystalline rocks, the Clara mine, Black Forest (Germany), *International Journal of Earth Sciences* **98**(7): 1727–1739.

Kim, H., Stinchcomb, G. and Brantley, S. L. (2017). Feedbacks among O2 and CO2 in deep soil gas , oxidation of ferrous minerals , and fractures : A hypothesis for steady-state regolith thickness, *Earth and Planetary Science Letters* **460**: 29–40.

Ruff, S. E., Humez, P., de Angelis, I. H., Diao, M., Nightingale, M., Cho, S., Connors, L., Kuloyo, O. O., Seltzer, A., Bowman, S., Wankel, S. D., McClain, C. N., Mayer, B. and Strous, M. (2023). Hydrogen and dark oxygen drive microbial productivity in diverse groundwater ecosystems, *Nature Communications* **14**(1): 3194.

Trinchero, P., Sidborn, M., Puigdomenech, I., Svensson, U., Ebrahimi, H., Molinero, J., Gylling, B., Bosbach, D. and Deissmann, G. (2019). Transport of oxygen into granitic rocks: Role of physical and mineralogical heterogeneity, *Journal of Contaminant Hydrology* **220**(November 2018): 108–118.

Winograd, Isaac. and Robertson, F. (1982). Deep Oxygenated Ground Water : Anomaly or Common Occurrence?, *Science* **216**(4551): 1227–1230.

III. THE PLOEMEUR CRITICAL ZONE OBSERVATORY

Contents

Chapter presentation

The Critical Zone Observatory (CZO) of Ploemeur was my experimental site during my PhD. This CZO is part of the French network of hydrogeological research sites (H+ network, `https://hplus.ore.fr/en/`) and of the French research infrastructure OZCAR (`https://www.ozcar-ri.org/`. The purpose of this chapter is twofold. Firstly, in the introductory section, it provides an overview of the research that has contributed to the understanding of the geological context and hydrogeological functioning of the study site, thereby establishing the state of the art view of the CZO. The second part of the chapter details two studies developed during this PhD that contribute to improving the understanding of the Ploemeur CZO: (1) a petrological and mineralogical characterization of the granite and micaschist lithologies and (2) a hydrochemical characterization of groundwater end-members in the catchment of Guidel. This second part is structured like a research work in which the methods are presented, followed by the results and a further discussion. Finally, a conclusion is presented for the chapter.

1 Introduction

1.1 A brief history of the research in the Ploemeur CZO

The Ploemeur CZO is the main french observatory related to crystalline rocks hydrogeology. It is composed of three main subsites: (1) the Kermadoye catchment, (2) the experimental site of Stand-Er-Brune (SEB) and (3) the Guidel catchment. Guidel and Kermadoye are the biggest subsites and are detailed in Section 1.3.

Historically, the pond of Lannenec was the main drinking water source for the Ploemeur village (about 17k inhabitants) but the degradation of its quality led the stakeholders to use groundwater as a new resource. In the early 1990's, pumping bores were drilled in the Kermadoye catchment and the aquifer was found to be of an outstanding productivity (about $10^6\ m^3.yr^{-1}$), positioning the pumping site of Kermadoye as the main drinking water source for the village. Despite of being in a geological context that is inherently heterogenous and complex as fractured crystalline rocks, the hydrogeological functioning of the site is well constrained. Research works that have contributed to the understanding of the Ploemeur CZO can be classified into some main stages (see Table III.1):

1. Hydrogeological approaches: determination of aquifer hydrodynamic properties and characterization of fracture's connectivity.

2. Geological approaches: mineralogy and petrophysics of the main lithological facies in the site (granite and micaschist). Hydrogeological modeling. Geothermal gradient determination.

3. Hydrochemical approaches: identification of groundwater end-members, groundwater age estimations. Reaction rates estimation for selected reactions (e.g. denitrification).

4. Microbiological approaches: diversity and phylogeny analysis of microbial communities, conceptualisation of the ecological controls.

As shown in Table III.1, most of the research has been carried out in Kermadoye. In recent years, attention on the Guidel catchment has increased because of plans to establish a pumping site for drinking water extraction similar to that of Kermadoye. In particular, these pumping plans for Guidel have raised research questions which revolve around the potential impact of pumping on water quality and watershed ecosystems. In fact, unlike Kermadoye, the Guidel catchment is characterized by markers of microbial activity associated to iron reactivity in mixing zones (i.e. reactivity hotspots) concentrated in the wetland area (Bochet et al.; 2020). Those hotspots of microbial activity have been identified in the surface (e.g. in the wetland) and in the subsurface where the boreholes intersect fractures where abundant microbial mats develop (Bochet et al.; 2020; Bethencourt et al.; 2020).

1.2 Geological aspects

1.2.1 Regional context: The Armorican Massif

The northwestern part of France (mainly Brittany but also parts of Normandie and Pays de la Loire) belongs to the Armorican Massif. This massif was shaped during the Cadomian (650-550 Ma) and Variscan (400-250 Ma) orogenies that explain the complex composition of the bedrock which includes plutonic, metamorphic, sedimentary and volcanic rocks (Ballèvre et al.; 2009).

The presence of two large scale late-Hercynian shear zones striking NW-SW divide the Armorican Massif into three major regions (Ballevre et al.; 2013): (1) the *North Armorican Zone*, essentially composed by Cadomian granites; (2) the *Central Armorican Zone*, mainly characterized by a Brioverian bedrock composed of clasts from the Cadomian orogeny and covered by a large sedimentary unit composed of Paleozoic sandstones and schists; and (3) the *South-Armorican Zone* that is essentially composed by low to intermediate grade

Table III.1: **Synthesis of main works contributing to the understanding of the Ploemeur CZO.** Codes in the Reference column correspond to 1: (Touchard; 1999), 2: (Le Borgne et al.; 2006a), 3: (Tarits et al.; 2006), 4: (Ayraud et al.; 2008), 5: (Druillennec; 2007), 6: (Belghoul; 2010), 7: (Ruelleu; 2010), 8: (Pauwels et al.; 2010), 9: (Klepikova et al.; 2011), 10: (Leray et al.; 2013), 11: (Jiménez-Martínez et al.; 2013), 12: (Leray et al.; 2014), 13: (Maamar et al.; 2015), 14: (Aquilina et al.; 2018), 15: (Roques et al.; 2018), 16: (Bochet et al.; 2020), 17: (Bethencourt et al.; 2020), 18: (Pouladi et al.; 2021), 19: (Guillaumot et al.; 2022)

Reference	Year	Methods	Contribution to CZO knowledge	Sub-site[a]
1	1999	Hydrogeophysics, hydrochemistry, mineralogy	First general characterization	Kermadoye
2	2006	Packer experiments, temperature and flow logs	Fractures connectivity, hydrodynamic properties	Kermadoye
3	2006	Major elements chemistry	Transient evolution of groundwater chemistry	Kermadoye
4	2008	Age tracers	Groundwater ages, apparent vertical velocities	Kermadoye
5	2007	Radon + mineralogical description	Mineralogical description of schist and granite	SEB
6	2010	Petrophysics	Porosity, permeability and electrical properties of basement (micaschist + granite)	SEB
7	2010	Geophysics (gravity methods)	Structural model of the micaschist-granite contact zone	CZO
8	2010	Sulfate-isotope tracing	Atmospheric and fertilizer origin of dissolved sulfur	Kermadoye
9	2011	Temperature logs	Geothermal gradient estimation	SEB
10	2013	3D numerical modeling	Gently dipping structures like the contact zone explain the high productivity of the aquifer	CZO
11	2013	Frequency domain analysis between rainfall and groundwater table levels	Kermadoye	
12	2014	Age tracer Modeling	Flows reorganization under transient pumping conditions, modeling of age tracer data	Kermadoye
13	2015	Microbiological and hydrological survey (Planktonic microbes)	Groundwater residence time as first order control on microbial community composition	Kermadoye
14	2018	Batch experiments and field hydrochemistry	Iron and sulfur in groundwater reflect biotite reactivity rather than pyrite's	Kermadoye
15	2018	End-member mixing analysis	Identification of groundwater end-members. Geochemistry and mixing evolution under transient pumping conditions	Kermadoye
16	2020	Packer experiments, conceptual modelling	Conceptual framework for subsurface hotspots where dissolved oxygen and iron react	Guidel (Pz26)
17	2020	Packer test + metagenomics (plaktonic microbes)	Genome reconstruction of microbial mats in subsurface hotspots. Redox conditions define ecological niches.	Guidel (Pz26)
18	2021	Geothermal modelling	Geothermal gradient, flow contribution per fracture in Pz26	Guidel (Pz26)
19	2022	Modelling, conceptualisation	Groundwater recharge, catchment-scale hydrodynamic parameters	Guidel, Kermadoye

[a]: abbreviation SEB corresponds to the Stang-er-brune experimental site whereas CZO indicates large scale studies without sub-site distinction

metamorphic schists and micaschists, while migmatites and granites originated during the Variscan intrude into these latter metamorphic structures.

The Critical Zone Observatory (CZO) of Ploemeur is located in this later South-Armorican Zone. The Ploemeur CZO is shaped by (1) a large leucogranite pluton intruded into a micaschist body, with the contact zone gently dipping 30º to the North (Touchard; 1999); and (2) several dextral-slip normal faults zone with strike North 20º and dip East 70º (N20E) (Ruelleu; 2010) (see Figure III.1-A and B). Both are the main transmissive structures of the fractured-bedrock aquifer.

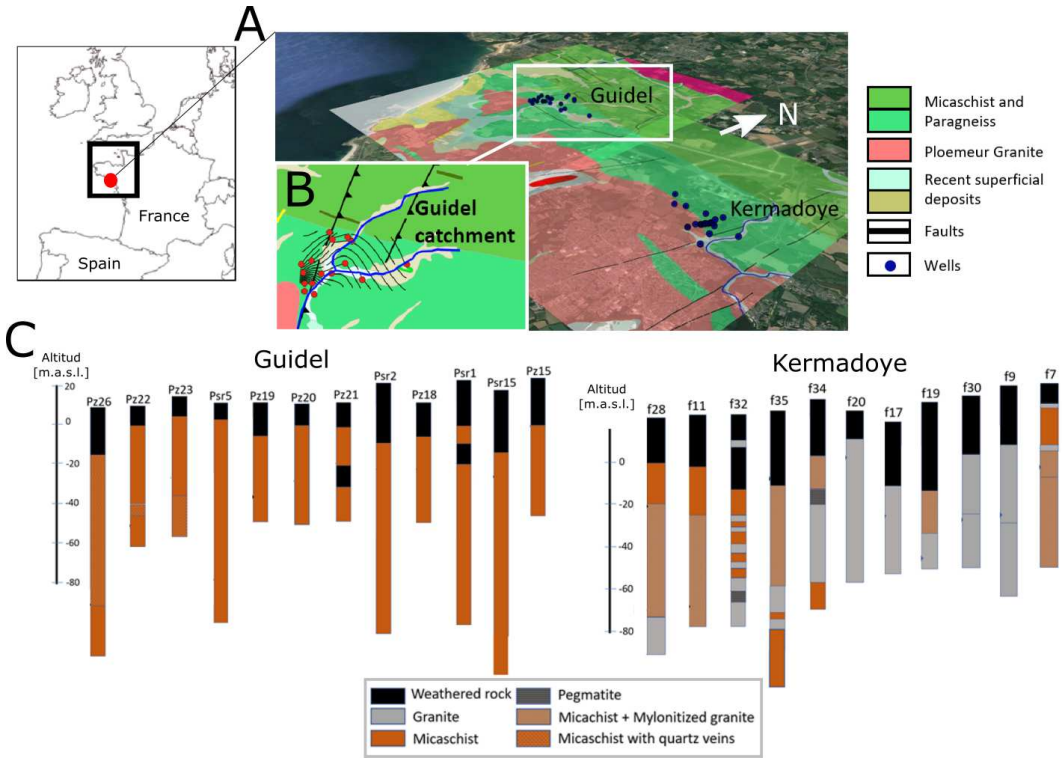

Figure III.1: **Geological context of the Guidel and Kermadoye catchments.** A) Local geological map (scale 1:50000) from (Béchennec et al.; 2012a). At Kermadoye, the geological maps shows the subvertical N20E fault that crosses the site. B) 3D structural model of Kermadoye featuring the 30º-North dipping geological contact zone and the subvertical normal fault N20E (Ruelleu; 2010). C) Lithological columns of selected boreholes, built upon drilling reports available in the Hplus database `https://hplus.ore.fr/en/ploemeur`. Arrows indicate the depth of main fracture contributing to the water column (blue when water is oxic, black when anoxic).

.

1.2.2 Aquifer architecture

The aquifer formation in the Ploemeur CZO is a typical case of fractured bedrock aquifer (see Figure III.2-A). We first describe the typical structures that compose these geological settings and describe their specific hydrogeological roles. Then, we relate them to the specific case of the Ploemeur CZO.

Ideally, a fractured bedrock aquifer is composed by the following structures:

1. The *regolith* compartment: this compartment has a clayey-sandy composition, with high porosities, comprised between 5 to 30%, and low permeabilities (Dewandel et al.; 2006). It plays the role of groundwater storage. The regolith compartment is subdivided into two layers:

   (a) The *alloterite* layer: a clayey horizon, part of the regolith compartment, in which the structure of the protolith has been lost due to weathering processes. In granitic rocks, this horizon is also known as *sandy regolith*.

(b) The *isalterite* compartment: horizon that also makes part of the regolith compartment, less weathered than the alloterite and still preserves the texture of the protolith. In granitic rocks, this horizon is usually laminated.

2. The *fissured or fractured* compartment: this compartment is highly fractured and assumes the transmissive role in the aquifer. It is usually characterized by dense network of mainly subhorizontal fractures that decreases with depth. The origin of this fractures are supposed to be due to WIF (Eggler et al.; 1969; Buss et al.; 2008), but also to lithostatic decompression or cooling stresses may play a role (Dewandel et al.; 2006).

3. The *protolith* compartment: that is impermeable and constitutes the bottom limit of the aquifer. Permeable paths are only present locally when tectonic fractures are present (Maréchal et al.; 2004).

Local studies characterizing these different structures in the Ploemeur CZO have been exclusively done in the Kermadoye catchment during the work of Touchard (1999) who used cuttings and geophysical approaches to characterize the main structures in the aquifer. Here we present the main aquifer structures identified in the Kermadoye catchment by Touchard (1999) and extend them to the Guidel catchment through the synthesis of borehole drilling reports presented in Figures III.2-B and C:

1. **A regolith compartment** characterized by presence of sandy and laminated layers as well as by the generalized presence of clays. Touchard (1999) reported the thickness of this compartment ranging from 25 to 40 meters, which is consistent with the data presented in Figure III.2-B. In the Guidel catchment however, more dominated by the presence of micaschist as introduced previously, the regolith (sandy + laminated regolith compartments) is generally thinner than in Kermadoye, ranging between 10 to 25 meters. Figure III.2-C reveals that the regolith thickness in Guidel varies with the altitude. While the sandy compartment is thin and varies around an average value of 6 meters, the laminated layer gets thicker the higher the altitude.

2. **A highly heterogeneous fractured compartment**. This compartment is notably influenced by the presence of a regional subhorizontal contact zone between granite and micaschist. The micaschist contains intrusions of granite veins, which become more abundant with greater depth and as they approach the top of the granite pluton. Boreholes intersecting the lithological contact such as f32 or f35 illustrate this structures (refer to Figure III.1-C). Remarkably, this compartment is also characterized by subvertical fractures around the major dextral-slip normal faults N20E that can favor the hydraulic connectivity between the surface and the subhorizontal structures (Touchard; 1999; Ruelleu et al.; 2010).

3. **A protolith compartment** composed of fresh unfractured granite situated below the lithological contact zone.

1.2.3 Lithological facies in the host-rock

According to Béchennec et al. (2012b), the two main lithological facies that compose the Ploemeur CZO bedrock are the *Ploemeur leucogranite* (from now on called *granite*) and the rocks of the *Groupe de Merrien*, described as mica-rich leucocrate paragneiss and micaschist (from now on called *micaschist*). The mineralogical composition of these two lithologies was reported by Béchennec et al. (2012b) and presented in Figure III.3-A. The main mineralogical differences between both lithologies stands on the content of K-feldspar, which are not reported in the micaschist while in the granite they represent 28%, and in the content of biotite, that is about ten times higher in micaschist than in granite.

The granite and micaschist lithologies have also been analysed to determine their bulk chemistry, especially in the work of Touchard (1999) who analysed different cutting samples from different boreholes in the Kermadoye site. Touchard (1999) showed that the elements that differentiated the most the two lithologies were silicon and

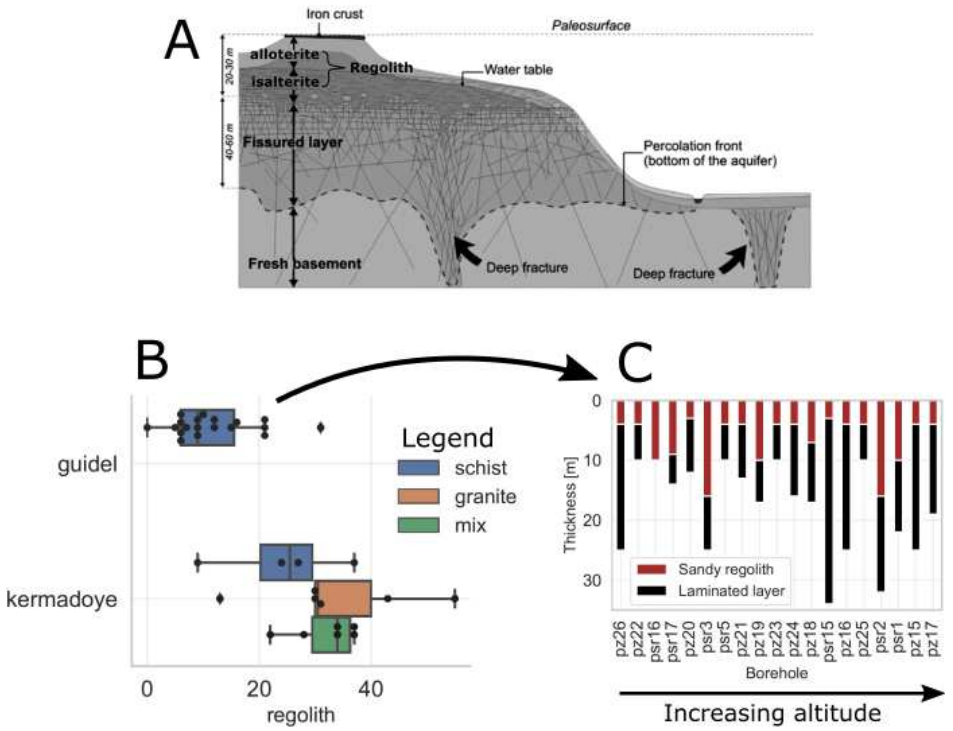

Figure III.2: **Regolith structure in the Ploemeur CZO.** A): Idealized architecture of a fractured-bedrock aquifer from (Dewandel et al.; 2006). B): average thickness of the regolith (sandy + laminated regolith compartments) and C): detail of the regolith compartment for the Guidel catchment. Data corresponds to thickness estimations based on the borehole drilling reports.

iron. Figure III.3-B shows the iron and silicon contents of the data reported by Touchard (1999) and completed with additional data acquired during this work (for the complete bulk analysis see Table in chapter's Appendix). The figure shows that granite's composition is quite homogeneous. While the high silicon contents in granites obey to the their higher proportion of quartz and feldspar, the low iron contents are related to the their lower proportion of biotite (Figure III.3-A).

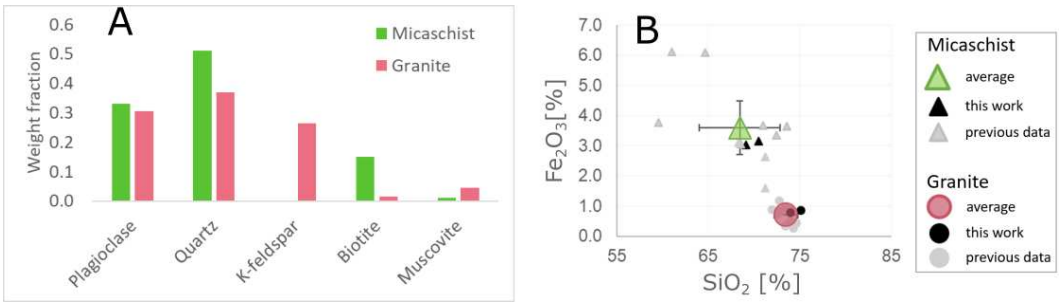

Figure III.3: **Description of the two main lithologies from the Ploemeur CZO: granite and micaschist.** (A) mineralogical composition as reported by Béchennec et al. (2012b). (B) bulk silicon and iron contents of the two lithologies. Sub-figure (B) includes previous reported data from (Touchard; 1999) and Anne-Catherine Pierson-Wickmann (personal communication) corresponding to ICP-OES analyses on bulk powders. The dataset is completed with additional ICP-OES and X-ray fluorescence measurements made in the framework of this work.

1.3 Hydrogeological aspects

1.3.1 Generalities

The Ploemeur CZO comprises two main sub-catchments: Guidel and Kermadoye. While both catchments are situated in comparable climatic, geologic and soil usage contexts (see Table III.2) owing to their proximity ($\sim 4kmfar$), they are mainly differentiated by the flow regime and their placement with respect to the geological contact zone between granite and micaschist (see Figure III.1-A). Kermadoye is a catchment pumped since 1991 at a flow rate of about 1 $mM^3.y^{-1}$. This catchment directly crosses the contact zone as inferred from the geological map and from the borehole lithologic columns, where some boreholes are reported in the granite while others are in the micaschist (Figure III.1-C). On the other hand, 4km west of Kermadoye is the Guidel site. This is a pristine catchment under natural gradient flow conditions. The boreholes were drilled in 2009 with the purpose of exploiting the aquifer at similar levels than in the Kermadoye catchment. None of the boreholes in Guidel crosses the granite lithology, which indicates that the contact zone in this area is deeper than 130 msnm (as indicated by the deepest borehole in the catchment, Psr15, see Figure III.1-C).

Table III.2: **General characteristics of the two catchments in the Ploemeur CZO.**

	Guidel	Kermadoye
Generalities		
Mean Altitude (m.a.s.l.)	15.1	26.7
Mean Slope (º)	2.8	2.1
Geology		
Dominant bedrock lithology	Mica-schist, Paragneiss	Granite
Age	Ordovician inf	Carboniferous
Mean [min, max] depth to fresh bedrock (m)	17 [4, 34]	30 [10, 44]
Climate		
Climate type	Oceanic	
Mean rainfall ($mm.yr^{-1}$)	880 ±120[a]	
Potential Evapotranspiration ($mm.yr^{-1}$)	760 ±50[a]	
Mean annual temperature (ºC)	12.2 ± 0.41[b]	
Hydrogeology		
Groundwater flow-regime	Natural circulation	Pumped since 1991
Number of boreholes	21	23
Potential recharge ($mm.yr^{-1}$)	242[c]	260[d]

[a]: data from Lann-Bihoué weather station, averaged from the period 1996-2017 (Guillaumot et al.; 2022)
[b]: data from Lann-Bihoué weather station, averaged from the period 2002-2018 (Osorio-Leon et al.; 2023)
[c]: Potential recharge in Guidel for the period 1996 - 2016 (Guillaumot et al.; 2022)
[c]: Potential recharge in Kermadoye for the period 2003 - 2010 (Jiménez-Martínez et al.; 2013)

1.3.2 Groundwater flow

From a hydrogeological point of view, both catchments are characterized by convergent groundwater flows (see Figure III.4). At Kermadoye, groundwater flow converges to three active pumping wells situated in the area of the N20E fault. Around the drawdown cone, the average drawdown is 10m and reaches a maximum value of about 25m in the pumping boreholes (Figure III.4-D). The decorrelation between groundwater levels and the topography shows that at Kermadoye, groundwater flow is controlled by the pumping. In the case of Guidel, groundwater flow converges towards a small wetland ($\sim 0.04km^2$ in surface) situated in the low topographies of the area (see Figure III.4-A). The wetland is located at the convergence area of two small streams whose flow rates are between the 1-5 $L.s^{-1}$. Unlike Kermadoye, the proximity of groundwater levels to topographic surface in Guidel (Figure III.4-C) along with the presence of several artesian boreholes indicate that groundwater flow in this catchment is controlled by topography and discharges into the wetland and surface streams.

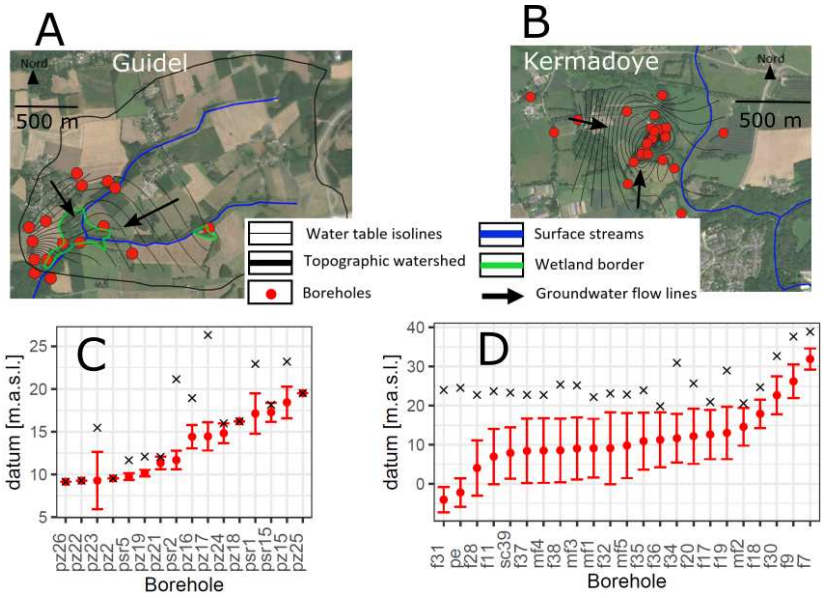

Figure III.4: **Hydrogeological maps of Guidel and Kermadoye catchments.** Flow lines show convergent flow in the two cases. While in Guidel flow converge to a wetland, in Kermadoye flows converge to the pumping well. Figures below show the average groundwater level on selected boreholes of C) Guidel and D) Kermadoye. Red points and error bars show the average value ($\pm 1\sigma$) for the period 2010-2018. Crosses show the altitude of the borehole head.

.

1.3.3 Hydrologic year and aquifer recharge

Groundwater head time-series show seasonal patterns for both catchments, with the high groundwater level season occurring between December and June (Figure III.5). The amplitude of the groundwater head changes (high or low GW levels) is stronger in Guidel than in Kermadoye, indicating for the latter that the seasonality is masked by the pumping influence. Moreover, the seasonality in groundwater levels shows a phase shift of about 2-3 months with respect to the rain season (Figure III.5-D), which is consistent with the work of Jiménez-Martínez et al. (2013) that estimated a transfer time of about 26 to 100 days. Aquifer recharge occurs mainly during the months of December and March (Jiménez-Martínez et al.; 2013) with the effective recharge being very similar between the Guidel and Kermadoye catchments, around $250 mm.yr^{-1}$ (see Table III.2).

1.3.4 Groundwater hydrochemistry

As presented in the literature review in Table III.1, hydrochemical studies in the Ploemeur CZO have been essentially conducted in the Kermadoye catchment, where Residence Time Tracers (RTT's) and water chemistry have been used to constrain groundwater end-members in the catchment and their compartmentalization in the aquifer. For instance, groundwater apparent ages, determined through CFC-11, CFC-12 and CFC-13 measurements (Ayraud et al.; 2008), are generally homogeneous in the regolith compartment (ranging from 10 to 20 years) while they increase linearly with depth in the fractured compartment. Ayraud et al. (2008) estimated this linear increase of groundwater age with depth at $3 m.y^{-1}$. More recently, a comprehensive study in Kermadoye (Roques et al.; 2018) identified three main groundwater end-members based on a multi-tracer analysis: (1) an isolated poorly-mobile end-member in the regolith compartment, (2) a modern-water end-member of apparent ages around 20-40y and low *Total Dissolved Solids* (TDS) and (3) an ancient-groundwater end-member with higher TDS and groundwater apparent ages older than 50 years. Hydrochemical time series showed that the old and ancient end-member proportions has increased in the water pumped out of the aquifer since the start of the pumping, at least 20 years after the start of operations (Roques et al.; 2018).

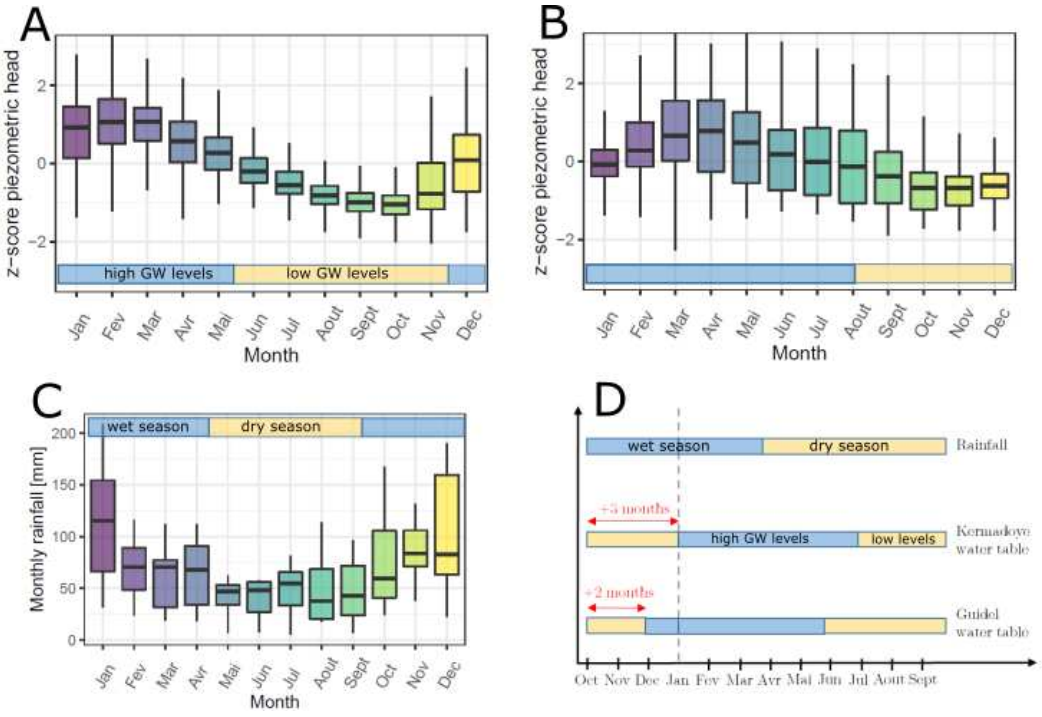

Figure III.5: **Seasons of the hydrogeologic year.** (A) and (B) represent z-score of the monthly groundwater (GW) levels for Guidel and Kermadoye, respectively. (C): average monthly rainfall measured in the Lann-Bihoue weather station. (D) synthesis of the seasons of the hydrogeologic year (high or low water table levels) and comparison with the hydrologic year (wet or dry season). Data corresponds to the period 2010-2018.

1.3.5 Distribution of DO in groundwater

In a recent work conducted in the Guidel catchment, Bochet et al. (2020) showed that oxic groundwater can be transported to depth by transmissive fractures during recharge periods. While the study of Bochet et al. (2020) established a first understanding of the redox structure of the aquifer (see Figure III.6), the authors did not consider two questions which are fundamental to understand the redox state of the catchment:

1. **Depth distribution of DO:** a fundamental problem for groundwater studies in fractured aquifers comes from the fact that groundwater enters boreholes through *discrete* fractures. This study assumed that the differences observed between boreholes were due to lateral differences in the catchment. However, the water column in boreholes is mostly representative of the most transmissive fracture intersecting the borehole and therefore, the geochemical composition of the water column is not correlated with depth within the borehole. This makes that spatial views referred to a depth layer, like the one in Figure III.6-B, become misleading in fractured aquifers. It is of major importance to evaluate the vertical stratification of DO concentrations in the aquifer by methods which overcome the limited view provided by the water column within boreholes. **What is a better view to look at redox, and more generally, hydrochemical parameters in a fractured-bedrock catchment?** To answer to this question, a methodology relying on temperature measurements as a proxy of depth in the aquifer is later proposed in Section 3.1.

2. **Reactive-transport mechanisms allowing the presence of DO in the subsurface:** while the evidence presented in Figure III.6-A supports the role of fractures as preferential flow paths for DO transport, a mechanistic view to explain why there are oxic and anoxic boreholes in the aquifer still missing. In particular, the reactive model proposed is based on a unique *effective* reaction which is not adapted to the complex reaction pathways known to consume O_2 in the subsurface. **What factors control the vertical stratification of DO in the aquifer, and how does the distribution of DO with depth provide insights into the reactive processes occurring in the subsurface?** We tackle this question in Chapter IV.

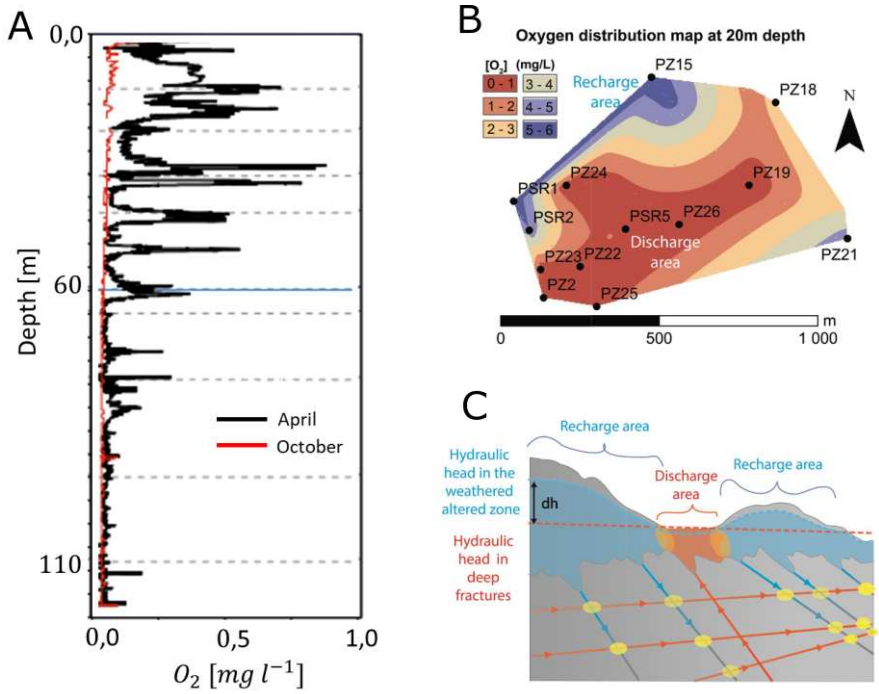

Figure III.6: **Distribution and conceptual transport model of dissolved oxygen (DO) in the Guidel catchment as proposed by Bochet et al. (2020).** (A) Seasonal measurements reveal that fractures can deliver DO into depth during recharge periods. (B) The DO distribution at 20m depth shows that oxic boreholes ($DO > 1mg.L^{-1}$) are related to high latitudes in the catchment, while the areas around the wetland and low topographies (discharge area) are mostly anoxic. (C) Conceptual model explaining the link between topography, redox zonation and formation of subsurface reactive hotspots (yellow circles) in the catchment.

1.4 Problematic and objectives

The Ploemeur CZO is the playground in which the following chapters of this work take place and where the reactive transport of DO is studied. In order to make it possible, there at least two basic questions that should be answered beforehand: **(1) which minerals present in the host-rock can react with DO? and (2) How are flow paths structured in the CZO?**

In relation to the first question, Section 1.2.3 presented a mineralogical composition reported by Béchennec et al. (2012b), which is based on major common minerals (see Figure III.3-A). **However information concerning redox-sensitive elements in minerals are missing, particularly iron, manganese and sulphur.**

In relation with the second question, Section 1.3.4 showed that hydrochemical surveys in the Ploemeur CZO have been essentially conducted in the Kermadoye site, allowing to build up a global view of the catchment functioning. Nonetheless, **a hydrochemical characterization of the Guidel site is essential for an accurate interpretation of groundwater flow paths at the site-scale and is still missing. The hydrochemical characterization of the Guidel site is also strategic since it opens the possibility to make comparative studies between the two catchments like the one in Chapter IV**. Thus, the following sections aim to cover these gaps. Firstly, a petrological characterization is conducted in order to provide additional information on mineral compositions, targeting redox-sensitive elements, and secondly, a hydrochemical characterization of the Guidel site is presented.

2 Petrological characterization of parent rocks in the Ploemeur CZO

2.1 Materials and Methods

Rock samples were taken from the rock core of the B2 borehole. This is a well preserved core that crosses granite and micaschist horizons. The B2 borehole belongs to the SEB sub-site in the Ploemeur CZO. The rock samples were treated following the workflow presented in Figure III.7 to reach three main purposes: (1) identify the main Fe-bearing mineral phases present in the granite and micaschist lithologies, (2) calculate the mineral formula of the main mineral phases and (3) calculate a normative mineralogical composition for each lithology. The following sections detail the methods used in the workflow of Figure III.7.

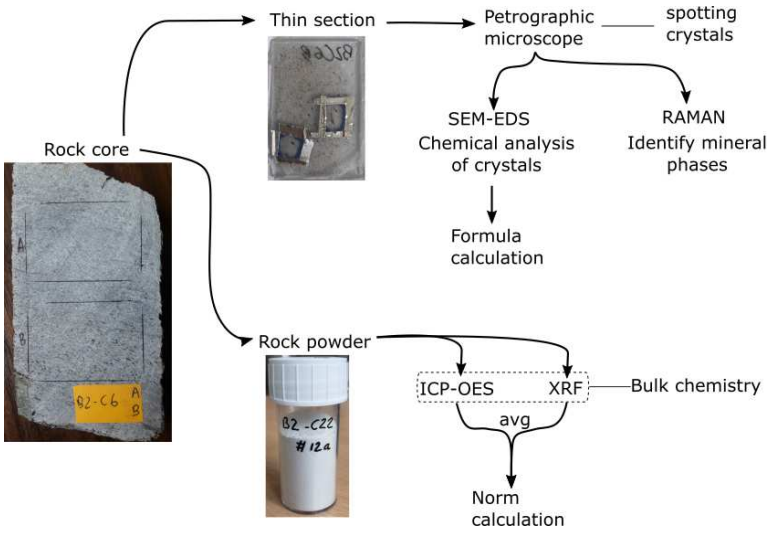

Figure III.7: **Workflow used for the petrological characterization of the granite and micaschist samples.** Method names correspond to SEM-EDS (Scanning Electron Microscope - Energy Dispersive X-ray Spectrometer), RAMAN (Raman spectroscopy), XRF (X-ray fluorescence) and ICP-OES (induced coupled plasma - optical emission spectroscopy)

2.1.1 Sample preparation

Granite and micaschist were sampled at different depths in the rock core of borehole B2. Granite was sampled at depths between 73 to 76m while Micaschist was sampled between 28 to 30m. A total of 8 polished thin sections (4 granites and 4 micaschists) of about 30μm-thick were fabricated in the rock-preparation service at University of Rennes. Similarly, about 2kg of each lithology, collected in the same depth ranges, were reduced to a powder with a particle size < 80μm) in the rock-preparation service at University of Rennes. Briefly, rock cores were first sawed with a diamond saw sprayed with water, then fed to a jaw crusher with steel-manganese alloy cylinders to obtain a particle size below 300μm. The crusher was carefully cleaned between samples to avoid contamination. A sub-sample of each lithology was collected by using a quarter which allowed to reduce the proportion of the sample while maintaining the homogeneity of the matrix. Finally, samples were fed into a two-position planetary ball micro-grinder equipped with agate balls to minimize contamination risks and obtain the particle size < 80μm.

2.1.2 Thin sections characterization

Thin sections were first analyzed in a petrographic microscope Leica PMLP equipped with a camera Leica Mc120HD at University of Rennes, for a first stage of mineral identification and spotting. The microscope was used under plane-polarized and cross-polarized light modes to identify the minerals and the texture of the rock.

The chemical composition of the spotted minerals was measured using a *Scanning Electron Microscope - Energy Dispersive X-ray Spectrometer* (SEM-EDS) JEOL IT 300 LA – Low vacuum, equipped with a tungsten-filament electron source, at CMEBA service at University of Rennes. Briefly, the SEM was set in backscattered-electron mode to enhance the chemical contrast between minerals and facilitate the identification of the spotted crystals. Then, the EDS detector was used to collect punctual X-ray spectra corresponding to a semi-quantitative chemical composition of the crystals. For the SEM-EDS analyses, voltage was set at 20.0 kV and probe current at 7.47 nA. Spectra integration was done with the instrument's software and provided semi-quantitative mode (without standard) elementary mass percent composition for every crystal. Several SEM-EDS analyses were acquired in mineral crystals of the same type. Their composition was then averaged to obtain an average semi-quantitative chemical composition per mineral.

Structural analysis were also conducted on the spotted minerals with a Confocal-Raman spectrometer Renishaw INVIA ® (Renishaw, Wotton-under-Edge, UK), equipped with a green laser (514nm), in collaboration with Hélène Bouquerel from the *Institut de Physique du Globe de Paris* (IPGP). The spectra analysis was done with the Wire 5.4 ® software of Renishaw. The spectra post-processing consisted of several steps: (1) identification and suppression of the spectra emitted by the resin used to glue the rock samples during the thin-section preparation (2) base-line correction to remove the sample's auto-fluorescence and finally (3) comparison with reference spectra from the Rruff opensource database (`https://rruff.info/`) in order to identify the mineral species. This last step was achieved with the Rruff software CrystalSleuth (`https://rruff.info/about/about_software.php`).

2.1.3 Mineral formulae calculation

Mineral formulae were calculated from the semi-quantitative chemical compositions determined by SEM-EDS. Mineral formulae were calculated with the standard method described by Ragland (1989).

2.1.4 Powder samples characterization

Bulk elemental analysis of the granite and micaschist were done by X-Ray Fluorescence (XRF) in a PANalytical AXIOS Max ® equipped with an X-ray source SST-mAX^{50} ® (Malvern Panalytical, Netherlands) at RRXG service in University of Montpellier in collaboration with Julien Fullenwarth and Bernard Fraisse. The analysis was done over a sample mass between 0.6 - 1 g. The detection limit depends on the analyzed element but for the majority of elements it corresponds to 0.05%. Duplicate samples were also analyzed for bulk elemental chemistry of major and minor elements, *loss on ignition* (LOI), and total sulphur contents at the *Service d'Analyse des Roches et des Minéraux* (CRPG) service of CNRS (Nancy, France). Major and minor elements were analyzed by ICP-OES in a ThermoScientific iCAP 6500 ® (Thermo Fisher Scientific, USA). Detection limit was 0.015% for Mn and Fe and increased upto 0.05% for lighter elements. The LOI was measured by gravimetric difference after heating the sample at 1020 °C. Total sulphur was measured in an EMIA-320V2 carbon and sulfur analyzer ® (HORIBA Scientific, Japan).

2.1.5 Norm calculation

In petrology, a norm is a mineralogical composition computed though a mass balance in which a bulk chemical analysis of a rock is attributed to a predefined set of minerals. In this case, a custom-made norm was made to fit with the observations of mineral phases identified in the thin sections (presented later in Table III.3) and the additional consideration of normative minerals such as apatite ($Ca_5(PO_4)_3(OH)$), pyrite (FeS_2), corundum (Al_2O_3) and rutile (TiO_2) to respectively close mass balances for P, S, Al and Ti.

2.2 Results

2.2.1 Average composition of silicate minerals

A total of 4 thin sections, two granites and two micaschists, were analyzed in the petrographical microscope. The main Fe-bearing minerals in the samples are:

- **Granite samples:** biotite crystals are very rare. They appear as brown crystals of round shapes or, more frequently, as chloritized biotite (green crystals of sheet shape). Chlorite crystals with radial shapes are found associated to walls in sealed fractures, indicating the nucleation of crystals possibly during hydrothermal circulations (see Figure III.8-A).
- **Micaschist samples:** biotite crystals are abundant and heterogeneous in shape and size (millimetric to submillimetric crystals). Biotite crystals are frequently associated with inclusions of opaque minerals, such as iron oxides or sulfides.

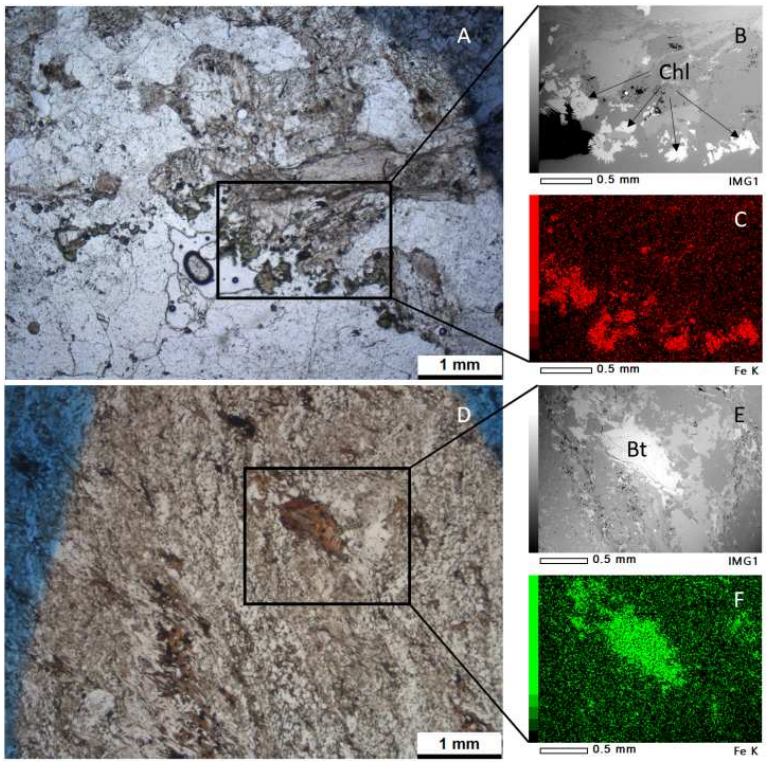

Figure III.8: **Thin section analyses for the petrological characterization.** Example of plain polarized light images of (A) *Ploemeur Granite* and (D) *Micaschiste Fort Bloqué* thin sections collected from the core of borehole B2. Biotite is abbreviated as "Bt" while chlorite crystals are indicated as "Chl". The black frames correspond to selected areas analyzed on SEM with backscattered electrons (B, E) and iron-specific EDS (C, F). In EDS images, the more intense the color, the higher the iron concentration in the mineral.

As shown by the SEM images in Figure III.8, both biotite and chlorite are iron rich. SEM-EDS point analyses were done over biotite, chlorite and other major minerals to determine their average chemical composition as reported in the chapter's Appendix. These compositions were then used to determine the average mineral formulae presented in the Table III.3. This table shows that the main iron-bearing minerals identified in the analyses are biotite, chlorite and pyrite, however iron was also detected in small proportions in muscovite crystals, where it can substitute structural aluminium. Biotite crystals presented a different composition depending on whether they were in granite or in micaschist samples. Biotite from granites has a higher iron proportion [Fe/(octahedral cations) = 0.53] than biotite from micaschist [Fe/(octahedral cations) = 0.39] which is consistent with the microscope observations where biotite in micachist is more weathered than in granite (see Figure III.8).

Likewise, chlorite crystals, that were more easily found in granite thin sections, have a higher Fe-proportion compared to biotite [Fe/(octahedral cations) = 0.73].

While minerals from granite thin sections are characterized by a higher iron-content than minerals in micaschist, they were in general less abundant in the inspected thin sections. In order to have a more global view of the abundance of these iron-bearing minerals in the granite and micaschist lithologies, the following section presents the results of the bulk chemistry composition of the rocks.

Table III.3: **Computed mineral formulae** based on the average compositions presented in the chapter's Appendix

Mineral	Computed formula based on SEM-EDS	Raman identification (Rruff ID)
Fe-bearing minerals		
Biotite		
in granite	$K_{0.58}Na_{0.05}(Mg_{0.15}Fe_{0.84}Ti_{0.06}Al_{0.55})(Si_{3.48}Al_{0.52}O_{10})(OH)_2$	Zinnwaldite (R040138)
in micaschist	$K_{0.76}Na_{0.01}(Mg_{0.77}Fe_{0.74}Ti_{0.12}Al_{0.27})(Si_{2.9}Al_{1.1}O_{10})(OH)_2$	[-]
Chlorite		
in granite	$(Mg_{0.35}Fe_{1.7}Ti_{0.01}Al_{0.28})(Si_{2.9}Al_{1.1}O_{10})(OH)_8$	Chamosite (R060188)
Other minerals		
K-feldspar	$K_{0.81}Na_{0.12}Ti_{0.1}(Al_{0.93}Si_{3.07})O_8$	Microcline (R050150)
Albite	$Na_{0.84}K_{0.07}(Al_{1.23}Si_{2.83})O_8$	Albite (R50402)
Muscovite	$K_{0.69}Na_{0.15}Fe_{0.16}Mg_{0.06}Al_{1.15}(Al_{0.82}Si_{3.18}O_{10})(OH)_2$	Muscovite (R061120)
Quartz	SiO_2[a]	Quartz (R040031)
Pyrite	FeS_2[a]	Pyrite (R050070)
Apatite	$Ca_5(PO_3)_4OH$[a]	Hydroxylapatite (R060180)

[a]: Ideal chemistry formula, not determined by SEM-EDS

2.2.2 Bulk composition of granite and micaschist

The bulk chemistry of crushed-rock powder samples (presented in Table III.4) was used in order to calculate a norm for every lithology, in which the bulk composition of the rock sample is mainly allocated, in a mass balance, to the minerals from Table III.3. Table III.5 presents the calculated normative compositions. After the norm calculation, it becomes apparent that the presence of Fe-bearing minerals is much more important in micaschist than in granites: there is 5 times more biotite and 2 times more chlorite. The bulk chemistry analyses in Table III.4 show that other than iron, redox-sensitive elements detected in the rocks are sulfur and manganese, yet their concentrations are between one and two orders of magnitude below iron concentrations.

Table III.4: **Bulk composition of granite and micaschist powder samples** as analyzed by XRF (X-ray fluorescence) and ICP-OES (induced coupled plasma - optical emission spectroscopy). Samples correspond to rock cores of borehole B2 from SEB, sections B2-C6#4 and B2-C22#12a.

		Granite			Micaschist		
Element	Units	XRF	ICP-OES	avg	XRF	ICP-OES	avg
Na_2O	[%wt]	4.56	3.962	4.263	2.68	2.412	2.548
MgO	[%wt]	0.20	0.150	0.175	0.86	0.911	0.886
Al_2O_3	[%wt]	14.35	14.270	14.309	15.47	15.445	15.456
SiO_2	[%wt]	75.10	73.940	74.518	70.54	69.100	69.818
P_2O_5	[%wt]	0.34	0.270	0.305	0.21	0.200	0.207
SO_3	[%wt]	0.03	-	0.032	0.21	-	0.211
K_2O	[%wt]	3.92	4.191	4.054	4.80	5.200	5.001
CaO	[%wt]	0.52	0.439	0.478	1.26	1.173	1.217
TiO_2	[%wt]	0.07	0.079	0.075	0.51	0.474	0.492
MnO	[%wt]	0.03	0.025	0.027	0.02	0.030	0.027
Fe_2O_3	[%wt]	0.87	0.772	0.820	3.16	3.029	3.096
ZnO	[%wt]	0.02	-	-	0.04	-	-
SrO	[%wt]	-	-	-	0.02	-	-
Y_2O_3	[%wt]	-	-	-	0.01	-	-
ZrO_2	[%wt]	-	-	-	0.04	-	-
BaO	[%wt]	-	-	-	0.17	-	-

Table III.5: **Normative mineralogical composition for granite and micaschist.** Mineral abbreviations correspond to albite (Ab), anorthite (An), K-feldspar (K-F), quartz (Qz), biotite (Bt), chlorite (Chl), muscovite (Ms), apatite (Ap) and pyrite (Py).

Mineral	Ab [vol%]	An [vol%]	K-F [vol%]	Qz [vol%]	Bt [vol%]	Chl [vol%]	Ms [vol%]	Ap [vol%]	Py [vol%]	Rutile [vol%]	Corundum [vol%]
granite	41.6	0.3	22.2	30.1	1.6	1.3	0.9	0.6	0.0	0.0	1.3
micaschist	25.3	5.2	24.2	30.2	8.3	3.5	0.9	0.4	0.1	0.2	1.7

2.3 Discussion

2.3.1 Mineralogical composition of the main lithological facies in the Ploemeur CZO

The petrological characterization presented in this chapter contributes to offer a more detailed view of the mineralogy of the granite and micaschist lithologies at the Ploemeur CZO (refer to the normative mineralogical composition in Table III.5). By comparison with the previous mineralogical composition of Béchennec et al. (2012b), the norm from Table III.5 reveals that micaschists have an important K-feldspar content that has not been reported in previous works. It is not clear the origin of the micaschist samples reported by Béchennec et al. (2012b), but Touchard (1999), in another study based on rock cores from the Kermadoye catchment, did not reported the presence of K-feldspar either. Nevertheless, our microscopic inventory of thin sections as well as the chemical analyses on the observed minerals are consistent with the presence of K-feldspar in the micaschist samples (refer to Table in chapter's Appendix). Since our measurements were performed in a single borehole which is different from those studied by Touchard (1999), future petrological characterizations of micaschist samples would be necessary to confirm the generality of our K-feldspar observations in micaschist from the CZO of Ploemeur. Other important minerals that were not computed in the previous composition of Béchennec et al. (2012b) and that were observed and assessed during this work include chlorite, apatite and pyrite. Those minerals were reported as accessory minerals by Béchennec et al. (2012b) and Touchard (1999), but our custom normative calculation allows to estimate their relative abundance in the rocks.

2.3.2 Reducing power of the CZO rocks

The petrological characterization of granite and micaschist samples has shown that the presence of electron donors in the host-rocks (i.e. rock's *reducing power*) is namely ensured by the presence of phylosilicate minerals such as biotite and chlorite. The calculated mineral formulae presented in Table III.3 shows that biotite from granites contains a relatively higher iron proportion than biotite from micaschists (granite biotite has 14% more iron in the octahedral sites), but at the same time, granite contains about 5 times less biotite than micaschists according to the normative mineralogical composition from Table III.5. This results in a net iron mass content that is about 3.7 higher in micaschists as shown by the bulk chemical analyses from Table III.4. The very low concentrations of sulfur and manganese detected in the bulk chemical analyses show that, while these two elements could potentially contribute to the reducing power of the host rocks, their effect is likely negligible. For instance, sulfur content in rocks indicates that pyrite only accounts for 0.1%vol of micaschist rocks, which is consistent with the very rare observations of pyrite crystals during thin-section microscopy.

2.3.3 Limitations of the petrological approach

All the samples used in the petrological characterization come from the same single borehole core for the borehole B2 from the SEB site in the Ploemeur CZO. This borehole crosses the granite-micaschist contact zone and was a practical opportunity to sample both lithologies in a core that is well preserved. Even if the SEB site is placed halfway between Guidel and Catchment, the petrological characterization done in this work is restricted to a single spatial location. The extension of the methodology to further samples covering different places in the CZO may be needed to better assess the variability of the measured data. Nevertheless, according

to the geological map of the area (Béchennec et al.; 2012a) the rock core used in this work belongs to the same common lithological facies found in Guidel and Kermadoye.

Part of the petrological methods in this chapter included the characterization of minerals using spectroscopic methods on the rock thin-sections. While the Raman spectra allowed to identify the mineral phases corresponding to crystals found by optical microscopy, their chemical composition was measured by SEM-EDS. This latter technique provides semi-quantitative chemical compositions because no standard was used for the measurements. As a consequence, the computed mineral formulae in Table III.3 should be used only as elemental proportions in the minerals and not as absolute values.

Finally, the petrological approach has been limited to unweathered samples of granite and micaschist since they are supposed to be more reactive than rocks from the regolith compartment, where electron donors have been already oxidized. Nevertheless, a mineralogical characterization of the regolith compartment could also shed light on the reaction products of the weathering reactions that could be explored in future works.

3 Hydrochemical characterization of the Guidel catchment and comparison with Kermadoye

3.1 Materials and Methods

The hydrochemical characterization of Guidel consisted of a multitracer approach aiming to identify the groundwater end-members and to use them to identify the evolution of flow paths in the catchment. A workflow that takes into account the heterogeneity of fractured media was used for this purpose (see Figure III.9).

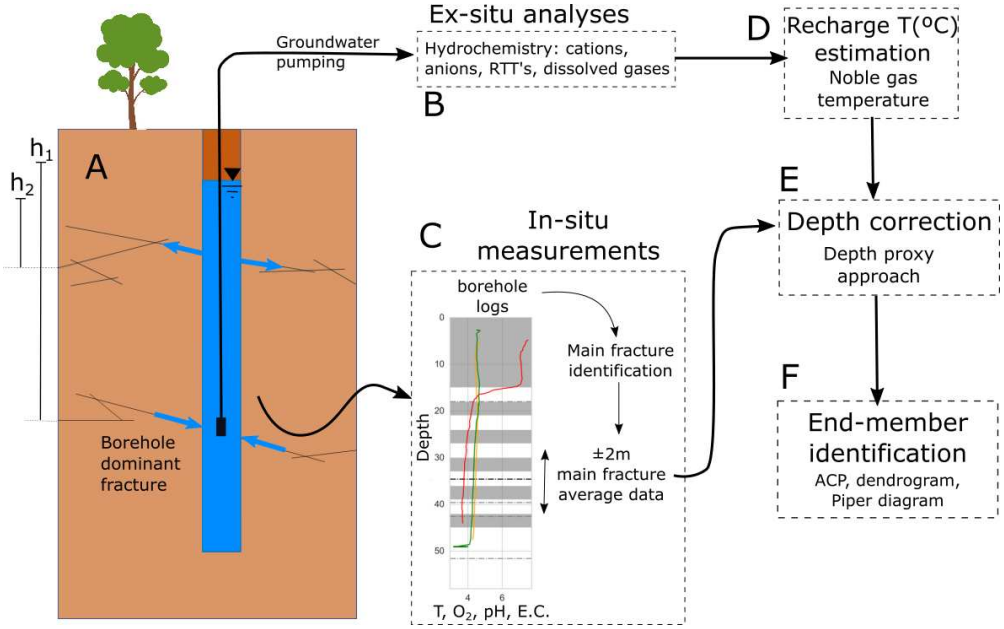

Figure III.9: **Workflow for the hydrochemical characterization.** (A) Groundwater was sampled by pumping in the dominant fracture of every borehole and (B) was analysed in multiple ex-situ analyses. (C) In-situ measurements consisted of multiparameter borehole logs. Borehole logs were poorly dependant of depth in the borehole, showing that the signal of the dominant fracture is propagated in the water column because of groundwater flow from the dominant fracture to the low-head fractures (h2 in the borehole sketch). Borehole logs were then reduced to an average value in a range of $\pm 2m$ around the dominant fracture. (D) measured noble gas concentrations were used to estimate the average recharge temperature. (E) The data from ex-situ and in-situ measurements was referenced to a depth representing the origin of water in the dominant fracture (by using the depth-proxy methodology). (F) Depth corrected data was then used in a multitracer analysis to identify the hydrochemical end-members.

3.1.1 Dominant fractures identification

Every borehole intersects a set of fractures with different hydraulic heads (Figure III.9-A). Under ambient conditions, groundwater flow and physico-chemical parameters in the borehole are usually controlled by the fracture with the highest hydraulic head (e.g. h_2 in Figure III.9-A). In order to identify the dominant fracture per borehole, a database of the fracture zones identified during drilling was built from borehole drilling reports (available online at `https://hplus.ore.fr/en/`). Among the listed fractures, the instantaneous flow rate during drilling (available in the borehole drilling reports) was used as a first distinguishing criteria, e.g. when a fracture presented an instantaneous flow rate that largely dominated over the others. In the case when the instantaneous flow rate was not decisive, temperature borehole logs combined with flowmetry measurements (Geovista Heatpulse) were used to identify the dominant fracture following the methodology of Chatelier et al. (2011). Thus, a single borehole was considered as representing a single fracture in a specific depth (only a few boreholes presented a more complex flow setting and were influenced by more than one fracture: Pz26, f28. In that case, every fracture was considered as an independent reservoir). As a consequence, physicochemical data from borehole logs (DO, temperature, pH and electrical conductivity) was averaged in a range of 2 m above and below the depth of the dominant fracture in the well, which was considered as a representative range of the fracture's influence in the water column.

3.1.2 In-situ measurements: borehole logs

For the multiparameter borehole logs (dissolved oxygen, temperature, electrical conductivity and pH) we used data acquired since 2003 that is available in the database of the French network of hydrogeological research sites (`https://hplus.ore.fr/en/`). This dataset was completed with three additional field campaigns in order to validate the historical data. Multiparameter borehole logs were acquired at two different times of the hydrologic year (high groundwater level's season and low level's season) using an Idronaut Ocean Seven multiparameter probe. The instrument was calibrated following the manufacturer's specification and the accuracy of the DO probe ($\pm 0.1 mg.L^{-1}$) was crosschecked by gas chromatography analyses at the University of Rennes.

3.1.3 Ex-situ measurements: hydrochemical analyses

Groundwater sampling consisted on descending a submersible MP1 pump (Grundfos) until the depth of the dominant fracture in the borehole. Physicochemical parameters in the pump discharge were monitored with a WTW probe. Groundwater was sampled after the monitored parameters were stable. Major and trace cations were quantified by *Inductively Coupled Plasma Mass Spectroscopy* (ICPMS) (Agilent Technologies, 7700x) in pre-acidified and 0.2 μm-filtered samples. Uncertainties were between 2 to 5%. Major anion samples (non-acidified) were analyzed by Ionic Chromatography in a Dionex DX-120 ® (Thermo Fisher Scientific, USA) with uncertainties below 4%. Dissolved Iron concentrations were determined using the 1,10-Phenanthroline colorimetric method (Fortune and Mellon; 1938). Samples for noble and reactive dissolved gases were collected in glass bottles, isolated from atmosphere, and analyzed after head-space extraction by Gas Chromatography with a thermal conductivity detector (μGC/TCD) in the 24h after sampling, following the method of Sugisaki and Taki (1987). Analytical precision is under 5%. Residence Time Tracers (RTT) CFC-11, CFC-12 and CFC-113 were sampled in steel ampoules and analyzed by the Purge & Trap method, using a Gas Chromatograph with an electron capture detector. Uncertainties are about 3% (Ayraud et al.; 2008). Water samples for RTT ^{36}Cl analyses were 0.2 μm-filtered, stored in acid-washed plastic bottles and then analyzed by *Accelerator Mass Spectroscopy* at the French AMS National facility, ASTER at CEREGE (Arnold et al.; 2010) in collaboration with Valéry Guillou and Lucilla Benedetti. Briefly, chloride from samples was extracted by precipitation and purification of AgCl. After drying, precipitates were pressed in 6.6 mm diameter Ni-target holders. Measured ^{36}Cl/Cl ratios were corrected from the blanks and total uncertainties, including internal errors and external reproducibility are 18% on average (Bouchez et al.; 2015).

3.1.4 Groundwater recharge temperature estimation

The recharge temperature of groundwater in the CZO was estimated from measured noble gas concentrations by following the Noble Gaz Temperature (NGT) model (Aeschbach-Hertig et al.; 2008). Briefly, the model uses noble gases (here, we use Ne and Ar) as conservative proxies of the paleorecharge conditions, since noble gases solubility depends on the recharge temperature of groundwater. The model also considers a correction for the excess of dissolved gases relative to solubility equilibrium, the so-called *excess air*, that is present in virtually all groundwaters (Aeschbach-Hertig et al.; 2008). Standard ($P = 1atm$) noble gas solubilities as a function of temperature from Hamme and Emerson (2004) were used to compute partial pressures referred to an average recharge altitude of 20m according to Table III.2. Excess-air corrected noble gas concentrations were computed as:

$$C_{gas}|_{EA} = \frac{PV_{EA}}{RT_{rech}} C_{gas}^{atm} + C_{gas}|_{EA=0} \tag{III.1}$$

With $C_{gas}|_{EA}$ the noble gas concentration corrected by excess air volume (V_{EA}), P is the pressure at the recharge altitude, R the ideal gas constant, T_{rech} the supposed paleorecharge temperature, C_{air}^{gas} is the average concentration of noble gas in the atmosphere and $C_{gas}|_{EA=0}$ is the solubility of noble gas referred to the recharge altitude.

3.1.5 The $Depth_{proxy}$ methodology for fractured media

Since fracture networks are highly heterogeneous (Le Borgne et al.; 2006b), one cannot directly rely the depth of an intersected fracture in a borehole with the representative depth of origin of the circulating fluid (Chatelier et al.; 2011). For instance, at the site scale, normal faults dipping of about 70°Ruelleu (2010) will globally favor subvertical circulations. At a more restricted scale, a fracture analysis in a borehole from the Guidel catchment Bochet et al. (2020) has shown that fracture's dip can vary from 20 to 80°.

Following this, the methodology developed by Chatelier et al. (2011) allowed to use groundwater temperature as a proxy of its depth of origin, i.e. the depth at which the fluid was in thermal equilibrium with the host rock (called here $Depth_{proxy}$). Hence, the $Depth_{proxy}$ was calculated as:

$$Depth_{proxy} = \frac{T - T_{rech}}{G_G} \tag{III.2}$$

T corresponds to groundwater temperature as measured from borehole logs at the depth of the sampled fracture ($Depth_{physical}$), T_{rech} corresponds to the average recharge temperature of the Ploemeur CZO, that is 12.2 °C from Table III.2, and G_G corresponds to the Geothermal Gradient. For the Ploemeur site, G_G has been estimated at 0.013 $°C.m^{-1}$ after Klepikova et al. (2011) and Pouladi et al. (2021). If the $Depth_{proxy}$ and the $Depth_{physical}$ are equal, it means that the fracture is close to horizontal. If the $Depth_{proxy}$ is higher than the $Depth_{physical}$, it means that the fracture is tilted and that flows are oriented upward.

3.1.6 Principal component and clustering analysis

A Principal Component Analysis (PCA) has been done using the Python's Scikit-learn library (Pedregosa et al.; 2011) in order to reduce the dimensionality of the dataset and identify correlation patterns between sampling points and environmental variables. Based on the PCA results, a Hierarchical Clustering Analysis (HCA) was used to identify main end-members in the catchment.

3.2 Results

3.2.1 Groundwater recharge temperature

Excess-air corrected Noble Gas Temperatures (NGT), calculated for the boreholes of Guidel and Kermadoye are presented in Figure III.10. NGT values indicate that average values for groundwater recharge temperature

range between 5 and 15 °C, with an average value for the CZO between 12 and 13 °C. This NGT recharge temperature is consistent with the annual average air temperature measured in the weather station in the period 2002-2018 (12.2 °C).

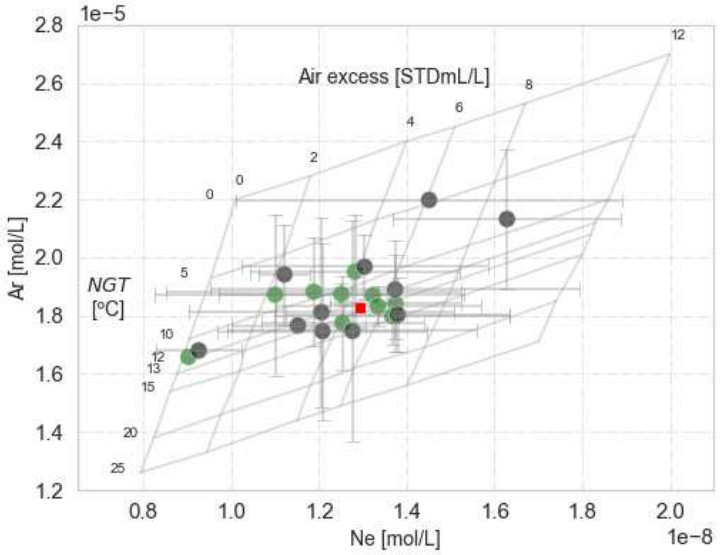

Figure III.10: **Groundwater recharge temperature in the Ploemeur CZO**. Noble Gas Temperature (NGT) for the different boreholes of Guidel (grey dots) and Kermadoye (green dots) computed from Ar and Ne concentrations and referred to a recharge altitude of 20m. The red square corresponds to the average Ar and Ne concentrations. Dots correspond to average values within 1σ from the period 2016-2022.

3.2.2 Identification of upwelling and downwelling flows in the catchment

Since $Depth_{proxy}$ is a function of two site-specific parameters (T_{rech} and G_G), the accuracy of the $Depth_{proxy}$ estimates depends on how good those two parameters can be constrained. This is illustrated in Figure III.11-A where a recharge temperature of 12.2 °C (the average value from the weather station, see Table III.2) would indicate that most of the boreholes in the CZO have upward flows. Conversely, a recharge temperature of 13 °C (as inferred from NGT in Figure III.10) results in a more consistent distinction between recharge and discharge zone boreholes, where the former present downward flows and the latter upward flows. Consistently with this view, Figure III.11-B compares the $Depth_{proxy}$ estimates with the physical depth of the dominant fracture for each borehole. Most of the samples located in the recharge zone are characterized by downward flows, i.e. their $Depth_{proxy} < Depth_{physical}$, while samples in the discharge zone are characterized by upward flows, i.e. $Depth_{proxy} > Depth_{physical}$. A more detailed view of the temperature logs for the Guidel boreholes allows to distinguish different flow paths in the catchment. Recharge boreholes (characterized by downward flows) are globally homogeneous, with a water column temperature that remains nearly constant around 13.6 °C. Exceptions to this are Psr15 and Pz25 boreholes, for which temperature profiles follow the geothermal gradient indicating poor circulation in the water column. On the other hand, discharge boreholes (characterized by upward flows) present a sparser temperature distribution, yet two main groups can be distinguished. First, a deep and hot group, including boreholes Pz26, Psr5, Psr6 and Pz19, that align in a same gradient indicating a common origin. Second, a group composed by Pz2, Pz20, Pz22 and Pz23 in which the temperatures are sparse indicating flow paths of variable depths.

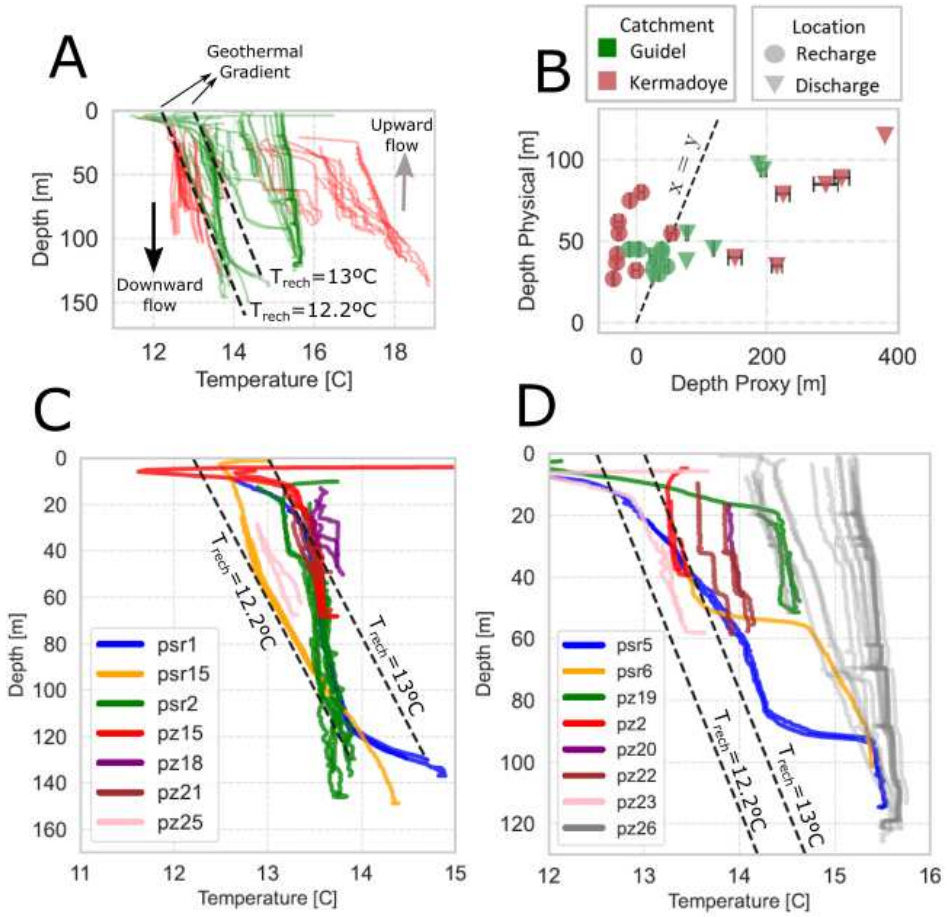

Figure III.11: **Use of temperature to characterize vertical flows in Boreholes from Guidel.**(A) Comparison of temperature profiles from Guidel and Kermadoye boreholes. The geothermal gradient is determined from profiles that are not perturbed by vertical borehole flows (Klepikova et al.; 2011) and is represented by considering two different recharge temperatures. (B) Comparison between $Depth_{physical}$ (the physical depth at which a fracture is sampled) and $Depth_{proxy}$ (the depth the fluid in the fracture should come from in order to have reached its temperature by thermal equilibrium with the host-rock). (C) and (D) present the detail of temperature logs for the Guidel site, respectively for recharge and discharge zone boreholes. Different logs for a same borehole correspond to different dates.

3.2.3 Hydrochemical facies

Figure III.12 shows a Piper diagram of the major cations and anions in all the boreholes from Guidel and Kermadoye. From a global perspective, the groundwater in the Critical Zone Observatory (CZO) corresponds to a sodium-chloride hydrochemical facies. Feldspars are major constituents (e.g. volume percents of Ab, An and K-F in Table III.5), which is consistent with the weathering of crystalline rocks. Anions are dominated by a Cl^{-}-NO_3^{-} component that, combined with the high Na concentrations, proximity to the coastline, and soil use in the catchments, indicates possible marine (Cl^{-}) or agricultural (NO_3^{-}) contributions to the total dissolved solids.

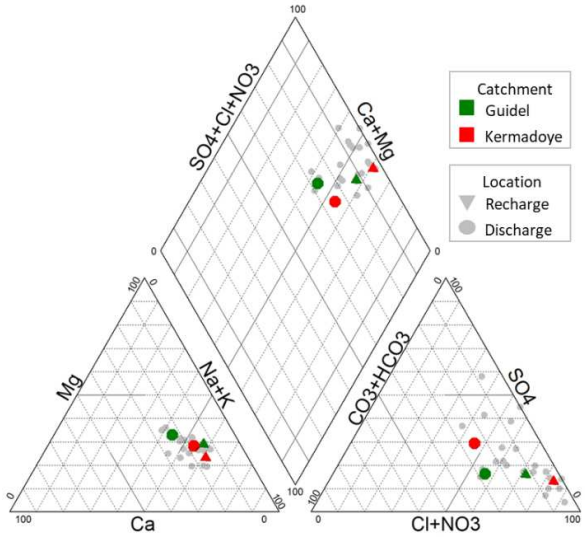

Figure III.12: **Piper diagram for the Guidel and Kermadoye catchments.** Points in color correspond to characteristic boreholes from recharge and discharge zones in the catchments, while points in grey correspond to the rest of the boreholes in the site.

3.2.4 Hydrochemical evolution in flow paths

Groundwater flow in a catchment occurs from recharge zones, where piezometric levels are high, to discharge zones where piezometric levels are low due to either topographic controls or pumping-induced drawdown. Thus, the hydrochemical parameters of boreholes in a catchment, classified according to their piezometric levels, can be visualized as a transect representing the hydrochemical evolution of flow paths. A representation of these hydrochemical transects is presented in Figure III.13 for both Guidel and Kermadoye catchments. The figure illustrates that both catchments globally show similar hydrochemical trends. Groundwater in recharge zones is oxidizing, with high concentration of electron acceptors like DO and NO_3^{-} that are progressively consumed along the transect, until depletion in the discharge areas where groundwater becomes reducing. The depletion of electron acceptors is consistent with an increase in groundwater residence time (i.e. decrease in CFC113 concentrations) which indicates that electron acceptors are likely consumed by reactivity along flow paths. Reducing discharge zones are characterized by increasing temperatures and electrical conductivities (E.C.). Moderate yet statistically significant contrasts in E.C. exist between recharge and discharge zones, with the latter showing higher E.C. values. For instance, E.C. values in Guidel are $422 \pm 35 \mu S.cm^{-1}$ in recharge and $505 \pm 64 \mu S.cm^{-1}$ in discharge zones (with a t-test p-value = 0.01), and in Kermadoye E.C.'s are $361 \pm 56 \mu S.cm^{-1}$ in recharge and $522 \pm 61 \mu S.cm^{-1}$ in discharge zones (with a t-test p-value = 0.001). The increase in E.C. indicates that the TDS of groundwater increases along the flow path as a consequence of mineral dissolution reactions. The increase in Mg and Fe concentrations suggests mica dissolution (i.e. biotite, chlorite or muscovite) but the trends between the two catchments show strong contrasts, especially in the iron concentrations that are about 3 orders of magnitude higher in Guidel than in Kermadoye.

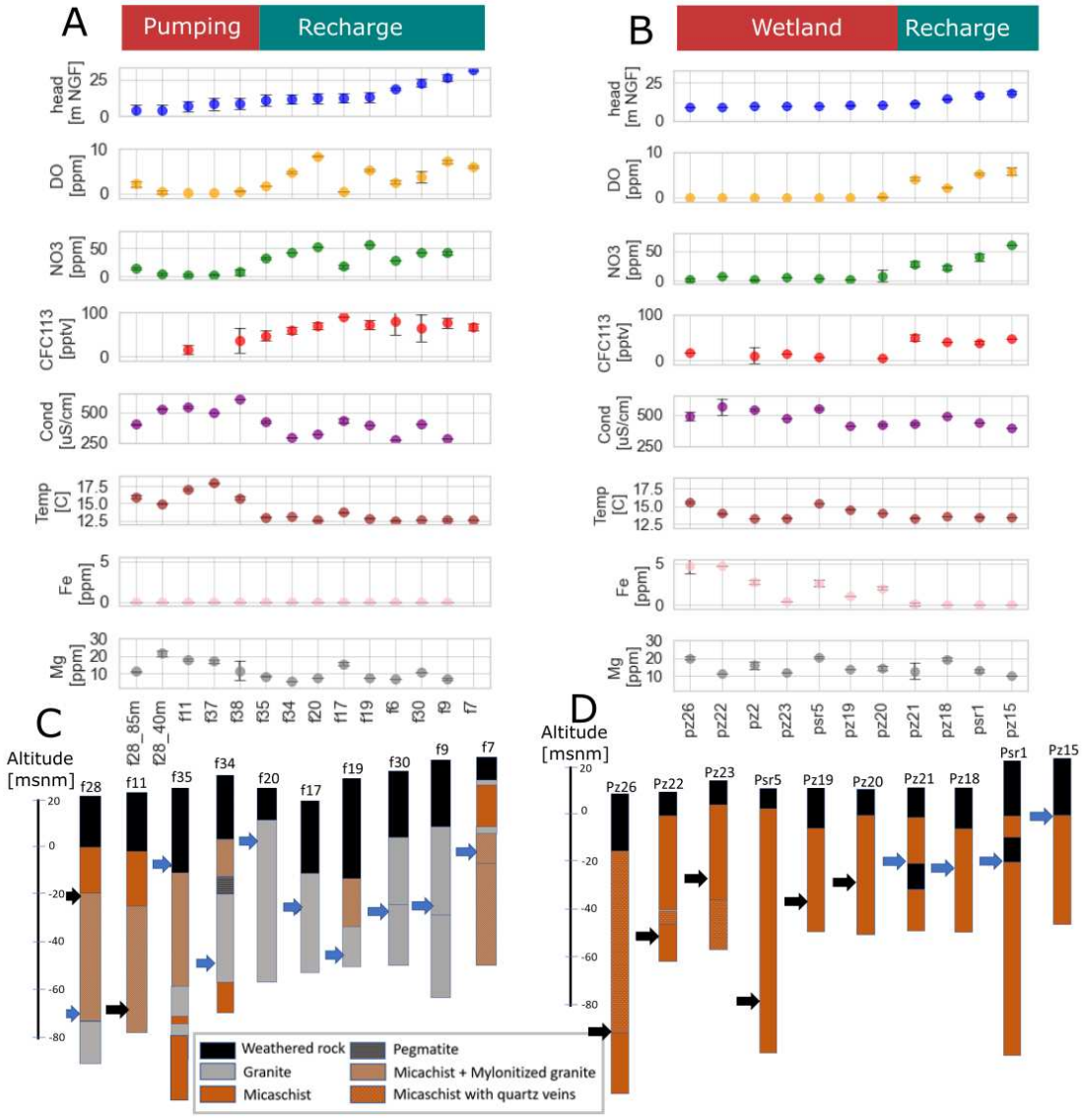

Figure III.13: **Hydrochemical transects for the boreholes of Kermadoye (left) and Guidel (right).** (A) and (B) are the hydrochemical transects of selected hydrochemical parameters measured in the dominant fracture. Boreholes are classed following groundwater levels in the catchment. The division between recharge and discharge (pumping and wetland) zones is defined as the point where groundwater DO concentrations shift to low values ($[DO] < 0.5mg.L^{-1}$). The main fracture per borehole is represented by the arrows in the lithological columns, (C) and (D) plots, where arrow colors indicate oxygenated (blue) or low-O_2 (black) groundwater flowing in the dominant fracture. Data for the hydrochemical transects corresponds to averages within 1σ for the period 2016-2022.

3.2.5 Groundwater end-members

Figure III.14 shows the results of a Principal Component Analysis (PCA) conducted on a dataset consisting of 18 measured parameters from 18 boreholes located in recharge and discharge zones of two catchments. The PCA identified two principal components that together explain 65.32% of the total variance. A third component, which accounts for 6.92% of the variance, is not shown. The purpose of the PCA was to identify patterns and relationships among the parameters and boreholes.

To reinforce the interpretation of the PCA results, we used Hierarchical Clustering Analysis (HCA) (Figure III.14). The HCA grouped the boreholes based on their proximity in the PCA space, allowing us to classify them into a small number of end-members. In our case, the HCA generated three end-members: one for the common recharge zone of Guidel and Kermadoye (end-member A) and two end-members (B and C) representing the discharge zones of both catchments, respectively. Additionally, a group of boreholes (D in Figure III.14) indicated points influenced mainly by mixing.

End-member A, which is correlated with the first principal component (PC1), represents a similar recharge end-member for both catchments. The variance of end-member A is explained by characteristic tracers of young groundwater such as CFCs, DO, and NO_3^-. On the other hand, the second principal component (PC2) explains the variance related to the discharge end-members and is associated with tracers characteristic of deep and old groundwater, such as temperature, electrical conductivity (EC), salinity, and rock dissolution products. For Guidel, the old end-member is correlated with higher salinity, Mn, and Fe contents, while for Kermadoye, the old end-member has higher temperatures, Si, SO_4, and Li concentrations.

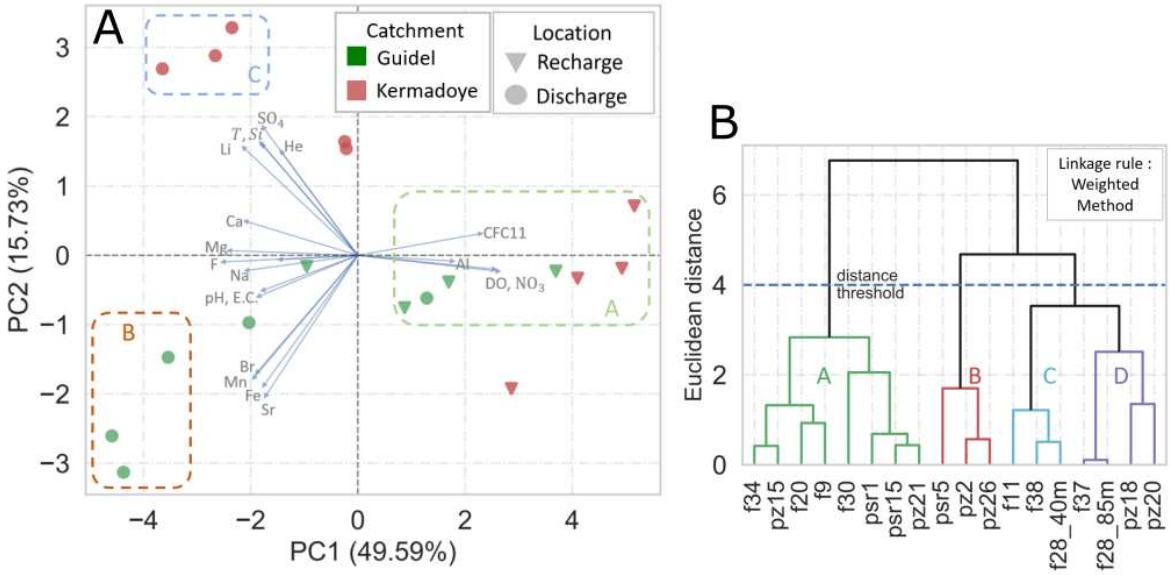

Figure III.14: Principal Component Analysis, PCA of hydrochemical parameters from Guidel and Kermadoye. (A): for selected boreholes from Kermadoye and Guidel catchments. Principal Component 1 (PC1) explains 57.26% of the variance while PC2 explains 14.52%. Arrows correspond to eigenvectors while dashed-boxes represent identified end-members (EM) from a Hierarchical Clustering Analysis, HCA (B) (A: Young EM, B: Kermadoye's Old EM and C: Guidel's Old EM).

3.3 Discussion

3.3.1 Groundwater flow paths in the Guidel catchment

The identification of vertical flows in the boreholes presented in Section 3.2.2 suggests that groundwater circulates in local flow paths: groundwater circulates downward from recharge zones in high topographies to reach upwelling flows in discharge zones situated in low altitudes. The negative correlation between groundwater temperature and CFC concentrations (see Figure III.13) indicates that higher groundwater temperatures are

related to longer flow paths. While most of recharge boreholes have similar temperature logs suggesting similar recharge conditions, artesian discharge boreholes have sparser temperatures which reflect a variety of flow path lengths in the catchment. Recharge boreholes Pz25 and Psr15 are the exception to this observation as shown in Figure III.11-C. Their cooler values and the slope of their temperature logs suggest that those boreholes sample flowpaths that are poorly connected. Interestingly, these are the only two boreholes located in the southern east part of the catchment that is isolated by a secondary fault (see Figure III.1-B). Similarly, discharge boreholes Pz26, Psr5, Psr6 and Pz19 show a particular behavior in Figure III.11. Indeed, their high temperature aligns in a common gradient meaning that they belong to a common flow path, possibly related to the drainance of the lithological contact by the presence of the subvertical normal fault that crosses the catchment in the wetland zone.

3.3.2 Links between groundwater end-members and lithology

The hydrochemical transects in Figure III.13 have shown that the electrical conductivity (E.C.) increases with residence time of groundwater in the catchment, which is consistent with the release of solutes by rock weathering. Therefore, the end-members identified in the PCA analysis (Figure III.14) can be viewed in the light of water-rock interactions and residence time in the catchment. For instance, the similarity of recharge boreholes in end-member A, independent of the catchment, suggests that lithology has little influence on the chemical signature of this group. This could be explained because of short reaction times (i.e. young groundwater) or because groundwater from these boreholes comes from shallow depths (Figure III.11), which have a higher probability of being in contact with less reactive minerals from the weathered zone.

A different situation occurs with old end-members, which are hydrochemically different according to the PCA. Two hypotheses could explain these differences. A first hypothesis, could be that the differences are produced because groundwater drains from different lithologies in every catchment. This could be a consequence of the catchment's position in relation to the lithological contact zone between granite and micaschist. Indeed, Guidel catchment is located farther from the outcropping part of the contact zone than Kermadoye (see Figure III.1). Therefore, most of the flow paths in Guidel would have been preferentially in contact with micaschists, while in Kermadoye, there would be a higher proportion of flow paths in the granite. As a result, the chemical composition of the old end-member should be influenced by the different water-rock interactions taking place in every catchment.

A second hypothesis to explain the differences could be that, even if both catchments drain the same lithologies, different groundwater residence times in the old end-member would result in different chemical compositions. In fact, even if the low CFC concentrations in old groundwater prevent the calculation of apparent ages, old groundwater in Kermadoye has higher temperatures than in the case of Guidel, respectively 17.4 °C and 14.7 °C. This difference of more than 2.5 °C indicates a deeper origin for the old end-member from Kermadoye and likely, a longer residence time of groundwater. In such case, the different hydrochemical signature of Kermadoye's old end-member could be the consequence of a more evolved state of water-rock interactions. However, the very low iron concentrations in the Kermadoye's old end-member (see Figure III.13) would not be consistent with the picture of Kermadoye being more chemically evolved than Guidel when both catchments drain the same lithology.

4 Chapter conclusion

This chapter provides a brief review of the geological and hydrogeological contexts of the Ploemeur CZO. The remarkable aquifer productivity in Kermadoye and the transient effects of pumping on groundwater chemistry have increased interest in geophysics and hydrochemistry in the last decade. More recently, microbial ecology has gained interest due to the subsurface microbial hotspots found in the Guidel catchment. However, **most Ploemeur CZO research has been conducted in the Kermadoye catchment, making it challenging to**

conduct comparative studies with Guidel. For instance, the proximity of both catchments allows for the study of their specificities, such as the groundwater flow regime (natural vs pumped) or the lithological context (granite vs micaschist). This chapter addresses provides complementary information on the petrological and hydrochemical characteristics of the Guidel catchment.

The petrological characterization provides a more detailed view of the mineralogy and reducing power of the granite and micaschist lithologies found in the Ploemeur CZO. **The reducing power of the rocks in the CZO is mainly ensured by the presence of mineral electron donors such as biotite and chlorite, with iron being the main electron donor present in the host-rocks**.

The hydrochemical characterization reveals clear contrasts between groundwater from recharge and discharge zones of the catchments. According to the PCA analysis, most of the sampled boreholes in every catchment can be classified either in a *young* or *old* end-member, which can be viewed in the light of water-rock interactions and residence time in the catchment. Although there are lithological differences between Guidel and Kermadoye catchments, **young end-members are hydrochemically similar in both catchments**, suggesting that short groundwater residence times are insufficient for weathering reactions to generate contrasts in groundwater chemical composition. Conversely, **old end-members between the two catchments suggest that the differences are more likely influenced by the lithological differences in the mineralogical compositions of the aquifer host rocks**. Figure III.15 presents the conceptual view of the CZO functioning based on the hydrochemical characterization.

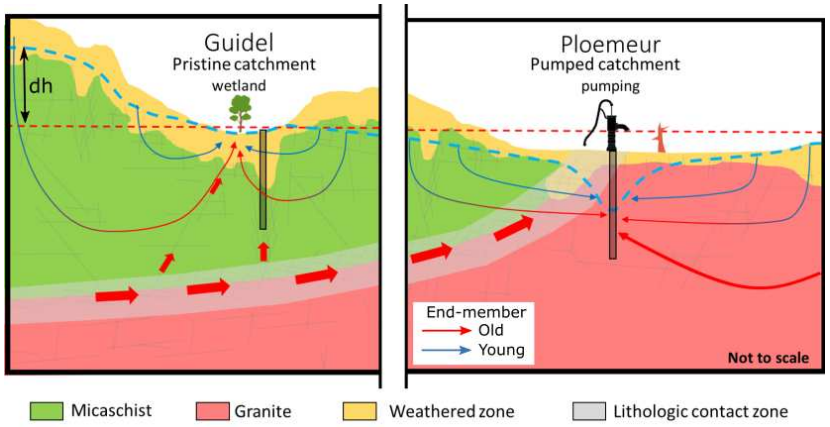

Figure III.15: Conceptual hydrogeological functioning of the two catchments as deduced from the flow regime and the geological setting

.

5 Take-home messages

An opportunity for comparative studies between Guidel and Kermadoye

In this chapter, we performed a petrological and hydrogeological study in the Guidel catchment to establish the hydrogeological functioning of the site. This detailed description provides a reference for future studies to address comparative questions that exploit the similarities between Guidel and Kermadoye catchments.

1. **Petrological study:**
    - Ferrous iron, Fe(II), is the main electron donor in the host-rocks of the CZO of Ploemeur, and is mainly present in silicate minerals such as biotite and chlorite.
    - Micaschist and granite are the main lithologies observed in the CZO. We provide an updated normative composition showing that micaschist has about 5 more times biotite than granite.
2. **Hydrogeological study:**
    - We conceptualize a flow path characterization through the analysis of upwelling and downwelling flows in Guidel.
    - The hydrochemical signatures of recharge end-members are similar between Guidel and Kermadoye. Conversely, discharge end-members are distinct and the differences seem controlled by whether groundwater circulates in granites or in micaschists.

The next chapter takes advantage of this knowledge basis and examines in more detail the hydrochemical differences observed between the old end-members of Guidel and Kermadoye. Moreover, we examine in detail the distribution of dissolved oxygen in the Guidel and Kermadoye catchments to relate it to the reactive-transport functioning of the site.

6 Chapter Acknowledgments

I want to thank Pavel Pitra for kindly answering to my questions during the petrological characterization. I also want to thank Thierry Labasque, Eliot Chatton and Camille Bouchez for presenting me the details of the Ploemeur CZO in our many trips to the field.

Bibliography

Aeschbach-Hertig, W., El-Gamal, H., Wieser, M., and Palcsu, L. (2008). Modeling excess air and degassing in groundwater by equilibrium partitioning with a gas phase. *Water Resources Research*, 44(8):1–12.

Aquilina, L., Roques, C., Boisson, A., Vergnaud-Ayraud, V., Labasque, T., Pauwels, H., Pételet-Giraud, E., Pettenati, M., Dufresne, A., Bethencourt, L., and Bour, O. (2018). Autotrophic denitrification supported by biotite dissolution in crystalline aquifers (1): New insights from short-term batch experiments. *Science of the Total Environment*, 619–620:842–853.

Arnold, M., Merchel, S., Bourlès, D. L., Braucher, R., Benedetti, L., Finkel, R. C., Aumaître, G., Gottdang, A., and Klein, M. (2010). The French accelerator mass spectrometry facility ASTER: Improved performance and developments. *Nuclear Instruments and Methods in Physics Research, Section B: Beam Interactions with Materials and Atoms*, 268(11-12):1954–1959.

Ayraud, V., Aquilina, L., Labasque, T., Pauwels, H., Molenat, J., Pierson-wickmann, A.-c., Durand, V., Bour, O., Tarits, C., Le, P., Fourre, E., Merot, P., and Davy, P. (2008). Compartmentalization of physical and chemical properties in hard-rock aquifers deduced from chemical and groundwater age analyses. *Applied Geochemistry*, 23(June):2686–2707.

Ballevre, M., Bosse, V., Dabard, M.-P., Ducassou, C., Fourcade, S., Paquette, J.-L., Peucat, J.-J., and Pitra, P. (2013). Histoire Géologique du massif Armoricain : Actualité de la recherche. *Bulletin de la Société Géologique et Minéralogique de Bretagne*, (D), 10–11:5–96.

Ballèvre, M., Bosse, V., Ducassou, C., and Pitra, P. (2009). Palaeozoic history of the Armorican Massif: Models for the tectonic evolution of the suture zones. *Comptes Rendus - Geoscience*, 341(2-3):174–201.

Béchennec, F., Hallégouët, B., Thiéblemont, D., and Thinon, I. (2012a). *Carte Géol. France (1/50 000), Feuille Lorient (383).* BRGM, Orleans.

Béchennec, F., Hallégouët, B., Thiéblemont, D., and Thinon, I. (2012b). *Notice Explicative, Carte Géol France (1/50 000), Feuille Lorient (383).* BRGM, Orléans.

Belghoul, A. (2010). *Caractérisation Pétrophysique et Hydrodynamique Du Socle Cristalli*. PhD thesis.

Bethencourt, L., Bochet, O., Farasin, J., Aquilina, L., Borgne, T. L., Quaiser, A., Biget, M., Michon-Coudouel, S., Labasque, T., and Dufresne, A. (2020). Genome reconstruction reveals distinct assemblages of Gallionellaceae in surface and subsurface redox transition zones. *FEMS Microbiology Ecology*, 96(5).

Bochet, O., Bethencourt, L., Dufresne, A., Farasin, J., Pédrot, M., Labasque, T., Chatton, E., Lavenant, N., Petton, C., Abbott, B. W., Aquilina, L., and Le Borgne, T. (2020). Iron-oxidizer hotspots formed by intermittent oxic–anoxic fluid mixing in fractured rocks. *Nature Geoscience*, 13(2):149–155.

Bouchez, C., Pupier, J., Benedetti, L., Deschamps, P., Guillou, V., Keddadouche, K., Aumaître, G., Arnold, M., and Bourlès, D. (2015). Isotope Dilution-AMS technique for 36Cl and Cl determination in low chlorine content waters. *Chemical Geology*, 404:62–70.

Buss, H. L., Sak, P. B., Webb, S. M., and Brantley, S. L. (2008). Weathering of the Rio Blanco quartz diorite , Luquillo Mountains , Puerto Rico : Coupling oxidation , dissolution , and fracturing. *Geochimica et Cosmochimica Acta*, 72:4488–4507.

Chatelier, M., Ruelleu, S., Bour, O., Porel, G., and Delay, F. (2011). Combined fluid temperature and flow logging for the characterization of hydraulic structure in a fractured karst aquifer. *Journal of Hydrology*, 400(3-4):377–386.

Dewandel, B., Lachassagne, P., Wyns, R., Maréchal, J. C., and Krishnamurthy, N. S. (2006). A generalized 3-D geological and hydrogeological conceptual model of granite aquifers controlled by single or multiphase weathering. *Journal of Hydrology*, 330:260–284.

Druillennec, T. L. (2007). Apport de la caractérisation de la variabilité des concentrations en radon-222 dans l ' eau à la compréhension du fonctionnement d ' un aquifère en milieu fracturé de socle : Exemple du site de. 33(0).

Eggler, D. H., Larson, E. E., and Bradley, W. C. (1969). Granites, grusses, and the Sherman erosion surface, southern Laramie Range, Colorado-Wyoming. *American Journal of Science*, 267(4):510–522.

Fortune, W. B. and Mellon, M. G. (1938). Determination of Iron with o-Phenanthroline: A Spectrophotometric Study. *Industrial and Engineering Chemistry - Analytical Edition*, 10(2):60–64.

Guillaumot, L., Longuevergne, L., Marçais, J., Lavenant, N., and Bour, O. (2022). Frequency domain water table fluctuations reveal recharge in fractured aquifers depends on both intense and seasonal rainfall and unsaturated zone thickness. *Hydrology and Earth System Sciences Discussions*, pages 1–38.

Hamme, R. C. and Emerson, S. R. (2004). The solubility of neon, nitrogen and argon in distilled water and seawater. *Deep Sea Research Part I: Oceanographic Research Papers*, 51(11):1517–1528.

Jiménez-Martínez, J., Longuevergne, L., Le Borgne, T., Davy, P., Russian, A., and Bour, O. (2013). Temporal and spatial scaling of hydraulic response to recharge in fractured aquifers: Insights from a frequency domain analysis. *Water Resources Research*, 49(5):3007–3023.

Klepikova, M. V., Le Borgne, T., Bour, O., and Davy, P. (2011). A methodology for using borehole temperature-depth profiles under ambient, single and cross-borehole pumping conditions to estimate fracture hydraulic properties. *Journal of Hydrology*, 407(1-4):145–152.

Le Borgne, T., Bour, O., Paillet, F. L., and Caudal, J. P. (2006a). Assessment of preferential flow path connectivity and hydraulic properties at single-borehole and cross-borehole scales in a fractured aquifer. *Journal of Hydrology*, 328(1-2):347–359.

Le Borgne, T., Paillet, F., Bour, O., and Caudal, J. P. (2006b). Cross-borehole flowmeter tests for transient heads in heterogeneous aquifers. *Ground Water*, 44(3):444–452.

Leray, S., de Dreuzy, J.-R., Aquilina, L., Vergnaud-Ayraud, V., Labasque, T., Bour, O., and Le Borgne, T. (2014). Temporal evolution of age data under transient pumping conditions. *Journal of Hydrology*, 511:555–566.

Leray, S., de Dreuzy, J. R., Bour, O., and Bresciani, E. (2013). Numerical modeling of the productivity of vertical to shallowly dipping fractured zones in crystalline rocks. *Journal of Hydrology*, 481:64–75.

Maamar, S. B., Aquilina, L., Quaiser, A., Pauwels, H., Michon-Coudouel, S., Vergnaud-Ayraud, V., Labasque, T., Roques, C., Abbott, B. W., and Dufresne, A. (2015). Groundwater isolation governs chemistry and microbial community structure along hydrologic flowpaths. *Frontiers in Microbiology*, 6(DEC):1–13.

Maréchal, J. C., Dewandel, B., and Subrahmanyam, K. (2004). Use of hydraulic tests at different scales to characterize fracture network properties in the weathered-fractured layer of a hard rock aquifer. *Water Resources Research*, 40(11).

Osorio-Leon, I., Bouchez, C., Chatton, E., Lavenant, N., Longuevergne, L., and Le Borgne, T. (2023). Hydrological and geological controls for the depth distribution of dissolved oxygen and iron in silicate catchments.

Pauwels, H., Ayraud-Vergnaud, V., Aquilina, L., and Molénat, J. (2010). The fate of nitrogen and sulfur in hard-rock aquifers as shown by sulfate-isotope tracing. *Applied Geochemistry*, 25(1):105–115.

Pedregosa, F., Varoquaux, G., Gramfort, A., Michel, V., Thirion, B., Grisel, O., Blondel, M., Prettenhofer, P., Weiss, R., Dubourg, V., Venderplas, J., Passos, A., Cournapeau, D., Brucher, M., Matthieu, P., and Duchesnay, É. (2011). Scikit-learn: Machine Learning in Python. *Journal of Machine Learning Research*, 12:2825–2830.

Pouladi, B., Bour, O., Longuevergne, L., de La Bernardie, J., and Simon, N. (2021). Modelling borehole flows from Distributed Temperature Sensing data to monitor groundwater dynamics in fractured media. *Journal of Hydrology*, 598(November 2020).

Ragland, P. C. (1989). *Basic Analytical Petrology*. Oxford University Press, New York.

Roques, C., Aquilina, L., Boisson, A., Vergnaud-Ayraud, V., Labasque, T., Longuevergne, L., Laurencelle, M., Dufresne, A., de Dreuzy, J. R., Pauwels, H., and Bour, O. (2018). Autotrophic denitrification supported by biotite dissolution in crystalline aquifers: (2) transient mixing and denitrification dynamic during long-term pumping. *Science of the Total Environment*, 619–620:491–503.

Ruelleu, S. (2010). Caractérisation hydrogéophysique des milieux fracturés : Développement instrumental et modélisation des vitesses d'écoulement en forage. page 248.

Ruelleu, S., Moreau, F., Bour, O., Gapais, D., and Martelet, G. (2010). Impact of gently dipping discontinuities on basement aquifer recharge: An example from Ploemeur (Brittany, France). *Journal of Applied Geophysics*, 70(2):161–168.

Sugisaki, R. and Taki, K. (1987). Simplified analyses in of He , natural Ne , waters and Ar dissolved. *Geochemical Journal*, 21:23–27.

Tarits, C., Aquilina, L., Ayraud, V., Pauwels, H., Davy, P., Touchard, F., and Bour, O. (2006). Oxido-reduction sequence related to flux variations of groundwater from a fractured basement aquifer (Ploemeur area, France). *Applied Geochemistry*, 21(1):29–47.

Touchard, F. (1999). *Caractérisation Hydrogéologique d'un Aquifère de Socle Fracturé : Site de Ploemeur (Morbihan).* PhD thesis, Université de Rennes 1.

IV. DELIMITING THE DEEP OXIC HYDROSPHERE IN FRACTURED ROCKS

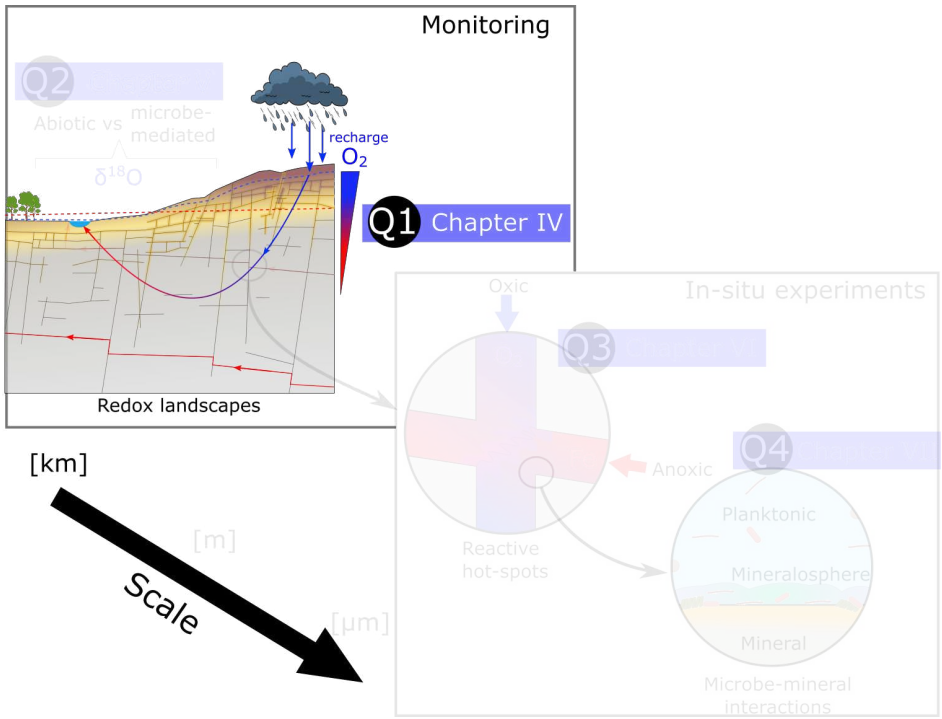

Contents

1 Chapter presentation

In the introductory part of this work we presented evidence suggesting that fractured rocks can be favorable to the presence of oxic groundwater [e.g. McMahon and Chapelle (2008); DeSimone et al. (2014)], possibly constituting a *deep oxic hydrosphere*. The limited content of organic carbon (Ehrlich et al.; 2015) and the presence of high transmissive flow paths such as fractures and faults (Bochet et al.; 2020), favor the hydraulic connectivity between the surface and the subsurface in fractured-bedrock systems. However, as highlighted in Chapter I, there is a lack of systematic inventories of the distribution of DO in fractured systems, leading to a poorly constrained understanding of the mechanisms that regulate its presence in the subsurface. We particularly identified two communities which have been interested on the reactive-transport of dissolved oxygen (DO) in fractured systems: the *rock weathering* community and the *nuclear waste disposal* community. Although these communities have provided, respectively, palaeohydrogeological evidences [e.g. Buss et al. (2008); Bazilevskaya et al. (2015); Antoniellini et al. (2017); Krone et al. (2021); Hampl et al. (2022)] and theoretical bases [e.g. Sidborn and Neretnieks (2007, 2008); Trinchero et al. (2018, 2019)] for the reactive transport of DO in deep fractures, they focus on geological timescales which can not be directly transposed to modern groundwater systems. There is in fact a knowledge gap concerning the reactive-transport of DO in modern aquifer systems, where groundwater residence times usually range between 10 to 10^2 years (Sprenger et al.; 2019). Little is known about the relative timescales between groundwater travel time and kinetic processes consuming DO, and how it impacts the redox landscapes in the subsurface. This leads to the central question of this chapter: **How deep can groundwater transport dissolved O_2 in aquifer systems and, which factors control this reactive-transport problem?**. In this chapter, we present an article published in Water Resources Research in which we tackle this question. In this article: (1) we develop a theoretical framework to define the reactive-transport problem of DO in fractured-aquifers, focused on modern systems, (2) we propose simple analytical solutions that relate the depth distributions of both dissolved O_2 and Fe with dimensionless numbers that give a synthetic view of the hydrological and geological factors that control these distributions, (3) we use a numerical model to validate the approximations of the analytical solutions and (4) we test the analytical model to constrain the factors controlling the depth distributions of both dissolved O_2 and Fe in the CZO of Ploemeur. Indeed, the work presented in the preceding Chapter III established a basis allowing for comparative studies between the Guidel and Kermadoye catchments. Therefore, we test the modeling framework developed in this chapter to constrain the factors that control the depth distributions of O_2 and Fe in both catchments. We close the chapter by presented a series of perspectives that can contribute to continue and improve this work.

2 Article "Hydrological and Geological Controls for the Depth Distribution of Dissolved Oxygen and Iron in Silicate Catchments"

Water Resources Research

RESEARCH ARTICLE
10.1029/2023WR034986

Special Section:
The Future of Critical Zone Science: Towards Shared Goals, Tools, Approaches and Philosophy

Hydrological and Geological Controls for the Depth Distribution of Dissolved Oxygen and Iron in Silicate Catchments

Ivan Osorio-Leon[1], Camille Bouchez[1], Eliot Chatton[1], Nicolas Lavenant[1], Laurent Longuevergne[1], and Tanguy Le Borgne[1]

[1]University Rennes—CNRS, Géosciences Rennes—UMR 6118, Rennes, France

Key Points:

- We derive a reduced analytical model to predict the depth distribution of dissolved O_2 and Fe^{2+} in silicate catchments
- The theory, validated from a reactive transport model, quantifies the hydrological and geological controls through two dimensionless numbers
- We use this framework to analyze and explain the O_2/Fe^{2+} distributions in two sites with contrasted chemical properties

Supporting Information:

Supporting Information may be found in the online version of this article.

Correspondence to:

I. Osorio-Leon and C. Bouchez,
idosoriole@unal.edu.co;
camille.bouchez@univ-rennes.fr

Citation:

Osorio-Leon, I., Bouchez, C., Chatton, E., Lavenant, N., Longuevergne, L., & Le Borgne, T. (2023). Hydrological and geological controls for the depth distribution of dissolved oxygen and iron in silicate catchments. *Water Resources Research*, *59*, e2023WR034986. https://doi.org/10.1029/2023WR034986

Received 28 MAR 2023
Accepted 29 JUL 2023

Author Contributions:

Conceptualization: Ivan Osorio-Leon, Camille Bouchez, Tanguy Le Borgne
Data curation: Ivan Osorio-Leon, Camille Bouchez, Eliot Chatton, Nicolas Lavenant, Tanguy Le Borgne

Abstract Dissolved Oxygen (DO) plays a key role in reactive processes and microbial dynamics in the critical zone. Recent observations showed that fractures can provide rapid pathways for oxygen penetration in aquifers, triggering unexpected biogeochemical processes. In the shallow subsurface, DO reacts with electron donors, such as Fe^{2+} coming from mineral dissolution. Yet, little is known about the factors controlling the spatial heterogeneity and distribution of oxygen with depth. Here we present a reduced analytical model describing the coupled evolution of DO and Fe^{2+} as a function of fluid travel time in silicate catchments. Our model, validated from fully resolved reactive transport simulations, predicts a linear decay of DO with time, followed by a rapid non-linear increase of Fe^{2+} concentrations up to a far-from-equilibrium steady-state. The relative effects of geological and hydrological forcings are quantified through a Damköhler number (Da) and a lithological number (Λ). We use this framework to investigate the depth distribution of DO and Fe^{2+} in two catchments with similar environmental contexts but contrasted hydrochemical properties. We show that hydrochemical differences are explained by small variations in Da but orders of magnitude variations in Λ. Therefore, we demonstrate that the hydrological and geological drivers controlling hydrochemistry in silicate catchments can be discriminated by analyzing jointly the O_2 and Fe^{2+} evolution with depth. These findings provide a new conceptual framework to understand and predict the evolution of DO in modern groundwater, which plays an important role in critical zone processes.

Plain Language Summary Dissolved Oxygen (DO) is involved in important biogeochemical reactions, such as the aerobic respiration of microbes, rock-weathering or contaminant degradation. The general view is that the deeper subsurface of continents is mostly anoxic. However, recent observations have shown that cracks in rocks can allow oxygen to reach deeper down, thus extending deeper the influence of oxygen in reactions. Here, we present a modeling framework validated with field data to understand and predict the hydrological and geological controls on DO evolution in silicate catchments, shedding new light on its influence on rock-weathering and microbial life in the continents.

1. Introduction

Oxygen is central in redox reactions because it is the most abundant and readily available electron acceptor in the environment (Korom, 1992; Stumm & Morgan, 1996) and offers a strong redox potential. In aquatic environments, dissolved oxygen (DO) is mostly produced by photosynthesis and consumed by aerobic respiration of organic matter (Mader et al., 2017). In the subsurface, the transport of DO and CO_2 by fluid flow triggers the weathering of silicate rocks (Fletcher et al., 2006; Kim et al., 2017; Li et al., 2017; Singha & Navarre-Sitchler, 2022), which represent a quarter of the outcropping Earth rocks (Hartmann & Moosdorf, 2012). The cycle of DO is thus closely related to the geochemical cycles of carbon (Bar-on et al., 2018; Petsch et al., 2004), iron (Kappler et al., 2021; Melton et al., 2014; Napieralski et al., 2019) and sulfur (Canfield, 2004; Gu et al., 2020). Besides abiotic processes, recent studies have pointed out that weathering reactions, particularly involving DO, are often mediated by microbes (Erable et al., 2012; Kappler et al., 2021; Napieralski et al., 2019) because the redox potential of the reaction offers an energy source for microbes to thrive (Emerson et al., 2010). DO thus also exerts a key ecological role by impacting the biodiversity (Hancock et al., 2005; Humphreys, 2009; Malard & Hervant, 1999) and activity of aerobic microbial metabolisms (Druschel et al., 2008; Mader et al., 2017; Maisch et al., 2019).

When DO is not depleted in soils, either because of a limited soil-thickness or a low organic matter availability, oxic water can enter the saturated zone in the bedrock. It then reacts with the electron donors available

Water Resources Research 10.1029/2023WR034986

Formal analysis: Ivan Osorio-Leon, Camille Bouchez, Eliot Chatton, Nicolas Lavenant
Funding acquisition: Camille Bouchez, Tanguy Le Borgne
Investigation: Ivan Osorio-Leon, Camille Bouchez, Tanguy Le Borgne
Methodology: Ivan Osorio-Leon, Camille Bouchez, Eliot Chatton, Tanguy Le Borgne
Project Administration: Camille Bouchez, Laurent Longuevergne, Tanguy Le Borgne
Resources: Camille Bouchez, Nicolas Lavenant
Software: Ivan Osorio-Leon
Supervision: Camille Bouchez, Tanguy Le Borgne
Validation: Ivan Osorio-Leon, Camille Bouchez, Tanguy Le Borgne
Visualization: Ivan Osorio-Leon
Writing – original draft: Ivan Osorio-Leon, Camille Bouchez, Tanguy Le Borgne
Writing – review & editing: Ivan Osorio-Leon, Camille Bouchez, Laurent Longuevergne, Tanguy Le Borgne

in the subsurface, such as Fe(II), Mn(II), CH_4, H_2, HS^- or petrogenic organic carbon (Canfield, 2004; Kartsen Pedersen, 1997; Tebo et al., 2005). Iron is the most abundant redox-sensitive element in the Earth crust (Frey & Reed, 2012), it is linked to biogeochemical cycles of carbon, sulfur and nitrogen (Casar et al., 2021; Kendall et al., 2012). The reduction of DO by iron can occur either by Fe(II)-sites on mineral surfaces (White et al., 1985) or by Fe^{2+} dissolved in water subsequently to the release of structural Fe(II) by mineral dissolution (White & Yee, 1985). The most common Fe(II)-bearing primary minerals in hard-rocks are silicates such as biotite (Aquilina et al., 2018; Hampl et al., 2021; Holbrook et al., 2019; Malmström et al., 1996), pyroxene (Behrens et al., 2015) and hornblende (Fletcher et al., 2006) and in less proportion, sulfides such as pyrite (Gu et al., 2020).

Several field works documenting weathering profiles in hard-rocks, either from outcrops (Antoniellini et al., 2017) or borehole cores (Bazilevskaya et al., 2013; Dideriksen et al., 2010; Hampl et al., 2021; Holbrook et al., 2019), have suggested that DO transport by subsurface flow could explain the presence of secondary minerals and weathering induced fracturing (WIF) in ferrous silicates (Bazilevskaya et al., 2013; Kim et al., 2017) from deep regolith. Likewise, evidence from field measurements in fractured-rock aquifers has shown that DO can effectively persist in deep aquifers(Bucher et al., 2009; DeSimone et al., 2014; Edmunds et al., 1984; Ruff et al., 2023; Sullivan et al., 2016; Winograd & Robertson, 1982). Based on field observations, the presence or absence of DO in the subsurface has been attributed to lithological differences of the bedrock (Malard & Hervant, 1999; Winograd & Robertson, 1982) or to the spatial distribution of oxidation fronts (Liao et al., 2022). However, it is still challenging to predict the expected depth of DO in silicate catchments.

Fractures can provide fast transport pathways in the subsurface and therefore influence reactive transport processes (Deng & Spycher, 2019). The transport and fate of DO in fractured rocks have been studied in the framework of risk assessments for DO penetration to nuclear waste repository sites. Numerical studies have simulated the advance of the redox front in the matrix of granitic rocks (Macquarrie et al., 2010; Spiessl et al., 2008; Trinchero et al., 2019) and in fracture networks (Trinchero et al., 2017) providing insights into the mechanisms driving oxygen transport in fractured rocks. Three main approaches have been used to model the reactive transport of oxygen in fractured media (Macquarrie et al., 2010): (a) Equivalent porous medium (EPM) models for fracture zones, (b) discrete fracture models with reactive in fill and no interaction with the adjacent rock matrix, and (c) fracture–matrix models in which the fracture and/or matrix may contain reactive minerals. The effect of matrix diffusion is particularly important in driving the long term (thousands of years) transport of oxygen, relevant for applications such as nuclear waste storage. In this context, approximate analytical solutions have been obtained (Sidborn & Neretnieks, 2007, 2008) by assuming that the dissolution of Fe(II) bearing minerals is rapid compared to transport, which is relevant for large time scales (thousands of years).

In the context of catchment dynamics, modern groundwater residence times are on the order of tens to hundreds of years (Sprenger et al., 2019). At these time scales, DO diffusion in the matrix may be assumed to be relatively small compared to advective fluxes while dissolution rates cannot assumed to be fast (Sidborn & Neretnieks, 2008; Trinchero et al., 2018). In this regime, how the interplay between dissolution rates and advective transport dynamics drives DO transport has not been quantified analytically. The coupling between transport and reaction rates at catchment scale has been conceptualized using the Damköhler number, defined as the ratio of the characteristic transport and reaction time scales (Maher, 2010; Maher & Chamberlain, 2014). In this approach, structures such as fractures and rock matrix are not represented explicitly but instead integrated into an effective fluid travel time, representing the time during which fluid has been exposed to reactive minerals (Seeboonruang & Ginn, 2006). In this study, we use a travel time formulation to develop reduced analytical model for coupled transport and reaction of DO and Fe^{2+} in silicate catchments.

We thus develop approximate analytical solutions for coupled oxygen and iron transport and reaction in a simple conceptual water-rock interaction model. We use a travel time formulation and a simple setting of two minerals accounting for dissolution and precipitation processes. We then use a full numerical model with a more realistic set of minerals to validate the approximations of the analytical approach. The reduced analytical model provides a mechanistic understanding of geological and hydrological controls of oxygen transport and reaction through two dimensionless numbers: Damköhler (Da) and a Lithological number (Λ). The former quantifies the relative effect of Fe(II)-bearing minerals abundance and transport velocity, while the latter quantifies the balance between dissolution and precipitation of primary and secondary minerals, respectively. We use this framework to interpret field data in two critical zone observatories with contrasted chemical properties.

Water Resources Research 10.1029/2023WR034986

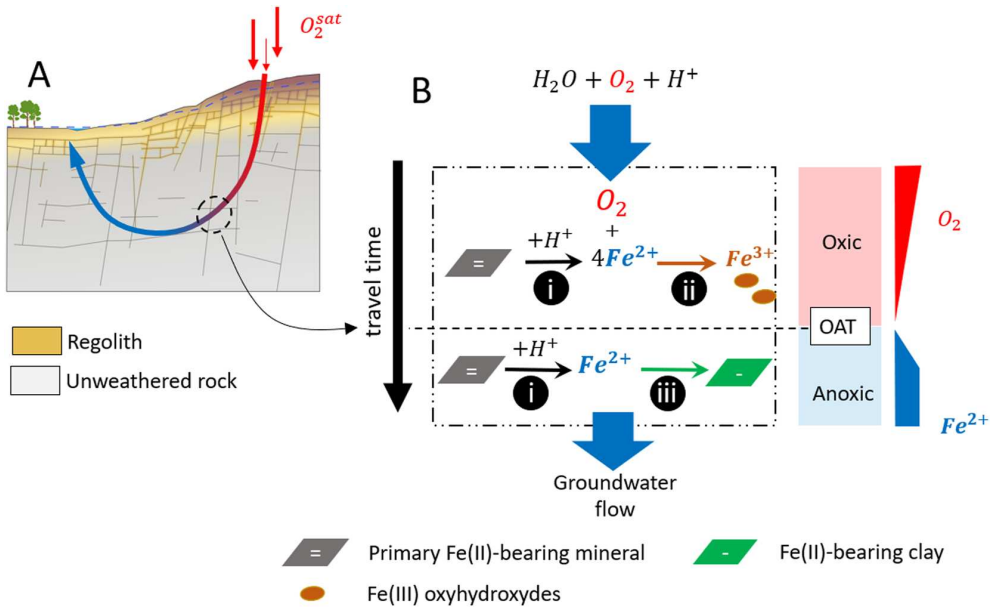

Figure 1. Conceptual model for the transport and reactivity of Dissolved Oxygen (DO) and Fe^{2+} along a flowpath (a). (b) In the unweathered rock, DO is consumed owing to the following reaction network (i) Fe(II)-bearing minerals dissolution, promoted by groundwater acidity, releases Fe^{2+} (ii) aqueous oxidation of dissolved iron by DO and precipitation of Fe(III) oxyhydroxydes (iii) incongruent mineral dissolution releases Fe^{2+} and forms Fe(II)-bearing clay. OAT indicates the Oxic-Anoxic Transition along the pathway.

2. Reactive Transport of Dissolved Oxygen and Iron

2.1. Model Conceptualization

The different conceptual models used for the reactive transport of oxygen in fractured media may consider advection in the fracture, reaction in the fracture, diffusion and reaction in the matrix (Macquarrie et al., 2010). It is not known how to solve the problem analytically with all these processes. However, analytical solutions can be derived by considering the dominant processes at different time scales. At long time scales (thousands of years), matrix diffusion is a key process, while reaction can be considered to be fast, which facilitates the derivation of analytical expressions for the oxic front propagation (Sidborn & Neretnieks, 2007, 2008). Here we focus on the short term regime (10^1–10^2 years), consistent with catchment residence times. We thus neglect the effect of matrix diffusion but include the impact of reaction kinetics, leading to both transport-limited and reaction-limited dynamics. Therefore, our model considers a fracture zone as an equivalent porous media with reactive infill and neglects matrix diffusion, following a common assumption (Trinchero et al., 2018).

To unravel the respective roles of hydrological and geological controls on DO and Fe^{2+}, we consider a travel time formulation (Maher, 2010). For a given flowpath, we model a reaction network in a parcel of transported fluid (i.e., we use a Lagrangian framework) as a kinetic system controlled by travel time (Figure 1). We thus assume that transport and mineral dissolution reactions are at steady state and identify travel time with reaction time in the model. We quantify interactions between oxic recharge water and Fe(II)-bearing minerals in a fracture zone. We assume advection dominated transport in the fracture zone and thus neglect diffusive DO inputs from the surface. We derive approximate analytical expressions of both DO and Fe^{2+} as a function of fluid travel time. We assume that the flowpath crosses a shallow regolith zone followed by an unweathered zone in which DO reacts with Fe^{2+} produced from minerals dissolution (Figure 1). In a second step, we relate travel time to depth using an average transport velocity and derive equations for the evolution with depth of DO and Fe^{2+}.

2.2. Geochemical System

We study the kinetic coupling between two geochemical reactions: the dissolution of iron-bearing minerals to produce dissolved iron (Fe^{2+}) followed by its oxidation with DO transported from recharge fluids (Figure 1). Even

Water Resources Research 10.1029/2023WR034986

if the oxidation of structural Fe(II) has been evidenced for Fe(II)-bearing minerals like Biotite (Buss et al., 2008) and Chlorite (Liao et al., 2022), here we neglect this process since its kinetics are still poorly constrained. Therefore, and similarly to previous works (Macquarrie et al., 2010; Sidborn & Neretnieks, 2008), we assume that Fe(II)-bearing minerals dissolve through a non-oxidative mechanism that liberates Fe^{2+} while consuming acidity, and that Fe(II)-bearing clays (Fe-clay) precipitate.

We model the dissolution and precipitation kinetics for mineral reactions using the Transition State Theory, expressing the reaction rate for a mineral j (R_j) as (Lasaga, 1984):

$$R_j = S_{V,j}\omega^{-1}\left(k_{j,H}a_H^{n_H} + k_j + k_{j,OH}a_{OH}^{n_{OH}}\right)e^{-\frac{E_{a,j}}{RT}}\left(1-\frac{Q_j}{K_{sp,j}}\right), \quad \text{with} \quad S_{V,j} = \frac{S_{M,j}\Phi_j MM_j}{V_{m,j}} \tag{1}$$

With ($k_{j,H}$, k_j, $k_{j,\mathrm{OH}}$) [mol m^{-2} s^{-1}] the intrinsic reaction constants at 25°C at acid, neutral and basic pH, respectively; a the activity and n the affinity factor of the indicated ion accounting for reaction catalysis by pH, $E_{a,j}$ the activation energy, Q_i the activity product and $K_{sp,j}$ the solubility product for mineral species j, ω is the fracture porosity, R is the ideal gas constant and T the absolute temperature. $S_{V,j}$ $\left[m^2.m_{pm}^{-3}\right]$ is the bulk surface area of the mineral species j, a function of the mineral specific surface area $S_{M,j}$, the mineral volume fraction Φ_j, the mineral molecular mass MM_j and the mineral molar volume $V_{m,j}$. A glossary containing the main variables in this manuscript is available in Table 1.

The aqueous reaction between DO and dissolved iron, and the corresponding kinetic law, are respectively:

$$4Fe^{2+} + O_2 + 4H^+ \rightarrow 4Fe^{3+} + 2H_2O \tag{2}$$

$$R_{ox} = k_{ox}C_{Fe^{2+}}P_{O_2}C_{OH^-}^2 \; for \; pH > 4.5, \tag{3}$$

with R_{ox} the rate of Fe^{2+} oxidation, k_{ox} the intrinsic reaction constant of oxidation ($1.3\times10^{12}\mathrm{M}^{-2}\,\mathrm{atm}^{-1}\,\mathrm{s}^{-1}$), C_i the concentration of species i in [mol L^{-1}] and P_{O_2} the partial pressure of oxygen in [atm] (Singer & Stumm, 1970).

Since groundwater in silicate catchments is commonly slightly acid to near-neutral (DeSimone et al., 2014), pH is here buffered at 7, Equations 1 and 2 reduce to:

$$R_j = S_{V,j}k'_j\omega^{-1}\left(1-\frac{Q_j}{K_{sp,j}}\right), \quad \text{with}\; k'_j = k_j|^{25°C}e^{-\frac{E_{a,j}}{RT}} \tag{4}$$

and

$$R_{ox} = k^*_{ox}C_{Fe^{2+}}C_{O_2}, \quad \text{with}\; k^*_{ox} = \frac{k_{ox}}{K_H}C_{OH^-}^2 \tag{5}$$

2.3. Reduced Analytical Model

At any moment, the change on DO and dissolved iron concentrations with respect to travel time (τ) is the result of the iron release from Fe(II)-bearing minerals dissolution R_d, and iron retention processes, resulting from Fe^{2+} oxidation R_{ox} and precipitation of clay, R_p. For the purpose of simplicity, we assume that there is only one species of Fe(II)-bearing mineral that dissolves and one species that precipitates:

$$\begin{cases} \frac{dC_{Fe^{2+}}}{d\tau} = \nu_d R_d - \nu_p R_p - R_{ox} \\ \frac{dC_{DO}}{d\tau} = -\frac{1}{4}R_{ox} \end{cases} \tag{6}$$

where ν_d and ν_p correspond to stoichiometric coefficients accounting for the number of Fe^{2+} per mineral formula in the dissolving or precipitating minerals respectively. R_d and R_p are described by Equation 4 and R_{ox} by Equation 5. In order to solve the system of Equation 6, we consider two regimes: (a) initially oxic conditions, (b) anoxic conditions once oxygen has been depleted.

AGU ADVANCING EARTH AND SPACE SCIENCES

Water Resources Research

10.1029/2023WR034986

Table 1
Glossary of Main Variables in the Text

Nomenclature	Units	Variable
a	$[mol.kg_w^{-1}]$	Activity
C	$[mol.kg_w^{-1}]$	Concentration
Da		Damköhler number
DO		Dissolved Oxygen
E_a	[kcal mol^{-1}]	Activation energy
Fe^{2+}		Dissolved Fe(II)
$Fe-clay$		Fe-rich clay (secondary mineral)
Φ	[-]	Volume fraction
γ	$[mol_{Fe}.kg_w^{-1}.s]$	Reducing or precipitation capacity of mineral
Q	[-]	Ionic Activity Product
Γ	[-]	Q for all ionic species in mineral excepting iron
j		Index standing for b: biotite, c: Fe-clay, d: dissolving mineral, p: precipitating mineral
K_H	$[mol.atm^{-1}.kg_w^{-1}]$	Henry's constant
K_{sp}	[-]	Solubility product for mineral
K_w	[mol^2 L^{-2}]	Auto-dissociation constant of water
k	[mol m^{-2} s^{-1}]	Kinetic constant for mineral dissolution
k_{ox}	[kg_w mol^{-1} s^{-1}]	Kinetic constant for iron oxidation by DO
Λ	[-]	Lithological parameter
ν	[-]	number of Fe^{2+} atoms per mineral formula
R	$[mol.kg_w^{-1}.s^{-1}]$	Reaction rate
s	$[mol.kg_w^{-1}]$	Mineral solubility
S_M	[m^2 g^{-1}]	Specific surface area
S_V	$[m^2.m_{pm}^{-3}]$	Bulk surface area
τ	[y]	Mean fluid travel time
τ_c	[y]	Characteristic time for DO consumption
τ_t	[y]	Characteristic time for DO transport
$\overline{v_a}$	[m y^{-1}]	Apparent vertical velocity
ω	[-]	Porosity
z_c	[m]	Reference depth for DO transport

2.3.1. Oxic Regime

At short travel times, DO is in excess with respect to Fe^{2+} and pH is close to neutrality. Under this condition, very little iron can persist in solution as it is rapidly oxidized according to Equation 2, which has a large kinetic constant. Due to this solute limitation and considering that primary minerals are more abundant than secondary minerals in unweathered rocks, we assume that $R_p \ll R_d$. Therefore, Equation 6 simplifies to:

$$\begin{cases} \frac{dC_{Fe^{2+}}}{d\tau} + R_{ox} = \nu_d R_d \\ \frac{dC_{DO}}{d\tau} = -\frac{1}{4} R_{ox} \end{cases} \quad (7)$$

Water Resources Research 10.1029/2023WR034986

As Fe(II)-bearing minerals are highly under-saturated, the saturation state of the mineral $\left(\frac{Q_j}{K_{sp,j}}\right)$ tends to zero in Equation 4. Rearranging Equation 7 with this assumption yields:

$$\frac{dC_{Fe^{2+}}}{d\tau} - 4\frac{dC_{DO}}{d\tau} = \nu_d S_{V,d} k'_d \omega^{-1}. \tag{8}$$

Since the oxidation reaction (consuming DO and Fe^{2+}) is much faster than the dissolution reaction (releasing Fe^{2+}), dissolved iron concentrations are low and vary little because of this kinetic limitation. Thus, $\frac{dC_{Fe^{2+}}}{d\tau} \ll \frac{dC_{DO}}{d\tau}$, which leads to

$$\frac{dC_{DO}}{d\tau} = -\frac{1}{4}\nu_d S_{V,d} k'_d \omega^{-1}. \tag{9}$$

Hence, the decay of oxygen is controlled by the amount of dissolved iron produced from mineral dissolution. We define the reducing capacity of a mineral j (γ_j) as the flux of iron produced by mineral reaction per unit of volume of fluid:

$$\gamma_j = \nu_j S_{V,j} k'_j \omega^{-1}, \tag{10}$$

By integration, considering the reducing capacity (γ_d) constant, the evolution of DO concentration with the fluid travel time τ is expressed by:

$$C_{DO} = C_{DO}(0)\left(1 - \frac{\tau}{\tau_c}\right), \forall\ \tau < \tau_c, \tag{11}$$

where τ_c is the characteristic time required to consume DO and reach anoxic conditions,

$$\tau_c = \frac{4C_{DO}(0)}{\gamma_d} \tag{12}$$

The concentration of dissolved iron $C_{Fe^{2+}}$ respects the kinetic law of Equation 5:

$$\frac{dC_{DO}}{d\tau} = -\frac{1}{4}k^*_{ox} C_{Fe^{2+}} C_{DO}. \tag{13}$$

Hence,

$$C_{Fe^{2+}} = -\frac{4}{k^*_{ox} C_{DO}}\frac{dC_{DO}}{d\tau}. \tag{14}$$

Inserting Equations 11 and 9 into the above expression leads to the evolution of iron concentration as a function of travel time in the oxic regime,

$$C_{Fe^{2+}} = \frac{4}{k^*_{ox}}\left(\frac{1}{\tau_c - \tau}\right), \forall\ \tau < \tau_c \tag{15}$$

This analytical model thus yields the following solutions for the coupled evolution of DO and Fe^{2+} for the oxic regime.

$$\begin{cases} C_{DO} = C_{DO}(0)\left(1 - \frac{\tau}{\tau_c}\right), \forall \tau < \tau_c \\ C_{Fe^{2+}} = \frac{4}{k^*_{ox}}\left(\frac{1}{\tau_c - \tau}\right), \forall\ \tau < \tau_c \end{cases} \tag{16}$$

We introduce the non-dimensional Damköhler number Da (Maher, 2010) as the ratio of the characteristic timescale for DO transport τ_t over the timescale for oxygen consumption τ_c (Equation 12):

$$Da = \frac{\tau_t}{\tau_c}. \tag{17}$$

with τ_t the characteristic time for DO transport up to a reference depth z_c while flowing at an apparent vertical velocity $\overline{v_a}$:

$$\tau_t = \frac{z_c}{\overline{v_a}}. \tag{18}$$

AGU ADVANCING EARTH AND SPACE SCIENCES

Water Resources Research 10.1029/2023WR034986

Da is thus proportional to the ratio of the reducing capacity (γ_d) to the apparent vertical velocity ($\overline{v_a}$):

$$Da = \frac{\gamma_d}{\overline{v_a}} \times \frac{z_c}{4C_{DO}(0)}. \tag{19}$$

The system of equations for DO and Fe^{2+} can be expressed in terms of the Damköhler regime, such as:

$$\begin{cases} C_{DO} = C_{DO}(0)\left(1 - Da\frac{\tau}{\tau_t}\right), \forall \tau < \tau_c \\ C_{Fe^{2+}} = \frac{4Da}{k^*_{ox}}\left(\frac{1}{\tau_t - Da\ \tau}\right), \forall \tau < \tau_c \end{cases} \tag{20}$$

For $Da > 1$, the timescale of DO transport τ_t is longer than the timescale of DO consumption τ_c. Thus, DO supply is transport-limited and the conditions transition from oxic to anoxic along flow paths. Conversely, for $Da < 1$ the timescale of DO consumption is longer than transport. In this case, DO is not depleted because transport overcomes DO consumption and the system remains oxic.

2.3.2. Anoxic Regime

Once the available DO has been depleted (i.e., $\tau \geq \tau_c$), the concentration of Fe^{2+} is no longer limited by oxidation (R_{ox} becomes negligible) and then Equation 6 reduces to:

$$\begin{cases} C_{DO} = 0 \\ \frac{dC_{Fe^{2+}}}{d\tau} = \nu_d R_d - \nu_p R_p \end{cases} \tag{21}$$

Since the dissolution rate of primary silicates is slow (Helgeson et al., 1969) and thermodynamics at low P-T impose a high K_{ps}, we assume that under reducing conditions, the dissolving Fe(II)-bearing mineral is still highly under-saturated $\left(\frac{Q_d}{K_{sp,d}} \ll 1\right)$ and releases elements in solution that increase the saturation of Fe(II)-bearing clay (Fe-clay) which then precipitates $\left(\frac{Q_p}{K_{sp,p}} \gg 1\right)$. Thus, Fe^{2+} is released from the dissolution of primary mineral and part of it precipitates in secondary minerals. According to the definition of R_j (Equation 4) and considering the above approximations for $\frac{Q_j}{K_{sp,j}}$, Equation 21 simplifies to:

$$\frac{dC_{Fe^{2+}}}{d\tau} = \gamma_d - \gamma_p \frac{Q_p}{K_{sp,p}}, \tag{22}$$

with both γ_d and γ_p, the reducing and precipitation capacities of respectively, the dissolving Fe(II)-bearing primary mineral and the precipitating Fe-clay, defined by Equation 10.

For a general composition of the mineral Fe-clay, the corresponding solubility reaction may be written as:

$$Fe_{\nu_p} Mg_a Al_b Si_c O_{10}(OH)_{m_1} + nH^+ \overset{K_{sp,p}}{\rightarrow} \nu_p Fe^{2+} + aMg^{2+} + bAl^{3+} + cSiO_2^c + m_2 H_2O \tag{23}$$

Assuming that activity coefficients are close to 1, the ionic activity product (Q) for the above reaction can be defined as follows:

$$Q_p = \frac{C^a_{Mg} C^b_{Al} C^c_{SiO_2}}{10^{-n\ pH}} C^{\nu_p}_{Fe^{2+}} = \Gamma_p C^{\nu_p}_{Fe^{2+}}, \tag{24}$$

where C_i is the concentration of species i and Γ_p the concentration product $\forall i \neq Fe^{2+}$ among the elements present in the Fe-clay mineral. The solubility product ($K_{sp,p}$) may be reformulated in an analogous way:

$$K_{sp,p} = \frac{(a\ s_p)^a (b\ s_p)^b (c\ s_p)^c}{10^{-n\ pH}} (\nu_p\ s_p)^{\nu_p} = \Gamma^s_p s_p^{\nu_p}, \tag{25}$$

where s_p is the solubility of Fe-clay and Γ^s_p is the solubility product $\forall i \neq Fe^{2+}$. Replacing the expressions for Q_p and $K_{sp,p}$ in Equation 22 and rearranging gives:

$$-\frac{\Lambda}{\gamma_d}\frac{dC_{Fe^{2+}}}{dt} = \left(\frac{C_{Fe^{2+}}}{s_p}\right)^{\nu_p} - \Lambda, \tag{26}$$

Water Resources Research 10.1029/2023WR034986

with the non-dimensional lithological parameter

$$\Lambda = \frac{\gamma_d \Gamma_p^s}{\gamma_p \Gamma_p} \tag{27}$$

which quantifies the relative reducing capacity between primary to secondary Fe(II)-bearing minerals (γ_d/γ_p) and the deviation from chemical equilibrium $\left(\Gamma_p^s/\Gamma_p\right)$. Owing to the definition of the reducing capacity (Equation 10), the lithological parameter introduced herein synthesizes the competition between rates of precipitation and dissolution of Fe(II)-bearing minerals.

The solution of the differential Equation 26 depends on the stoichiometric coefficient for iron per mineral formula of Fe(II)-bearing clay (ν_p). Here, we assume $\nu_p = 2$, which characterizes a typical Fe(II)-rich clay composition according to Sugimori et al. (2008). Solving Equation 26 leads to the following solutions under anoxic conditions:

$$\begin{cases} C_{DO} = 0 \\ C_{Fe^{2+}} = s_p\sqrt{\Lambda}\tanh\left(\frac{\gamma_d}{s_p\sqrt{\Lambda}}\,\tau\right), \forall \tau \geq \tau_e. \end{cases} \tag{28}$$

For travel times larger than $\tau > 2\frac{s_p\sqrt{\Lambda}}{\gamma_d}$, the transient term in Equation 28 rapidly tends to 1 and the concentration of dissolved iron approaches a steady-state expressed by:

$$\lim_{\tau\to\infty} C_{Fe^{2+}} = s_p\sqrt{\Lambda} \tag{29}$$

Under anoxic conditions, the concentration of dissolved iron in Equation 29 represents a far-from-equilibrium steady-state that is only affected by geological factors (the balance between dissolution and precipitation rates of Fe(II)-bearing minerals), here synthesized through the lithological parameter Λ and the solubility of Fe-clay s_p.

2.4. Fully Resolved Reactive Transport Simulations

2.4.1. Base Case Simulation

To test the validity of the approximate analytical expressions derived above, we perform reactive transport simulations using the code CrunchFlow (Steefel et al., 2015). As in the analytical model, here we use a Lagrangian approach to simulate a parcel of water traveling along a flow path, following the kinetics of a batch system. We assume an homogeneous bedrock composition and that mineral dissolution reactions are at steady state. We use an effective travel time formulation in which the simulation time in Crunchflow represents the contact time between groundwater and the minerals in the host rock. We simulate the evolution of DO and Fe^{2+}, as a result of reactions between oxic water with a composition typical of recharge groundwater (see Table S1 in Supporting Information S1) and a more realistic set of minerals with respect to the simplified analytical case. We consider a silicate rock lithology containing quartz, feldspars, biotite and muscovite, with an initial porosity (ω) of 1% (see Table S2 in Supporting Information S1 for details on the mineralogical composition). In unweathered silicate rocks, biotite is an ubiquitous Fe(II)-bearing mineral present in high proportions (Bazilevskaya et al., 2013; Hampl et al., 2021; Holbrook et al., 2019; Kim et al., 2017) and it has been pointed out as a key mineral for DO consumption (Spiessl et al., 2008). Unlike other reactive-transport models in which each primary mineral is modeled with an independent specific surface area (S_M), for example, Heidari et al. (2017), in this work we used the same S_M for all primary minerals. We assume that this S_M is representative of the texture and the exposed rock-surface in fractures that is then affected by the mineral volume fraction (Φ) to obtain the bulk surface area (S_V) in Equation 1.

Precipitation and dissolution of secondary minerals are allowed to simulate incongruent dissolution of silicate phases. The incongruent dissolution of feldspars is simulated with the formation of kaolinite according to mineral stability diagrams (see Figure S1 in Supporting Information S1). Biotite weathering is commonly described as an incongruent dissolution process in which the hydration and progressive replacement of inter-layer cations (i.e., K^+) forms a wide range of Fe-bearing clays (Fe-clay) and Fe(III) oxyhydroxides depending on the leaching and redox conditions (Acker & Bricker, 1992; Dideriksen et al., 2010; Hampl et al., 2021; Murakami et al., 2003; Scott & Amonette, 1985; Sequeira Braga et al., 2002; Tullborg et al., 2008). In the present simulations, we consider

Water Resources Research 10.1029/2023WR034986

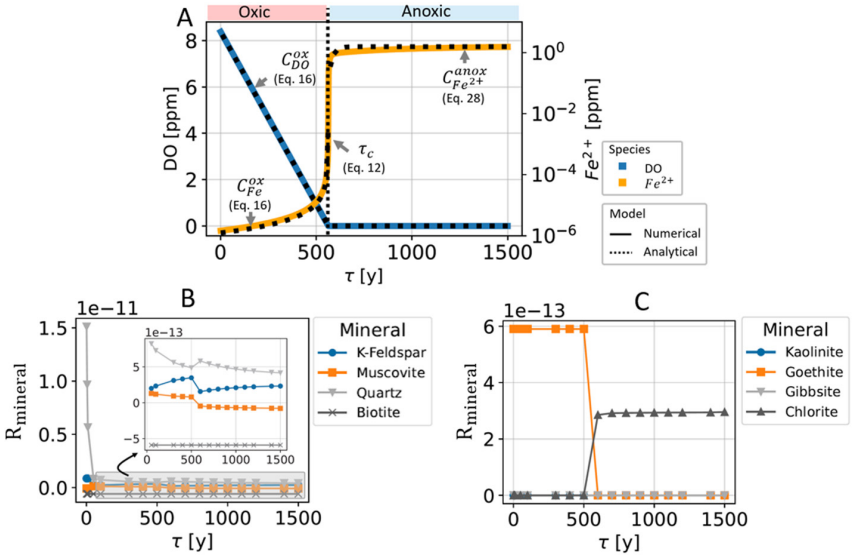

Figure 2. Simulation results for the Base Case scenario, obtained with Crunchflow for a lithological composition with $\gamma_d = 2 \times 10^{-3} mol\ .m_{pm}^{-3}.y^{-1}$, $\Lambda = 4 \times 10^4$. (a) Evolution of Dissolved Oxygen (DO) and iron concentration as a function of travel time (τ). C_{DO}^{ox} and C_{Fe}^{ox} correspond to concentrations under oxic conditions, whereas C_{DO}^{anox} and C_{Fe}^{anox} represent concentrations at anoxic conditions. τ_c is the characteristic time for DO depletion. (b and c) correspond to actual reaction rates for minerals ($R_{mineral}\left[mol\ .m_{pm}^3.s^{-1}\right]$) as a function of fluid travel time for primary and secondary minerals, respectively.

the precipitation of goethite since it is a typical Fe-oxyhydroxyde found in oxic weathering fronts (Dideriksen et al., 2010). For anoxic conditions, Sugimori et al. (2008) have documented that Fe-rich corrensite forms as the dominant secondary phase. However, since thermodynamic and kinetic parameters for corrensite are poorly known, we allow the formation of chlorite in our simulation because this mineral has a similar stability field and paragenetic relationships with corrensite (Beaufort et al., 1997).

Figure 2 presents the evolution of DO and Fe^{2+} aqueous concentrations as well as actual reaction rates ($R_{mineral}$) for minerals with mean fluid travel time (τ), as simulated with the numerical model over a period of 1,500 years. We use this extended simulation time to illustrate the stability of the numerical model in the anoxic regime. Although, we prevent the reader that the purpose of analytical model is to focus on travel times that are relevant for modern groundwater residence times in aquifers, typically <1,000 years (Sprenger et al., 2019), where diffusion can be neglected (Sidborn & Neretnieks, 2008; Trinchero et al., 2018).

DO decreases linearly until it gets depleted and a non-linear transition from oxic to anoxic conditions is observed. The evolution of the reaction rates of mineral species with the mean fluid travel time (Figures 2b and 2c) indicates that iron is being released from biotite during both oxic and anoxic conditions ($R_{biotite} < 0$ indicates dissolution). Under oxic conditions, the Fe^{2+} concentration is driven by the presence of DO and its oxidation into Goethite ($R_{goethite} > 0$ indicates precipitation). On the other hand, when $\tau \geq \tau_c$, the Fe^{2+} concentration is driven by the precipitation of Fe(II)-bearing clay as indicated by the change on $R_{chlorite}$ from dissolution (oxic regime) to precipitation (anoxic regime) conditions.

2.4.2. Validation of Analytical Expressions

We compare fully resolved numerical simulations with the reduced analytical solutions derived for the evolution of both DO and Fe^{2+} concentrations under oxic (Equation 16) and anoxic (Equation 28) conditions (Figure 2a). Thermodynamic parameters from Table 2 and mineral compositions are used to calculate the parameters of the analytical solutions. The analytical expressions for both DO and Fe^{2+} accurately capture the fully resolved numerical simulations and the predicted characteristic time τ_c (Equation 12) coincides with the non-linear oxic-anoxic transition from the full numerical model, which validates the assumptions made to derive the reduced analytical model.

To further evaluate the validity of the analytical approximations, a sensitivity analysis is carried out by varying the main parameters identified from the reduced analytical model. With the full numerical model and the reduced

Water Resources Research 10.1029/2023WR034986

Table 2
Geochemical Parameters Used in the Numerical Modeling and to Calculate Non-Dimensional Numbers in the Analytical Solutions

Parameter		Value		Source
		biotite[a]	Fe-clay[b]	
Molar volume [$cm^3\ mol^{-1}$]	V_m	149.65	215.88	(1)
Molecular mass [$g\ mol^{-1}$]	MM	417.3	713.5	
Solubility product [-]	K_{sp}	$10^{41.1}$	$10^{47.6}$	(2)
Solubility @ $pH = 7\ [mol.kg_w^{-1}]$	s	$10^{-3.49}$	$10^{-6.85}$	
Activation energy [$kcal\ mol^{-1}$]	E_a	5.26	21.03	(3)
kinetic dissolution constant [$mol\ m^{-2}\ s^{-1}$]	k_d	$10^{-12.55}$	$10^{-12.52}$	(3)
Aqueous parameters				
Kinetic oxidation constant [$L^2\ mol^{-2}\ atm^{-1}\ s^{-1}$]	k_{ox}	$10^{12.12}$		(4)
Modified k_{ox} from Equation 5 [$L\ mol^{-1}\ s^{-1}$]	k^*_{ox}	10.2		
Initial DO concentration $[mol.kg_w^{-1}]$	$C_{DO}(0)$	2.62×10^{-4}		
Henry's constant for O_2 [$mol\ atm^{-1}\ L^{-1}$]	K_H	$10^{-2.89}$		
Water auto-dissociation constant [$mol^2.L^{-2}$]	K_w	10^{-14}		
pH		7.0		

Note. References in column *Source* correspond to (1) (Robie & Philip, 1962), (2) (Malmstrom et al., 1995), (3) (Palandri & Kharaka, 2004), (4) (Singer & Stumm, 1970).
[a]Values for phlogopite. [b]Based on properties for chlorite.

analytical solutions in Equation 16, we evaluate (a) the influence of the reducing capacity (Equation 10) and of the mean fluid travel time on DO and Fe^{2+} concentrations (Figures 3a and 3b) in the oxic regime; (b) the influence of the reducing capacity of biotite on the characteristic time for oxygen consumption τ_c (Figure 3c); (c) the influence of the clay precipitation capacity on the steady-state concentration of Fe^{2+} (Figure 3d). The sensitivity on the reducing capacity of biotite is tested by varying the specific surface area ($S_{M,d}$) and the volume fraction of biotite (Φ_d), both included in the bulk surface area definition (see Equation 1). The specific surface area S_M varies over four orders of magnitude, and the volume fraction of biotite in the rock Φ_d by a factor 20. The sensitivity on the clay precipitation capacity is tested by varying the specific surface area S_M over 3 orders of magnitude and the initial fraction of clay in the rock Φ_p over 4 orders of magnitude.

The reduced analytical model is in good agreement with the simulations for the full range of tested parameters and simulation times. As expected, less oxic conditions occur in systems with higher biotite contents (Figures 3a and 3b). Insets in Figures 3a and 3b show that longer mean fluid travel times can counterbalance low reducing capacity (low biotite content, Φ_d and/or low Specif Surface Area, S_M), leading to more persistent oxic conditions. This interplay between the reducing capacity and travel time is captured by the characteristic time for oxygen consumption τ_c (Equation 12) in agreement with simulations (Figure 3c). The characteristic time for oxygen consumption decreases with the reducing capacity (both with Φ_d and S_M), leading to a longer persistence of oxic conditions in low reducing capacity rocks. The steady-state Fe^{2+} concentration in Figure 3d decreases as the initial clay precipitation capacity (γ_p) approaches the reducing capacity of biotite (γ_p) (either due to higher initial Fe(II)-clay content $\Phi_p(0)$ or a higher specific surface area $S_{M,p}$), showing that the precipitation of Fe(II)-clays works as a regulator of dissolved iron at anoxic conditions. This effect explains the various $C_{Fe^{2+}}$ levels that are reached under anoxic conditions in Figure 3a, as they relate to different γ_d/γ_p ratios.

2.5. Hydrological and Geological Drivers for DO and Fe^{2+} Concentrations

While the full numerical model allows for a complex and realistic reactive modeling framework, the reduced analytical model provide a framework to understand and quantify the hydrological and geological drivers for the evolution of DO and Fe^{2+} in silicate catchments (Figure 4).

The DO concentration predicted by Equation 20 is represented as a function of the fluid travel time (τ) and the reducing capacity (γ_{Bt}), the two main parameters expressing the hydrological and geological controls in the

Water Resources Research 10.1029/2023WR034986

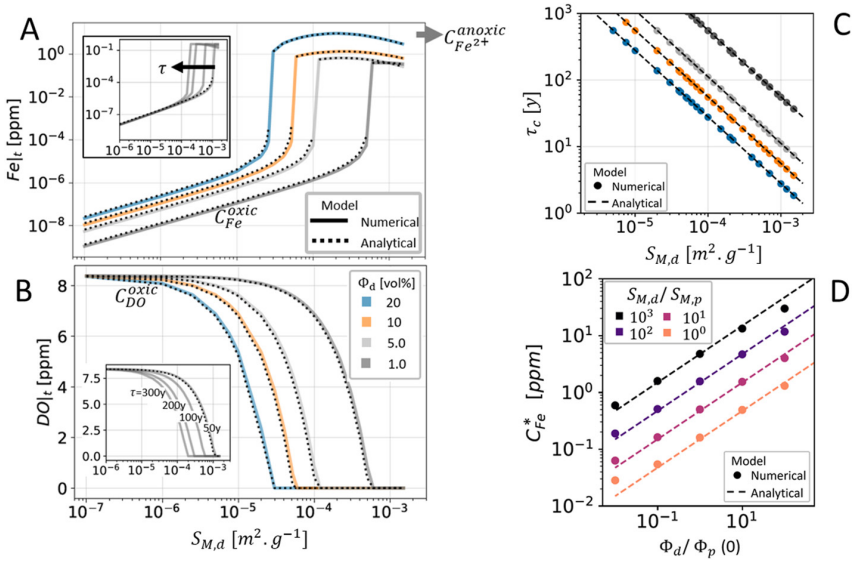

Figure 3. Sensitivity analysis for the numerical and analytical models using the lithological composition in Table S2 in Supporting Information S1. Variations in Φ_d or Φ_p are compensated by changing Φ_{quartz} to keep porosity in 1%. Subfigures (a and b) present sensitivities of, respectively, Dissolved Oxygen and Fe^{2+} concentrations to the Specific Surface Area ($S_{M,d}$). Main plots correspond to concentrations computed at a transit time $\tau = 100$ years under different scenarios of Fe(II)-bearing mineral content (Φ_d), while inserts show different travel time scenarios for the $\Phi_d = 1\%$ case. Analytical solutions are represented by Equations 16 and 28. Subfigure (c) presents the sensitivity of τ_c to $S_{M,d}$ under the same Φ_d scenarios (i.e., to the reducing capacity in Equation 12). Subfigure (d) presents the sensitivity of the steady-state Fe^{2+} concentration $\left(C^*_{Fe}\right)$ to the initial clay precipitation capacity (i.e., to both clay's initial volume fraction $\Phi_p(0)$ and specific surface area $S_{M,p}$). Subscript *d* stands for dissolving mineral (e.g., biotite) and subscript *p* stands for precipitating mineral (e.g., Fe-clay).

Damköhler number (Figure 4). The counteracting effects of fluid travel time and reducing capacity imply that there is a fundamental indeterminacy on the hydrological and geological drivers when considering oxygen alone. A given concentration of oxygen can be obtained by a range of different combinations of hydrological and

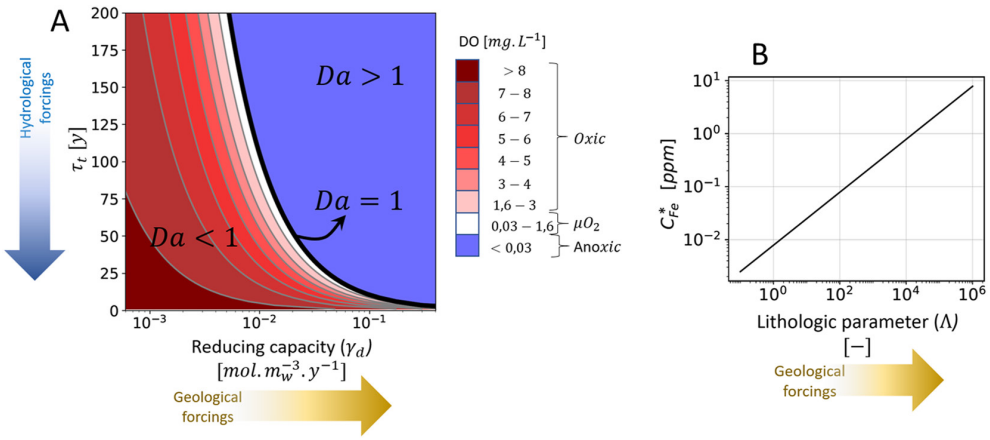

Figure 4. (a) Dependence of Dissolved Oxygen (DO) concentrations to geological (*x*-axis) and hydrological (*y*-axis) forcings. Multiple combinations of reducing capacity (γ_d) and characteristic transport time (τ_t) can result in a same prediction of DO concentration (e.g., iso-concentration lines for C_{DO}). Stronger geological forcings (higher reducing capacity of a certain lithology as in Equation 10) limit the persistence of DO to very short τ_t (favor anoxic conditions) and vice versa. Higher hydrological forcings in *y*-axis (faster groundwater velocities) favor deeper transport of DO for a same characteristic transport time, τ_t (Equation 30). (b) Dependence of the steady-state iron concentration $\left(C^*_{Fe}\right)$ to the lithological parameter (Λ) at anoxic conditions. The lithological parameter is defined in Equation 26.

Water Resources Research 10.1029/2023WR034986

Table 3
General Characteristics of the Study Site

	Guidel	Kermadoye
Generalities		
Latitude	47°45'16"N	47°44'50"N
Longitude	3°28'51"W	3°25'38"W
Altitude (m.a.s.l.)	15.1	26.7
Groundwater flow-regime	Natural circulation	Pumped since 1991
Geology		
Dominant bedrock lithology	Mica-schist, Paragneiss	Granite
Age	Ordovician inf	Carboniferous
Mean [min, max] depth to fresh bedrock (m)	17 [4, 34]	30 [10, 44]
Climate		
Climate type	Oceanic	
Mean annual rainfall (mm)	924[a]	
Mean annual temperature (°C)	12.1[a]	

[a]Data from Lann-Bihoué weather station, averaged from the period 2006–2014.

geological parameters. In rocks with low reducing capacities, DO concentrations are poorly sensitive to travel time since DO consumption is very slow ($Da < 1$). For high reducing capacity values, DO concentrations evolve rapidly with travel time due to fast reaction kinetics ($Da > 1$).

When oxygen is depleted, Fe^{2+} concentrations tend toward a far-from-equilibrium steady-state concentration (Equation 29), which is controlled by the relative abundance of primary and secondary Fe(II)-bearing minerals expressed through the non-dimensional number Λ (Equation 27). As a consequence, Fe^{2+} concentrations under anoxic conditions are mainly driven by the geological context of the subsurface. Therefore, the joint analysis of both DO and Fe^{2+} concentrations gives independent constraints on the potential roles of hydrological and geological processes on the distribution of oxygen in the subsurface, which we discuss using field data in the following section.

3. Field Study at the Ploemeur CZO (France)

To evaluate the modeling framework presented above, we test it against extensive field observations of DO and Fe^{2+} concentrations in the subsurface available at the Critical Zone Observatory (CZO) of Ploemeur (France). The Ploemeur CZO includes two subcatchments located at a distance of about 4 km: the Kermadoye site and the Guidel site. Both catchments are characterized by a fractured bedrock with similar lithologies and an oceanic climate but differ significantly in their DO and Fe^{2+} concentrations. It is thus well suited to test the concepts presented above.

3.1. Site Presentation

The Ploemeur CZO belongs to the H+ hydrogeological network (http://hplus.ore.fr/en/), the French network of critical zone observatories OZCAR (https://www.ozcar-ri.org/fr/) and the e-LTER european infrastructure (https://deims.org/731f3ced-148d-4eb5-aa46-870fa22be713). It is located in the southern part of the Armorican massif in Brittany, France. The region is characterized by the intersection of two main tectonic features: (a) a gently dipping (around 30° to the north) contact zone between a Late Hercynian granite and the surrounding micaschist rock; and (b) a dextral-slip normal fault zone which strike north 20° and dip East 70° (Ruelleu et al., 2010). Both are the main transmissive structures of the fractured-bedrock aquifer, characterized by a relatively large average transmissivity on the order of 10^{-3} m^2/s sustained by a well connected fracture network (Jiménez-Martínez et al., 2013; Le Borgne et al., 2007).

The Ploemeur CZO hosts two main catchments, Guidel and Kermadoye (see Table 3). The Kermadoye aquifer has been exploited for drinkable water supply since 1991 at an average pumping rate of 1 Mm^3 yr^{-1}. This particularly high production rate is attributed to the presence of the regional contact zone which flows toward the vertical faults (Jiménez-Martínez et al., 2013; Leray et al., 2013; Roques et al., 2016). The Kermadoye catchment is monitored with 22 boreholes, with depths ranging from 50 to 150 m. The majority of them cross the contact zone between

Water Resources Research 10.1029/2023WR034986

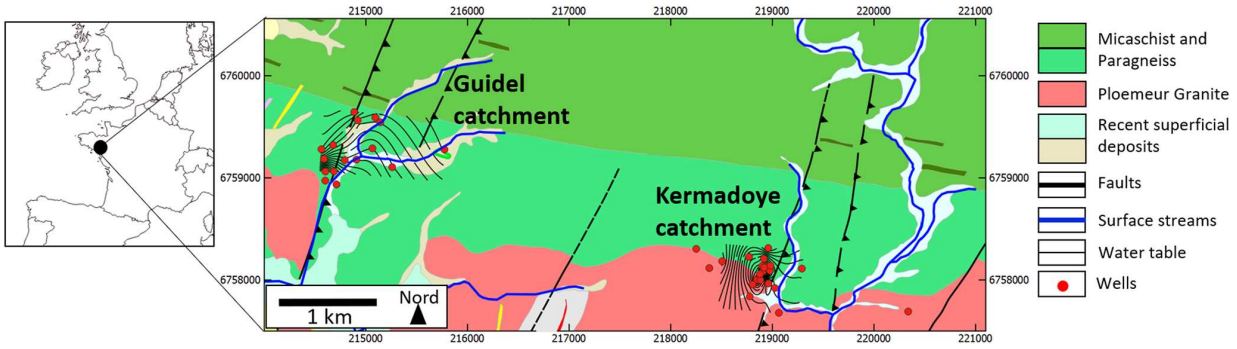

Figure 5. Geographical location, geological and hydrogeolocical maps of the Ploemeur Critical Zone Observatory and its two catchments, Guidel and Kermadoye. The geological map is reproduced from Béchennec et al. (2012).

micaschist and granite or are entirely in the granite. The Guidel catchment is not pumped, although it has similar hydraulic properties as the Kermadoye catchment. Natural groundwater flows converge to supply a stream and a wetland. The Guidel catchment is located to the north of the contact zone (see Figure 5). It has been monitored since 2009 with 25 boreholes of depths ranging from 50 to 150 m. These boreholes intersect mostly micaschists. Recent studies have shown that the mixing of oxygen rich and iron rich fluids at fracture intersections or in the wetland, sustains microbial hotspots, dominated by iron-oxidizing bacteria (FeOB) (Bethencourt et al., 2020; Bochet et al., 2020). Understanding and modeling DO and Fe^{2+} concentrations at this site is thus of particular interest.

The comparison of the two sites is particularly interesting as the hydrological forcing is stronger at the Kermadoye site due to pumping. Furthermore, while the two sites have comparable geology, the contact zone is deeper at Guidel site, which may be more influenced by the micaschist lithology. Since the two sites have contrasted DO and Fe^{2+} signatures, they are particularly relevant test grounds to resolve the hydrological and geological controls on these chemical properties.

3.2. DO and Fe^{2+} Depth Profiles

The DO and iron concentrations measured in the two catchments are represented as a function of depth in Figure 6. Each point represents the concentration measured in front of the main transmissive fracture in each borehole (see Texts S1 and S2 in Supporting Information S1 for Fe^{2+} and DO measurement methods, respectively). Following the methodology proposed by Chatelier et al. (2011), we converted the fracture depth to an effective depth (*depth proxy*) representative of larger scale flow path. To do so, we used temperature anomalies measured in boreholes and the depth of origin of water (shallow vs. deep) was derived by comparison with the geothermal gradient (details on the depth conversion methodology are presented in Text S3 in Supporting Information S1). DO concentrations decrease with depth, from values close to saturation down to values close to the detection limit (0.1 mg L^{-1}). Both catchments reach the oxic-anoxic transition, but at significantly different depths. The oxic-anoxic transition takes place between 100 and 150 m depth at the Guidel site. At the Kermadoye site it takes place between 200 and 400 m depth. The decrease in DO is associated with an opposite gradient of Fe^{2+} (see Figure 6b). Fe^{2+} concentrations in Guidel increase up to an average value of 2.8 ± 1.7 ppm, while in Kermadoye, Fe^{2+} concentrations increase up to $6.3 \times 10^{-2} \pm 2.7 \times 10^{-2}$ ppm, that is, about two orders of magnitude lower than in Guidel.

Both catchments show apparent differences between recharge and discharge zones: high DO and low Fe^{2+} concentrations relate to recharge groundwater while discharge zones are characterized by anoxic groundwater and high Fe^{2+} concentrations.

3.3. Model Application to Field Data

To compare field data to our model, we transform travel time to depth based on an apparent vertical velocity $(\overline{v_a})$ that can be constrained from age tracer data (Ayraud et al., 2008):

$$\tau = \frac{z}{\overline{v_a}} \tag{30}$$

Water Resources Research 10.1029/2023WR034986

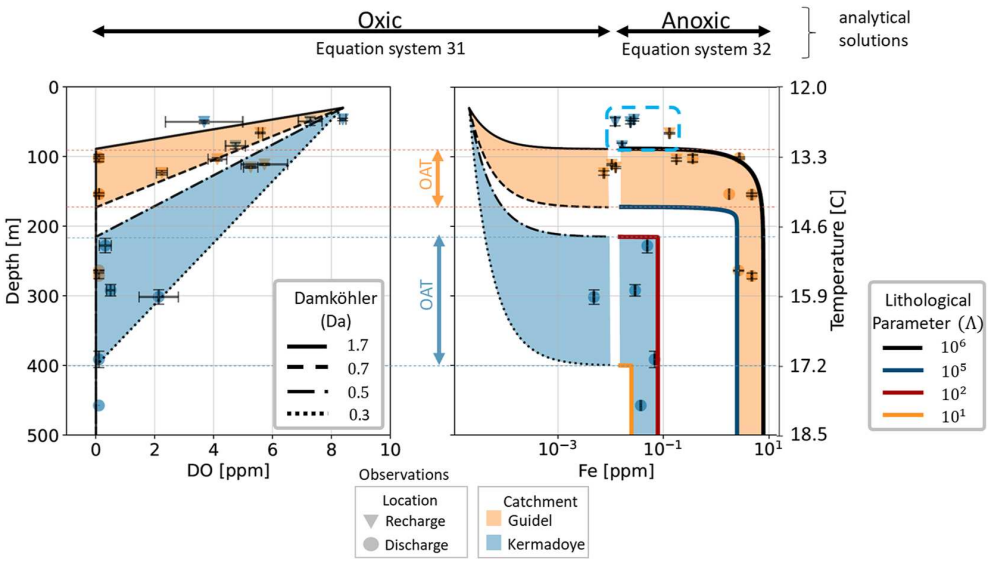

Figure 6. Distribution of Dissolved Oxygen (DO) and total iron (Fe_T) concentrations as a function of depth for the two catchments. Measured field data is represented with dots and triangles for sampling points from discharge or recharge zones in the catchments. In the oxic part, analytical solutions are drawn as curves with different values of Da for DO and Fe^{2+} (Equation 31). The blue box in the right-hand side plot highlights iron data from oxic boreholes that is not explained by the model (see Section 3.4 for details). In the anoxic part, analytical solutions for Fe^{2+} are drawn with different values of Λ (Equation 32). Sample depth has been inferred using temperature as a proxy (see Section 3.2 for details). OAT corresponds to the Oxic-Anoxic Transition ranges.

Thus, the system of equations describing DO and Fe^{2+} concentration profiles can be expressed as a function of depth:

$$oxic: \begin{cases} C_{DO}(z) = C_{DO}(0)\left(1 - Da\frac{z}{z_c}\right), \forall z < \frac{z_c}{Da} \\ C_{Fe^{2+}}(z) = \frac{4v_a}{k^*_{ox}}\left(\frac{1}{z_c - Da\, z}\right), \forall\, z < \frac{z_c}{Da} \end{cases} \tag{31}$$

$$anoxic: \begin{cases} C_{DO}(z) = 0 \\ C_{Fe}(z) = s_p\sqrt{\Lambda}\tanh\left(\frac{4C_{DO}(0)Da}{s_p\sqrt{\Lambda}}\frac{z}{z_c}\right), \forall\, z \geq \frac{z_c}{Da} \end{cases} \tag{32}$$

with z_c the reference depth in Equation 18. Here, we define $z_c = 100$ m, which corresponds to the average depth of our measurements (Figure 6). The dissolved iron concentration C_{Fe} only depends on both Da and Λ for $z < \frac{z_c s_p\sqrt{\Lambda}}{4C_{DO(o)}Da}$. At deeper depths, C_{Fe} only depends on the lithological parameter and Equation 32 approaches a steady-state concentration (Equation 29).

3.4. Comparison of Field Data and Model Simulations of DO and Fe^{2+}

The reduced analytical model for DO and Fe^{2+} for the oxic and anoxic regimes (Equations 20 and 29) are fitted to the measured DO and total soluble iron (Fe_T) depth-profiles at the two sites. Based on previous works in the study site (Bochet et al., 2020), discrepancies between Fe_T and Fe^{2+} are negligible for the purpose of our study (Fe^{2+}/Fe_T ratio ranges from 93% to 98% in groundwater).

To fit the model to the data, we manually adjusted both dimensionless numbers Da and Λ while the rest of the parameters were fixed to values given in Table 2. The apparent vertical velocity $(\overline{v_a})$, that influences the Fe^{2+} concentration under oxic conditions (Equation 31), was fixed at 3 m·y^{-1} as assessed by Ayraud et al. (2008) for the study site. Under oxic conditions, the solution for DO has one parameter, the Damköhler number Da, and the solution for Fe^{2+} depends on both Da and on the apparent vertical velocity $(\overline{v_a})$ (Equation 20). Theoretically, the

Water Resources Research 10.1029/2023WR034986

combined resolution of the two equations for DO and Fe^{2+} should allow to fit Da and $\overline{\upsilon_a}$, and thus to estimate the reducing capacity of the bedrock (γ).

The reduced analytical model captures the approximate linear decrease in DO with depth in both catchments (Figure 6). The reduced model is also compatible with the evolution of Fe_T on both sites. For the Guidel site this evolution is well defined over about three orders of magnitude in concentration. For the Kermadoye site, the model describes well the data at anoxic conditions, however, some discrepancies appear between the model and the field data from shallow oxic samples (see blue box in Figure 6). Indeed, the model predicts iron concentrations that significantly lower than those measured from field samples. We hypothesize that these discrepancies are due to a large Fe(III)/Fe_T ratio in the field measurements. This can be either due to pH effects (shallow waters are normally slightly acid which favorise the solubility of Fe(III) or to the formation of Fe(III)-colloids, particularly if organic matter is available (Nordstrom, 2011; Serikov et al., 2009; Wolthoorn et al., 2004).

The range of Damköhler numbers can be relatively well constrained as consistent values of Da explain jointly the linear decrease of DO and the non-linear increase of Fe^{2+}. The Da values range between 0.7 and 1.7 at the Guidel site and between 0.3 and 0.5 at the Kermadoye site (Figure 6). On the other hand, the value of $\overline{\upsilon_a}$ influences the very low concentrations of Fe^{2+} at shallow depths (see Figure S4 in Supporting Information S1). However, the discrepancy between measured and modeled Fe^{2+} data at oxic conditions (blue box in Figure 6) prevent us from directly constraining $\overline{\upsilon_a}$ from these data. Under anoxic conditions, Fe^{2+} concentrations show a transient phase that depends on both Da and Λ (Equation 32) and that rapidly converges to the steady-state Fe^{2+} concentration from Equation 29. The later depends only on the lithological properties (i.e., Λ). The parameter Λ is relatively well constrained since the maximum Fe^{2+} is very different between the two sites: Λ ranges between 10^1 and 10^2 for the Kermadoye site, and between 10^5 and 10^6 for the Guidel site (Figure 6). The large difference in the two values of Λ suggests that the contrast of the main lithological properties of the two sites is likely more important than possible differences in hydrological properties.

Therefore, the analysis of DO and Fe^{2+} concentration data under oxic conditions provides a good constrain on the Damköhler number, suggesting that the Guidel catchment is more reaction-limited than the Kermadoye catchment. However, this still leaves an uncertainty on whether this difference may be explained by a hydrological or geological contrast. An additional constrain is given when analyzing Fe^{2+} concentrations in the anoxic regime, suggesting an important lithological difference between the two catchments.

4. Discussion

4.1. Discriminating Hydrological and Geological Controls From Field Data

Despite geographical, climatic and lithological similarities between the two sites, the DO and Fe^{2+} depth-profiles are significantly different. According to our model, this difference may be explained by a factor 3 in the Damköhler numbers Da, the ratio of the transport to reaction time scales, and a factor of 10^4 in the Λ number, which represents geochemical properties such as the reducing capacity of Fe(II)-bearing minerals and the deviation from chemical equilibrium for clay precipitation. The difference in Damköhler numbers can be either due to a contrast in transport velocity or dissolution rates; or by both effects acting at the same time. We discuss two end-member hypotheses in the following.

We first consider the hypothesis that would attribute DO and Fe^{2+} differences to a contrast mostly caused by hydrological properties. This may be plausible since the Kermadoye site is pumped while the Guidel site is not. Under this hypothesis, the smaller Da for the Kermadoye site would indicate a factor three increase in average groundwater velocity compared to the Guidel site. In such case, travel times should be shorter in the pumped catchment and the apparent age distribution would be expected to have a stronger contribution of young groundwater. However, a geochemical analysis at the Kermadoye site has shown that pumping tends to increase travel times due to the increase of the contribution of deep groundwater flow paths (Roques et al., 2018). This was confirmed by a hydrogeological model of the site (Leray et al., 2014). Therefore, it is unlikely that flow acceleration due to pumping would explain the factor three contrast in Damköhler number.

We now consider the second hypothesis stating that the difference in Da would be mostly caused by a 3-fold contrast in the reducing capacity of the host rock (γ_d). The Guidel site is composed mostly of micaschists, while the Kermadoye site is composed of both micaschists and granites (Figure 5). Mineralogical analyses carried on

Water Resources Research 10.1029/2023WR034986

the two rocks indicate that micaschists contain about 7 times more biotite than granite. Therefore, assuming that about 50% of groundwater flowpaths were interacting with granites and 50% with micaschists, the average reducing capacity of the Kermadoye aquifer would be around 3 times lower than the reducing capacity of the Guidel site. This hypothesis would therefore explain a difference of 3 in the Da of the two catchments. The difference in the lithology of both catchments is also supported by the large difference in the parameter Λ, that is entirely related to geochemical parameters (Equation 27). Higher inherited clay contents in granite may account for the 4 orders of magnitude difference in Λ between the two sites. According to Goldich (1938), granites have higher proportions of plagioclase, which easily weathers into clay. This is further reinforced by the occurrence of kaolins near the granite's edge in the location (Béchennec et al., 2012). However, the large difference in Λ could also be related to mineral surface areas which are hard to constrain and vary by orders of magnitude in rocks (Ackerer et al., 2020; Wild et al., 2019).

In summary, the key element that motivates our interpretation is that the difference in Damköhler numbers is of a factor 3, while the difference in Λ are in the order of 10^4. An assumption of similar γ_p for the two catchments, would imply a 10^4 contrast in γ_d in order to explain the Λ differences. However, since the Damköhler number also depends on γ_d, we should also observe a difference of the same order for Da, unless it is compensated by a 10^4 contrast in the velocities, which seems unlikely. Following this reasoning, our hypothesis that the order of magnitude difference in Λ is mostly related to the clay content, that is, to γ_p rather than to γ_d.

The analysis of DO and Fe^{2+} data with the presented modeling framework provides key constraints on the hydrological and geological drivers of reactive transport processes. Although the two considered sites are a priori very similar in terms of hydrological and geological contexts, our findings suggest that differences in the proportion of granite and micaschist lead to a strong contrast in DO penetration with depth and Fe^{2+} concentrations. Moreover, we provide new constraints on the hydrogeological functioning of the sites. While previous studies suggested that groundwater was recharged and transported through the micaschist and deeper collected at the contact zone between granite and micaschist (Leray et al., 2013) at the Kermadoye site, this analysis suggests here that there is also a significant proportion of groundwater flowing through the granite.

4.2. Controls of DO and Iron Concentrations in Silicate Catchments

The depth of the oxic-anoxic transition in silicate catchments is controlled by the relative importance of the reducing capacity of the rocks and the effective transport of oxygen from the surface, quantified here by the Damköhler number (Figure 6a). Consistently with our model, linear trends in DO with depth have been seen in various hard-rock systems, including the Clara mine in Germany (Bucher et al., 2009) or the Western Canadian Sedimentary Basin (Ruff et al., 2023).

The reducing capacity can be considered as a value inherited from the geology, that varies slowly in time. For instance, Macquarrie et al. (2010) showed a decrease of 0.2% of biotite content in 2 ky under oxic conditions. On the other hand, groundwater table fluctuations or perturbations of the flow regime (e.g., pumping) can be very rapid (timescales ranging from days to the season (Guillaumot et al., 2022; Jiménez-Martínez et al., 2013; Molenat et al., 1999)). Thus, temporal changes in the oxic-anoxic depth in a particular system are likely mostly due to hydrological fluctuations.

The steady-state Fe^{2+} concentration at anoxic conditions is determined by the Lithological Parameter (Λ) that controls the balance between dissolution and precipitation of primary and secondary minerals, respectively. Here, the rationale to introduce the Λ parameter considers a silicate as secondary mineral but the conceptual framework still holds with other types of secondary minerals such as carbonates (see Text S6 in Supporting Information S1 for further details). As described by Equation 32, the steady-state Fe^{2+} concentration depends on the simplified assumption that after DO depletion, no other oxidants can oxidize Fe^{2+}. While this model works for our case study, it is possible that in hydrogeological systems the presence of alternative oxidizing agents such as Nitrates or Mn(IV) can promote iron oxidation under anoxic conditions (Kappler et al., 2021). In such case, the predicted rise of Fe^{2+} concentrations up to the steady-state iron concentration would be shifted deeper until the depletion of the alternative oxidizing species.

4.3. Model Limitations and Uncertainty in Parameter Estimations

The numerical and analytical models developed in this study are intended to capture the first-order trends in the catchment-scale distributions of DO and Fe^{2+}. We therefore introduced several simplifications that could be lifted

Water Resources Research 10.1029/2023WR034986

in future studies. The dominance of advective transport over matrix diffusion is justified here by the considered relatively short time scales (10 to hundreds of years), consistent with catchment travel times. However, at longer time scales, matrix diffusion would act as an additional buffer for oxygen (Macquarrie et al., 2010). The assumption of negligible mixing among streamlines is based on the discrete nature of flow pathways in the considered crystalline rocks, where flow paths of different travel times only meet in few localized mixing zones (Bochet et al., 2020). Yet, the effect of mixing on DO and Fe dynamics is an interesting question that should be addressed in future studies.

We did not take into account here the spatial heterogeneity in the lithological (constant reducing capacities, γ) or hydraulic properties (spatially uniform vertical velocity, $\overline{v_a}$). Since our model omits the water-rock interactions in the soil compartment, we used as initial condition for the water chemistry the composition of a typical recharge water instead of rainwater. This choice allows us to focus on the first order impact of other important controlling hydrological and geological factors in the saturated zone without introducing significant bias in the model (see Text S5 in Supporting Information S1 for further details). Similarly, we did not take into account the contribution of microbiological communities in fluid-mineral reactions or the oxidation of structural iron in minerals, since those processes are still poorly constrained. Although, both processes are expected to increase the reducing capacity of the media and have large scale impacts (Buss et al., 2008; Liao et al., 2022; Napieralski et al., 2019). Thus, they should be addressed in future works.

Despite of the above simplifications, the reduced model proposed here provides a simple yet informative tool to identify the processes controlling the evolution of DO and Fe^{2+} with depth. To this end, our model relies on the representation of spatial heterogeneities through effective parameters. This is a common approach in large-scale hydrological and geological models that allows to overcome the still open question of scaling of physical and biogeochemical properties in earth sciences (Li et al., 2017).

As a consequence of this effective modeling approach, the model parameters cannot be fully determined beforehand, and need to be adjusted to field data. This uncertainty in parameter estimation is inherent to reactive transport modeling at the field scale (White & Peterson, 1990), where effective parameters such as the specific surface need to be fitted to the data (Bao et al., 2017; Heidari et al., 2017; Moore et al., 2012). Beyond the precise estimation of these parameters, the interest of the reduced analytical model is to demonstrate that the two sites have different Damköhler and Lambda numbers, which provides insights into the dominant reactive transport processes occurring at the catchment scale.

4.4. Persistence of Dissolved Oxygen in the Subsurface

Subsurface environments for which the timescales of DO transport are shorter than timescales of DO consumption (i.e., transport-limited regime, $Da > 1$) favor the deep transport of DO in silicate catchments, which has a major impact on biogeochemical processes in the critical zone. The occurrence of DO in bedrock is responsible for deep WIF (Buss et al., 2008; Kim et al., 2017; Liao et al., 2022), which has been observed in 100 m-deep rock cores (Antoniellini et al., 2017; Bazilevskaya et al., 2013; Dideriksen et al., 2010; Hampl et al., 2021; Holbrook et al., 2019; Krone et al., 2021). By quantifying the dynamics of DO and the parameters controlling the distribution of DO, we provide controls on the conditions favorable for the active oxidative weathering of the deep subsurface. For instance, Bazilevskaya et al. (2013) attributed the thicker regolith in felsic rocks (e.g., granites) compared to mafic rocks (e.g., micaschists) to higher degree of fracturing and higher advective transport of DO with groundwater. We argue that, besides differences in advective transport, the lower reducing capacity of felsic rocks could also explain deeper penetration of DO in the subsurface.

Furthermore, DO exerts a first control on subsurface microbial processes, such as aerobic respiration or denitrification (Dalsgaard et al., 2014; Kolbe et al., 2019) and therefore structures the habitability of subsurface ecosystems. The respiration of Fe-oxidizing bacteria (FeOB) is of particular interest because of the ubiquity of both iron and FeOB (Kappler et al., 2021; Melton et al., 2014) as well as the coupling of the iron cycle with biogeochemical cycles of carbon, sulfur and nitrogen (Casar et al., 2021). The activity of FeOB at near-neutral pH environments requires the simultaneous presence of Fe^{2+} and microaerobic DO concentrations (Druschel et al., 2008; Maisch et al., 2019) while Fe^{2+} and *DO* often do not coexist because of the rapid oxidation of Fe^{2+}. From observations at the Guidel site, Bochet et al. (2020) suggested that the formation of subsurface FeOB hot-spots is favored by the mixing of oxic recharge water with deep anoxic iron-rich water at fracture intersections. As discussed above,

Water Resources Research 10.1029/2023WR034986

the steady-state Fe^{2+} concentration (Equation 29) is much lower for granite than for micaschist (Figure 6-b). Therefore, even if oxic and anoxic groundwater mix in granite system, the low dissolved iron concentrations do not favor the formation of FeOB hot-spots because Fe^{2+} is limiting. The depth of formation of subsurface FeOB hot-spots therefore not only depends on the transport of DO but also on the availability of Fe^{2+}, which is a function of the geological context.

5. Conclusions

In this study, we developed a reduced model to describe the depth-distributions of dissolved O_2 and Fe^{2+} concentrations in silicate catchments, which play a central role in a large range of biogeochemical processes. We derived a reduced analytical model, validated with reactive transport simulations, that quantify the parameters controlling jointly DO and Fe^{2+} evolution in fracture zones. Under oxic conditions, DO concentrations decrease linearly with fluid travel time following a slope that is function of the reducing capacity of the bedrock. In this regime, dissolved Fe^{2+} remains low because its aqueous oxidation by DO is faster than its release by mineral dissolution. At the Oxic-Anoxic Transition, DO is depleted and Fe^{2+} concentrations show a rapid non-linear increase up to a far-from-equilibrium steady-state concentration. This concentration is controlled by the relative abundance of primary to secondary Fe(II)-bearing minerals. These reactive transport dynamics can be understood with two non-dimensional paramers: the Damköhler number Da and the lithological parameter Λ.

We use this framework to interpret DO and Fe^{2+} concentrations measured extensively over two neighboring silicate catchments with similar hydrogeological properties but contrasted chemical properties. The differences in the depth of the oxic-anoxic transition and in the Fe^{2+} steady-state concentration are successfully modeled and explained by differences in Da and Λ. The interpretation of DO alone leads to a fundamental indeterminacy in the respective role of geological and hydrological properties that may explain the difference in Damköhler numbers. However, the joint investigation of DO and Fe^{2+} provides additional constraints and points to the role of a geological contrast, here likely due to a difference in the relative proportion of granite and micaschist in the two sites.

The methodology presented here may be implemented on other sites and contexts, to understand and model the depth of the oxic-anoxic transition. The two non-dimensional numbers can be estimated from field data as a guide for DO transport in the subsurface. Here, we investigated the oxidation of Fe^{2+} by DO and assumed that no other oxidants could oxidize Fe^{2+} after DO depletion. However, the presence of alternative oxidizing agents such as Nitrates or Mn(IV) could promote further iron oxidation under anoxic conditions. In this case, the predicted rise of Fe^{2+} concentrations up to the steady-state concentration $\left(C^*_{Fe^{2+}}\right)$ would be shifted deeper until the depletion of all oxidizing species. The derivation of the analytical solutions can also be adapted to other reactions involving dissolved reactants and minerals, as long as a silicate mineral is the dominant control on DO consumption and flow occurs through fractures. While here we considered a simplified approach based on an effective travel time, it would be interesting to investigate the form of the analytical solutions and the corresponding dimensionless parameters when representing explicitly structural heterogeneities and fracture-matrix exchanges.

Data Availability Statement

Numerical simulation were run with the Crunchflow code (Steefel et al., 2015) and figures were made using Matplotlib version 3.5.1 (Hunter, 2007), available under the Matplotlib license at https://matplotlib.org/. Data from the Ploemeur fractured rock observatory, which is part of the French network of hydrogeological observatories H+ (http://hplus.ore.fr/en/), was used to create this manuscript. All field data as well as Crunchflow input files and databases to build upon this research are available in the H+ database by following the permanent DOI: https://doi.org/10.26169/hplus.ploemeur_field_data_dissolved_oxygen_and_iron_landscapes.

Acknowledgments
This research was funded, in whole, by ANR EQUIPEX CRITEX project (ANR-11-EQPX-0011) and the ERC project ReactiveFronts (648377). We thank the French Ministry of Higher Education, Research and Innovation and the ANR IRONSTONE (ANR-21-CE01-0008) for funding. A CC-BY public copyright license has been applied by the authors to the present document and will be applied to all subsequent versions up to the Author Accepted Manuscript arising from this submission, in accordance with the grant's open access conditions. We are very grateful to the french networks of hydrogeological sites H+ (https://hplus.ore.fr/en/) and of critical zone observatories OZCAR (https://www.ozcar-ri.org/) for providing access to the Ploemeur CZO. We also thank the technical services of Geosciences Rennes CONDATEAU and GeOHeLiS for their support with dissolved gases and groundwater chemistry analysis. The authors would also like to extend their appreciation to the anonymous reviewers for their insightful comments and suggestions, which significantly improved the quality of this manuscript.

References

Acker, J. G., & Bricker, O. P. (1992). The influence of pH on biotite dissolution and alteration kinetics at low temperature. *Geochimica et Cosmochimica Acta*, *56*(8), 3073–3092. https://doi.org/10.1016/0016-7037(92)90290-Y

Ackerer, J., Jeannot, B., Delay, F., Weill, S., Lucas, Y., Fritz, B., et al. (2020). Crossing hydrological and geochemical modeling to understand the spatiotemporal variability of water chemistry in a headwater catchment (Strengbach, France). *Hydrology and Earth System Sciences*, *24*(6), 3111–3133. https://doi.org/10.5194/hess-24-3111-2020

Antoniellini, M., Mollema, P., & Del Sole, L. (2017). Application of analytical diffusion models to outcrop observations: Implications for mass transport by fluid flow through fractures. *Water Resources Research*, *53*(7), 5545–5566. https://doi.org/10.1111/j.1752-1688.1969.tb04897.x

Aquilina, L., Roques, C., Boisson, A., Vergnaud-Ayraud, V., Labasque, T., Pauwels, H., et al. (2018). Autotrophic denitrification supported by biotite dissolution in crystalline aquifers (1): New insights from short-term batch experiments. *Science of the Total Environment*, *619–620*, 842–853. https://doi.org/10.1016/j.scitotenv.2017.11.079

Ayraud, V., Aquilina, L., Labasque, T., Pauwels, H., Molenat, J., Pierson-wickmann, A.-c., et al. (2008). Compartmentalization of physical and chemical properties in hard-rock aquifers deduced from chemical and groundwater age analyses. *Applied Geochemistry*, *23*(June), 2686–2707. https://doi.org/10.1016/j.apgeochem.2008.06.001

Bao, C., Li, L., Shi, Y., & Duffy, C. (2017). Understanding watershed hydrogeochemistry: 1. Development of RT-flux-PIHM. *Journal of the American Water Resources Association*, *53*(3), 2328–2345. https://doi.org/10.1111/j.1752-1688.1969.tb04897.x

Bar-on, Y. M., Phillips, R., & Milo, R. (2018). The biomass distribution on Earth. *Proceedings of the National Academy of Sciences of the United States of America*, *115*(25), 6506–6511. https://doi.org/10.1073/pnas.1711842115

Bazilevskaya, E., Lebedeva, M., Pavich, M., Rother, G., Parkinson, D. Y., Cole, D., & Brantley, S. L. (2013). Where fast weathering creates thin regolith and slow weathering creates thick regolith. *Earth Surface Processes and Landforms*, *38*(8), 847–858. https://doi.org/10.1002/esp.3369

Beaufort, D., Baronnet, A., Lanson, B., & Meunier, A. (1997). Corrensite; A single phase or a mixed-layer phyllosilicate in saponite-to-chlorite conversion series? A case study of Sancerre-Couy deep drill hole (France). *American Mineralogist*, *82*(1–2), 109–124. https://doi.org/10.2138/am-1997-1-213

Béchennec, F., Hallégouët, B., Thiéblemont, D., & Thinon, I. (2012). Notice explicative, Carte géol France (1/50 000), feuille Lorient (383). In BRGM (Ed.), *Orléans: BRGM*.

Behrens, R., Bouchez, J., Schuessler, J. A., Dultz, S., Hewawasam, T., & Von Blanckenburg, F. (2015). Mineralogical transformations set slow weathering rates in low-porosity metamorphic bedrock on mountain slopes in a tropical climate. *Chemical Geology*, *411*, 283–298. https://doi.org/10.1016/j.chemgeo.2015.07.008

Bethencourt, L., Bochet, O., Farasin, J., Aquilina, L., Borgne, T. L., Quaiser, A., et al. (2020). Genome reconstruction reveals distinct assemblages of Gallionellaceae in surface and subsurface redox transition zones. *FEMS Microbiology Ecology*, *96*(5). https://doi.org/10.1093/femsec/fiaa036

Bochet, O., Bethencourt, L., Dufresne, A., Farasin, J., Pédrot, M., Labasque, T., et al. (2020). Iron-oxidizer hotspots formed by intermittent oxic–anoxic fluid mixing in fractured rocks. *Nature Geoscience*, *13*(2), 149–155. https://doi.org/10.1038/s41561-019-0509-1

Bucher, K., Zhu, Y., & Stober, I. (2009). Groundwater in fractured crystalline rocks, the Clara mine, Black Forest (Germany). *International Journal of Earth Sciences*, *98*(7), 1727–1739. https://doi.org/10.1007/s00531-008-0328-x

Buss, H. L., Sak, P. B., Webb, S. M., & Brantley, S. L. (2008). Weathering of the Rio Blanco quartz diorite, Luquillo Mountains, Puerto Rico: Coupling oxidation, dissolution, and fracturing. *Geochimica et Cosmochimica Acta*, *72*(18), 4488–4507. https://doi.org/10.1016/j.gca.2008.06.020

Canfield, D. (2004). Canfield, D. E. The early history of atmospheric oxygen: Homage to Robert M. Garrels. *Annual Review of Earth and Planetary Sciences*, *33*, 1–36. https://doi.org/10.1146/annurev.earth.33.092203.122711

Casar, C. P., Momper, L. M., Kruger, B. R., & Osburn, M. R. (2021). Iron-fueled life in the continental subsurface: Deep mine. *Applied and Environmental Microbiology*, *87*(20). https://doi.org/10.1128/aem.00832-21

Chatelier, M., Ruelleu, S., Bour, O., Porel, G., & Delay, F. (2011). Combined fluid temperature and flow logging for the characterization of hydraulic structure in a fractured karst aquifer. *Journal of Hydrology*, *400*(3–4), 377–386. https://doi.org/10.1016/j.jhydrol.2011.01.051

Dalsgaard, T., Stewart, F. J., Thamdrup, B., De Brabandere, L., Revsbech, N. P., Ulloa, O., et al. (2014). Oxygen at nanomolar levels reversibly suppresses process rates and gene expression in anammox and denitrification in the oxygen minimum zone off northern Chile. *mBio*, *5*(6), 019666–e2014. https://doi.org/10.1128/mBio.01966-14

Deng, H., & Spycher, N. (2019). Modeling reactive transport processes in fractures. *Reviews in Mineralogy and Geochemistry*, *85*(1), 49–74. https://doi.org/10.2138/rmg.2019.85.3

DeSimone, L., Mcmahon, P. B., & Rosen, M. (2014). *The quality of our Nation's waters—Water quality in Principal Aquifers of the United States, 1991-2010 (Tech. Rep.)* (Vol. 1360). U.S. Geological Survey Circular. https://doi.org/10.3133/cir1360

Dideriksen, K., Christiansen, B. C., Frandsen, C., Balic-Zunic, T., Mørup, S., & Stipp, S. L. S. (2010). Paleo-redox boundaries in fractured granite. *Geochimica et Cosmochimica Acta*, *74*(10), 2866–2880. https://doi.org/10.1016/j.gca.2010.02.022

Druschel, G. K., Emerson, D., Sutka, R., Suchecki, P., & Luther, G. W. (2008). Low-oxygen and chemical kinetic constraints on the geochemical niche of neutrophilic iron(II) oxidizing microorganisms. *Geochimica et Cosmochimica Acta*, *72*(14), 3358–3370. https://doi.org/10.1016/j.gca.2008.04.035

Edmunds, W. M., Miles, D., & Cook, J. (1984). A comparative study of sequential redox processes in three British aquifers. *Hydrochemical balances of freshwater systems*, *50*, 55–70.

Emerson, D., Fleming, E. J., & McBeth, J. M. (2010). Iron-oxidizing bacteria: An environmental and genomic perspective. *Annual Review of Microbiology*, *64*(1), 561–583. https://doi.org/10.1146/annurev.micro.112408.134208

Erable, B., Féron, D., & Bergel, A. (2012). Microbial catalysis of the oxygen reduction reaction for microbial fuel cells: A review. *ChemSusChem*, *5*(6), 975–987. https://doi.org/10.1002/cssc.201100836

Fletcher, R. C., Buss, H. L., & Brantley, S. L. (2006). A spheroidal weathering model coupling porewater chemistry to soil thicknesses during steady-state denudation. *Earth and Planetary Science Letters*, *244*(1–2), 444–457. https://doi.org/10.1016/j.epsl.2006.01.055

Frey, P. A., & Reed, G. H. (2012). The ubiquity of iron. *ACS Chemical Biology*, *7*(9), 1477–1481. https://doi.org/10.1021/cb300323q

Goldich, S. S. (1938). A study in rock-weathering. *The Journal of Geology*, *46*(1), 17–58. https://doi.org/10.1086/624619

Gu, X., Heaney, P. J., Reis, F. D., & Brantley, S. L. (2020). Deep abiotic weathering of pyrite. *Science*, *370*(6515), 370. https://doi.org/10.1126/science.abb8092

Guillaumot, L., Longuevergne, L., Marçais, J., Lavenant, N., & Bour, O. (2022). Frequency domain water table fluctuations reveal recharge in fractured aquifers depends on both intense and seasonal rainfall and unsaturated zone thickness. *Hydrology and Earth System Sciences Discussions*, 1–38. https://doi.org/10.5194/hess-2022-201

Hampl, F. J., Schiperski, F., Byrne, J. M., Schwerdhelm, C., Kappler, A., Bryce, C., et al. (2021). The role of iron-bearing minerals for the deep weathering of a hydrothermally altered plutonic rock in semi-arid climate (Chilean coastal cordillera). *Chemical Geology*, *604*, 120922. https://doi.org/10.1016/j.chemgeo.2022.120922

Hancock, P. J., Boulton, A. J., & Humphreys, W. F. (2005). Aquifers and hyporheic zones: Towards an ecological understanding of groundwater. *Hydrogeology Journal*, *13*(1), 98–111. https://doi.org/10.1007/s10040-004-0421-6

Hartmann, J., & Moosdorf, N. (2012). The new global lithological map database GLiM: A representation of rock properties at the Earth surface. *Geochemistry, Geophysics, Geosystems*, *13*(12), 1–37. https://doi.org/10.1029/2012GC004370

Heidari, P., Li, L., Jin, L., Williams, J. Z., & Brantley, S. L. (2017). A reactive transport model for Marcellus shale weathering. *Geochimica et Cosmochimica Acta*, *217*, 421–440. https://doi.org/10.1016/j.gca.2017.08.011

Water Resources Research 10.1029/2023WR034986

Helgeson, H. C., Garrels, R. M., & MacKenzie, F. T. (1969). Evaluation of irreversible reactions in geochemical processes involving minerals and aqueous solutions—II. Applications. *Geochimica et Cosmochimica Acta*, *33*(4), 455–481. https://doi.org/10.1016/0016-7037(69)90127-6

Holbrook, W. S., Marcon, V., Bacon, A. R., Brantley, S. L., Carr, B. J., Flinch, B. A., et al. (2019). Links between physical and chemical weathering inferred from a 65-m-deep borehole through Earth's critical zone. *Scientific Reports*, *9*, 1–11. https://doi.org/10.1038/s41598-019-40819-9

Humphreys, W. F. (2009). Hydrogeology and groundwater ecology: Does each inform the other? *Hydrogeology Journal*, *17*(1), 5–21. https://doi.org/10.1007/s10040-008-0349-3

Hunter, J. D. (2007). Matplotlib: A 2d graphics environment [Software]. Computing in Science & Engineering, *9*, 90–95. https://doi.org/10.1109/MCSE.2007.55

Jiménez-Martínez, J., Longuevergne, L., Le Borgne, T., Davy, P., Russian, A., & Bour, O. (2013). Temporal and spatial scaling of hydraulic response to recharge in fractured aquifers: Insights from a frequency domain analysis. *Water Resources Research*, *49*(5), 3007–3023. https://doi.org/10.1002/wrcr.20260

Kappler, A., Bryce, C., Mansor, M., Lueder, U., Byrne, J. M., & Swanner, E. D. (2021). An evolving view on biogeochemical cycling of iron. *Nature Reviews Microbiology*, *19*(6), 360–374. https://doi.org/10.1038/s41579-020-00502-7

Kendall, B., Anbar, A. D., Kappler, A., & Konhauser, K. O. (2012). The global iron cycle. *Fundamentals of Geobiology*, 65–92. https://doi.org/10.1002/9781118280874.ch6

Kim, H., Stinchcomb, G., & Brantley, S. L. (2017). Feedbacks among O2 and CO_2 in deep soil gas, oxidation of ferrous minerals, and fractures: A hypothesis for steady-state regolith thickness. *Earth and Planetary Science Letters*, *460*, 29–40. https://doi.org/10.1016/j.epsl.2016.12.003

Kolbe, T., De Dreuzy, J. R., Abbott, B. W., Aquilina, L., Babey, T., Green, C. T., et al. (2019). Stratification of reactivity determines nitrate removal in groundwater. *Proceedings of the National Academy of Sciences of the United States of America*, *116*(7), 2494–2499. https://doi.org/10.1073/pnas.1816892116

Korom, S. F. (1992). Natural denitrification in the saturated zone: A review. *Water Resources Research*, *28*(6), 1657–1668. https://doi.org/10.1029/92WR00252

Krone, L. V., Hampl, F. J., Schwerdhelm, C., Bryce, C., Ganzert, L., Kitte, A., et al. (2021). Deep weathering in the semi-arid coastal cordillera, Chile. *Scientific Reports*, *11*(1), 1–15. https://doi.org/10.1038/s41598-021-90267-7

Lasaga, A. C. (1984). Chemical kinetics of water-rock interactions. *Journal of Geophysical Research*, *89*(B6), 4009–4025. https://doi.org/10.1029/JB089iB06p04009

Le Borgne, T., Bour, O., Riley, M. S., Gouze, P., Pezard, P. A., Belghoul, A., et al. (2007). Comparison of alternative methodologies for identifying and characterizing preferential flow paths in heterogeneous aquifers. *Journal of Hydrology*, *345*(3–4), 134–148. https://doi.org/10.1016/j.jhydrol.2007.07.007

Leray, S., de Dreuzy, J.-R., Aquilina, L., Vergnaud-Ayraud, V., Labasque, T., Bour, O., & Le Borgne, T. (2014). Temporal evolution of age data under transient pumping conditions. *Journal of Hydrology*, *511*, 555–566. https://doi.org/10.1016/j.jhydrol.2014.01.064

Leray, S., de Dreuzy, J. R., Bour, O., & Bresciani, E. (2013). Numerical modeling of the productivity of vertical to shallowly dipping fractured zones in crystalline rocks. *Journal of Hydrology*, *481*, 64–75. https://doi.org/10.1016/j.jhydrol.2012.12.014

Li, L., Maher, K., Navarre-sitchler, A., Druhan, J., Meile, C., Lawrence, C., et al. (2017). Expanding the role of reactive transport models in critical zone processes. *Earth-Science Reviews*, *165*, 280–301. https://doi.org/10.1016/j.earscirev.2016.09.001

Liao, R., Gu, X., & Brantley, S. L. (2022). Weathering of chlorite from grain to watershed: The role and distribution of oxidation reactions in the subsurface. *Geochimica et Cosmochimica Acta*, *333*, 284–307. https://doi.org/10.1016/j.gca.2022.07.019

Macquarrie, K. T. B., Mayer, K. U., Jin, B., & Spiessl, S. M. (2010). The importance of conceptual models in the reactive transport simulation of oxygen ingress in sparsely fractured crystalline rock. *Journal of Contaminant Hydrology*, *112*(1–4), 64–76. https://doi.org/10.1016/j.jconhyd.2009.10.007

Mader, M., Schmidt, C., van Geldern, R., & Barth, J. A. (2017). Dissolved oxygen in water and its stable isotope effects: A review. *Chemical Geology*, *473*(September), 10–21. https://doi.org/10.1016/j.chemgeo.2017.10.003

Maher, K. (2010). The dependence of chemical weathering rates on fluid residence time. *Earth and Planetary Science Letters*, *294*(1–2), 101–110. https://doi.org/10.1016/j.epsl.2010.03.010

Maher, K., & Chamberlain, C. P. (2014). Hydrologic regulation of chemical weathering and the geologic carbon cycle. *Science*, *343*(6178), 1502–1504. https://doi.org/10.1126/science.1250770

Maisch, M., Lueder, U., Laufer, K., Scholze, C., Kappler, A., & Schmidt, C. (2019). Contribution of Microaerophilic iron(II)-Oxidizers to iron(III) mineral formation. *Environmental Science and Technology*, *53*(14), 8197–8204. https://doi.org/10.1021/acs.est.9b01531

Malard, F., & Hervant, F. (1999). Oxygen supply and the adaptations of animals in groundwater. *Freshwater Biology*, *41*, 1–30. https://doi.org/10.1046/j.1365-2427.1999.00379.x

Malmstrom, M., Banwart, S., Duro, L., Wersin, P., & Bruno, J. (1995). Biotite and chlorite weathering at 25°C (Tech. Rep. No. January).

Malmström, M., Banwart, S., Lewenhagen, J., Duro, L., & Bruno, J. (1996). The dissolution of biotite and chlorite at 25°C in the near-neutral pH region. *Journal of Contaminant Hydrology*, *21*(1–4), 201–213. https://doi.org/10.1016/0169-7722(95)00047-x

Melton, E. D., Swanner, E. D., Behrens, S., Schmidt, C., & Kappler, A. (2014). The interplay of microbially mediated and abiotic reactions in the biogeochemical Fe cycle. *Nature Reviews Microbiology*, *12*(12), 797–808. https://doi.org/10.1038/nrmicro3347

Molenat, J., Davy, P., Gascuel-Odoux, C., & Durand, P. (1999). Study of three subsurface hydrologic systems based on spectral and cross-spectral analysis of time series. *Journal of Hydrology*, *222*(1–4), 152–164. https://doi.org/10.1016/s0022-1694(99)00107-9

Moore, J., Lichtner, P. C., White, A. F., & Brantley, S. L. (2012). Using a reactive transport model to elucidate differences between laboratory and field dissolution rates in regolith. *Geochimica et Cosmochimica Acta*, *93*, 235–261. https://doi.org/10.1016/j.gca.2012.03.021

Murakami, T., Utsunomiya, S., Yokoyama, T., & Kasama, T. (2003). Biotite dissolution processes and mechanisms in the laboratory and in nature: Early stage weathering environment and vermiculitization. *American Mineralogist*, *88*(2–3), 377–386. https://doi.org/10.2138/am-2003-2-314

Napieralski, S. A., Buss, H. L., Brantley, S. L., Lee, S., Xu, H., & Roden, E. E. (2019). Microbial chemolithotrophy mediates oxidative weathering of granitic bedrock. *Proceedings of the National Academy of Sciences of the United States of America*, *116*(52), 26394–26401. https://doi.org/10.1073/pnas.1909970117

Nordstrom, D. K. (2011). Hydrogeochemical processes governing the origin, transport and fate of major and trace elements from mine wastes and mineralized rock to surface waters. *Applied Geochemistry*, *26*(11), 1777–1791. https://doi.org/10.1016/j.apgeochem.2011.06.002

Palandri, J., & Kharaka, Y. (2004). A compilation of rate parameters of water-mineral interaction kinetics for application to geochemical modeling.

Pedersen, K. (1997). Microbial life in deep granitic rock. *FEMS Microbiology Reviews*, *20*(3–4), 399–414. https://doi.org/10.1016/S0168-6445(97)00022-3

Petsch, S. T., Bolton, E., Mok, U., & Evans, B. (2004). The weathering of sedimentary organic matter as a control on athmospheric O_2: I. Analysis of a black shale. *American Journal of Science*, *304*(3), 234–249. https://doi.org/10.2475/ajs.304.3.234

Robie, A. R., & Philip, M. B. (1962). *Molar volumes and densities of minerals—TEI-822 (Tech. Rep.)*. USGS.

AGU ADVANCING EARTH AND SPACE SCIENCES

Water Resources Research 10.1029/2023WR034986

Roques, C., Aquilina, L., Boisson, A., Vergnaud-Ayraud, V., Labasque, T., Longuevergne, L., et al. (2018). Autotrophic denitrification supported by biotite dissolution in crystalline aquifers: (2) transient mixing and denitrification dynamic during long-term pumping. *Science of the Total Environment*, *619–620*, 491–503. https://doi.org/10.1016/j.scitotenv.2017.11.104

Roques, C., Bour, O., Aquilina, L., & Dewandel, B. (2016). High-yielding aquifers in crystalline basement: Insights about the role of fault zones, exemplified by Armorican massif, France. *Hydrogeology Journal*, *24*(8), 2157–2170. https://doi.org/10.1007/s10040-016-1451-6

Ruelleu, S., Moreau, F., Bour, O., Gapais, D., & Martelet, G. (2010). Impact of gently dipping discontinuities on basement aquifer recharge: An example from Ploemeur (Brittany, France). *Journal of Applied Geophysics*, *70*(2), 161–168. https://doi.org/10.1016/j.jappgeo.2009.12.007

Ruff, S. E., Humez, P., de Angelis, I. H., Diao, M., Nightingale, M., Cho, S., et al. (2023). Hydrogen and dark oxygen drive microbial productivity in diverse groundwater ecosystems. *Nature Communications*, *14*(1), 3194. https://doi.org/10.1038/s41467-023-38523-4

Scott, A. D., & Amonette, J. (1985). Role of iron in mica weathering. In *Iron in soils and clay minerals* (pp. 537–605). Bad Windsheim: Reidel Publishing Company. https://doi.org/10.1007/978-94-009-4007-9

Seeboonruang, U., & Ginn, T. R. (2006). Upscaling heterogeneity in aquifer reactivity via exposure-time concept: Forward model. *Journal of Contaminant Hydrology*, *84*(3–4), 127–154. https://doi.org/10.1016/j.jconhyd.2005.12.011

Sequeira Braga, M. A., Paquet, H., & Begonha, A. (2002). Weathering of granites in a temperate climate (NW Portugal): Granitic saprolites and arenization. *Catena*, *49*(1), 41–56. https://doi.org/10.1016/S0341-8162(02)00017-6

Serikov, L. V., Tropina, E. A., Shiyan, L. N., Frimmel, F. H., Metreveli, G., & Delay, M. (2009). Iron oxidation in different types of groundwater of Western Siberia. *Journal of Soils and Sediments*, *9*(2), 103–110. https://doi.org/10.1007/s11368-009-0069-x

Sidborn, M., & Neretnieks, I. (2007). Long term redox evolution in granitic rocks: Modelling the redox front propagation in the rock matrix. *Applied Geochemistry*, *22*(11), 2381–2396. https://doi.org/10.1016/j.apgeochem.2007.05.007

Sidborn, M., & Neretnieks, I. (2008). Long-term oxygen depletion from infiltrating groundwaters: Model development and application to intra-glaciation and glaciation conditions. *Journal of Contaminant Hydrology*, *100*(1–2), 72–89. https://doi.org/10.1016/j.jconhyd.2008.05.010

Singer, P. C., & Stumm, W. (1970). Acidic mine drainage: The rate-determining step. *Science*, *167*(3921), 1121–1123. https://doi.org/10.1126/science.167.3921.1121

Singha, K., & Navarre-Sitchler, A. (2022). The importance of groundwater in critical zone science. *Ground Water*, *60*(1), 27–34. https://doi.org/10.1111/gwat.13143

Spiessl, S. M., Macquarrie, K. T. B., & Mayer, K. U. (2008). Identification of key parameters controlling dissolved oxygen migration and attenuation in fractured crystalline rocks. *Journal of Contaminant Hydrology*, *95*(3–4), 141–153. https://doi.org/10.1016/j.jconhyd.2007.09.002

Sprenger, M., Stumpp, C., Weiler, M., Aeschbach, W., Allen, S. T., Benettin, P., et al. (2019). The demographics of water: A review of water ages in the critical zone. *Reviews of Geophysics*, *57*(3), 800–834. https://doi.org/10.1029/2018RG000633

Steefel, C. I., Appelo, C. A. J., Arora, B., Jacques, D., Kalbacher, T., Kolditz, O., et al. (2015). Reactive transport codes for subsurface environmental simulation [Software]. Computational Geosciences, *19*, 445–478. https://doi.org/10.1007/s10596-014-9443-x

Stumm, W., & Morgan, J. J. (1996). Oxidation and reduction: Equilibria and microbial mediation. In J. Schnoor & A. Zehnder (Eds.), *Aquatic chemistry: Chemical equilibria and rates in natural waters* (3rd ed., pp. 425–515). Wiley.

Sugimori, H., Iwatsuki, T., & Murakami, T. (2008). Chlorite and biotite weathering, Fe^{2+}-rich corrensite formation, and Fe behavior under low Po_2 conditions and their implication for Precambrian weathering. *American Mineralogist*, *93*(7), 1080–1089. https://doi.org/10.2138/am.2008.2663

Sullivan, P. L., Hynek, S. A., Gu, X., Singha, K., White, T., West, N., et al. (2016). Oxidative dissolution under the channel leads geomorphological evolution at the shale hills catchment. *American Journal of Science*, *316*(10), 981–1026. https://doi.org/10.2475/10.2016.02

Tebo, B. M., Johnson, H. A., McCarthy, J. K., & Templeton, A. S. (2005). Geomicrobiology of manganese(II) oxidation. *Trends in Microbiology*, *13*(9), 421–428. https://doi.org/10.1016/j.tim.2005.07.009

Trinchero, P., Molinero, J., Ebrahimi, H., Puigdomenech, I., Gylling, B., Svensson, U., et al. (2018). Simulating oxygen intrusion into highly performance computing. *Mathematical Geosciences*, *50*(5), 49–51. https://doi.org/10.1007/s11004-017-9718-6

Trinchero, P., Puigdomenech, I., Molinero, J., Ebrahimi, H., Gylling, B., Svensson, U., et al. (2017). Continuum-based DFN-consistent numerical framework for the simulation of oxygen infiltration into fractured crystalline rocks. *Journal of Contaminant Hydrology*, *200*, 60–69. https://doi.org/10.1016/j.jconhyd.2017.04.001

Trinchero, P., Sidborn, M., Puigdomenech, I., Svensson, U., Ebrahimi, H., Molinero, J., et al. (2019). Transport of oxygen into granitic rocks: Role of physical and mineralogical heterogeneity. *Journal of Contaminant Hydrology*, *220*, 108–118. https://doi.org/10.1016/j.jconhyd.2018.12.001

Tullborg, E. L., Drake, H., & Sandström, B. (2008). Palaeohydrogeology: A methodology based on fracture mineral studies. *Applied Geochemistry*, *23*(7), 1881–1897. https://doi.org/10.1016/j.apgeochem.2008.02.009

White, A. F., & Peterson, M. L. (1990). *Role of reactive-surface-area characterization in geochemical kinetic models*. ACS Publications.

White, A. F., & Yee, A. (1985). Aqueous oxidation-reduction kinetics associated with coupled electron-cation transfer from iron-containing silicates at 25°C. *Geochimica et Cosmochimica Acta*, *49*(5), 1263–1275. https://doi.org/10.1016/0016-7037(85)90015-8

White, A. F., Yee, A., & Flexser, S. (1985). Surface oxidation-reduction kinetics associated with experimental basalt-water reaction at 25°C. *Chemical Geology*, *49*(1–3), 73–86. https://doi.org/10.1016/0009-2541(85)90148-2

Wild, B., Daval, D., Beaulieu, E., Pierret, M. C., Viville, D., & Imfeld, G. (2019). In-situ dissolution rates of silicate minerals and associated bacterial communities in the critical zone (Strengbach catchment, France). *Geochimica et Cosmochimica Acta*, *249*, 95–120. https://doi.org/10.1016/j.gca.2019.01.003

Winograd, I., & Robertson, F. (1982). Deep oxygenated ground water: Anomaly or common occurrence? *Science*, *216*(4551), 1227–1230. https://doi.org/10.1126/science.216.4551.1227

Wolthoorn, A., Temminghoff, E. J., Weng, L., & Van Riemsdijk, W. H. (2004). Colloid formation in groundwater: Effect of phosphate, manganese, silicate and dissolved organic matter on the dynamic heterogeneous oxidation of ferrous iron. *Applied Geochemistry*, *19*(4), 611–622. https://doi.org/10.1016/j.apgeochem.2003.08.003

References From the Supporting Information

Blanc, P., Lassin, A., Piantone, P., Azaroual, M., Jacquemet, N., Fabbri, A., & Gaucher, E. C. (2012). Thermoddem: A geochemical database focused on low temperature water/rock interactions and waste materials [Dataset]. Applied Geochemistry, *27*, 2107–2116. https://doi.org/10.1016/j.apgeochem.2012.06.002

Klepikova, M. V., Le Borgne, T., Bour, O., & Davy, P. (2011). A methodology for using borehole temperature-depth profiles under ambient, single and cross-borehole pumping conditions to estimate fracture hydraulic properties. *Journal of Hydrology*, *407*(1–4), 145–152. https://doi.org/10.1016/j.jhydrol.2011.07.018

Water Resources Research 10.1029/2023WR034986

Le Borgne, T., Paillet, F., Bour, O., & Caudal, J. P. (2006). Cross-borehole flowmeter tests for transient heads in heterogeneous aquifers. *Ground Water*, *44*(3), 444–452. https://doi.org/10.1111/j.1745-6584.2005.00150.x

Pouladi, B., Bour, O., Longuevergne, L., de La Bernardie, J., & Simon, N. (2021). Modelling borehole flows from distributed temperature sensing data to monitor groundwater dynamics in fractured media. *Journal of Hydrology*, *598*, 126450. https://doi.org/10.1016/j.jhydrol.2021.126450

Sugisaki, R., & Taki, K. (1987). Simplified analyses in of He, natural Ne, waters and Ar dissolved. *Geochemical Journal*, *21*(1), 23–27. https://doi.org/10.2343/geochemj.21.23

3 Chapter conclusion: extending the limit of the oxic hydrosphere

Through a systematic study of the distribution of dissolved oxygen in the fractured-bedrock aquifer of the CZO of Ploemeur, we present a comprehensive dataset that supports the presence of an often overlooked oxic subsurface. We identified the oxic-anoxic interface at depths of about 150 and 300m in the Guidel and Kermadoye catchments, respectively. These results extend the single-borehole measurements of Bochet et al. (2020) and put them in the context of the reactive-transport functioning in the Guidel catchment. While the depth of the oxic-anoxic interface is site-specific and depends on the balance between geological and hydrological forcings, our study indicates that the bottom limit of the oxic hydrosphere can reach several hundred meters below surface. As a result, a substantial portion of the continental subsurface is potentially influenced by aerobic biogeochemical processes which are sensitive to O_2 fluxes from the surface. We propose to call this portion of the subsurface as the *deep oxic hydrosphere*. This chapter also highlighted the importance of mixing processes to drive the activity of iron oxidizing bacteria (FeOB), that require the simultaneous presence of both O_2 and Fe. Our model predicts that in a single flow path, groundwater is either O_2-rich or Fe-rich but not both simultaneously. Our conceptual development thus reinforces the idea of Bochet et al. (2020) about mixing processes as potential drivers of reactive hotspots in the subsurface. Nevertheless, the concept of the steady-state iron concentration at anoxic conditions, developed in this chapter, implies that mixing processes are not always likely to be reactive, since the geological contexts can limit the availability of dissolved iron. To sum it up, this chapter provides a conceptual framework that explains the first order controls on the redox compartmentalization in the continental subsurface. Oxic subsurface environments potentially impact biogeochemical processes in the continental subsurface. These processes can however be dominated by abiotic or microbe-mediated processes. In the following chapter we use the isotope composition of DO as a tracer of the abiotic and microbe-mediated processes at catchment scale.

4 Perspectives

1. **Systematic campaigns in other hydrogeological observatories:** The conceptual framework, along with the observations of a deep oxic hydrosphere in the CZO of Ploemeur provided in this chapter, suggests that this could be a general case in fractured silicate rocks. Similar systematic inventories of the distribution of dissolved O_2 in groundwater could be conducted in other critical zone observatories to further support our model.

2. **Dynamics of the oxic-anoxic interface:** as established in the conceptual framework of this chapter, the input of O_2 to the subsurface is closely related to the hydraulic connectivity with the surface, which facilitates the advective transport of oxic water. Hydraulic forcings that influence advection velocities are subject to seasonality, which governs variations in groundwater recharge and the water table level of aquifers. Hence, seasonal variations in hydrological forcings can potentially induce fluctuations in the depth of the oxic-anoxic interface in the aquifer. Relating the redox variations in the subsurface to fluctuations in hydrological forcings could offer a dynamic comprehension of the reactive-transport problem developed in this chapter. This analysis could potentially be conducted using frequency-domain approaches [e.g. (Durand et al.; 1999; Jiménez-Martínez et al.; 2013)] allowing to relate hydrological timeseries in the surface with DO timeseries in the aquifer. In such a scenario, obtaining time series data for dissolved O_2 concentrations, which are currently unavailable, would be essential. To address this, additional monitoring endeavors should focus on utilizing autonomous *in-situ* probes to capture time series of O_2 concentrations in the aquifer.

5 Take-home messages

Factors controlling redox landscapes in the continental subsurface

This chapter established a simple and effective conceptual framework to predict the catchment-scale distribution of dissolved oxygen and iron in fractured aquifers:

1. **The distribution of O_2 and Fe is a reactive-transport problem** that relates hydrological forcings that transport O_2 from the surface, and geologic forcings that consume oxygen through the oxidation of Fe^{2+} coming from rock weathering. We demonstrated that the joint study of both O_2 and Fe allows to constrain the reactive-transport problem to predict oxic-anoxic zones in aquifers.

2. **We developed a simple analytical model to predict both O_2 and Fe depth profiles in aquifers.** The model is parameterized with dimensionless numbers such as the Damköhler number (Da) and a new Lithological number (Λ) which allow to identify whether hydrological or geological forcings limit the depth distributions of O_2 and Fe, respectively.

3. Under favorable hydrological and geological conditions, **the oxic-anoxic interface can reach depths of several hundred-meters.** We propose to call this portion of the subsurface the *deep oxic hydrosphere.*

4. **Mixing between redox-contrasted flow paths is necessary to allow for the simultaneous presence of O_2 an Fe**, however the geological context can lead to non-reactive mixing, possibly limiting microbial activity.

6 Chapter acknowledgments

While this chapter is mainly focused on a modelling work, this would have not been possible without a huge effort acquiring data in the field. I would like to thank the many people that made the field campaigns possible with their kind help: Eliot Chatton, Camille Bouchez, Nicolas Lavenant, Thierry Labasque, Marion Agullo, Barbara Yvard and Remy Henocq.

Also thanks to Tanguy and Camille for the fascinating discussions that led us to figure out the model. I really enjoyed those moments!

Bibliography

Antoniellini, M., Mollema, P., and Del Sole, L. (2017). Application of analytical diffusion models to outcrop observations: Implications for mass transport by fluid flow through fractures. *Water Resources Research*, 53:5545–5566.

Bazilevskaya, E., Rother, G., Mildner, D. F., Pavich, M., Cole, D., Bhatt, M. P., Jin, L., Steefel, C. I., and Brantley, S. L. (2015). How Oxidation and Dissolution in Diabase and Granite Control Porosity during Weathering. *Soil Science Society of America Journal*, 79(1):55–73.

Bochet, O., Bethencourt, L., Dufresne, A., Farasin, J., Pédrot, M., Labasque, T., Chatton, E., Lavenant, N., Petton, C., Abbott, B. W., Aquilina, L., and Le Borgne, T. (2020). Iron-oxidizer hotspots formed by intermittent oxic–anoxic fluid mixing in fractured rocks. *Nature Geoscience*, 13(2):149–155.

Buss, H. L., Sak, P. B., Webb, S. M., and Brantley, S. L. (2008). Weathering of the Rio Blanco quartz diorite , Luquillo Mountains , Puerto Rico : Coupling oxidation , dissolution , and fracturing. *Geochimica et Cosmochimica Acta*, 72:4488–4507.

DeSimone, L., Mcmahon, P. B., and Rosen, M. (2014). The quality of our Nation's waters - Water quality in Principal Aquifers of the United States, 1991-2010. Technical report, U.S. Geological Survey Circular 1360.

Durand, P., Gascuel-Odoux, C., Davy, P., and Molenat, J. (1999). Study of Three Subsurface Hydrologic Systems Based on Spectral and Cross-Spectral Analysis of Time Series. *Journal of Hydrology*, 222:152–164.

Ehrlich, H. L., Newman, D. K., and Kappler, A., editors (2015). *Ehrlich's Geomicrobiology*. CRC Press, 0 edition.

Hampl, F. J., Schiperski, F., Byrne, J. M., Schwerdhelm, C., Kappler, A., Bryce, C., von Blanckenburg, F., and Neumann, T. (2022). The role of iron-bearing minerals for the deep weathering of a hydrothermally altered plutonic rock in semi-arid climate (Chilean Coastal Cordillera). *Chemical Geology*, 604:120922.

Jiménez-Martínez, J., Longuevergne, L., Le Borgne, T., Davy, P., Russian, A., and Bour, O. (2013). Temporal and spatial scaling of hydraulic response to recharge in fractured aquifers: Insights from a frequency domain analysis. *Water Resources Research*, 49(5):3007–3023.

Krone, L. V., Hampl, F. J., Schwerdhelm, C., Bryce, C., Ganzert, L., Kitte, A., Übernickel, K., Dielforder, A., Aldaz, S., Oses-Pedraza, R., Perez, J. P. H., Sanchez-Alfaro, P., Wagner, D., Weckmann, U., and von Blanckenburg, F. (2021). Deep weathering in the semi-arid Coastal Cordillera, Chile. *Scientific Reports*, 11(1):1–15.

McMahon, P. B. and Chapelle, F. H. (2008). Redox processes and water quality of selected principal aquifer systems. *Ground Water*, 46(2):259–271.

Sidborn, M. and Neretnieks, I. (2007). Long term redox evolution in granitic rocks: Modelling the redox front propagation in the rock matrix. *Applied Geochemistry*, 22(11):2381–2396.

Sidborn, M. and Neretnieks, I. (2008). Long-term oxygen depletion from infiltrating groundwaters: Model development and application to intra-glaciation and glaciation conditions. *Journal of Contaminant Hydrology*, 100(1-2):72–89.

Sprenger, M., Stumpp, C., Weiler, M., Aeschbach, W., Allen, S. T., Benettin, P., Dubbert, M., Hartmann, A., Hrachowitz, M., Kirchner, J. W., Mcdonnell, J. J., Orlowski, N., Penna, D., Pfahl, S., Rinderer, M., Rodriguez, N., Schmidt, M., and Werner, C. (2019). The demographics of water : A review of water ages in the critical zone. *Reviews of Geophysics*, 57.

Trinchero, P., Molinero, J., Ebrahimi, H., Puigdomenech, I., Gylling, B., Svensson, U., Bosbach, D., and Deissmann, G. (2018). Simulating Oxygen Intrusion into Highly Performance Computing. *Mathematical Geosciences*, pages 49–51.

Trinchero, P., Sidborn, M., Puigdomenech, I., Svensson, U., Ebrahimi, H., Molinero, J., Gylling, B., Bosbach, D., and Deissmann, G. (2019). Transport of oxygen into granitic rocks: Role of physical and mineralogical heterogeneity. *Journal of Contaminant Hydrology*, 220(November 2018):108–118.

V. STABLE ISOTOPES OF DISSOLVED OXYGEN AS A TRACER OF BIOTIC AND ABIOTIC PROCESSES IN THE DEEP CONTINENTAL SUBSURFACE

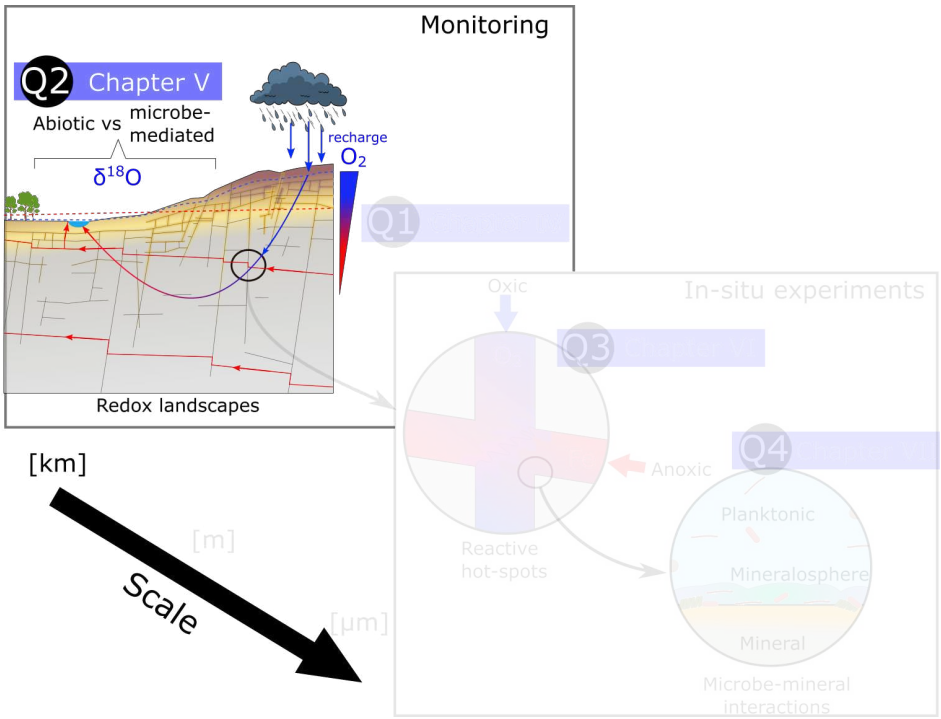

Contents

1 Introduction

Oxygen has generally three stable isotopes, the most abundant being ^{16}O (99.757‰), followed by two minor isotopes, ^{17}O (0.038‰) and ^{18}O (0.205‰) (Bao et al.; 2016). Due to differences in their masses, resulting from different numbers of neutrons, they have slightly different physico-chemical properties in certain environmental conditions and processes. Mass-dependent processes cause fractionation between the isotopes, resulting in different relative abundances between compartments. For example, heavier isotopes tend to be more soluble in water (Kroopnick and Craig; 1972), while lighter isotopes diffuse more quickly (Hendry et al.; 2002) and are preferentially consumed by biogeochemical reactions (Mader et al.; 2017; Ash et al.; 2020). A particular case is photosynthesis, which produces oxygen with the same isotopic composition as oxygen in the water molecule used in the reaction (Guy et al.; 1993).

Stable oxygen isotopes are measured, for simplicity, as variations in isotopic ratios (R) ($^{18}O/\ ^{16}O$ and $^{17}O/\ ^{16}O$) relative to the international standard adopted by convention: the average value of seawater, SMOW (Gonfiantini; 1978). Isotopic fractionations are expressed with the delta notation, $\delta^{18}O$ and $\delta^{17}O$, taking SMOW as the reference with a value of $\delta^{18}O = \delta^{17}O = 0$ ‰:

$$\delta[‰] = \left(\frac{R_{sample}}{R_{standard}} - 1\right) \times 1000 \tag{V.1}$$

where R corresponds to $^{18}O/^{16}O$ isotopic ratios of dissolved O_2. The systematic study of oxygen isotopes in different terrestrial compartments initially focused on the atmosphere and ocean, particularly motivated by the discovery of the Dole effect (Dole; 1936). The Dole effect refers to the observation of an excess of 23.88 ‰ in $\delta^{18}O$, much larger than the expected equilibrium value of 5 ‰(Kroopnick and Craig; 1972). This disequilibrium of the atmosphere represents the sum of all respiration and photosynthesis processes on Earth (Luz and Barkan; 2005). Thus, efforts to explain the Dole effect have led to the determination of characteristic fractionations associated with many processes and the characterization of isotopic compositions of different terrestrial compartments (Mader et al.; 2017).

In the particular context of dissolved oxygen (DO), oxygen isotopes have been used to estimate respiration and gross primary production rates in surface, continental, and oceanic waters (Jurikova et al.; 2016; Peeters et al.; 2019; Tromboni et al.; 2020). It is important to note that the majority of studies on DO isotopes focus on surface waters, and the only studies on subsurface environments have focused on the unsaturated zone and the hyporheic zone (Aggarwal and Dillon; 1998; Smith et al.; 2011).

Although subterranean aerobic reactions are biogeochemical reactions with important consequences for rock weathering processes and biogeochemical cycles of iron and carbon Napieralski et al. (2019); Kappler et al. (2021), these reactions remain poorly constrained. The question of their biotic or abiotic nature is, so far, mostly based on the response of microorganisms to different ranges of DO concentration tested in the laboratory, which have suggested that microbial DO consumption mostly occurs at the *microaerobic range*, i.e. for DO concentrations ranging between 1.6 and 0.01 $mg.L^{-1}$ Druschel et al. (2008); Maisch et al. (2019). Is is yet not clear whether these laboratory observations are representative of the biotic and abiotic DO consumption under *in-situ* conditions. In this chapter, we study the stable isotopic composition of DO and use it as a tool to investigate the biotic and abiotic nature of reactive processes involving DO in subsurface environments. In addition to arguments based on laboratory concentration ranges, these results should improve our understanding of the drivers of primary productivity in underground environments.

2 Article "Dissolved oxygen isotopes as a tracer of biotic and abiotic processes in the deep subsurface", in prep. for *Groundwater*

Dissolved oxygen isotopes as a tracer of biotic and abiotic processes in the deep subsurface

Ivan-David Osorio-Leon[1], Camille Bouchez[1], Eliot Chatton[1], Marlene Dordoni[2], David Piatka[2], Johannes Barth[2], Tanguy Le Borgne[1]

[1]Univ Rennes – CNRS, Géosciences Rennes - UMR 6118. Rennes, France
[2]GeoZentrum Nordbayern – Friedrich-Alexander University, Erlangen-Nuremberg, Germany

Key Points:

- We study the isotopic composition of dissolved oxygen (DO) in the continental subsurface and use it to unravel O_2 sources and sinks in groundwater.
- $\delta^{18}O_{DO}$ values at the study site reveal an unexpected isotopic depletion of DO in recharge-zone boreholes, possibly related to mixing processes in the aquifer.
- Deeper groundwater displays higher $\delta^{18}O_{DO}$ values that we relate to the occurence of iron oxidizer hotspots.

Corresponding author: Ivan-David Osorio-Leon, idosoriole@unal.edu.co

Corresponding author: Camille Bouchez, camille.bouchez@univ-rennes.fr

Abstract

The possible persistence of dissolved oxygen (DO) in deep groundwater can play on important role to sustain microbial life and biogeochemical reactions. In aquifers, the spatial and temporal distribution of DO is often heterogeneous, intermittent and poorly constrained. In this study, we investigate the potential of dissolved oxygen as a tracer of biotic and abiotic processes in the deep subsurface. To this end, we investigate DO dynamics in a fractured-bedrock aquifer in Brittany, characterized by strong surface-groundwater connectivity, rapid hydrologic response and the presence of deep O2-dependent microorganisms. Oxygen stable isotopes of DO ($\delta^{18}O_{DO}$), major dissolved gases, chlorofluorocarbons (CFCs), ^{36}Cl and major cations and anions were analyzed in rainwater and in groundwater. We sampled eight piezometers located in recharge and discharge zones of the catchment, with depths ranging from 60 to 150m-deep. DO concentrations decrease with increasing water residence time while $\delta^{18}O_{DO}$ signatures show two different trends depending on DO concentrations. In recharge-zone boreholes, DO concentrations decrease from 10 to 1.6 mg/L and $\delta^{18}O_{DO}$ values decrease from 24.8 to 18.1 ‰. This unexpected depletion of ^{18}O in DO is not likely due to reactive processes that are known to produce an enrichment effect, i.e. increasing $\delta^{18}O_{DO}$ values. We thus hypothesize that it is induced by the mixing of fracture fluids with water from the unconfined aquifer in the regolith zone. The latter is isotopically depleted because of the faster diffusion of ^{16}O at the water table interface. In the discharge-zone boreholes, DO concentrations decrease from 1.6 to 0.04 mg/L, while the $^{18}O_{DO}$ values show a clear increase from 18.1 to 25.3 ‰. All DO concentrations are within the micro-aerobic range, theoretically favorable to a microbial consumption of DO. The simultaneous decrease in DO and increase in $^{18}O_{DO}$ is consistent with a reaction that positively fractionates DO in the remaining dissolved phase, which could be associated with microbial activity. The fractionation factor calibrated on the field-data is however significantly lower than those reported from lab experiments for microbial iron oxidation. These findings hence provide new insights on the potential use of DO isotope composition to differentiate and elucidate the reactive pathways of DO consumption in subsurface environments.

Plain Language Summary

1 Introduction

Dissolved oxygen (DO) is an essential environmental variable in the critical zone (CZ), the thin layer of our planet where life meets water and rocks (Brantley, 2010). In Earth's surface, DO is produced by photosynthesis and is mostly consumed by respiration metabolisms in aerobic organisms (Malard & Hervant, 1999; Mader et al., 2017). In the continental subsurface, the absence of light prevents the production of oxygen derived from photosynthesis, except for some specific processes that can produce dark oxygen such as water radiolysis (Gutsalo, 1971) and chlorate (Rikken et al., 1996; van Ginkel et al., 1996) or intra-aerobic respiration (Ettwig et al., 2010). However, dark oxygen production is restricted either to depths greater than 2 km or to the presence of specific contaminants and microbial communities (Rikken et al., 1996; van Ginkel et al., 1996; Ettwig et al., 2010).

Subsurface oxygen is mainly replenished from the atmosphere to the subsurface by advective transport of air-equilibrated water that infiltrates in soils (Malard & Hervant, 1999). Diffusion at the water table interface can also represent an important oxygen input in unconfined aquifers (Rose & Long, 1988). Depending on the organic carbon content of soils, DO can be depleted in the unsaturated zone due to its high reactivity. DO is indeed the most important electron acceptor in nature (Korom, 1992; Stumm & Morgan, 1996) and therefore it is consumed in redox reactions, among which the degradation of organic matter during aerobic respiration in soils is the major O_2-sink (Lasaga & Ohmoto, 2002). However, in certain geological contexts characterized by limited soil

thickness or low organic carbon content, such as hard-rock aquifers, DO can reach the saturated zone of aquifers (Winograd & Robertson, 1982; McMahon & Chapelle, 2008) where it impacts the oxidation state of metallic trace elements (Hee et al., 2007; Nordstrom, 2011; Lezama-Pacheco et al., 2015), the weathering of reduced minerals (Buss et al., 2008; Kim et al., 2017), the activation of anaerobic processes such as denitrification (Kolbe et al., 2019), the aerobic biodegradation of contaminants (Borden & Bedient, 1986; Fry et al., 1996) and the biodiversity and activity of oxygen-dependant organisms (Malard & Hervant, 1999; Humphreys, 2009; Druschel et al., 2008; Mader et al., 2017; Napieralski et al., 2019).

DO concentrations in the saturated zone generally decrease with flow path length depending on the balance between transport-fluxes and reaction-consumption (Osorio-Leon et al., 2023). Since iron is the fourth most abundant element in crustal rocks, the oxidation of ferrous iron (Fe^{2+}) by oxygen is the foremost DO-consuming reaction in groundwater (Melton et al., 2014):

$$4\,Fe^{2+} + O_2 + 10\,H_2O \longrightarrow Fe(OH)_3 + 8\,H^+ \quad (1)$$

The electron transfer that operates in this reaction provides an energy source for neutrophilic iron oxidizing bacteria (FeOB) that thrive at oxic-anoxic interfaces where dissolved iron is available (Emerson et al., 2010). FeOB cultures in laboratory have shown, nonetheless, that the contribution of microbes to Equation 1 is restricted to microaerobic concentrations, i.e. $0.01 < DO[mg.L^{-1}] < 1.6$ (Druschel et al., 2008; Eggerichs et al., 2014; Maisch et al., 2019), where microbes can outcompete the abiotic kinetics of Equation 1 (Emerson et al., 2010). The activity of autotrophic microbes, such as FeOB, thus connects the oxygen and iron cycles to the primary production of biomass in the subsurface (Eggerichs et al., 2014), which can represent a major sink in the global carbon cycle (Overholt et al., 2022). However, the extent at which DO actually contributes to the production of deep subsurface biomass is poorly understood, particularly because the DO uptake within abiotic and microbe-mediated reactions is not well constrained.

To overcome these limitations, we investigate the potential of the isotopic composition of DO as a tracer to differentiate between abiotic and microbe-mediated consumption of DO. Indeed, the coupled study of DO concentrations and stable isotope $^{18}O/^{16}O$ ratios (i.e. $\delta^{18}O$) has proven useful to decrypt DO sources and sinks in a diversity of aquatic environments, e.g. Mader et al. (2017); Dordoni et al. (2022). Considering atmospheric molecular oxygen as the main source for DO in water, air-equilibrated water presents an initial isotopic composition with a $\delta^{18}O_{DO}$ value around +24.6‰ (Mader et al., 2017) with respect to the Standard Mean Ocean Water standard (VSMOW) (Barkan & Luz, 2005). $\delta^{18}O_{DO}$ values can be then affected by different reactive and physical processes with characteristic enrichment factors (ε), such as photosynthesis (Guy et al., 1993), microbial respiration (Taylor et al., 1984), oxidation of anions (Oba & Poulson, 2009a, 2009b), gas-liquid diffusive exchanges (Hendry et al., 2002), mixing between compartments (Druhan & Maher, 2017; Mader et al., 2018) or velocity and temperature fields (Johnson & DePaolo, 1994; Tromboni et al., 2020). Regardless of their nature and extent, reactive processes have been found to preferentially consume light isotopologues (i.e. $^{16}O^{16}O$), thus enriching the remaining DO pool in the heavier isotopologues ($^{18}O^{16}O$ and $^{17}O^{16}O$). The enrichment factor (ε) expresses the changes between an initial and a final condition by: $\varepsilon \simeq \delta^{18}O_{DO}|_{t=0} - \delta^{18}O_{DO}|_{t=t}$. Reactive processes thus result in negative ε values, indicating an enrichment in heavy isotopologues (i.e. higher $\delta^{18}O_{DO}$ as DO is consumed), and microbe-mediated processes have been reported to result in stronger (i.e. more negative) enrichment factors than their abiotic counterparts (Taylor et al., 1984). In the specific case of iron oxidation by oxygen (Equation 1), Oba and Poulson (2009b) measured abiotic enrichment factors in laboratory experiments within a range of $-7.3 < \varepsilon[‰] < -10.3$ while Pati et al. (2016) found an ϵ value of -15‰ in a similar experiment. Köhler et al. (2021) reported a $\delta^{18}O$ enrichment of DO in a field study in an iron rich spring. However the authors did not estimate the associated enrichment factor. To the best of

our knowledge, there are currently no measurements of enrichment factors of DO, either in laboratory or in the field, corresponding to the microbe-mediation of Equation 1.

While stable isotopes of oxygen have been extensively studied in surface water bodies, subsurface environments have received little attention. The few available studies that investigated $\delta^{18}O_{DO}$ in the subsurface mainly focused on the vadose zone [e.g. Hendry et al. (2002); Wassenaar and Hendry (2007)] or on very shallow boreholes ranging from 3 to 6 meters depth (Smith et al., 2011; Parker et al., 2014; Mader et al., 2018). While the expected negative correlation between DO concentrations and $\delta^{18}O_{DO}$ values was found by Wassenaar and Hendry (2007) and Révész et al. (1999), an unexpected isotopic depletion has been detected in most of the subsurface studies (Wassenaar & Hendry, 2007; Smith et al., 2011; Parker et al., 2014; Mader et al., 2018; Köhler et al., 2021). Several processes have been hypothesized to explain these isotopic anomalies, including the splitting of water molecules by radiolysis [e.g. Gutsalo (1971)], isotopic exchanges between water and DO molecules [e.g. Urey and Greiff (1935)], radial oxygen loss of plant roots (Armostrong & Armstrong, 2005) and diffusive exchanges at the water table interface (Wassenaar & Hendry, 2007; Smith et al., 2011; Mader et al., 2018). This latter hypothesis has received the most attention, but further work in groundwater environments is needed to better constrain the unexpected isotopic depletion of DO reported in these works.

In this study, we investigate the potential of stable isotopes of DO to trace sources and sinks of DO in the continental subsurface. For this, we performed a multi-tracer study in a French fractured-bedrock aquifer where boreholes cover depths up to 150 meters below surface. We first identify the main groundwater flow paths in the aquifer and their links with the main geological structures in the catchment. The use of hydrochemical tracers allows us to identify groundwater end-members in the aquifer and to relate groundwater composition to residence time in the aquifer. In a second part, we use $\delta^{18}O$ data to show that DO concentrations in recharge and discharge zones of the catchment obey to different controlling processes.

2 Materials and methods

2.1 Study Site presentation

The Guidel catchment is an integral part of the Ploemeur Critical Zone Observatory (CZO), which belongs to the H+ hydrogeological network (`http://hplus.ore.fr/en/`), the French research infrastructure OZCAR (`https://www.ozcar-ri.org/fr/` and the e-LTER european infrastructure (`https://deims.org/731f3ced-148d-4eb5-aa46-870fa22be713`). The Guidel catchment is located in the southern part of the Armorican massif in Brittany, France. The Armorican massif is a crystalline massif formed during the Hercynian orogeny. Within the CZO, there is a presence of a granitic pluton that outcrops in the southwest part of the catchment, intruding into a micaschist-paragneiss massif (Figure 1). The contact zone between the Late Hercynian granite body and the surrounding micaschist rock is a significant geological feature gently dipping around 30^{o} towards the North (Touchard, 1999) and acting as a major transmissive structure (see Figure 1-B). Furthermore, the Guidel catchment is intersected by two dextral-slip normal faults that strike at North 20^{o} and dip to the east (N20E) (Ruelleu, 2010; Béchennec et al., 2012b).

The Guidel catchment is an agricultural catchment under a natural flow regime, which is monitored by 25 wells drilled in 2009. In this catchment, groundwater flows converge as depicted by the water table shown in Figure 1. An important microbial activity in the aquifer has been revealed, with the formation of microbial mats at the intersection of deep fractures. The microbial communities are dominated by iron-oxidizing bacteria (FeOB) that derive their energy from the oxidation of iron (Bethencourt et al.,

2020; Bochet et al., 2020). In this catchment, DO is thus a crucial reactant for the deep subsurface ecosystem.

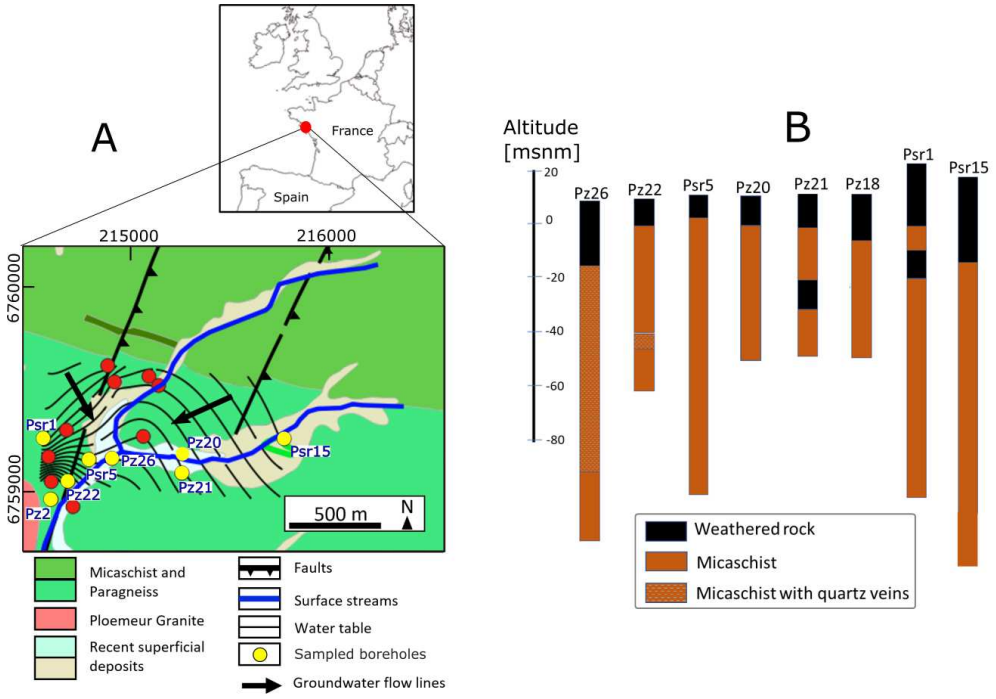

Figure 1. Geographical location, geological and hydrogeolocical maps of Guidel catchment. Geological map corresponds to (Béchennec et al., 2012b)

2.2 Sampling and analysis

2.2.1 Physico-chemical data: in-situ measurements

Multiparameter borehole logs under ambient conditions (dissolved O_2, temperature, electrical conductivity and pH) have been acquired since 2009, and available in the database of the French network of hydrogeological research sites (`https://hplus.ore.fr/en/`). This dataset was completed with two additional field campaigns at two different times of the hydrologic year: high-groundwater-level season (late fall 2022) and low groundwater-level season (late spring 2021) using an Idronaut Ocean Seven multiparameter probe (resolution $\pm$ 0.01 $mg.L^{-1}$). The instrument was calibrated following the manufacturer's specification and the accuracy of the DO probe was crosschecked by gas chromatography analyses at the University of Rennes. Borehole logs were averaged in a range of 2 m above and below the depth of the dominant fracture in the well identified in a previous study (Osorio-Leon et al., 2023).

2.2.2 Hydrochemical data: ex-situ analyses

Groundwater sampling consisted in descending a submersible MP1 pump (Grundfos) to the depth of the dominant fracture in the borehole (see Figure 2-A). Physicochemical parameters in the pump discharge were monitored with a WTW probe. Groundwater was sampled after the monitored parameters were stable.

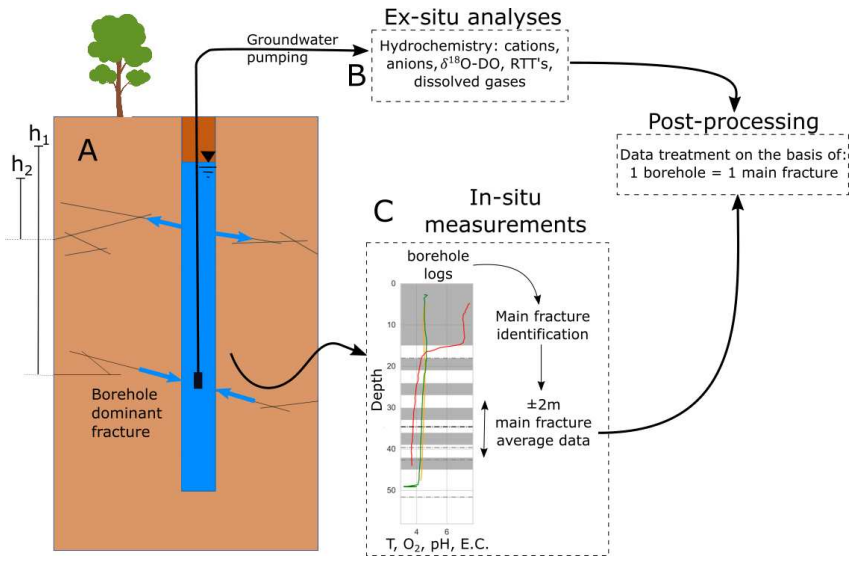

Figure 2. Workflow for the hydrochemical characterization. (A) Groundwater was sampled by pumping in the dominant fracture of every borehole and (B) was analyzed in multiple ex-situ analyses. (C) *In-situ* measurements consisted of multiparameter borehole logs. Borehole logs were poorly dependent of the depth within the borehole, showing that the signal of the dominant fracture is propagated in the water column because of groundwater flowing from the dominant fracture to the low-head fractures (h2 in the borehole sketch). Borehole logs were then reduced to an average value in a range of $\pm 2m$ around the dominant fracture.

Major and trace cations were quantified by Inductively Coupled Plasma Mass Spectroscopy (Agilent Technologies, 7700x) in pre-acidified and 0.2 μm-filtered samples. Uncertainties were between 2 to 5%. Major anion samples (non-acidified) were analyzed by Ionic Chromatography (Dionex DX-120) with uncertainties below 4%. Dissolved Iron concentrations were determined using the 1,10-Phenanthroline colorimetric method (Fortune & Mellon, 1938). Samples for noble and reactive dissolved gases were collected in glass bottles, isolated from the atmosphere, and analyzed after head-space extraction by Gas Chromatography with a thermal conductivity detector (μGC/TCD) in the 24h after sampling, following the method of (Sugisaki & Taki, 1987). Analytical precision is under 5%. Residence Time Tracers (RTT) CFC-11, CFC-12 and CFC-113 were sampled in steel ampoules and analyzed by the Purge & Trap method, using a Gas Chromatograph with an electron capture detector. Uncertainties were within 3% (Ayraud et al., 2008).

Water samples for RTT ^{36}Cl analyses were 0.2 μm-filtered, stored in acid-washed plastic bottles and then analyzed by Accelerator Mass Spectroscopy at the French AMS National facility, ASTER at CEREGE (Arnold et al., 2010). Chloride from samples was extracted by precipitation and purification of $AgCl$. After drying, precipitates were pressed in 6.6 mm diameter Ni-target holders. Measured $^{36}Cl/Cl$ ratios were corrected from the blanks and total uncertainties, including internal errors and external reproducibility were 18% on average (Bouchez et al., 2015).

Samples for analyses of the isotopic composition of dissolved O_2 ($\delta^{18}O_{DO}$) consisted of groundwater pre-filtered with 0.45 μm nylon syringe filters (Sartorius^{TM}) and stored in pre-poisoned 12 mL vials (LABCO LTD. Exetainer^{TM}) containing 20 μL of a super-saturated mercuric chloride ($HgCl_2$) solution in order to prevent microbial consumption. Triplicate samples were stored in the dark at 4°C and sent for analysis at GeoZentrum

Nordbayern where they were analyzed within one week by GC-IRMS (Barth et al., 2004). Isotope values are reported using the standard δ-notation versus the Vienna Standard Mean Ocean Water (VSMOW) standard:

$$\delta[‰] = \left(\frac{R_{sample}}{R_{standard}} - 1 \right) \times 1000 \quad (2)$$

where R corresponds to $^{18}O/^{16}O$ isotopic ratios of dissolved O_2. Standard deviations (1σ) were less than 0.1 ‰.

2.3 Groundwater age estimations

Different RTTs were measured in order to estimate the apparent age of groundwater: ^{4}He, CFC-11, CFC-12, CFC-113 and ^{36}Cl. The different measured tracers are complementary. ^{4}He is produced by α decay in rocks, it accumulates in groundwater, and is particularly accurate to date groundwater older than 50 years (Suckow, 2014). The other tracers, whose atmospheric concentrations were artificially increased by processes such as industrial emissions (CFC-11, CFC-12, CFC-113) or nuclear bomb tests (^{36}Cl), allow to investigate groundwater ages below 70 years (Sprenger et al., 2019).

2.4 Isotope fractionation modeling

Groundwater can be considered as a closed system with respect to dissolved O_2, whose isotopic composition can be modeled by a classic Rayleigh model:

$$R = R_0 f^{\alpha - 1} \quad (3)$$

where R and R_0 are respectively, the instantaneous and the initial $^{18}O^{16}O/^{16}O^{16}O$ (from now on written $^{18}O/^{16}O$ for simplicity) isotopic ratios of dissolved O_2, f is the remaining molar fraction of DO in groundwater and α is the *intrinsic* fractionation factor (i.e. the fractionation factor measured in batch experiments). Values of $\alpha < 1$ indicate an isotopic enrichment of DO (i.e. higher $^{18}O/^{16}O$ values as DO concentration decreases) whereas $\alpha > 1$ indicate isotopic depletion (i.e. lower $^{18}O/^{16}O$ with decreasing DO concentrations). The fractionation factor (α) is related to the enrichment factor (ε) by the following expression:

$$\varepsilon[‰] = (\alpha - 1) \times 1000 \quad (4)$$

At the scale of investigation of this study (i.e. catchment scale), transport processes like fluid mixing or dispersion can impact the observed isotope partitioning. As a result, α estimates from Equation 6 correspond to an apparent fractionation factor (α_{eff}) that usually underestimates the intrinsic value of α (Abe & Hunkeler, 2006; Green et al., 2010; Van Breukelen & Rolle, 2012). A recent model has been developed to overcome this limitation, that accounts for dispersion-based mixing in the catchment (Druhan & Maher, 2017):

$$R = \frac{R_0}{\alpha + f(1 - \alpha)} \quad (5)$$

This modified expression incorporates mixing effects in the catchment by considering an exponential transit time distribution, while keeping the intrinsic fractionation factor (α). Therefore, it is possible to compare the α obtained by fitting Equation 7 with intrinsic values published in the literature.

Since the isotope data measured on field samples is reported in $\delta^{18}O_{DO}$ values, both equations 6 and 7 have been modified considering the δ-notation. Thus, the classic Rayleigh

model in δ-notation corresponds to:

$$\frac{\delta + 1000}{\delta_0 + 1000} = f^{\alpha - 1} \tag{6}$$

while the modified Rayleigh model in δ-notation reduces to:

$$\frac{\delta + 1000}{\delta_0 + 1000} = \frac{1}{\alpha + f(1 - \alpha)} \tag{7}$$

3 Results

3.1 Upwelling and downwelling flows in the catchment

Based on the local geothermal gradient, the analysis of temperature profiles (Figure 3-A) allows the identification of upwelling and downwelling flows in the catchment from recharge and discharge-zone boreholes. Dissolved O_2 concentrations were used to classify by recharge (DO $> 1 mg.L^{-1}$) and discharge (DO $< 1\ mg.L^{-1}$) zone boreholes. Most of the samples located in the recharge zone are characterized by downward flows, i.e. the measured temperature (T_{log}) is cooler than the geothermal gradient (T_{GG}), while samples in the discharge zone are characterized by upward flows, i.e. $T_{log} > T_{GG}$. A more detailed view of the temperature logs (figures 3-B and C) allows to distinguish different flow paths in the catchment. Recharge boreholes (characterized by downward flows) are globally homogeneous, with a water-column temperature that remains nearly constant around 13.6 °C. Borehole Psr15 is an exception to this: temperature profiles follow the geothermal gradient indicating poor circulation in the water column. Moreover, Psr15 follows a geothermal gradient that is cooler than in the other boreholes. On the other hand, discharge boreholes (characterized by upward flows) present a sparser temperature distribution, where two main groups can be distinguished. First, a deep and hot group, including boreholes Pz26 and Psr5, that align in a same gradient indicating a common origin from fractures deeper than 100 m. Second, a shallower group composed by Pz2, Pz20 and Pz22 in which the temperatures are closer to the geothermal gradient and sparse between $\pm 1°C$, indicating flow paths of variable depths.

3.2 Hydrochemical evolution in flow paths

Table 1 synthesizes average values of the geochemical tracers measured in groundwater of the Guidel catchment. The measurements indicate circumneutral to acid conditions with electrical conductivity ranging from 300 to 800 $\mu S.cm^{-1}$ and temperatures ranging from 12.5 to 16 $°C$. DO values range between 9.73 and 0.04 $mg.L^{-1}$ indicating both oxic and anoxic groundwater.

To derive a catchment-scale understanding of the evolution of the groundwater chemistry, a synthetic transect of the aquifer is built by ordering the boreholes according to their hydraulic head (Figure 4: high hydraulic heads in the left and low hydraulic heads in the right). This graphical representations highlights the general direction of flowpaths and the associated geochemical evolution. Groundwater in recharge zones is oxidizing, with high concentrations of electron acceptors like DO and NO_3^-. These concentrations progressively decrease as groundwater moves towards the discharge area, where the groundwater is reducing. This trend aligns with an increase in groundwater residence time, as indicated by a decrease in CFC113 concentrations. The reducing discharge zone is characterized by increasing temperatures and electrical conductivities (E.C.). Moderate yet statistically significant contrasts in E.C. exist between recharge and discharge zones, with the latter showing higher E.C. values. For instance, E.C. values in Guidel are 422±35 $\mu S.cm^{-1}$ in recharge and 505±64 $\mu S.cm^{-1}$ in discharge zones (with a t-test p-value = 0.01). The increase in E.C. indicates that the TDS of groundwater increases along the flow paths as a consequence of mineral dissolution reactions. The increase in Mg and Fe concentrations suggests mica dissolution (i.e. biotite, chlorite or muscovite).

Table 1. Averaged multiparameter logs in a range of 2m above and below the main fracture for every borehole. Values correspond to averages within 1σ except for isotope data that present averages within 2σ. Data corresponds to the period 20016-2022. MF Depth indicates the depth of the Main Fracture. RW corresponds to rainwater, *bdl* indicates measures below detection limits and [-] indicates not measured.

	Location		Recharge				Discharge			
	BH		RW	Psr1	Psr15	Pz18	Pz21	Psr5	Pz2	Pz20	Pz26
	MF Depth	[m to ref]		45	45	34.6	34.6	97.6	28	38	94
	Zref	[msnm]		22.9	18.1	16.2	12.1	11.7	9.5	10.6	9.1
From logs	T	[C]		13.5	12.9	13.6	13.3	15.4	13.3	14.0	15.5
	DO	$[mg.L^{-1}]$		5.3	5.6	2.2	4.1	0.04	0.10	0.06	0.49
	E.C.	$[\mu S.cm^{-1}]$		425	621	424	356	806	720	334	485
	pH	[-]		5.9	6.8	7.4	6.2	6.2	6.5	6.7	6.8
From sampling in Main Fracture	CFC12	[pptv]		473	436	266	245	57.7	20.4	50.5	79.2
	CFC11	[pptv]		161	207	114	121	9.1	14.2	8.8	20.0
	CFC113	[pptv]		39.3	60.0	40.7	42.2	9.3	7.1	4.5	17.4
	$^{36}Cl/Cl$	$[at.at^{-1}] \times 10^{-15}$		50.0	72.4	29.2	36.4	29.2	3.3	42.0	25.2
	$\delta^{18}O_{DO}$	[‰]	24.85	20.2	22.0	18.1	-	25.3	-	24.4	23.8[a]; 23.9[b]
	He	[M] $\times 10^{-8}$		0.41	0.34	0.55	0.47	1.38	1.92	0.67	1.52
	Ne	[M] $\times 10^{-8}$		1.21	1.38	1.45	1.63	1.28	1.21	1.37	1.30
	Ar	[M] $\times 10^{-5}$		1.75	1.80	2.20	2.13	1.75	1.81	1.89	1.97
	N_2	[M] $\times 10^{-4}$		7.56	7.78	9.91	10.2	9.60	9.08	9.64	9.73
	CO_2	[M] $\times 10^{-4}$		4.81	5.16	1.87	3.93	3.53	1.60	6.24	7.73
	Cl	[ppm]	10	70.0	66.0	62.6	76.2	89.4	96.8	66.3	100.5
	NO_3	[ppm]	*bdl*	39.4	48.9	19.6	27.0	1.1	1.1	1.2	1.2
	SO_4	[ppm]	2	28.1	15.4	27.1	28.7	41.4	42.1	33.7	39.7
	Br	[ppm]$\times 10^{-1}$	*bdl*	3.08	2.48	2.01	2.77	3.71	5.32	3.17	4.04
	F	[ppm]$\times 10^{-2}$	*bdl*	8.02	6.97	18.17	9.50	19.0	22.3	22.4	22.6
	Li	[ppm]$\times 10^{-2}$		3.27	3.14	5.15	3.25	3.35	5.80	5.22	4.17
	Na	[ppm]		47.0	45.1	45.1	50.7	41.5	51.1	44.5	47.5
	Mg	[ppm]		13.1	16.1	18.8	13.3	20.8	16.0	15.2	19.9
	Al	[ppm]$\times 10^{-3}$		2.36	1.56	2.07	2.90	1.28	1.44	0.69	1.12
	K	[ppm]		3.7	4.2	4.2	3.5	4.1	3.8	3.7	4.4
	Ca	[ppm]		10.0	18.7	21.0	11.4	25.7	15.8	13.0	23.1
	Mn	[ppm]$\times 10^{-2}$		0.23	0.53	1.74	1.95	35.6	74.9	26.9	62.0
	Fe	[ppm]$\times 10^{-2}$		1.77	13.0	0.75	17.7	264	274	176	475
	Sr	[ppm]$\times 10^{-2}$		6.65	8.33	9.31	7.43	9.59	13.7	9.93	13.0
	DOC	[M] $\times 10^{-2}$		2.12	*bdl*	*bdl*	1.90	*bdl*	*bdl*	*bdl*	3.79
	TIC[c]	[M] $\times 10^{-3}$		2.27	4.66	2.29	3.22	2.04	1.50	2.12	1.59[a]; 1.80[b]
	$log[pCO_2]$[c]	[-]		-1.44	-1.16	-2.3	-1.24	-2.0	-1.91	-1.78	-1.99[a]; -1.93[b]
	H_4SiO_4	[ppm]		44.1	45.9	43.2	37.7	44.0	51.6	51.8	46.0[a]; 45.2[b]

[a]: values for fracture at -47m below reference (f47)
[b]: values for fracture at -54m below reference (f54)
[c]: values calculated in PHREEQC by using HCO_3^- to ensure water charge balance

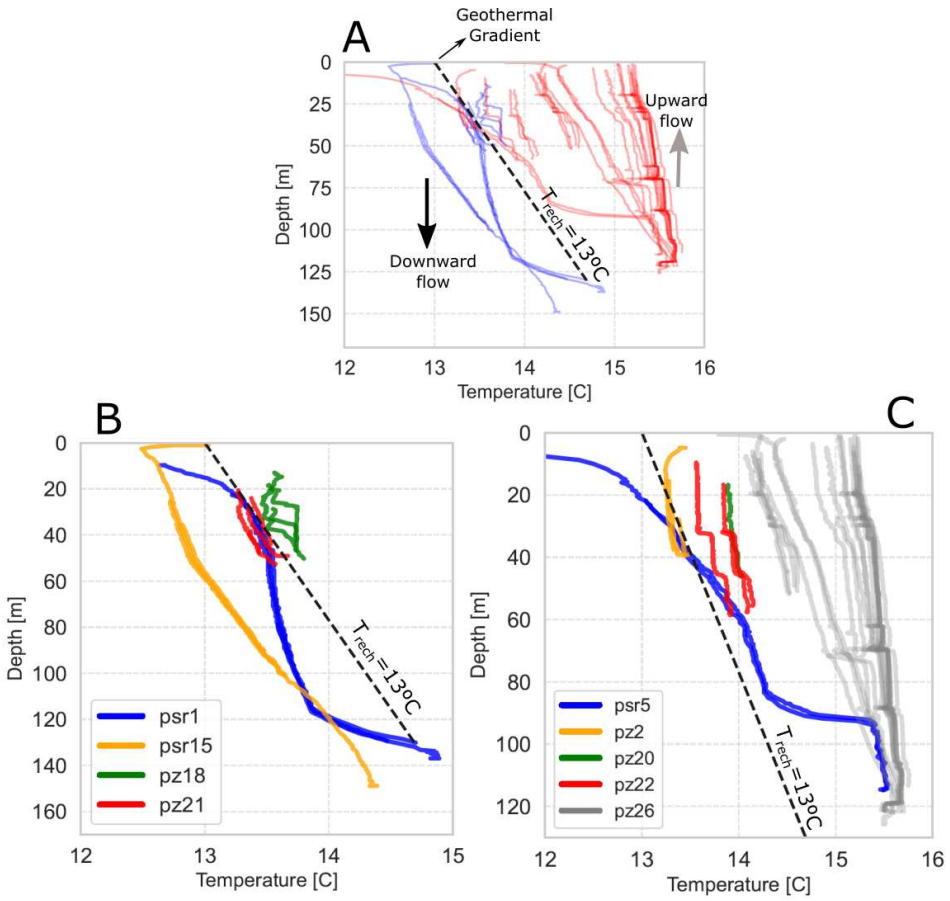

Figure 3. Use of temperature to characterize vertical flows in Boreholes.(A) Comparison of temperature profiles from recharge and discharge-zone boreholes. The geothermal gradient is determined from profiles that are not perturbed by vertical borehole flows (Klepikova et al., 2011) and is represented by considering a recharge temperature of 13 °C determined by a Noble Gas Temperature analysis (see supplementary information). (B) and (C) present the detail of temperature logs for, respectively, the recharge and discharge-zone boreholes. Different logs for a same borehole correspond to different dates for the period 2009 - 2022.

A Principal Component Analysis (PCA) was carried on a dataset containing 21 measured parameters of 9 selected boreholes covering recharge and discharge zones in both catchments. The first principal component (PC1) accounts for 82.6 % of the explained variance and represents young vs old groundwater. Indeed, PC1 strongly correlates with electron acceptors such as DO and NO_3 and RTTs which are present in young groundwater such as CFCs, $\delta^{18}O-H_2O$ and ^{36}Cl. Likewise, PC1 anticorrelates with proxies of old groundwater such as total dissolved solids content (e.g. anions, cations, E.C.), helium and temperature. Boreholes from the recharge zone plot on positive values of PC1 while boreholes from discharge zone plot on the opposite side. The second principal component (PC2) accounts for 17 % of the explained variance. It correlates with Na, Li and He and anticorrelates with T, Mg, Ca and K. Thus, negative values of PC2 indicate a stronger influence of plagioclase (related to Ca and K) and mica (related to K and Mg) dissolution. The third principal component accounts for 7.9 % of the variance and is not

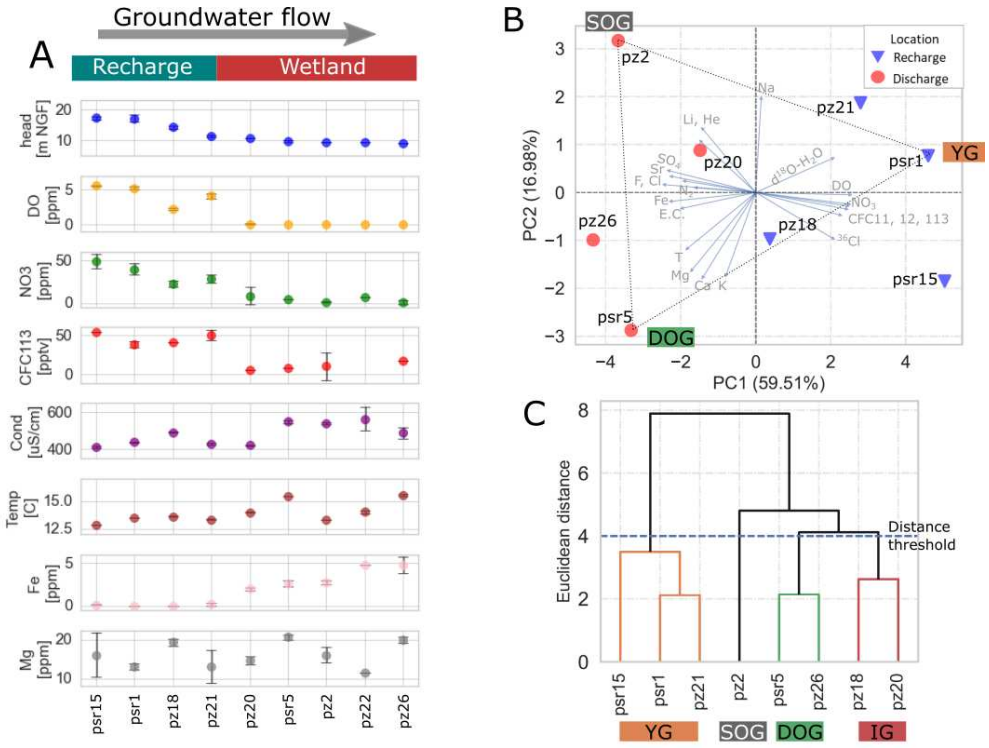

Figure 4. Main fracture's Physico-Chemical transects (A) and end-member analyses (B and C). Points correspond to historical average values for the period 2016 to 2022 reported in Table 1. (B): multi-tracer PCA showing the hydrochemical signatures of boreholes from recharge and discharge zones in the catchment. (C): Hierarchical Clustering Analysis (HCA) showing the hydrochemical similarity of the boreholes in terms of their euclidean distance in the PCA space of plot subplot B. Borehole groups correspond to YG: young group, RG: regional group, LG: local group, IG: intermediate group,

shown. On the basis of the euclidean distance on the PCA space, Hierarchichal Clustering (HCA) allows to classify individuals into a small number of groundwater groups. A *young* group (YG: Psr15, Psr1 and Pz21), a *deep-old* group (DOG: Psr5 and Pz26), a *shallow-old* group (SOG: Pz2) and an *intermediate* group (IG: Pz18 and Pz20). Borehole Pz2 is a particular case: according to PC1, it globally belongs to the old group (OG) but it has a contrasted PC2 signature compared with Pz26 and Psr5.

3.3 Groundwater apparent age estimation

Figure 5 presents the measured concentrations of RTTs in the boreholes. CFC11 values range between 200 and 8 pptv and CFC113 values range between 60 and 5 pptv. ^{36}Cl ranges between 8 and 0.3×10^{-14} and He ranges from 2.5 to 0.3×10^{-8} M. This RTTs dataset is coherent as recharge boreholes have high CFCs and high ^{36}Cl, indicating a recharge after the 1960s, which is consistent with their low He levels. Discharge boreholes have low ^{36}Cl and low CFCs, indicating recharge prior to the 1960s, and consistently higher He concentrations. In all cases, Psr15 is the borehole with the highest concentrations and therefore, with the most recent groundwater. CFC113 concentrations exhibit no discernible variations among the remaining recharge boreholes. In contrast, the concentrations of both CFC11 and ^{36}Cl align, indicating a progressive increase in age among the recharge boreholes in the following sequence: Psr15, Psr1, Pz21, and Pz18. On the other hand, boreholes from the discharge zone group together in a cluster of low values in the CFCs plot (Figure 5-A), indicating the presence of old groundwater. Similarly, the discharge boreholes exhibit diminished levels of ^{36}Cl (Figure 5-B). Helium concentrations, which provide a more reliable estimation of the age of old groundwater, demonstrate a gradual rise in groundwater age in the following order: Pz20, Psr5, Pz26, and Pz2 (refer to Figure 5-B). This multi-tracer RTT analysis thus allows for the identification of the gradual rise of groundwater age in the following order : Psr15, Psr1, Pz21, Pz18, Pz20, Psr5, Pz26, and Pz2 which is in really good accordance with the synthetic transect previously described in Figure 4.

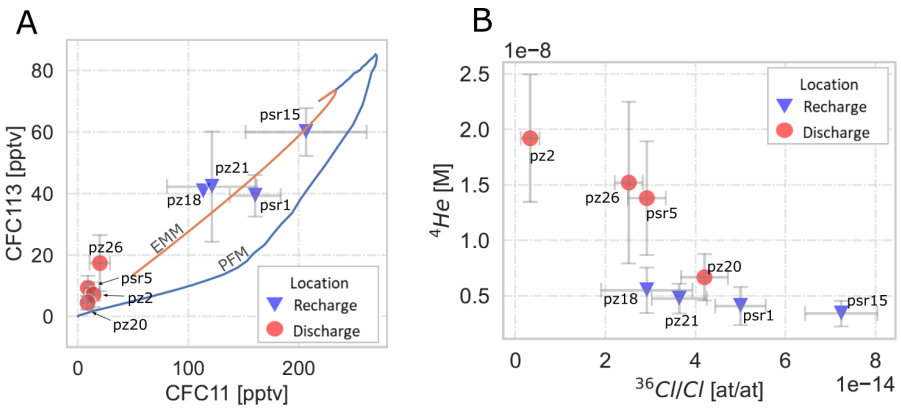

Figure 5. Concentration of residence time tracers (RRTs) corresponding to average values based on data for the period 2016-2022 with error bars within 1σ. (A): scatterplot of CFCs concentrations plotted with lumped parameter models using an exponential mixing model (EMM) and a piston flow model (PFM). (B): scatterplot of He concentrations and $^{36}Cl/Cl$ ratios.

Furthermore, apparent ages can be derived from the RTT data. Regarding the CFC data, we used Lumped Parameter Models in the TracerLPM software (Jurgens et al., 2012) and applied the exponential mixing (EMM) and the piston flow (PFM) models with a

maximum groundwater age of 150 years. For the ^4He data, we used the formulation of Trinchero et al. (2019) that accounts for the double porosity of fractured aquifer and the production of He in the matrix:

$$t_w \approx \frac{C - C_0}{G}\omega_f \quad (8)$$

Where t_w is the ^4He-based apparent age for groundwater, C and C_0 are, respectively, the ^4He concentrations in the sampled water and in the recharge. $G = 1.2{\times}10^{-10}\ mol.m^{-3}.y^{-}$ is the ^4He production rate in the rock matrix (Trinchero et al., 2014) and ω_f is the fracture volume fraction, for which an intermediate value of $1{\times}10^{-3}$ was assumed (Trinchero et al., 2019). We assume that our total He measurements correspond to ^4He which is the most abundant helium isotope.

The apparent ages of groundwater, based on the RTTs data, are presented in Table 2. Apparent ages of recharge-zone boreholes range between 30 and 40 years according to CFCs data, and between 11 and 30 years according to He data. Discharge-zone boreholes exhibit older ages ranging from 99 to 143 years. Borehole Pz20 is a particular case for which CFCs concentrations are low (indicating old groundwater) but both ^4He and ^{36}Cl concentrations are intermediate, which could indicate important mixing in the borehole.

Table 2. Apparent groundwater ages calculated based on different residence time tracers (RTTs). CFC-based ages are computed on the basis of a piston flow model (PFM)

Location	BH	CFC12	CFC11	CFC113	Average-CFC	He
	[y]	[y]	[y]	[y]	[y]	
Recharge	Psr1	29 (3,4)	40 (1)	35 (2,5)	35 (7.4)	17 (14)
Recharge	Psr15	31 (4,8)	34 (2,8)	31 (4,2)	32 (11.9)	11 (10)
Recharge	Pz21	43 (0,4)	44 (3,3)	34 (3,2)	40 (7.2)	23 (11)
Recharge	Pz18		42 (0,1)	44 (3,4)	43 (3.4)	29 (17)
Discharge	Pz20					39 (17)
Discharge	Psr5					99 (43)
Discharge	Pz26					110 (61)
Discharge	Pz2					143 (48)

3.4 Dissolved O_2 depletion in the aquifer

Due to the close similarities in physical properties between Argon and Oxygen (similar Henry constant and diffusion coefficients), Argon can be used as a conservative tracer for the physical behavior of oxygen (Craig & Hayward, 1987) and we thus normalized DO to Ar. Hence, if the DO/Ar ratio remains constant while DO concentrations decrease, it indicates a dispersion-induced dilution. Here, we observe that the DO/Ar ratio diminished together with DO, which indicates a consumption of DO along the flowpath (Figure 6-A).

The isotopic composition of dissolved O_2 is presented as a function of DO concentrations and show two opposite trends (Figure 6-B). At high DO concentrations, in recharge-zone groundwater, the $\delta^{18}O_{DO}$ decreases with decreasing DO concentrations, i.e. the isotopic composition of DO becomes lighter. Considering $\delta^{18}O_{DO}$ in rainwater as the input isotopic signature to the system, $\delta^{18}O_{DO}$ values start at +24.85 ‰ (close to the expected atmospheric equilibration value of +24.6 ‰) and decrease down to +18.10 ‰ in borehole Pz18. At low DO concentrations ($< 1.6\ mg.L^{-1}$) in the discharge-zone groundwater, the $\delta^{18}O_{DO}$ trend reverses: DO becomes isotopically heavier when DO is consumed, reaching $\delta^{18}O_{DO}$ values as high as +25.33 ‰ in Psr5. Dissolved iron concentrations are also distinctive of these two trends: dissolved iron is limited when DO concentrations

are high and iron concentrations reach values around 2.5 $mg.L^{-1}$ when DO concentrations are within the microaerobic range (see Figure 6), i.e. the oxygen range at which iron-oxidizing bacteria (FeOB) have been reported to thrive (Druschel et al., 2008; Eggerichs et al., 2014; Maisch et al., 2019). We have fitted the data with the two Rayleigh models presented in equations 6 (classic model) and 7 (modified model) and the associated fractionation factors (α) were calibrated using a non-linear least squares solver. We have divided the fitting procedure in two parts to account for the different isotope trends observed for C_{DO} values above and below 1.5 $mg.L^{-1}$. Based on Figure 6, it appears that the traditional Rayleigh model fails to accurately represent the observed trends in the field data. In contrast, the modified Rayleigh model allows to accurately represent the observed field trends. The coefficient of determination (R^2) from the model fitting is 0.99 for the case $C_{DO} > 1.6$ $mg.L^{-1}$ and 0.93 when $C_{DO} < 1.6$ $mg.L^{-1}$.

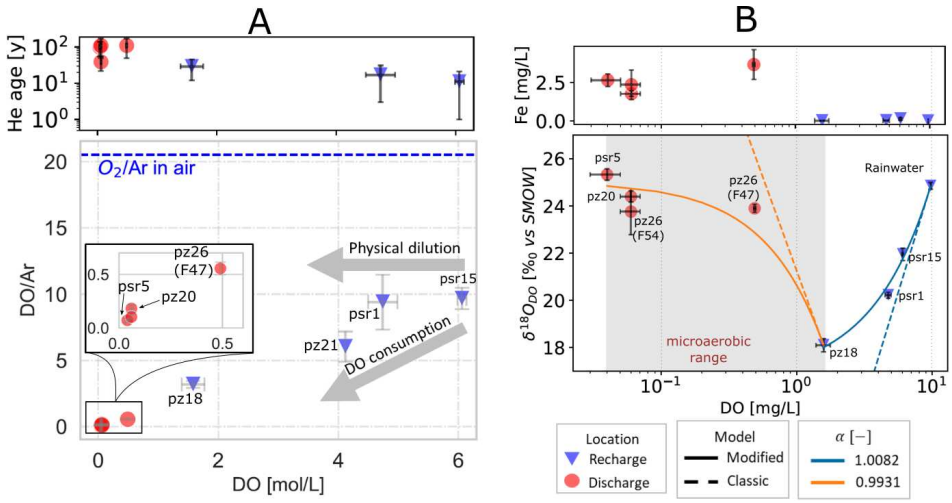

Figure 6. Dissolved O_2 (DO) depletion in the aquifer. (A) decreasing DO:Ar ratios as a function of DO concentration show that DO is being effectively consumed by reactive processes. The blue dashed line indicates the O_2/Ar ratio in air, that is representative of the rainwater signature. (B) DO isotope composition ($\delta^{18}O_{DO}$) and dissolved iron (Fe^{2+}) as a function of the DO concentration. Values correspond to averages of triplicate measurements with error bars within 1σ. The gray shaded zone corresponds to the limits of the *microaerobic* zone in which iron oxidizing bacteria (FeOB) develop optimally (Druschel et al., 2008; Maisch et al., 2019). Dashed and continuous lines represent, respectively, the *classic* Rayleigh model (Equation 6) and the *modified* model to account for mixing processes (Equation 7). The models are presented with the best fitting α parameters as determined by fitting the modified model to the data.

4 Discussion

4.1 Identification and distribution of groundwater flow paths in the catchment

The use of temperature logs to identify upwelling and downwelling flows in the catchment (Figure 3) provides insights into the behavior of boreholes in the area. These groups of boreholes reveal a compartmentalization of flow paths that can be related to geological structures in the catchment as illustrated in Figure 7. In the recharge zone, most boreholes exhibit similar temperatures, except for Psr15, which displays a negative tem-

perature anomaly. This low temperature along with the presence of a small wetland near Psr15, the high water table in this borehole and its young apparent age (refer to Table 2) are indicators of a low horizontal transmissivity in the eastern fault that may lead to a short flow path. Groundwater from the discharge zone divide into a deeper old group (DOG, composed by Psr5 and Pz26) and a shallower old group (SOG, composed by Pz2 and Pz22). The large temperature differences of the two old groups (DOG et SOG) indicate flow paths of different depths. DOG originate from at least 100 m deeper than SOG and therefore could be part of a larger circulation flow cell, potentially related to the regional highly transmissive contact zone between the granite pluton and the micas-chist (Figure 7). Indeed, this lithological contact has been identified as a pathway for regional flow paths in the neighboring catchment of Kermadoye (Ruelleu, 2010), that is just 4 km away. Even if none of the boreholes from Guidel reaches the lithological contact, the subvertical faults in the catchment can serve as a drain for the deep regional flow paths (Bense et al., 2013; Roques et al., 2014).

According to the apparent groundwater ages (Table 2) and the temperature logs (Figure 3), groundwater apparent age is not necessarily correlated with temperature for the discharge boreholes. Indeed, groundwater temperature can be used as a proxy for the flow path depth [e.g. Chatelier et al. (2011)]. Provided similar groundwater velocities in the flow paths, higher temperatures should correspond to deeper flows and therefore, to longer residence times. In the case of the SOG group, the lower temperatures are related to the longer apparent ages, which suggests that these boreholes are probably related to low groundwater velocities and shallow subhorizontal structures. The link of the SOG group with different structures could also explain the different signature of Pz2 in the PCA space (Figure 4-B). Future efforts on groundwater modeling at the catchment scale could be helpful to support the interpretation of Figure 7.

4.2 The Guidel catchment as a biogeochemical reactor

The different hydrochemical signatures observed in the end-member analysis (see Figure 4) support the compartmentalization of flow paths presented above. Boreholes from old end-members [shallow (SOG) and deep (DOG) groups] have contrasted hydrochemical signatures compared with the young end-member (YG in Figure 4-B and C). Based on the variables that correlate with the principal components in Figure 4-B, the distinct hydrochemical signatures of end-members are generally related to groundwater residence time and the accumulation of solutes coming from the dissolution of minerals. Indeed, although flow paths in the catchment are compartmentalized in relation with the geological structures, their hydrochemical signatures can be explained by considering the same underlying weathering reactions (biotite dissolution and Fe^{2+} oxidation) as shown in a former work (Osorio-Leon et al., 2023). Therefore, the catchment can be assimilated to a reactive system in which flow paths probe different advance states of the rock weathering kinetic processes, corresponding to the apparent ages reported in Table 2.

A clear change in the nature of the processes affecting DO along flowpaths is highlighted by the isotopic composition. At high DO concentrations, the consumption of DO leads towards an unexpected reverse isotope fractionation: $\delta^{18}O_{DO}$ values decrease with decreasing DO concentrations (i.e. the DO pool enriches in $^{18}O^{16}O$ as DO is depleted) instead of increasing as expected with reactive processes that preferentially consume the lighter isotopes ($^{16}O^{16}O$) (Aggarwal & Dillon, 1998; Révész et al., 1999). Similar reverse trends have been previously reported in the literature (Wassenaar & Hendry, 2007; Smith et al., 2011; Parker et al., 2014; Mader et al., 2018; Köhler et al., 2021). These previous studies were all conducted either in streams or in shallow aquifers with depths between 3 to 6 m, but our similar observations in a 40m fractured bedrock suggest that these effects may occur in shallow groundwater. Different hypotheses have been proposed to explain the isotopic depletion of DO: (1) physical processes such as the faster diffusion of the lighter isotopologue ($^{16}O^{16}O$) in the gas-liquid interface of unconfined aquifers (Smith

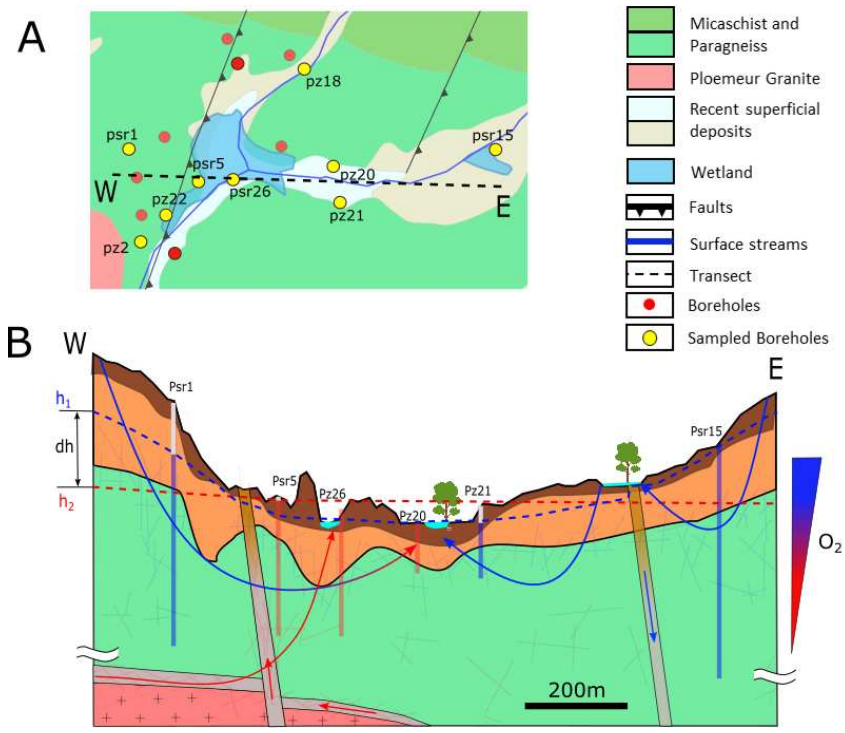

Figure 7. Flow paths in the Guidel catchment as inferred from borehole temperature logs and the hydrochemical characterization. (A): geological map of (Béchennec et al., 2012a) and localisation of the sampled boreholes and the geological transect presented in (B). Local flow paths (in blue) and regional flow paths (in red) mix in the subsurface to originate the reactive hotspots reported by Bochet et al. (2020) and Bethencourt et al. (2020). The depth scale has been arbitrarily modified for clarity.

et al., 2011; Parker et al., 2014; Mader et al., 2018; Köhler et al., 2021) or (2) chemical or biological processes such as water radiolysis [e.g. Gutsalo (1971)], isotope exchange between water and DO and radial oxygen loss from plant roots [e.g. Armostrong and Armstrong (2005)] or dark oxygen production (Rikken et al., 1996; van Ginkel et al., 1996; Ettwig et al., 2010).

While water radiolysis is restricted to depths between 2-3 km (Gutsalo, 1971) and is therefore unlikely in the shallow context of this work, the soil use and geological contexts in the Guidel catchment could favor dark oxygen production by "intra-aerobic" denitrification (Ettwig et al., 2010). Indeed, the Guidel catchment is an agricultural catchment in which shallow groundwater contains high NO_3^- concentrations (20 to 50 ppm according to Table 1). If there is any release of NO_3^--derived oxygen, it could affect $\delta^{18}O_{DO}$ values depending on the NO_3^- isotope composition. However, the "intra-aerobic" pathway relies on specific enzymes [qNORs, described by Ettwig et al. (2012)] for which the protein-coding genes have not been detected in former metagenomic surveys in the Guidel catchment (Bethencourt et al., 2020). Therefore, there is no evidence so far to support dark oxygen production in the study site.

On the other hand, ^{16}O enriched DO in unconfined aquifers has been pointed out as the most likely process in most of the studies that have found similar isotopic compositions to those measured in the recharge zone of Guidel (Smith et al., 2011; Parker et al., 2014; Mader et al., 2018; Köhler et al., 2021). Indeed, because of differences in the diffusion coefficient of O_2 isotopologues (i.e. ^{16}O diffuses faster into water than ^{18}O), DO diffuses below the water table with a light isotopic composition. Based on the Graham's law, (Mader et al., 2018) estimated a $\delta^{18}O_{DO}$ value of +10.6‰ for this "shallow water-table" end-member in which groundwater is sensitive to DO diffusion. Furthermore, a simple diffusive model proposed by (Smith et al., 2011) showed that the "light" isotopic signal diffuses over several meters on time scales of about 10^2 years.

Is the occurrence of light oxygen likely to occur the considered fractured aquifer ? The studied aquifer is a fractured bedrock overlaid with a few meters of regolith that act as an unconfined aquifer. Therefore, diffusive exchanges through the regolith could create a light-isotope "shallow water-table" end-member and groundwater from the regolith would further be mixed in the fractured zone. This hypothesis is supported by our modeling results showing that an exponential mixing model explains both RTTs distributions and the observed isotopic fractionation of DO. Such a mixing model is consistent with the role of fractures as preferential flow paths (Le Borgne et al., 2006) and the observations of fast recharge in fractures in the study site (Bochet et al., 2020). We note that for the discharge-zone boreholes, this effect is less important because they are related to other geological structures in the aquifer (Figure 7).

4.3 ^{18}O enrichment in the discharge zone

Figure 6-B shows that the change in the DO isotopic trend is correlated to boreholes with high concentrations of dissolved iron. Moreover, the coincidence of the isotopic enrichment with the microaerobic range (refer to Figure 6-B) suggests a signature of the activity of iron oxidizing bacteria that have been previously characterized at the site (Bochet et al., 2020; Bethencourt et al., 2020). Based on the best-fit fractionation factor α in Figure 6-B, our data is described by an *in-situ* enrichment factor (ε, Equation 4) of -6.9 ‰ that is in similar ranges as previous reported values for the oxidation of dissolved iron by oxygen. Indeed, Oba and Poulson (2009b) found ε values ranging between -10.3 to -7.3 ‰ for the abiotic iron oxidation at near-neutral pH. Similarly, Pati et al. (2016) reported an average ε of -15 ‰ in a similar batch experiment. The experiments of Oba and Poulson (2009b) and Pati et al. (2016) are restricted to the abiotic oxidation of iron by oxygen, but this reaction is usually catalyzed by iron oxidizing bacteria [e.g. Emerson et al. (2010)]. Furthermore, it has been shown that microbe-mediated

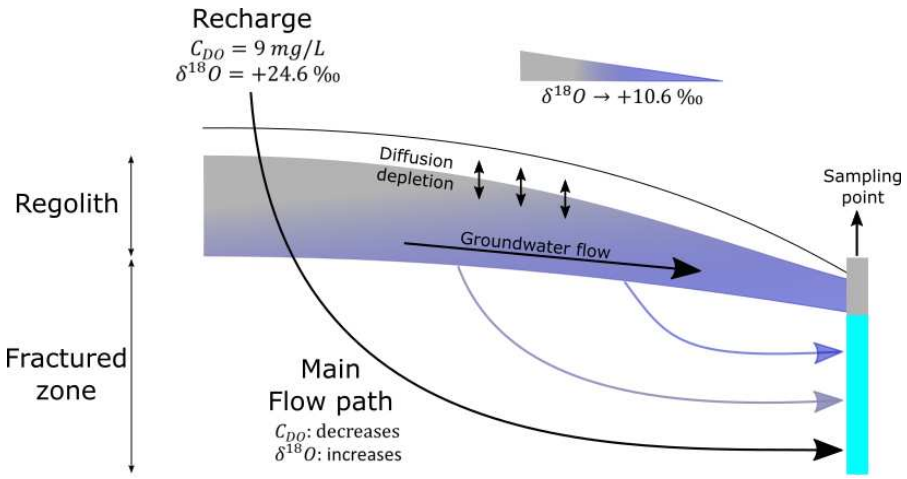

Figure 8. Conceptualization of the exponential mixing model between fracture flow paths and the $\delta^{18}O_{DO}$ depleted end-member in the regolith.

reactions lead to stronger isotopic fractionations (i.e. even more negative ε values) compared to abiotic processes (Taylor et al., 1984). Under natural conditions, where biogeochemical reactivity falls into the continuum between microbe-mediated and abiotic processes, the overall isotopic fractionation should thus be even stronger than the one reported by Oba and Poulson (2009b) and Pati et al. (2016). Nevertheless, the ε value found in our case study suggests that the DO-isotopic fractionation observed in the Guidel catchment is lower than the abiotic values of Oba and Poulson (2009b) and Pati et al. (2016).

The lab-field discrepancy in the enrichment factor suggests that the laboratory-determine ε values may not be directly transposed to field conditions. For instance, other than mixing effects (Druhan & Maher, 2017), velocity and temperature fields can also affect isotopic fractionation (Johnson & DePaolo, 1994; Tromboni et al., 2020), resulting in *effective* enrichment factors which are less negative than those determined under laboratory conditions. In fractured-bedrock aquifers these effects are therefore expected since the multi-scale heterogeneity of fracture networks enhances dispersion processes (Martinez-Landa et al., 2012) and flow path mixing (Bochet et al., 2020). Moreover, in natural aquifers microbial communities are complex (Anantharaman et al., 2016) and the effect of their interactions on isotopic compositions have not yet been assessed. Overall, the fractionation factor α determined in Figure 6-B corresponds to an effective fractionation factor that integrates reactive and transport processes.

5 Conclusions

In this study, we investigated the use of dissolved oxygen isotopes as a tracer of biotic and abiotic processes in the subsurface, based on a field case study in a fractured-rock aquifer. We used borehole temperature logs and hydrochemical measurements to identify different groundwater flow paths in the aquifer. The transmissivity of faults favors mixing between iron and O_2-rich groundwater flow paths which sustain previously reported iron-oxidizing microbial hotspots. Dissolved oxygen (DO) concentrations are highly correlated with groundwater apparent age.

The isotopic composition of DO provided further information about the processes controlling the DO concentrations in the catchment. At high DO concentrations (DO $> 1.6\ mg.L^{-1}$), we observed a decreasing trend in $\delta^{18}O_{DO}$ values with groundwater age,

similar to trends reported in shallow groundwater contexts (3 to 6m depth). We observed this trend in fractures as deep as 40m, suggesting that this depleted isotopic signature of DO is more widespread than previously expected. We hypothesize that mixing with $\delta^{18}O_{DO}$ depleted groundwater from the regolith compartment leads to this isotopic signal in the recharge zone. In contrast, the isotopic signatures was different in zones where DO concentrations were within the microaerobic range (DO $< 1.6\ mg.L^{-1}$), characterized by higher Fe^{2+} concentrations and microbial hot-spots. We observed an isotopic enrichment of DO consistent with the activity of iron oxidizing bacteria. However, the apparent enrichment factor (ε) that better describes our data is slightly lower than values reported from laboratory experiments. We attribute this lab-field discrepancy to extrinsic factors related to heterogeneity in natural environments that can lead to lower effective enrichment factors.

To the best of our knowledge, this study is the first to study the isotopic composition of DO in *in-situ* relevant samples representative of the first 200 meters below surface. Our findings suggest that the isotopic composition of DO may be a useful tracer to unravel transport, reaction and microbial processes in these environments.

6 Open Research

All figures were made using Matplotlib version 3.5.1 (Hunter, 2007), available under the Matplotlib license at `https://matplotlib.org/`. Data from the Ploemeur fractured rock observatory, which is part of the French network of hydrogeological observatories H+ (`http://hplus.ore.fr/en/`), was used to create this manuscript.

Acknowledgments

This research was funded, in whole, by ANR EQUIPEX CRITEX project (ANR-11-EQPX-0011), the ERC project ReactiveFronts (648377), the ThéGéo program of Géosciences Rennes and the French Ministry of Higher Education, Research and Innovation. Authors are grateful to the french networks of hydrogeological sites H+ (https://hplus.ore.fr/en/) and of critical zone observatories OZCAR (https://www.ozcar-ri.org/) for providing access to the Ploemeur CZO and to the CONDATEAU service at University of Rennes for their support with dissolved gases and groundwater chemistry analyses. We are also grateful to the "Laboratoire National des Nucléides Cosmogéniques" (LN2C) and to the ASTER-CEREGE Isotope Geochemistry Plateform for their support during the ^{36}Cl analyses.

References

Abe, Y., & Hunkeler, D. (2006, March). Does the Rayleigh Equation Apply to Evaluate Field Isotope Data in Contaminant Hydrogeology? *Environmental Science & Technology*, *40*(5), 1588–1596. doi: 10.1021/es051128p

Aggarwal, P. K., & Dillon, M. A. (1998). Stable isotope composition of molecular oxygen in soil gas and groundwater: A potentially robust tracer for diffusion and oxygen consumption processes. *Geochimica et Cosmochimica Acta*, *62*(4), 577–584. doi: 10.1016/S0016-7037(97)00377-3

Anantharaman, K., Brown, C. T., Hug, L. A., Sharon, I., Castelle, C. J., Probst, A. J., ... Banfield, J. F. (2016). Thousands of microbial genomes shed light on interconnected biogeochemical processes in an aquifer system. *Nature Communications*, *7*, 1–11. doi: 10.1038/ncomms13219

Armostrong, W., & Armstrong, J. (2005, September). Stem Photosynthesis not Pressurized Ventilation is Responsible for Light-enhanced Oxygen Supply

to Submerged Roots of Alder (Alnus glutinosa). *Annals of Botany*, *96*(4), 591–612. doi: 10.1093/aob/mci213

Arnold, M., Merchel, S., Bourlès, D. L., Braucher, R., Benedetti, L., Finkel, R. C., ... Klein, M. (2010). The French accelerator mass spectrometry facility ASTER: Improved performance and developments. *Nuclear Instruments and Methods in Physics Research, Section B: Beam Interactions with Materials and Atoms*, *268*(11-12), 1954–1959. doi: 10.1016/j.nimb.2010.02.107

Ayraud, V., Aquilina, L., Labasque, T., Pauwels, H., Molenat, J., Pierson-wickmann, A.-c., ... Davy, P. (2008). Compartmentalization of physical and chemical properties in hard-rock aquifers deduced from chemical and groundwater age analyses. *Applied Geochemistry*, *23*(June), 2686–2707. doi: 10.1016/j.apgeochem.2008.06.001

Barkan, E., & Luz, B. (2005). High precision measurements of 17O/16O and 18O/16O ratios in H2O. *Rapid Communications in Mass Spectrometry*, *19*(24), 3737–3742. doi: 10.1002/rcm.2250

Barth, J. A. C., Tait, A., & Bolshaw, M. (2004). Automated analyses of 18 O / 16 O ratios in dissolved oxygen from 12-mL water samples. *Limnology and Oceanography: Methods*, *2*, 35–41.

Béchennec, F., Hallégouët, B., Thiéblemont, D., & Thinon, I. (2012a). *Carte géol. France (1/50 000), feuille Lorient (383).* (BRGM, Ed.). Orleans: BRGM.

Béchennec, F., Hallégouët, B., Thiéblemont, D., & Thinon, I. (2012b). *Notice explicative, Carte géol France (1/50 000), feuille Lorient (383)* (BRGM, Ed.). Orléans: BRGM.

Bense, V., Gleeson, T., Loveless, S., Bour, O., & Scibek, J. (2013, December). Fault zone hydrogeology. *Earth-Science Reviews*, *127*, 171–192. doi: 10.1016/j.earscirev.2013.09.008

Bethencourt, L., Bochet, O., Farasin, J., Aquilina, L., Borgne, T. L., Quaiser, A., ... Dufresne, A. (2020). Genome reconstruction reveals distinct assemblages of Gallionellaceae in surface and subsurface redox transition zones. *FEMS Microbiology Ecology*, *96*(5). doi: 10.1093/femsec/fiaa036

Bochet, O., Bethencourt, L., Dufresne, A., Farasin, J., Pédrot, M., Labasque, T., ... Le Borgne, T. (2020). Iron-oxidizer hotspots formed by intermittent oxic–anoxic fluid mixing in fractured rocks. *Nature Geoscience*, *13*(2), 149–155. doi: 10.1038/s41561-019-0509-1

Borden, R. C., & Bedient, P. B. (1986). Transport of dissolved hydrocarbons influenced by oxygen-limited biodegradation: 1. Theoretical development. *Water Resources Research*, *22*(13), 1973–1982. doi: 10.1029/WR022i013p01973

Bouchez, C., Deschamps, P., Goncalves, J., Hamelin, B., Sylvestre, F., Claude Doumnang, J., ... Luc Seidel, J. (2015). Investigation of 36Cl Distribution: Towards a New Estimation of Groundwater Residence Times in the Confined Aquifer of the LCB? *Procedia Earth and Planetary Science*, *13*, 147–150. doi: 10.1016/j.proeps.2015.07.035

Brantley, S. L. (2010). Bedrock to soil: Where rocks meet life in the critical zone. In *GEOCHIMICA ET COSMOCHIMICA ACTA* (Vol. 74, pp. A118–A118). PERGAMON-ELSEVIER SCIENCE LTD THE BOULEVARD, LANGFORD LANE, KIDLINGTON ....

Buss, H. L., Sak, P. B., Webb, S. M., & Brantley, S. L. (2008). Weathering of the Rio Blanco quartz diorite , Luquillo Mountains , Puerto Rico : Coupling oxidation , dissolution , and fracturing. *Geochimica et Cosmochimica Acta*, *72*, 4488–4507. doi: 10.1016/j.gca.2008.06.020

Chatelier, M., Ruelleu, S., Bour, O., Porel, G., & Delay, F. (2011). Combined fluid temperature and flow logging for the characterization of hydraulic structure in a fractured karst aquifer. *Journal of Hydrology*, *400*(3-4), 377–386. doi: 10.1016/j.jhydrol.2011.01.051

Craig, H., & Hayward, T. (1987). Oxygen supersaturation in the ocean: Biological

versus physical contributions. *Science*, *235*(4785), 199–202.

Dordoni, M., Seewald, M., Rinke, K., Schmidmeier, J., & Barth, J. A. (2022). Novel evaluations of sources and sinks of dissolved oxygen via stable isotopes in lentic water bodies. *Science of the Total Environment*, *838*(April), 156541. doi: 10.1016/j.scitotenv.2022.156541

Druhan, J., & Maher, K. (2017). The influence of mixing on stable isotope ratios in porous media: A revised Rayleigh model. *Water Resources Research*, *53*, 1101–1124. doi: 10.1002/2016WR019666

Druschel, G. K., Emerson, D., Sutka, R., Suchecki, P., & Luther, G. W. (2008). Low-oxygen and chemical kinetic constraints on the geochemical niche of neutrophilic iron(II) oxidizing microorganisms. *Geochimica et Cosmochimica Acta*, *72*(14), 3358–3370. doi: 10.1016/j.gca.2008.04.035

Eggerichs, T., Opel, O., Otte, T., & Ruck, W. (2014). Interdependencies between Biotic and Abiotic Ferrous Iron Oxidation and Influence of pH, Oxygen and Ferric Iron Deposits. *Geomicrobiology Journal*, *31*(6), 461–472. doi: 10.1080/01490451.2013.870620

Emerson, D., Fleming, E. J., & McBeth, J. M. (2010). Iron-Oxidizing Bacteria: An Environmental and Genomic Perspective. *Annual Review of Microbiology*, *64*(1), 561–583. doi: 10.1146/annurev.micro.112408.134208

Ettwig, K. F., Butler, M. K., Le Paslier, D., Pelletier, E., Mangenot, S., Kuypers, M. M. M., ... Strous, M. (2010, March). Nitrite-driven anaerobic methane oxidation by oxygenic bacteria. *Nature*, *464*(7288), 543–548. doi: 10.1038/nature08883

Ettwig, K. F., Speth, D. R., Reimann, J., Wu, M. L., Jetten, M. S., & Keltjens, J. T. (2012). Bacterial oxygen production in the dark. *Frontiers in Microbiology*, *3*.

Fortune, W. B., & Mellon, M. G. (1938). Determination of Iron with o-Phenanthroline: A Spectrophotometric Study. *Industrial and Engineering Chemistry - Analytical Edition*, *10*(2), 60–64. doi: 10.1021/ac50118a004

Fry, V. A., Istok, J. D., & O'Reilly, K. T. (1996). Effect of Trapped Gas on Dissolved Oxygen Transport — Implications for In Situ Bioremediation. *Groundwater*, *34*(2), 200–210. doi: 10.1111/j.1745-6584.1996.tb01880.x

Green, C. T., Böhlke, J. K., Bekins, B. A., & Phillips, S. P. (2010). Mixing effects on apparent reaction rates and isotope fractionation during denitrification in a heterogeneous aquifer. *Water Resources Research*, *46*(8). doi: 10.1029/2009WR008903

Gutsalo, L. K. (1971). Radiolysis of water as the source of free oxygen in the underground hydrosphere. *Geochem. Int.*, *8*(6), 897–903.

Guy, R. D., Fogel, M. L., & Berry, J. A. (1993). Photosynthetic fractionation of the stable isotopes of oxygen and carbon. *Plant Physiology*, *101*(1), 37–47. doi: 10.1104/pp.101.1.37

Hee, S. M., Komlos, J., & Jaffé, P. R. (2007). Uranium reoxidation in previously bioreduced sediment by dissolved oxygen and nitrate. *Environmental Science and Technology*, *41*(13), 4587–4592. doi: 10.1021/es063063b

Hendry, M. J., Wassenaar, L. I., & Birkham, T. K. (2002). Microbial respiration and diffusive transport of O2, 16O2, and 18O16O in unsaturated soils: A mesocosm experiment. *Geochimica et Cosmochimica Acta*, *66*(19), 3367–3374. doi: 10.1016/S0016-7037(02)00949-3

Humphreys, W. F. (2009). Hydrogeology and groundwater ecology: Does each inform the other? *Hydrogeology Journal*, *17*(1), 5–21. doi: 10.1007/s10040-008-0349-3

Hunter, J. D. (2007). Matplotlib: A 2d graphics environment [software]. *Computing in science & engineering*, *9*(03), 90–95.

Johnson, T. M., & DePaolo, D. J. (1994). Interpretation of isotopic data in groundwater-rock systems: Model development and application to Sr iso-

655 tope data from Yucca Mountain. *Water Resources Research*, *30*(5), 1571–1587.
656 doi: 10.1029/94WR00157
657 Jurgens, B. C., Böhlke, J. K., & Eberts, S. M. (2012). *TracerLPM (Version 1): An*
658 *Excel® workbook for interpreting groundwater age distributions from environ-*
659 *mental tracer data: U.S. Geological Survey Techniques and Methods Report*
660 *4-F3* (Tech. Rep.). U.S. Geological Survey Techniques and Methods.
661 Kim, H., Stinchcomb, G., & Brantley, S. L. (2017). Feedbacks among O2 and CO2
662 in deep soil gas , oxidation of ferrous minerals , and fractures : A hypothesis
663 for steady-state regolith thickness. *Earth and Planetary Science Letters*, *460*,
664 29–40. doi: 10.1016/j.epsl.2016.12.003
665 Klepikova, M. V., Le Borgne, T., Bour, O., & Davy, P. (2011). A methodology for
666 using borehole temperature-depth profiles under ambient, single and cross-
667 borehole pumping conditions to estimate fracture hydraulic properties. *Journal*
668 *of Hydrology*, *407*(1-4), 145–152. doi: 10.1016/j.jhydrol.2011.07.018
669 Köhler, I., Martinez, R. E., Piatka, D., Herrmann, A. J., Gallo, A., Gehringer,
670 M. M., & Barth, J. A. C. (2021, August). How are oxygen budgets influenced
671 by dissolved iron and growth of oxygenic phototrophs in an iron-rich spring
672 system? Initial results from the Espan Spring in Fürth, Germany. *Biogeo-*
673 *sciences*, *18*(15), 4535–4548. doi: 10.5194/bg-18-4535-2021
674 Kolbe, T., De Dreuzy, J. R., Abbott, B. W., Aquilina, L., Babey, T., Green, C. T.,
675 ... Pinay, G. (2019). Stratification of reactivity determines nitrate removal in
676 groundwater. *Proceedings of the National Academy of Sciences of the United*
677 *States of America*, *116*(7), 2494–2499. doi: 10.1073/pnas.1816892116
678 Korom, S. F. (1992). Natural denitrification in the saturated zone: A review. *Water*
679 *Resources Research*, *28*(6), 1657–1668. doi: 10.1029/92WR00252
680 Lasaga, A. C., & Ohmoto, H. (2002). The oxygen geochemical cycle: Dynamics and
681 stability. *Geochimica et Cosmochimica Acta*, *66*(3), 361–381. doi: 10.1016/
682 S0016-7037(01)00685-8
683 Le Borgne, T., Paillet, F., Bour, O., & Caudal, J. P. (2006). Cross-borehole flowme-
684 ter tests for transient heads in heterogeneous aquifers. *Ground Water*, *44*(3),
685 444–452. doi: 10.1111/j.1745-6584.2005.00150.x
686 Lezama-Pacheco, J. S., Cerrato, J. M., Veeramani, H., Alessi, D. S., Suvorova, E.,
687 Bernier-Latmani, R., ... Bargar, J. R. (2015). Long-Term in Situ Oxidation
688 of Biogenic Uraninite in an Alluvial Aquifer: Impact of Dissolved Oxygen and
689 Calcium. *Environmental Science and Technology*, *49*(12), 7340–7347. doi:
690 10.1021/acs.est.5b00949
691 Mader, M., Roberts, A. M., Porst, D., Schmidt, C., Trauth, N., van Geldern, R.,
692 & Barth, J. A. C. (2018, September). River recharge versus O2 supply from
693 the unsaturated zone in shallow riparian groundwater: A case study from the
694 Selke River (Germany). *Science of The Total Environment*, *634*, 374–381. doi:
695 10.1016/j.scitotenv.2018.03.230
696 Mader, M., Schmidt, C., van Geldern, R., & Barth, J. A. (2017). Dissolved oxy-
697 gen in water and its stable isotope effects: A review. *Chemical Geology*,
698 *473*(September), 10–21. doi: 10.1016/j.chemgeo.2017.10.003
699 Maisch, M., Lueder, U., Laufer, K., Scholze, C., Kappler, A., & Schmidt, C. (2019).
700 Contribution of Microaerophilic Iron(II)-Oxidizers to Iron(III) Mineral For-
701 mation [Research-Article]. *Environmental Science and Technology*, *53*(14),
702 8197–8204. doi: 10.1021/acs.est.9b01531
703 Malard, F., & Hervant, F. (1999). Oxygen supply and the adaptations of animals in
704 groundwater. *Freshwater Biology*, *41*, 1–30.
705 Martinez-Landa, L., Carrera, J., Dentz, M., Fernàndez-Garcia, D., Nardí, A.,
706 & Saaltink, M. W. (2012). Mixing induced reactive transport in frac-
707 tured crystalline rocks. *Applied Geochemistry*, *27*(2), 479–489. doi:
708 10.1016/j.apgeochem.2011.09.016
709 McMahon, P. B., & Chapelle, F. H. (2008). Redox processes and water quality of se-

lected principal aquifer systems. *Ground Water*, *46*(2), 259–271. doi: 10.1111/j.1745-6584.2007.00385.x

Melton, E. D., Swanner, E. D., Behrens, S., Schmidt, C., & Kappler, A. (2014). The interplay of microbially mediated and abiotic reactions in the biogeochemical Fe cycle. *Nature Reviews Microbiology*, *12*(12), 797–808. doi: 10.1038/nrmicro3347

Napieralski, S. A., Buss, H. L., Brantley, S. L., Lee, S., Xu, H., & Roden, E. E. (2019). Microbial chemolithotrophy mediates oxidative weathering of granitic bedrock. *Proceedings of the National Academy of Sciences of the United States of America*, *116*(52), 26394–26401. doi: 10.1073/pnas.1909970117

Nordstrom, D. K. (2011). Hydrogeochemical processes governing the origin, transport and fate of major and trace elements from mine wastes and mineralized rock to surface waters. *Applied Geochemistry*, *26*(11), 1777–1791. doi: 10.1016/j.apgeochem.2011.06.002

Oba, Y., & Poulson, S. R. (2009a). Oxygen isotope fractionation of dissolved oxygen during abiological reduction by aqueous sulfide. *Chemical Geology*, *268*(3-4), 226–232. doi: 10.1016/j.chemgeo.2009.09.002

Oba, Y., & Poulson, S. R. (2009b). Oxygen isotope fractionation of dissolved oxygen during reduction by ferrous iron. *Geochimica et Cosmochimica Acta*, *73*(1), 13–24. doi: 10.1016/j.gca.2008.10.012

Osorio-Leon, I., Bouchez, C., Chatton, E., Lavenant, N., Longuevergne, L., & Le Borgne, T. (2023). Hydrological and geological controls for the depth distribution of dissolved oxygen and iron in silicate catchments.

Overholt, W. A., Trumbore, S., Xu, X., Bornemann, T. L. V., Probst, A. J., Krüger, M., ... Küsel, K. (2022). Carbon fixation rates in groundwater similar to those in oligotrophic marine systems.

Parker, S. R., Darvis, M. N., Poulson, S. R., Gammons, C. H., & Stanford, J. A. (2014). Dissolved oxygen and dissolved inorganic carbon stable isotope composition and concentration fluxes across several shallow floodplain aquifers and in a diffusion experiment. *Biogeochemistry*, *117*(2-3), 539–552. doi: 10.1007/s10533-013-9899-0

Pati, S. G., Bolotin, J., Brennwald, M. S., Kohler, H.-p. E., Werner, R. A., & Hofstetter, T. B. (2016). Measurement of oxygen isotope ratios (18 O / 16 O) of aqueous O 2 in small samples by gas chromatography / isotope ratio mass spectrometry. *Rapid Communications in Mass Spectroscopy*, *30*, 684–690. doi: 10.1002/rcm.7481

Révész, K. M., Böhlke, J. K., Smith, R. L., & Yoshinari, T. (1999). Delta 18-O composition of dissolved O2 undergoing respiration in a contaminated ground water. *IAEA Repport*, *IAEA Inter*.

Rikken, G. B., Kroon, A. G. M., & van Ginkel, C. G. (1996, April). Transformation of (per)chlorate into chloride by a newly isolated bacterium: Reduction and dismutation. *Applied Microbiology and Biotechnology*, *45*(3), 420–426. doi: 10.1007/s002530050707

Roques, C., Bour, O., Aquilina, L., Dewandel, B., Leray, S., Schroetter, J. M., ... Mougin, B. (2014). Hydrological behavior of a deep sub-vertical fault in crystalline basement and relationships with surrounding reservoirs. *Journal of Hydrology*, *509*, 42–54. doi: 10.1016/j.jhydrol.2013.11.023

Rose, S., & Long, A. (1988). Dissolved oxygen systematics in the Tucson Basin Aquifer. *Water Resources Research*, *24*(1), 127–136. doi: 10.1029/WR024i001p00127

Ruelleu, S. (2010). Caractérisation hydrogéophysique des milieux fracturés : Développement instrumental et modélisation des vitesses d'écoulement en forage. , 248.

Smith, M. G., Parker, S. R., Gammons, C. H., Poulson, S. R., & Hauer, F. R. (2011). Tracing dissolved O2 and dissolved inorganic carbon stable iso-

765 tope dynamics in the Nyack aquifer: Middle Fork Flathead River, Mon-
766 tana, USA. *Geochimica et Cosmochimica Acta*, *75*(20), 5971–5986. doi:
767 10.1016/j.gca.2011.07.033
768 Sprenger, M., Stumpp, C., Weiler, M., Aeschbach, W., Allen, S. T., Benettin, P., ...
769 Werner, C. (2019). The demographics of water : A review of water ages in the
770 critical zone. *Reviews of Geophysics*, *57*. doi: 10.1029/2018RG000633
771 Stumm, W., & Morgan, J. J. (1996). Oxidation and Reduction: Equilibria and
772 Microbial Mediation. In J. Schnoor & A. Zehnder (Eds.), *Aquatic Chemistry:*
773 *Chemical Equilibria and Rates in Natural Waters* (pp. 425–515). Wiley.
774 Suckow, A. (2014). The age of groundwater - Definitions, models and why we do not
775 need this term. *Applied Geochemistry*, *50*(May 2014), 222–230. doi: 10.1016/j
776 .apgeochem.2014.04.016
777 Sugisaki, R., & Taki, K. (1987). Simplified analyses in of He , natural Ne , waters
778 and Ar dissolved. *Geochemical Journal*, *21*, 23–27.
779 Taylor, B. E., Wheeler, M. C., & Nordstrom, D. K. (1984, December). Sta-
780 ble isotope geochemistry of acid mine drainage: Experimental oxidation
781 of pyrite. *Geochimica et Cosmochimica Acta*, *48*(12), 2669–2678. doi:
782 10.1016/0016-7037(84)90315-6
783 Touchard, F. (1999). *Caractérisation hydrogéologique d'un aquifère de socle frac-*
784 *turé : Site de Ploemeur (Morbihan).* (Unpublished doctoral dissertation). Uni-
785 versité de Rennes 1.
786 Trinchero, P., Delos, A., Molinero, J., Dentz, M., & Pitkänen, P. (2014, May).
787 Understanding and modelling dissolved gas transport in the bedrock of
788 three Fennoscandian sites. *Journal of Hydrology*, *512*, 506–517. doi:
789 10.1016/j.jhydrol.2014.03.011
790 Trinchero, P., Sidborn, M., Puigdomenech, I., Iraola, A., Bosbach, D., & Deissmann,
791 G. (2019). Groundwater age dating in fractured rock using 4He data. *Journal*
792 *of Hydrology X*, *4*(July), 100036. doi: 10.1016/j.hydroa.2019.100036
793 Tromboni, F., Dodds, W. K., Chandra, S., Poulson, S. R., Pandey, A., & Schechner,
794 A. (2020). Respiration in rivers fractionates stable isotopes of dissolved oxygen
795 ; a global investigation on the influences of temperature and flow. *Biogeochem-*
796 *istry*, *147*(2), 199–210. doi: 10.1007/s10533-020-00636-z
797 Urey, H., & Greiff, L. (1935). Isotopic Exchange. *Journal of the American Chemical*
798 *Society*, *57*(2), 321–327. doi: 10.1055/sos-sd-014-00066
799 van Ginkel, C. G., Rikken, G. B., Kroon, A. G. M., & Kengen, S. W. M. (1996,
800 November). Purification and characterization of chlorite dismutase: A novel
801 oxygen-generating enzyme. *Archives of Microbiology*, *166*(5), 321–326. doi:
802 10.1007/s002030050390
803 Van Breukelen, B. M., & Rolle, M. (2012, July). Transverse Hydrodynamic Dis-
804 persion Effects on Isotope Signals in Groundwater Chlorinated Solvents'
805 Plumes. *Environmental Science & Technology*, *46*(14), 7700–7708. doi:
806 10.1021/es301058z
807 Wassenaar, L. I., & Hendry, M. J. (2007). Dynamics and stable isotope composition
808 of gaseous and dissolved oxygen. *Ground Water*, *45*(4), 447–460. doi: 10.1111/
809 j.1745-6584.2007.00328.x
810 Winograd, Isaac., & Robertson, F. (1982). Deep Oxygenated Ground Water :
811 Anomaly or Common Occurrence? *Science*, *216*(4551), 1227–1230. doi:
812 10.1126/science.216.4551.1227

3 Chapter conclusion

The study presented in this chapter constitutes the first investigation of the isotopic fractionation of DO during its consumption in the deep continental subsurface. We observed that there is a discrepancy between enrichment factors derived in the lab and those that explain the isotopic fractionation of DO in the field. While laboratory experiments report *intrinsic* fractionation factors, our data suggests that exponential mixing in fractured rocks particularly influences the DO isotope composition, leading to the determination of *effective* enrichment factors. Nevertheless, the strong contrasts in the apparent enrichment factors added to hydrochemical information proved useful to identify reactive zones in the catchment that are related to microbial activity of iron-oxidizing bacteria (FeOB). The DO isotope composition showed an isotopic enrichment by the action of FeOB that is remarkably consistent with the microaerobic range, reported as favorable for FeOB activity in previous laboratory studies. Overall, the isotopic composition of DO proved useful to identify reactive zones in the catchment that are related to microbial activity, providing a valuable tool that can be used for future assessments of primary production in aquifers.

4 Perspectives

1. **Laboratory reactive-transport experiments and modeling to constrain the transport effects on effective enrichment factors:** *intrinsic* enrichment factors are usually determined in well-mixed laboratory experiments that discard transport limitations. Our results showed, however, that transport effects can limit the use of laboratory-derived enrichment factors to explain isotopic fractionations of DO in natural settings. A way to constrain the influence of transport effects on DO isotope fractionation would be by conducting reactive-transport experiments in column setups in which the transport effects can be controlled to unravel their influence. Ultimately, these experiments can result in models decoupling transport effects from *effective* enrichment factors, thus improving our capacity to transpose *intrinsic* enrichment factors of specific reactive pathways to observations in the field.

2. **Concentration and isotopic composition of DO in the regolith compartment:** the anomalous DO isotope trend observed in shallow groundwater in our study site, coupled to our modeling results of both groundwater age and DO isotope fractionation, suggested an unexpected mixing between deep groundwater with groundwater from the unconfined aquifer in the regolith. In order to further validate our modeling interpretations, future characterizations of the regolith compartment will be needed. In particular, it is needed to characterize the concentration and the isotopic composition of DO in this compartment as well as the variability of these two variables with altitude and position in the catchment.

5 Take-home messages

Factors controlling redox landscapes in the continental subsurface

1. **The isotopic composition of DO is a promising tool to disentangle the reactive processes in the subsurface**, in particular to distinguish between abiotic and biotic reactions.
2. **We found a DO isotope enrichment which is coherent with the activity of iron oxidizing bacteria (FeOB)**. The range of DO concentrations at which FeOB operate in the field is consistent with the microaerobic range reported in laboratory incubations.
3. **We observed an unexpected depletion of heave oxygen isotopologues as DO is depleted in the range from air saturation to** 1.6 $mg.L^{-1}$**. Observations from other study sites suggest this is potentially a common case in shallow groundwater environments**. Our data suggests this is a result of exponential mixing with a light $\delta^{18}O$ end-member in the aquifer's regolith.
4. **We observed a "lab-field" discrepancy on the enrichment factors**. The isotopic fractionation during DO consumption requires field-adapted interpretation tools to account for non-reactive processes that also influence DO isotope composition, such as transport effects.

6 Chapter acknowledgments

To my collaborators from the Geozentrum Nordbayern: Johannes Barth, Marlene Dordoni and David Piatka. Thank you very much for accepting to collaborate with the IRMS analyses and then for holding the interesting discussions that shaped an essential part of this work. A special thank you also to Eliot Chatton for his invaluable assistance during the two field campaigns that made this work possible. And, of course, a big thank you to Camille Bouchez for proposing the seminal idea behind this work and for her supervision and support throughout the project.

Bibliography

Aggarwal, P. K. and Dillon, M. A. (1998). Stable isotope composition of molecular oxygen in soil gas and groundwater: A potentially robust tracer for diffusion and oxygen consumption processes. *Geochimica et Cosmochimica Acta*, 62(4):577–584.

Ash, J. L., Hu, H., and Yeung, L. Y. (2020). What fractionates oxygen isotopes during respiration? insights from multiple isotopologue measurements and theory. *ACS Earth and Space Chemistry*, 4(1):50–66.

Bao, H., Cao, X., and Hayles, J. A. (2016). Triple Oxygen Isotopes: Fundamental Relationships and Applications. *Annual Review of Earth and Planetary Sciences*, 44:463–492.

Dole, M. (1936). The relative atomic weight of oxygen in water and in air. *The Journal of Chemical Physics*, 4(12):778–780.

Druschel, G. K., Emerson, D., Sutka, R., Suchecki, P., and Luther, G. W. (2008). Low-oxygen and chemical kinetic constraints on the geochemical niche of neutrophilic iron(II) oxidizing microorganisms. *Geochimica et Cosmochimica Acta*, 72(14):3358–3370.

Gonfiantini, R. (1978). Standards for stable isotope measurements in natural compounds. *Nature*, 271(5645):534–536.

Guy, R. D., Fogel, M. L., and Berry, J. A. (1993). Photosynthetic fractionation of the stable isotopes of oxygen and carbon. *Plant Physiology*, 101(1):37–47.

Hendry, M. J., Wassenaar, L. I., and Birkham, T. K. (2002). Microbial respiration and diffusive transport of O2, 16O2, and 18O16O in unsaturated soils: A mesocosm experiment. *Geochimica et Cosmochimica Acta*, 66(19):3367–3374.

Jurikova, H., Guha, T., Abe, O., Shiah, F.-k., Wang, C.-h., and Liang, M.-c. (2016). Variations in triple isotope composition of dissolved oxygen and primary production in a subtropical reservoir. *Biogeosciences*, 13:6683–6698.

Kappler, A., Bryce, C., Mansor, M., Lueder, U., Byrne, J. M., and Swanner, E. D. (2021). An evolving view on biogeochemical cycling of iron. *Nature Reviews Microbiology*, 19(6):360–374.

Kroopnick, P. and Craig, H. (1972). Atmospheric oxygen: Isotopic composition and solubility fractionation. *Science*, 175(4017):54–55.

Luz, B. and Barkan, E. (2005). The isotopic ratios17O/16O and18O/16O in molecular oxygen and their significance in biogeochemistry. *Geochimica et Cosmochimica Acta*, 69(5):1099–1110.

Mader, M., Schmidt, C., van Geldern, R., and Barth, J. A. (2017). Dissolved oxygen in water and its stable isotope effects: A review. *Chemical Geology*, 473(September):10–21.

Maisch, M., Lueder, U., Laufer, K., Scholze, C., Kappler, A., and Schmidt, C. (2019). Contribution of Microaerophilic Iron(II)-Oxidizers to Iron(III) Mineral Formation. *Environmental Science and Technology*, 53(14):8197–8204.

Napieralski, S. A., Buss, H. L., Brantley, S. L., Lee, S., Xu, H., and Roden, E. E. (2019). Microbial chemolithotrophy mediates oxidative weathering of granitic bedrock. *Proceedings of the National Academy of Sciences of the United States of America*, 116(52):26394–26401.

Peeters, F., Hofmann, H., and Encinas, J. (2019). On the calculation of lake metabolic rates : Diel O 2 and technique ndez. *Water Research*, 165.

Smith, A., Popa, R., Fisk, M., Nielsen, M., Wheat, C. G., Jannasch, H. W., Fisher, A. T., Becker, K., Sievert, S. M., and Flores, G. (2011). In situ enrichment of Ocean crust microbes on igneous minerals and glasses using an osmotic flow-through device. *Geochemistry, Geophysics, Geosystems*, 12(6):1–19.

Tromboni, F., Dodds, W. K., Chandra, S., Poulson, S. R., Pandey, A., and Schechner, A. (2020). Respiration in rivers fractionates stable isotopes of dissolved oxygen ; a global investigation on the influences of temperature and flow. *Biogeochemistry*, 147(2):199–210.

VI. FIELD EXPERIMENT 1: THE DEEP OXIC HYDROSPHERE AS A DYNAMIC SYSTEM

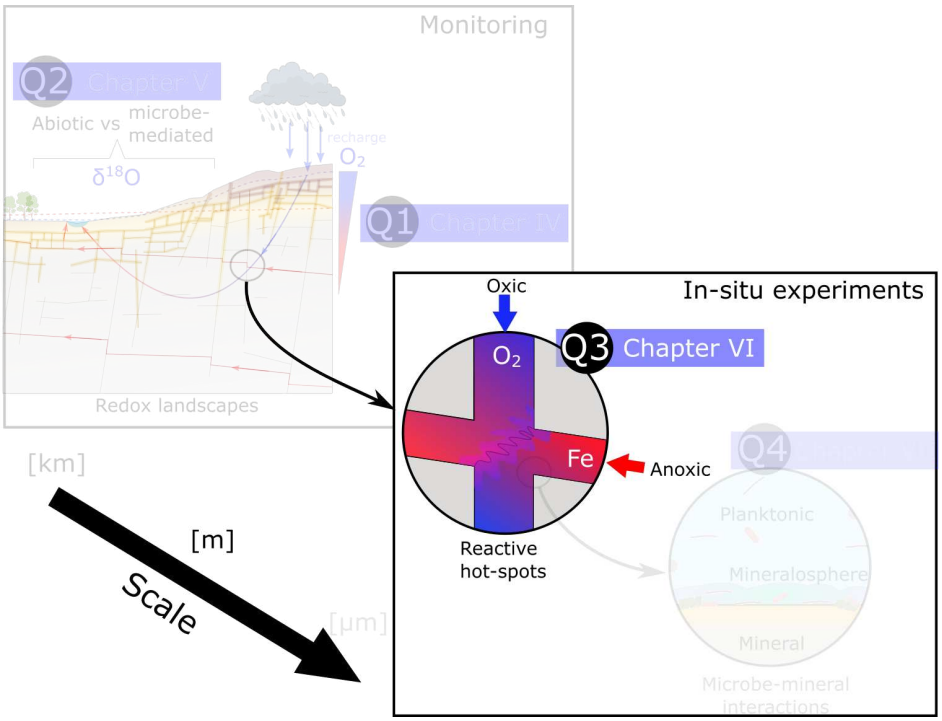

Contents

1 Introduction

In chapters IV and V we studied different biogeochemical processes resulting from the interactions between both dissolved O_2 and Fe. In these two chapters, we used interannual average concentrations measured at Ploemeur, which allowed to draw a steady-state spatial landscape of iron-oxidation. However, we have highlighted the importance of hydrological forcings in the transport of dissolved oxygen (DO) in the subsurface. The modeling framework developed in Chapter IV, for instance, quantitatively demonstrated how hydrological forcings counterbalance the biogeochemical DO-consuming reactions and allow for the persistence of DO in aquifers. In addition, Bochet et al. (2020) provided field evidence of the dynamic nature of DO concentrations in the subsurface. Based on seasonal measurements, the authors inferred that fractures serve as preferential flow paths, promoting the rapid transport of oxic groundwater during recharge events. This connectivity between surface and subsurface environments is further supported by our findings in Chapter V: the interpretation of both residence time tracers and DO isotope compositions converged, indeed, towards an exponential mixing model for the Guidel catchment.

The deep oxic hydrosphere is thus a dynamic environment and its dynamic nature directly comes from its connection with the surface where varying recharge conditions can propagate into the subsurface through complex fracture networks. Nonetheless, tracking the dynamics of dissolved oxygen (DO) concentrations and the reactions induced in subsurface environments can be challenging. **Here, we develop an experimental approach to artificially reproduce a recharge-event in the subsurface.**

Iron-oxidizing bacteria (FeOB) have been observed in the Pz26 borehole located in the Guidel catchment (Bochet et al.; 2020). The authors assumed that this important microbial community is sustained by oxic-water flowing in transmissive fractures that reacts with dissolved iron from deep fractures in the following reaction:

$$4\,Fe^{2+} + O_2 + 10\,H_2O \longrightarrow Fe(OH)_3 + 8\,H^+ \tag{VI.1}$$

This site is thus ideal to test the impact of intermittent DO inputs on subsurface ecosystems. The general idea of our *in-situ* experiment is to isolate a reducing fracture (in the borehole Pz26), naturally containing high concentrations of dissolved Fe, and to inject into it a known volume of the fracture fluid that has been previously enriched with both conservative (fluorescein) and reactive (dissolved O_2) tracers. For this, we use a specially engineered double-packer device developed at Geociences Rennes. The double-packer system is equipped with probes for the *in-situ* monitoring of temperature, pressure, fluorescence and dissolved O_2 concentration and was used to isolate a transmissive 20-meter deep fracture in which anoxic and iron-rich groundwater flows. Two single borehole push-pull tests (PPT1 and PPT2) were carried out in order to reproduce a subsurface hot-spot of biogeochemical reactivity as hypothesized by Bochet et al. (2020), where a reducing groundwater system (the reducing fracture) mixes with oxic water through a rapid recharge event (the tracer-enriched solution).

This chapter is structured as follows: first, we present the experimental setup to conduct the two reactive push-pull tracer tests. We continue by presenting the results of the experiment followed by a discussion section. Finally, we close the chapter by presenting the conclusions from this field experiment and some possible perspectives on this work.

2 Materials and methods

2.1 Double packer device for fracture isolation

A customized double inflatable packer (Geosciences Rennes - Geopro S.A.) was used for the isolation of a targeted fracture intersecting the borehole wall (see Figure VI.1). The packer was inflated with water in order to avoid any small contamination by air. In order to validate the hydraulic isolation of the fracture, we did a pumping test in the isolated chamber and checked that pressure was not changing above and below the packer

(see Figure VI.1). The absence of a transient pressure signal above and below the inflatable packers, while pumping in the fracture chamber, was interpreted as a correct hydraulic isolation. Isolation pumping tests are available in the chapter's Appendix.

The isolated chamber between packers is equipped with sensors for in-situ real-time (sampling interval: 3 s) monitoring of fluorescence (Unilux® Fluorometer, Chelsie Technologies, UK), temperature (RBRcoda T.D®, RBR, Canada), dissolved oxygen (RBRcoda T.ODO®, RBR, Canada) and pressure (PCDR/PTX 1830 Series Druck ®, General Electric, USA), see Figure VI.1. All signals were processed in a data acquisition unit in the surface. The chamber was also connected to injection/pumping pipelines allowing to sample groundwater from the fracture or to inject tracers in the fracture. Both injection and pumping pipelines were connected to a flow meter to accurately measure pumping rates and injection rates.

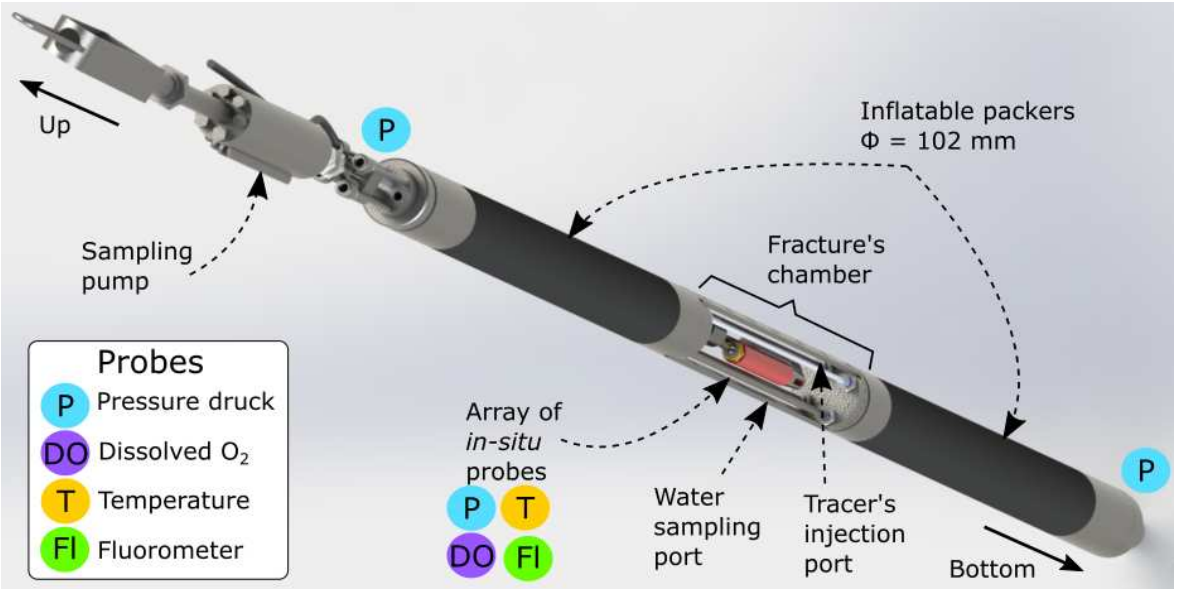

Figure VI.1: **Description of the novel double-packer device.** A targeted fracture inside a borehole can be isolated inside the fracture chamber by the action of the two inflatable packers. *In-situ* probes allow for a high-frequency monitoring of selected parameters as detailed in the color legend. The double-packer has been especially engineered at Geosciences Rennes by Nicolas Lavenant and Camille Bouchez, in association with the Geopro company (Belgium).

2.2 Choice of the fracture to conduct the reactive-tracer test

Before performing tracer tests, we carried out a hydrochemical characterization of the different fractures of the borehole. Small variations in the hydrochemical compositions of the different fractures are observed (Figure VI.2). All fractures are characterized by low DO and CFC12 contents, as well as high Fe contents, indicative of old groundwater with stable anoxic conditions. Moreover, previous metagenomic characterizations have shown little variations of microbial diversity in the fractures, which is dominated by the presence of iron-oxidizing *Gallionellaceae* (Bethencourt et al.; 2020). For practical reasons, we further conducted the reactive tracer tests in the most accessible fracture fulfilling the anoxic condition at 20 m.

2.3 Reactive push-pull test protocol

A reactive push-pull test is a single-borehole methodology allowing the estimation of *in-situ* reaction rates (Haggerty et al.; 1998). The push-pull test consists of four stages (see Figure VI.3): (1) the "injection phase" during which a "tracer-enriched" solution is injected into the isolated fracture, (2): the "push-phase" in which a "chaser" solution, consisting on pristine fracture fluid, is injected to further push the tracers into the fracture, (3): an "incubation" phase during which the injected fluid stays in the fracture, potentially flowing and reacting

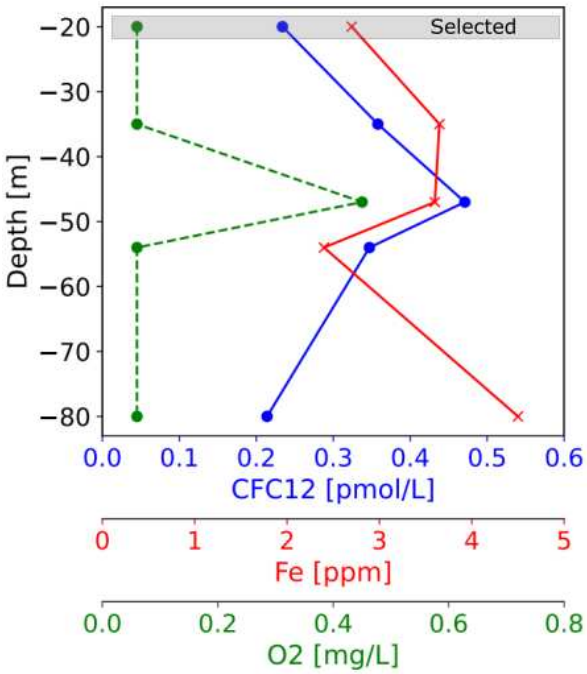

Figure VI.2: **Hydrochemical characterization of the main fractures from the borehole Pz26 from the Guidel catchment.** All fractures were sampled for characterization by installing the double-packer device. The fracture at -20 m was selected to perform the reactive-tracer test in it.

within the fracture and (4) a "pull phase" in which the injected fluids are pumped back to the surface until the concentration of the conservative tracer gets back to the background level. The tracer-solution is enriched with a conservative tracer (fluorescein) and dissolved oxygen, which is the reactive tracer that we are interested in. The use of a conservative tracer allows to compensate potential dispersion/dilution effects in the measured concentrations of the reactive tracer. Moreover, by comparing the injected vs retrieved mass of the conservative tracer, we can compute the tracer loss attributed to ambient divergent flows during the incubation phase. To make the mass balances possible, the concentrations and flow rates of all injected or extracted fluids from the fracture are carefully measured. While the double-packer device tracks the *in-situ* concentration of both conservative and reactive tracers, the groundwater pumped during the "pull phase" is sampled in the surface to analyze the potential products of the putative biogeochemical reactions that occurred during the experiment (Figure VI.3).

We performed two sequential and independent push-pull tests (PPTs), only differing by the duration of the incubation phase that was three hours in the PPT1 and eight hours in the PPT2. The interval between the end of PPT1 and the beginning of PPT2 was 12 hours. During this period, we flushed the fracture to prevent any perturbation of the fracture system by the PPT1.

2.4 Preparation of the injection solutions for the push-pull tests

We prepared between 100 and 200 liters of two injection solution for the tracer tests: the "tracer-enriched" solution and the "chaser" solution (see Figure VI.3). We used the natural fracture fluid as the base for both tracer-enriched and chaser solutions in order to avoid any external perturbation of the groundwater chemistry or the *in-situ* planktonic consortia, other than the one related to the reactive tracer. To prepare the tracer-enriched solution, the fracture groundwater was amended with 100 mL of a 1000 ppm solution of fluorescein sodium salt to reach a final concentration of 100 ppb. Then, the solution was bubbled with a gas sparger connected to a ultra-pure oxygen bottle (O_2> 99.9995%, Alphagaz ® 1 oxygen, Air Liquide). The bubbling was performed until reaching a 100 % saturation in dissolved oxygen as measured with a WTW multiparameter probe (WTW M226569) installed in the solution container. A second gas sparger was used to bubble standard quality CO2

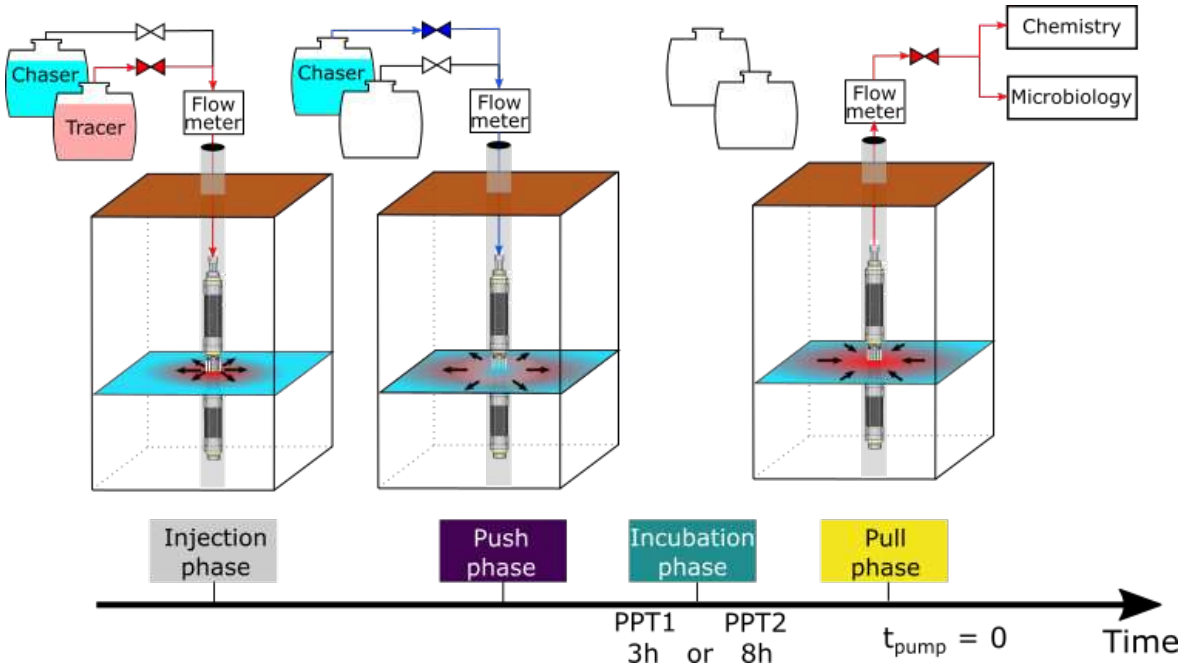

Figure VI.3: **Experimental setup of the reactive push-pull test.**

(CO_2 > 99.7%, Industrial quality CO_2, Air Liquide) to prevent any pH variation from the *in-situ* condition. Finally, the chaser solution consisted of unperturbated fracture fluid. The composition of both tracer-enriched and chaser solutions are presented in Table VI.1.

Table VI.1: **Composition of the fracture fluid and the injection solutions for the push-pull tests.** The characteristics of the aquifer background are presented for reference. PPT1 and PPT2 correspond to the first and second push-pull tracer tests, respectively. The "Volume" column indicates the volumes effectively injected in the isolated fracture. The "O_2" column stands for the reactive tracer, i.e. dissolved oxygen, while the "Fluo" column stands for the conservative tracer, i.e. fluorescein sodium salt.

Solution	Test	O_2 [μM]	Fluo [ppb]	pH	E.C. [$\mu S.cm^{-1}$]	T [°C]	Fe^{2+} [ppm]	Volume [L]
Tracer-enriched	PPT1	324	100	6.66	535	15.7	3.11	110
Tracer-enriched	PPT2	319	100	6.67	529	14	2.14	107
Chaser	PPT1	8.12	-	6.79	530	15.4	2.644	190
Chaser	PPT2	-	-	-	-	-	-	169
Aquifer background	-	2.22	-	6.79	530	14.36	2.649	-

2.5 Groundwater sampling for geochemical and microbiological analyses

Samples for geochemical and microbiological analyses were taken before the start of the experiments and during the "pull phase" of the tracer tests. With the double-packer device installed at the fracture depth, we pumped the fracture fluid until the measurements of DO and temperature in the fracture chamber were stable. We then sampled groundwater to characterize both geochemical and microbiological properties in the fracture. Chemical analyses included anions, cations and dissolved gases following the methods described in Osorio-Leon et al. (2023). For the microbiological analyses, we sampled planktonic consortia in triplicate samples. Sampling of planktonic consortia consisted on filtering 10 liters of fracture fluid in each of three Sterivex ® filters that were then frozen at -80 °C and sent to the EcoGeno service (ECOBIO, University of Rennes) for DNA extraction and quantification. The same series of analyses were conducted during the pull-phase of the tracer tests. We sampled groundwater at three key moments that were representative of the different stages of the breakthrough

curve, i.e. raising stage, peak and tail. Additionally, we sampled groundwater to measure dissolved Fe^{2+} by the 1,10-Phenanthroline colorimetric method Fortune and Mellon (1938). Samples for Fe^{2+} were taken about every five to ten minutes during the pull-phase of the experiments.

2.6 Estimation of *in-situ* reaction rates

Assuming a negligible ambient flow and low mass loses during the experiment, the injected volume can be considered as a closed system and can be treated as a batch reactor in order to estimate *in-situ* reaction rates. Following (Haggerty et al.; 1998), we use the conservative tracer BTC to account for dilution effects during the push pull tracer test and estimate the *dilution corrected* O_2 concentration in the fracture:

$$C^*_{O_2} = C_{O_2}.\frac{C_{Fluo}|_0}{C_{Fluo}} \tag{VI.2}$$

This approach allows treating the tracer test data as a batch system. In this batch interpretation framework, the iron concentration at a given time can be expressed as the difference between the initial concentration and the iron that has been consumed:

$$C^*_{Fe} = C_{Fe}|_{amb} - \nu_{Fe}\left(C_{O_2}|_0 - C^*_{O_2}\right) \tag{VI.3}$$

where ν_{Fe} is the stoichiometric coefficient of reaction VI.1 and $C_{Fe}|_{amb}$ is the initial iron concentration in the fracture that corresponds to the ambient concentration in the pristine fracture fluid. From the reaction mechanism in equation VI.1, the stoichiometric coefficient should be $\nu_{Fe} = 4$.

At near-neutral pH, the aqueous reaction between DO and dissolved iron is generally described by a second-order kinetic law Singer and Stumm (1970):

$$\frac{dC^*_{O_2}}{dt} = -k_2 C^*_{Fe} C^*_{O_2}, \tag{VI.4}$$

where k_2 is the second-order kinetic constant. C_{O_2} and C_{Fe} are the oxygen and iron concentrations. The solution of this equation is (Rivas-Perez et al.; 2005):

$$C^*_{O_2}(t) = \frac{\nu_{Fe}.C_{O_2}|_0^2 - C_{Fe}|_{amb} * C_{O_2}|_0}{\nu_{Fe}.C_{O_2}|_0 - C_{Fe}|_{amb}.\exp k_2.t.\left(C_{Fe}|_{amb} - \nu_{Fe}C_{O_2}|_0\right)} \tag{VI.5}$$

Note that this batch interpretation framework is simplified and is theoretically exact only for first order reactions. As such it neglects the possible coupling between dispersion and non-linear reactions (Hubert et al.; 2020; Le Traon; 2021). We are currently developing an explicit reactive transport model to test these effects. Yet, this simplified interpretation framework provides useful information on the considered biogeochemical processes.

3 Results

3.1 Experiment overview

An overview of the tracer concentrations at the different phases of the tracer tests as well as the flow rates associated to fluid injection (injection and push phases) and pumping (pull phase) are presented in Figure VI.4. Flow rates were fairly stable at the different stages of the experiment, allowing to relate the conservative tracer variations to transport phenomena in the investigated fracture while ensuring minimum pumping artefacts. The duration of the injection breakthrough curve (about one hour in both tracer tests, see injection-push phases in Figure VI.4) is short compared to the rest of the phases in the experiment. During the push phase, the concentrations rapidly decrease down to the background levels, indicating that the tracer-solution has been successfully pushed inside the fracture. However, a remnant of DO was still detected in the fracture chamber

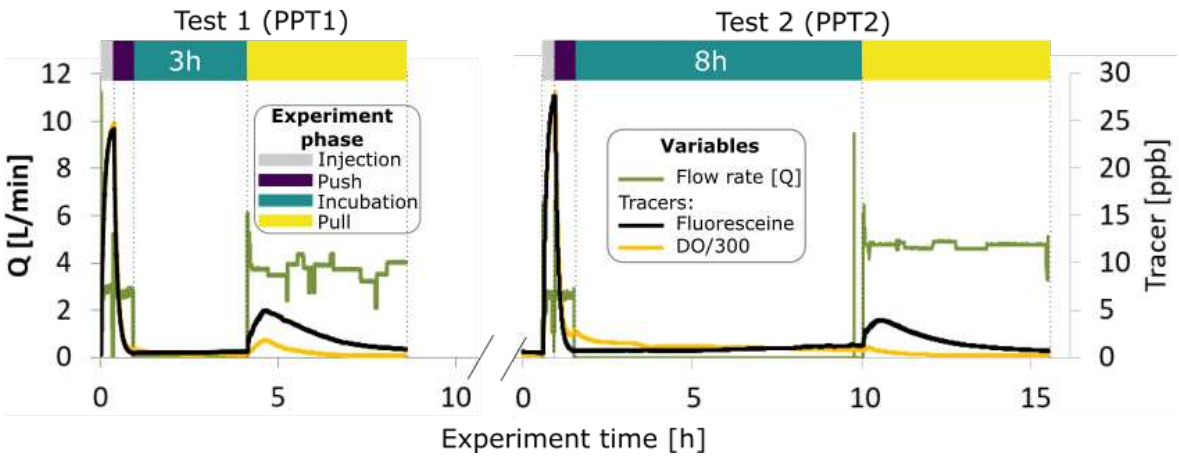

Figure VI.4: **Overview of the two tracer tests conducted in the borehole Pz26.** The color flags correspond to the different phases of the push-pull protocol as indicated in Figure VI.3. Dissolved oxygen (DO) concentrations have been downscaled by a factor 300 for visualization purposes.

in both tracer tests. The general stability of the concentrations during the incubation time indicate that, at the temporal scale of the experiment, the ambient flow in the fracture was negligible.

Table VI.2: **Mass balances for the two tracer tests.** Mass balances were computed as the integral of the break through curves of the injection-push and pull phases in the experiments.

	PPT1			PPT1		
	Fluo [mg]	O_2 [mmol]	Fe [mmol]	Fluo [mg]	O_2 [mmol]	Fe [mmol]
Injected mass[a]	11.0	35.6	42.0[b]	10.7	34.1	79.4[b]
Retrieved mass[a]	11.6	9.72	32.0	12.0	4.44	51.1
Reacted mass[a]	-	25.9	9.96[c]	-	29.6	28.3[c]
Recovery [%]	106	27.2	76.3	113	13.0	64.4
Reacted [%]	-	73.8	23.7	-	87.0	35.6

[a]: values computed as the integral of the breakthrough curves from the injection-push phase(injected mass) and the pull phase (retrieved mass).
[b]: corresponds to the ideally extracted mass of iron assuming no variations during the experiment.
[c]: corresponds to the difference between the "injected mass" row and the iron BTC integral.

The breakthrough curves of the pull phases reveal important differences between the conservative and reactive tracer curves which are due to the consumption of the reactive tracer during the incubation phase. The peak concentrations of dissolved O_2 in both tracer tests correspond to microaerobic levels: in PPT1, the peak O_2 value is about 20 μM (0.64 ppm) while in the PPT2 the peak value is about 10 μM (0.32 ppm). The high recovery percent of the conservative tracer (Table VI.2), confirms that ambient flows in the fracture are negligible at the time scale of the experiment. Values above 100 % are likely related to uncertainties in pumping rate measurements. About 74 % and 87 % of the injected dissolved O_2 mass reacted during experiments PPT1 and PPT2, respectively (Table VI.2). During the two experiments, the consumption of O_2 is large and consistently higher in the case of longer incubation time.

3.2 Biogeochemical response of the reactive hotspot

In order to further investigate the reaction pathways responsible for the O_2 consumption, the breakthrough curves are presented together with iron concentrations measured in the fluid. Iron BTC exhibits an opposing and symmetric shape with respect to the BTC of dissolved O_2 (see Figure VI.5). The synchronicity of both Fe

and O_2 BTCs strongly suggests that the consumption of dissolved O_2 is related to the oxidation of dissolved iron (Reaction VI.1). This reaction has been previously identified as the major DO sink in the study site (Bochet et al.; 2020). Apart from iron, no other cations or anions showed a significant variation in concentration during the experiment, which supports an iron-oxidizing dominated reaction. Furthermore, the extracted-DNA data in Figure VI.5 suggests that the reactive hotspot strongly influences the biogeochemical activity in the sampled planktonic communities. Taking as reference the DNA content in the pristine fracture (initial condition in Figure VI.5), the extracted DNA during the experiment exceeds the initial value by one order of magnitude in PPT1 and a factor 4 in PPT2.

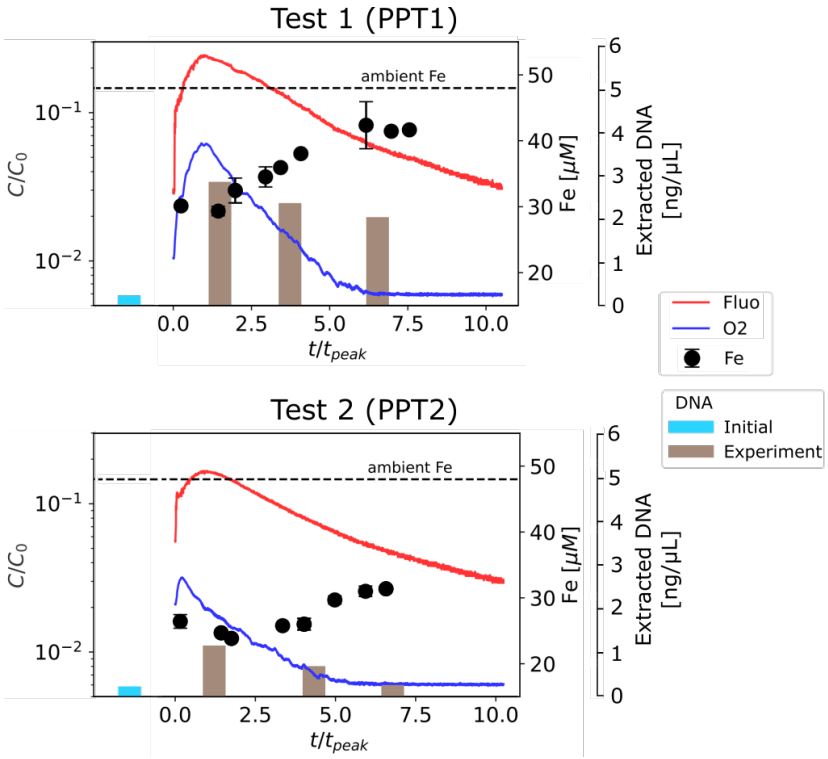

Figure VI.5: **Pull-phase breakthrough curves (BTCs) for both tracer tests and taxonomic composition of planktonic consortia sampled during the experiment.** The concentrations of tracers are presented as dimensionless concentrations, normalized by the initial concentration of the respective tracer in the "tracer-enriched" solution (see Table VI.1). The experimental time is presented as dimensionless time, normalized by the time to reach the peak of the conservative tracer in the respective PPT. The "ambient Fe" concentration corresponds to the background iron concentration for the fracture as reported in Figure VI.2. DNA data corresponds to DNA extracted from planktonic consortia sampled during the experiment and before any perturbation in the fracture ("initial").

3.3 Estimation of *in-situ* rate constants

Figure VI.6-A presents the dilution-corrected DO breakthrough curves (BTCs), normalized by the initially injected concentration. The reference value of $C*/C_0 = 1$ indicates that the tracer concentration is equal to the injected concentration, i.e. no reaction. The curves initially vary around a value of 1.0, then at a given moment, indicated by the black arrows, the concentrations decrease monotonously indicating consumption by reactions. For modeling purposes, we considered the time before the monotonous decrease of concentrations as a lag time. We thus only modeled the monotonous decreasing regions of the curves. Figure VI.6-B presents the fitting of Equation VI.5 on DO concentrations for both tracer tests. We used a non-linear least squares to fit the analytical model in Equation VI.5 to the O_2 BTCs. The model in Equation VI.5 has two fitting parameters: k_2 and $C_{Fe}|_{amb}$. The latter parameter corresponds to the concentration of dissolved iron in the pristine fracture fluid. Even if we measured this parameter before the PPT1 (see Table VI.1), we allowed both k_2 and $C_{Fe}|_{amb}$

to vary during the fitting process for the sake of comparison.

In Figure VI.6-B we present the best fitted models and the best-fitting parameters (k_2 and $C_{Fe}|_{amb}$). The modeled O_2 BTCs capture the data with fair accuracy. For the first tracer test (PPT1), the estimated second-order rate constant is $1.3 \times 10^3 M^{-}1.h^{-}1$ and the estimated initial concentration of iron in the fracture is 100 μM. For the second tracer test (PPT2), the estimated second-order rate constant is $5.8 \times 10^3 M^{-}1.h^{-}1$ and the estimated initial concentration of iron in the fracture is 75 μM.

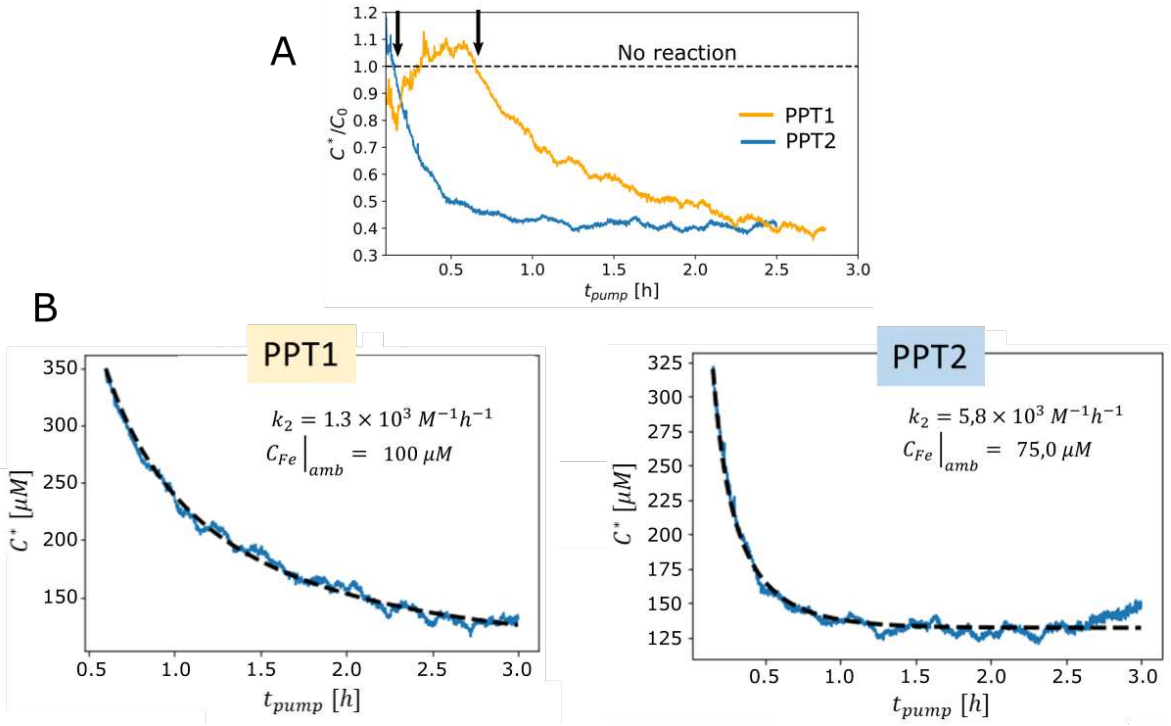

Figure VI.6: **Model fitting for the Pull-phase breakthrough curves of DO.** (A): dilution-corrected DO BTCs normalized by the initial DO concentration. The reference "no reaction" corresponds to no variations with respect to the initially injected concentration. The reaction is considered to start when the normalized concentrations decrease monotonously (point indicated by the black arrows). (B): Model fitting on the monotonous decreasing DO concentrations from A. Concentrations are corrected by dilution with Equation VI.2. The fitted model corresponds to Equation VI.5 is used to model the O_2.

We note that the model fitting of PPT2 indicates that the ambient concentration of iron during this experiment was about 37.6 muM. This is about ten units lower than the ambient concentration in the fracture measured before the experiments. This estimation seems, however, consistent with the late tailing behavior of the Fe BTC in the PPT1, that stabilized at a lower iron concentration than the expected ambient-Fe value.

4 Discussion

4.1 *In-situ* rates of DO consumption

The rates of DO consumption estimated during our tracer tests are in the same order of magnitude as second-order rate constants reported from laboratory experiments for similar reactions (see Table VI.3). It is worth noting that the rate constants presented in Table VI.3 correspond to abiotic conditions and heterogeneous reactions (DO consumption by the oxidation of structural iron from minerals). These heterogeneous reactions occur under a different reaction mechanism than the one presented in Equation VI.1. Only the reaction setting of Singer and Stumm (1970) corresponds to the mechanism from Equation VI.1, i.e. aqueous reaction between both dissolved iron and oxygen. Although the aqueous reaction VI.1 is effectively occurring in our experiments as confirmed by the synchronicity between Fe and DO BTCs in Figure VI.5, our estimated *in-situ* rate constants

are about two orders of magnitude slower than measured by Singer and Stumm (1970). Our values are thus closer to rate constants measured under less reactive settings in which iron is only available at mineral surfaces. These differences to possible transport limitations and non-linear couplings between dispersion and reactions (Le Traon; 2021).

Table VI.3: **Rates of DO consumption in this study and in published works**.

Reference	log k2 [M-1.h-1]	Reaction type	Condition
This study, PPT1	3.11	*in-situ*	FeOB hotspot
This study, PPT2	3.76	*in-situ*	FeOB hotspot
(Rivas-Perez et al.; 2003)	2.56	Heterogeneous (Granite)	Abiotic, pH 7
(White and Yee; 1985)	3.85	Heterogeneous (Biotite)	Abiotic
(White et al.; 1985)	3.75	Heterogeneous (Augite)	Abiotic
(Lane et al.; 1984)	3.79	Heterogeneous (Hornblende)	Abiotic
(Singer and Stumm; 1970)	5.17	Homogeneous	Abiotic

4.2 Biogeochemical activity driven by redox variations in the subsurface

The reactive push-pull tests presented in this work have evidenced that the deep continental subsurface is a system with the capacity to respond rapidly to changes in redox conditions. The high consumption percentages of DO in both tracer tests confirms the expected reactivity of this element. In an iron-rich fracture such as the one selected to conduct this experiment, dissolved O_2 is expected to be mainly consumed by iron oxidation (reaction VI.1) mediated by FeOB, which account for the majority of the plaktonic consortia in the fracture (Bethencourt et al.; 2020). This assumption is supported by the opposing and symmetric behavior of both O_2 and Fe BTCs. Reaction VI.1 has been reported to have abiotic and microbe-mediated mechanisms depending on the DO concentrations. In fact, reaction VI.1 is mostly microbe-mediated for DO concentrations within the *microaerobic* range ($0.01 < DO\ [ppm] < 1.6$) (Druschel et al.; 2008; Eggerichs et al.; 2014; Maisch et al.; 2019) and mostly abiotic for concentrations above this range (Emerson et al.; 2010). In our experiments, the peak O_2 concentrations in the fracture chamber during the injection-push phase were about 8.7 and 8.2 ppm in PPT1 and PPT2, respectively, whereas during the pull phase, at end of the experiment, the peak O_2 concentrations were 0.58 and 0.32 ppm in PPT1 and PPT2, respectively. The proximity of these concentrations to the microaerobic range suggests that the consumption of DO in reaction VI.1 during our experiment was driven mainly by microbe-mediated processes.

The extracted DNA from planktonic communities, presented in Figure VI.5, confirms an enhanced microbial activity in the fracture as a consequence of the induced change in redox conditions during the tracer tests. The anti-correlation between O_2 and Fe concentrations suggests that this microbial activity is related to iron oxidizing bacteria that can thrive from reaction VI.1 at microaerobic oxygen concentrations. Nonetheless, the mass balance presented in Figure VI.2 reveals that the observed stoichiometric ratio between both O_2 and Fe did not follow the expected ratio from reaction VI.1. In fact, the expected 4:1 ratio between Fe and O_2 would have result in a total consumption of Fe in the fracture. The *effective* stoichiometric ratio (Fe/O_2) obtained from the mass balance calculations corresponds to 0.4 during PPT1 and 0.95 during PPT2. These molar ratios suggest that the reaction pathways may be complex and involve multiple steps. As stated in Section 3.2, dissolved iron was the only dissolved species that showed a significant variation during the tracer tests, indicating that O_2 consumption, by pathways other than reaction VI.1, is probably related to either heterotrophic respiration processes, iron cycling or to reactions which involve non-aqueous species. We discuss these possibilities below.

We first discuss the potential contribution of heterotrophic respiration. Unlike autotrophs such as iron oxidizing bacteria, which couple O_2 reduction to the oxidation of inorganic electron donors such as iron, heterotrophic organisms can use dissolved O_2 as electron acceptor while using organic matter as an electron

donor. As a consequence, heterotrophic activity could result in the consumption of dissolved O_2 without impacting the concentration of other dissolved electron donors. Further 16s rRNA analyses of the planktonic communities sampled in this study, not shown here and being part of a future companion paper of this work, have revealed a important presence of heterotrophs belonging to the *Aquabacterium* genus. *Aquabacterium* have the ability to use dissolved O_2 as an electron acceptor during the degradation of organic matter (Kalmbach et al.; 1999). The evidence of their presence in the planktonic communities during our experiment supports this hypothesis.

Iron cycling in the reactive hotspot is another possible explanation for our observations. Indeed, the iron oxides that form as a result of the activity of Fe(II) oxidizing bacteria can be recycled by the action of dissimilatory Fe(III)-reducing (FeRB) bacteria (Roden et al.; 2004) through the following reaction:

$$Fe(OH)_3 + e^- \longrightarrow Fe^{2+} + 3\,OH^- \tag{VI.6}$$

FeRB bacteria are commonly heterotrophs, e.g. *Shewanella algae* (Roden et al.; 2004), and therefore their recycling activity can result in the regeneration of iron that can react again with O_2. We hypothesize this is also a likely mechanism in our experiment since the presence of iron oxidizers and iron reducers has been confirmed by the 16s rRNA analyses that will be developed in a future companion paper of this work.

Another hypothesis that could explain the anomalous stoichiometric ratio between O_2 and Fe during our experiments is that dissolved O_2 can also be consumed by reactive processes with non-aqueous species. Our experimental setting only allows us to track aqueous chemical species such as cations and anions. However, the presence of reduced minerals in the host-rock can also potentially react with dissolved O_2 without impacting the concentration of dissolved iron. This hypothesis is suggested by the model fitting in Figure VI.3, where the fitted $C_{Fe}|_{amb}$ concentrations exceed the measured ambient concentration in the fracture before the PPT1, i.e. 47.3 μM (2.65 ppm). This indicates that additional iron sources would be needed to explain the DO consumption. However, the fact the the more readily available and highly reactive iron, i.e. aqueous iron, was not consumed likely indicates that reaction pathways other than iron consumption were operating in the fracture. In an analogous way, in our experiment we only studied the planktonic communities in the fracture. However, there is also a potentially non-negligible contribution of the mineral-attached microbial communities that we can not assess with our experimental approach.

4.3 Do redox fluctuations restructure the biogeochemical state of inertial deep subsurface environments?

It is interesting to note the fast response of the microbial communities to the redox changes during the tracer tests. We observed up to one order of magnitude increase in extracted DNA during the tracer tests compared with the pristine fracture fluid (see Figure VI.5). Such a significant increase in the extracted DNA suggests that microbial activity was enhanced despite of the short time frame of our experiment (three and eight hours of incubation in PPT1 and PPT2, respectively). Such a fast response of the fracture ecosystem contrasts with the common view of the deep continental subsurface as an inertial environment where growth rates are low (Templeton and Caro; 2023). The doubling time of iron oxidizing bacteria in laboratory cultures has been reported to be between 8 to 13 hours (Emerson and Moyer; 1997). The fast response of microbial communities during our tracer tests suggest that under *in-situ* conditions and high redox potentials created by water mixing, the growth rates can potentially be faster than estimated in the lab. An alternative possibility to explain the fast increase in planktonic extracted DNA could be due to the active detachment of mineral-attached microbes under the modified redox-conditions in the fluid. Indeed, it has been shown that microbes can actively attach or detach from mineral surfaces depending on the availability of nutrients in the surrounding fluid (Jones and Bennett; 2017). Is it thus possible that the input of O_2 in the fracture induced the detachment of mineral-attached prokaryotes. A better understanding of the mineral-attached biomass in the fracture is however needed

to determine whether this mechanism is actually producing the increase in planktonic DNA.

It is also worth noting that the two tracer tests developed in this study were sequential in time, with a lag time of 12 hours between the experiments. While the principle of a push-pull tracer test is to extract all the injected fluids, therefore not leaving any perturbation in the environment, this is potentially not the case. Indeed, the late tailing values of dissolved iron in PPT1 were below the expected ambient-Fe which is also consistent with a lower ambient-Fe concentration calibrated for the second experiment. The late tailing value in the PPT2 exhibits a similar behavior: it stabilises at an iron concentration that is lower than the *new* ambient-Fe concentration in the PPT2. Taken together, these observations suggest that the redox fluctuations induced by our experiments, results in a new biogeochemical state of the fracture environment that persists even after the retrieval of the injected tracer solutions and the return to the original redox conditions.

The new biogeochemical state, induced by the redox fluctuations in our experiment, possibly affected the thermodynamic potential of the fracture system. In fact, after the first redox cycle (PPT1) the new ambient-Fe concentration was lower than before the experiment. This resulted in a lower reactive potential for reaction VI.1, and for iron-oxidizing bacteria that thrive from this reaction. We hypothesize that this reduction in the reaction potential is a likely explanation for the lower concentration of extracted-DNA in PPT2 compared to PPT1.

The adaptation of microbial communities to fluctuating redox conditions has been suggested previously and has been related to an enhanced activity of the microbial consortia (DeAngelis et al.; 2010). By studying soil microbial communities, DeAngelis et al. (2010) indeed showed that the fluctuation redox conditions enhanced the activity of metabolisms that usually are restricted to environments where redox conditions are either oxic or anoxic. We expect a similar effect induced by the transport of oxic groundwater following recharge events, a situation that is common in fractured environments (Bochet et al.; 2020; Osorio-Leon et al.; 2023). In a fluctuating environment, the changing redox potential could favor, in a same environment, the activity of metabolisms requiring contrasted redox conditions.

5 Conclusion

In this chapter, we presented a field experiment that allowed us to, *in-situ*, reproduce a groundwater recharge event producing fluctuating redox conditions in a reducing fracture-environment. Our experimental setup allowed us to successfully track the biogeochemical response of an *in-situ* reactive hotspot that was induced by the mixing between iron-rich reducing groundwater and an O_2-enriched solution injected in a fracture at -20 m deep. The observed breakthrough curves suggested that the dominant reaction in the reactive hotspot was the oxidation of iron by oxygen, that is correlated to a fast response in the activity of planktonic microbial communities, as suggested by extracted-DNA measurements. We determined *in-situ* rate constants for the DO consumption in the fracture that resulted in values which are 2 orders of magnitude below the expected aqueous rates for the aqueous oxidation of iron by DO. Based on the observed breakthrough curves and the stoichiometric ratios between O_2 and Fe, we conclude that the induced reactive hotspot triggered a more complex reactive network around dissolved O_2. This network is primarily related to the activity of iron-oxidizing bacteria but, additionally, it might also be linked to processes such as the respiration of heterotrophic microorganisms or iron cycling by the activity of Fe(III) reducers. Collectively, our results suggest that fluctuating redox conditions in the subsurface, that can be induced by groundwater recharge events, have the potential to modify the biogeochemical conditions and the reactive potential of subsurface environments.

6 Chapter conclusion: the deep continental subsurface as a dynamic system

In this chapter, we have presented a field experiment using a double-packer device that allowed us to mimic a groundwater recharge event. This approach is especially valuable for imaging events that are challenging to

observe under natural conditions in the field. Indeed, the transport of oxic groundwater into the subsurface can result from hydrologic forcings such as large recharge events, that are difficult to predict. By conducting two sequential reactive push-pull tests (PPTs), we introduced a fluctuating redox perturbation in a reducing fracture. Each of these two tracer tests resulted in the creation of a hotspot of biogeochemical reactivity that was dominated by the iron oxidation by oxygen and a consequent activity of iron oxidizing bacteria (FeOB). We determined *in-situ* reaction rates for the iron oxidation reaction by DO that highlight that in-situ rates are lower than laboratory predictions. Furthermore, stoichiometric ratios between Fe and DO demonstrated that mechanisms other than iron consumption are likely to consume DO in the subsurface such as potential heterotrophic metabolisms that can be triggered by the activity of FeOB. Remarkably, the response of the fracture biogeochemical system was fast compared to laboratory-derived growth rates for FeOB. Furthermore, our measurements also revealed that the redox fluctuations resulted in a change of the biogeochemical conditions of the fracture system that durably persisted after the experiments. To summarize, the evidence presented in this chapter challenges the view of the continental subsurface as an inertial environment where microbial activity is low and slow. Our results suggest that hydrological forcings resulting in groundwater redox fluctuations, provide a dynamic stimulus with the potential to enhance the biogeochemical activity in the continental subsurface.

While the experimental setup presented in this chapter allowed us to sample and characterize the aqueous reactions and planktonic prokaryote communities, it also raises questions about the potential role of mineral attached prokaryotes. Part of the questions pertaining to the continental subsurface are:

1. **Are non-aqueous water-rock reactions also affected by contrasts in redox conditions?**
2. **Can redox conditions affect the mineral-attached biomass and its metabolic functions?**

In the following chapter, we will delve into this complementary aspect of the deep continental subsurface, focusing on mineral-attached prokaryotes and the reactivity of rock-forming minerals. We will employ a novel experimental approach to explore these questions in a second field experiment.

7 Perspectives

We present here some perspectives that can be considered to further exploit the data from this experiment or to plan new push-pull experiments in the future.

- To further exploit the experimental dataset:
    1. **Modeling of transport processes during the PPT:** to model the breakthrough curves in this chapter we used a simplified framework that considered the push-pull experiment as a batch system Haggerty et al. (1998). While our simplified model described remarkably well the monotonous decrease of DO break through curves, the measured effective reaction rates are possibly affected by transport limitations and mixing processes (Le Traon; 2021). We are currently developing a fully resolved reactive transport model to investigate these effects. This may provide further insights to better constrain the observed lab-field discrepancy on the *in-situ* reaction rates.
    2. **Metagenomic and metatranscriptomic analyses of the planktonic microbial communities:** this perspective is part of the future companion article of this work that will be first-authored by one of the co-authors of this chapter (Melissa Garry) and therefore is not presented here. Indeed, during the experiment we extracted both DNA and RNA from the planktonic communities at three key moments of the breakthrough curves. This samples have been analysed for metagenomics (DNA) and metatranscriptomics (RNA) in order to disentangle the metabolic functions that were, respectively, present and active during the experiment. This information will provide further insights on the biogeochemical processes that were stimulated by the fluctuating redox conditions induced in our experiment. Moreover, the metagenomic and metatranscriptomic analyses could

provide useful information to explain the fast increase in planktonic DNA observed during the tracer tests. It is not clear whether the fast DNA increase is due to particular physiological states of the indigenous consortia or to the active attachment-detachment of microbes from mineral surfaces. A taxonomic analysis of the microbial diversity during the experiment could for example evidence the presence of taxons which are characteristic of mineral-attached rather than of planktonic communities. Nevertheless, this requires to be accompanied by a characterization of the microbial diversity of mineral-attached prokaryotes which has not been so far. This aspect is tackled in the next chapter.

3. **Isotopic labeling of reactive tracers:** future reactive-tracer tests could include the use of isotope-labeled reactive tracers such as ^{18}O or ^{13}C. The use of oxygen isotopes could be useful to further confirm the link between oxygen consumption and microbe-mediated reactions as it was the case in Chapter V. On the other hand, the use of carbon isotopes could be useful to relate the bigeochemical reactivity in the hotspot to the primary production of biomass. Primary production of biomass is related to the activity of autotrophic organisms that fix CO_2 to synthesize organic molecules. Therefore, the use of a labeled carbon source such as $^{13}CO_2$ in the reactive tracer solution could provide useful information in the production of autotrophic biomass, ultimately linking the fluctuations of groundwater redox conditions to biomass production in the subsurface.

8 Take home messages

The deep continental subsurface as a dynamic system

- We designed an experimental setup that allows to reproduce, *in-situ*, a recharge event in which oxic groundwater intrudes in a fracture hosting reducing groundwater.
- The mixing between oxic and reducing groundwaters results in a reactive hotspot of biogeochemical activity, mainly dominated by the microbe-mediated oxidation of dissolved iron by oxygen.
- We estimated *in-situ* rate constants for the iron oxidation by oxygen. The estimated rates are about 2 orders of magnitude than representative laboratory measurements.
- In-situ planktonic consortia exposed to an induced redox fluctuation exhibited a physiological response that is faster than laboratory derived growth rates.
- Our findings challenge the view of the continental subsurface as an inertial and low-activity environment.

9 Chapter acknowledgements

This research was funded, in whole, by ANR EQUIPEX CRITEX project (ANR-11-EQPX-0011) and the ERC project ReactiveFronts (648377). This research was made possible by a great team work. I want to thank all the members of the team that were present in the field during the month of october 2020, despite of the difficult weather and the visit of the unexpected "Alex" storm: the experiment leaders Camille Bouchez and Tanguy Le Borgne, my PhD colleague Melissa Garry and the associated researchers and engineers Olivier Bochet, Eliot Chatton, Julien Farasin, Nicolas Lavenant, Francesco Gomez, Thierry Labasque. It was great to spend this time in the field with you all !

Bibliography

Bethencourt, L., Bochet, O., Farasin, J., Aquilina, L., Borgne, T. L., Quaiser, A., Biget, M., Michon-Coudouel, S., Labasque, T. and Dufresne, A. (2020). Genome reconstruction reveals distinct assemblages of Gallionellaceae in surface and subsurface redox transition zones, *FEMS Microbiology Ecology* **96**(5).

Bochet, O., Bethencourt, L., Dufresne, A., Farasin, J., Pédrot, M., Labasque, T., Chatton, E., Lavenant, N., Petton, C., Abbott, B. W., Aquilina, L. and Le Borgne, T. (2020). Iron-oxidizer hotspots formed by intermittent oxic–anoxic fluid mixing in fractured rocks, *Nature Geoscience* **13**(2): 149–155.

DeAngelis, K. M., Silver, W. L., Thompson, A. W. and Firestone, M. K. (2010). Microbial communities acclimate to recurring changes in soil redox potential status, *Environmental microbiology* **12**(12): 3137–3149.

Druschel, G. K., Emerson, D., Sutka, R., Suchecki, P. and Luther, G. W. (2008). Low-oxygen and chemical kinetic constraints on the geochemical niche of neutrophilic iron(II) oxidizing microorganisms, *Geochimica et Cosmochimica Acta* **72**(14): 3358–3370.

Eggerichs, T., Opel, O., Otte, T. and Ruck, W. (2014). Interdependencies between Biotic and Abiotic Ferrous Iron Oxidation and Influence of pH, Oxygen and Ferric Iron Deposits, *Geomicrobiology Journal* **31**(6): 461–472.

Emerson, D., Fleming, E. J. and McBeth, J. M. (2010). Iron-Oxidizing Bacteria: An Environmental and Genomic Perspective, *Annual Review of Microbiology* **64**(1): 561–583.

Emerson, D. and Moyer, C. (1997). Isolation and Characterization of Novel Iron-Oxidizing Bacteria That Grow at Circumneutral pH, *Applied and Environmental Microbiology* **63**(12): 4784–4792.

Fortune, W. B. and Mellon, M. G. (1938). Determination of Iron with o-Phenanthroline: A Spectrophotometric Study, *Industrial and Engineering Chemistry - Analytical Edition* **10**(2): 60–64.

Haggerty, R., Schroth, M. and Istok, J. (1998). Simplified method of "push-pull" test data analysis for determining in situ reaction rate coefficients, *Groundwater* **36**(2): 314–324.

Hubert, A., Aquino, T., Tabuteau, H., Méheust, Y. and Le Borgne, T. (2020). Enhanced and non-monotonic effective kinetics of solute pulses under michaelis–menten reactions, *Advances in Water Resources* **146**: 103739.

Jones, A. A. and Bennett, P. C. (2017). Mineral Ecology : Surface Specific Colonization and Geochemical Drivers of Biofilm Accumulation , Composition , and Phylogeny, *Frontiers in Microbiology* **8**(March): 1–14.

Kalmbach, S., Manz, W., Wecke, J. and Szewzyk, U. (1999). Aquabacterium gen. nov., with description of aquabacterium citratiphilum sp. nov., aquabacterium parvum sp. nov. and aquabacterium commune sp. nov., three in situ dominant bacterial species from the berlin drinking water system, *International Journal of Systematic and Evolutionary Microbiology* **49**(2): 769–777.

Lane, D., Jones, T. and West, M. (1984). Preliminary assessment of oxygen consumption and redox conditions in a nuclear waste repository in basalt, ACS Publications.

Le Traon, C. (2021). *Gradients chimiques dans les systèmes hydrologiques-origine, dynamique et conséquences sur les réactions chimiques*, PhD thesis, Université de Rennes 1.

Maisch, M., Lueder, U., Laufer, K., Scholze, C., Kappler, A. and Schmidt, C. (2019). Contribution of Microaerophilic Iron(II)-Oxidizers to Iron(III) Mineral Formation, *Environmental Science and Technology* **53**(14): 8197–8204.

Osorio-Leon, I., Bouchez, C., Chatton, E., Lavenant, N., Longuevergne, L. and Le Borgne, T. (2023). Hydrological and geological controls for the depth distribution of dissolved oxygen and iron in silicate catchments.

Rivas-Perez, J., Banwart, S. A. and Puigdomenech, I. (2005). The kinetics of O 2 (aq) reduction by structural ferrous iron in naturally occurring ferrous silicate minerals, *Applied Geochemistry* **20**: 2003–2016.

Rivas-Perez, J., Tullborg, E.-L. and Banwart, S. A. (2003). The kinetics of O2(aq) reduction during oxidative weathering of naturally occurring fracture minerals in groundwater, *Mineralogical Magazine* **67**(02): 399–414.

Roden, E. E., Sobolev, D., Glazer, B. and Luther, G. W. (2004). Potential for microscale bacterial Fe redox cycling at the aerobic-anaerobic interface, *Geomicrobiology Journal* **21**(6): 379–391.

Singer, P. C. and Stumm, W. (1970). Acidic Mine Drainage: The Rate-Determining Step, *Science* **167**(3921): 1121–1123.

Templeton, A. S. and Caro, T. A. (2023). The Rock-Hosted Biosphere, *Annual Review of Earth and Planetary Sciences* **51**(1): 493–519.

White, A. F. and Yee, A. (1985). Aqueous oxidation-reduction kinetics associated with coupled electron-cation transfer from iron-containing silicates at 25°C, *Geochimica et Cosmochimica Acta* **49**(5): 1263–1275.

White, A. F., Yee, A. and Flexser, S. (1985). Surface oxidation-reduction kinetics associated with experimental basalt-water reaction at 25°C, *Chemical Geology* **49**(1-3): 73–86.

VII. FIELD EXPERIMENT 2: MICROBE-MINERAL INTERACTIONS UNDER CONTRASTED REDOX LANDSCAPES

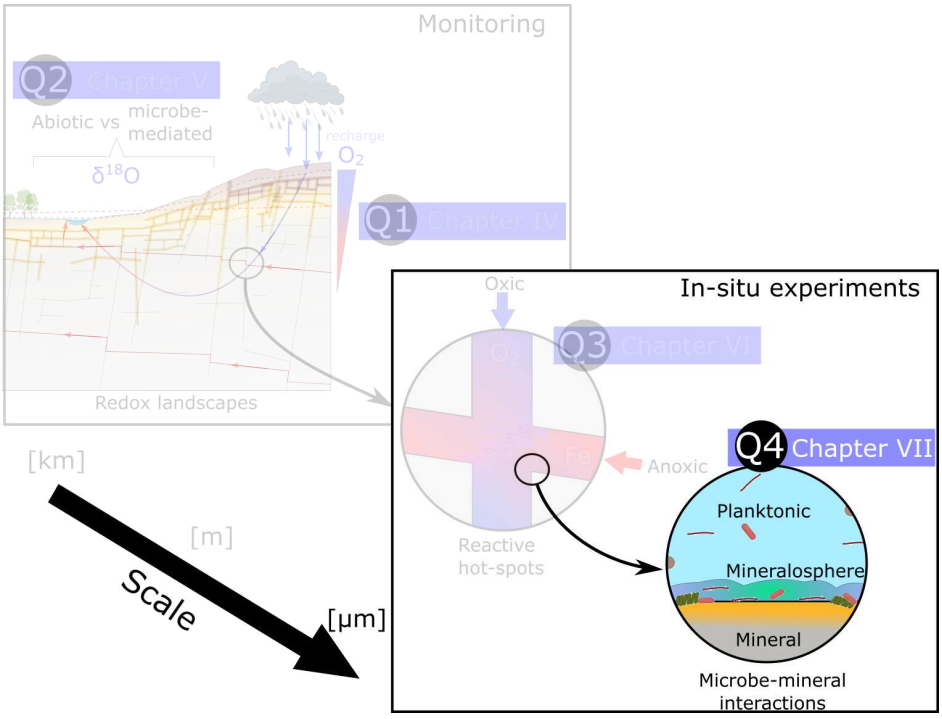

Contents

In Chapter VI we have seen that the presence of dissolved oxygen (DO) can affect the planktonic (i.e. suspended) microbial communities by enhancing the activity of aerobic metabolisms. *In-situ* planktonic communities can be easily sampled by groundwater pumping as we have shown in Chapter VI. However, several studies have reported that the majority of the subsurface biomass occurs in the form of mineral-attached prokaryotes [e.g. Flemming and Wuertz (2019)]. For instance, Whitman et al. (1998) estimated that attached cells in the continental subsurface are about 10^3 times more abundant than planktonic cells. Therefore, the mineral-attached biomass represents at least 99% of the deep continental subsurface biomass (Flemming and Wuertz; 2019) and has been identified as a particular ecological niche called the *mineralosphere* (Uroz et al.; 2015).

By their attached nature, mineral-attached biofilms are difficult to sample and the big majority of the research on the deep subsurface biomass has focused on planktonic prokaryotes [e.g. Overholt et al. (2022)]. *In-situ* mineral-attached communities have been mainly studied during drilling campaigns in sedimentary environments, where researchers can easily access drilling cuttings or sediment cores [e.g. Kölbel-Boelke et al. (1988); Sinclair and Ghiorse (1989); Balkwill (1989); Hazen et al. (1991); Lehman et al. (2001b); Flynn et al. (2012)]. Drilling methods have the advantage of allowing access to pristine rock samples, but preserving samples from contamination with drilling muds can be challenging. This is why the incubation of surrogate minerals in *in-situ* microcosms [e.g. Alfreider et al. (1997); Griebler et al. (2002); Reardon et al. (2004); Converse et al. (2015); Casar et al. (2020)] or *laboratory* microcosms [e.g. Lehman et al. (2001a); Jones and Bennett (2017); Nuppunen-Puputti et al. (2022)] has become a common alternative over the years. While laboratory approaches are effective at disentangling processes, it is usually challenging to extrapolate their results to the natural environment given the simplifications required to put together viable laboratory settings. *In-situ* incubations, on the other hand, can be particularly valuable to obtain information more relevant to the field, even if experimental conditions are still challenging to constrain in the field.

Box VII.1 - The deep continental biosphere's global biogeochemical influence is underestimated.

Estimates based solely on planktonic consortia have suggested that carbon fixation rates in the continental subsurface can rival those observed in marine environments (Overholt et al.; 2022). This high carbon-fixation potential, calculated solely from the minority planktonic fraction, implies a significant underestimation of the potential impact that the deep biosphere may have on global biogeochemical cycles such in the carbon case. Metagenomic surveys have consistently revealed that mineral-attached consortia possess a higher abundance of metagenomes containing genes involved in elemental cycling, compared to their planktonic counterparts (Anantharaman et al.; 2016). Nonetheless, sampling the mineral-attached biosphere remains challenging, resulting in a significantly smaller body of research compared to the planktonic biosphere. There is therefore a need for sampling methods tailored to the mineral-attached biosphere.

In this chapter, we designed proof-of-concept experimental setting to, *in-situ*, incubate surrogate minerals while decoupling critical experimental variables such as the nature of the mineral substrate, the redox conditions of groundwater and the microbe-mineral contact. We designed a passive incubation device allowing to accommodate a set of mineral substrates in three different sample supports: (1) "mineral coupons", (2) "rock thin sections" and (3) "mineral powders". See Figure VII.1 for further details. To prepare the mineral coupons and powders we used rock-forming minerals such as: biotite, pyrite, olivine and quartz. Following the incubation time of the surrogate minerals (10 months in our case), we recover the device containing both mineral-attached biofilms and *in-situ* weathered mineral surfaces for downstream analysis. The mineral substrates are incubated in two redox-contrasted open-hole boreholes of the CZO of Ploemeur, one with oxic-recharge water (Psr1 borehole) and the other with anoxic-discharge water (Psr5 borehole). The incubation device was placed at the depth of the main fracture in each borehole, based on prior characterization of the site's hydrogeology (Osorio-Leon

et al.; 2023).

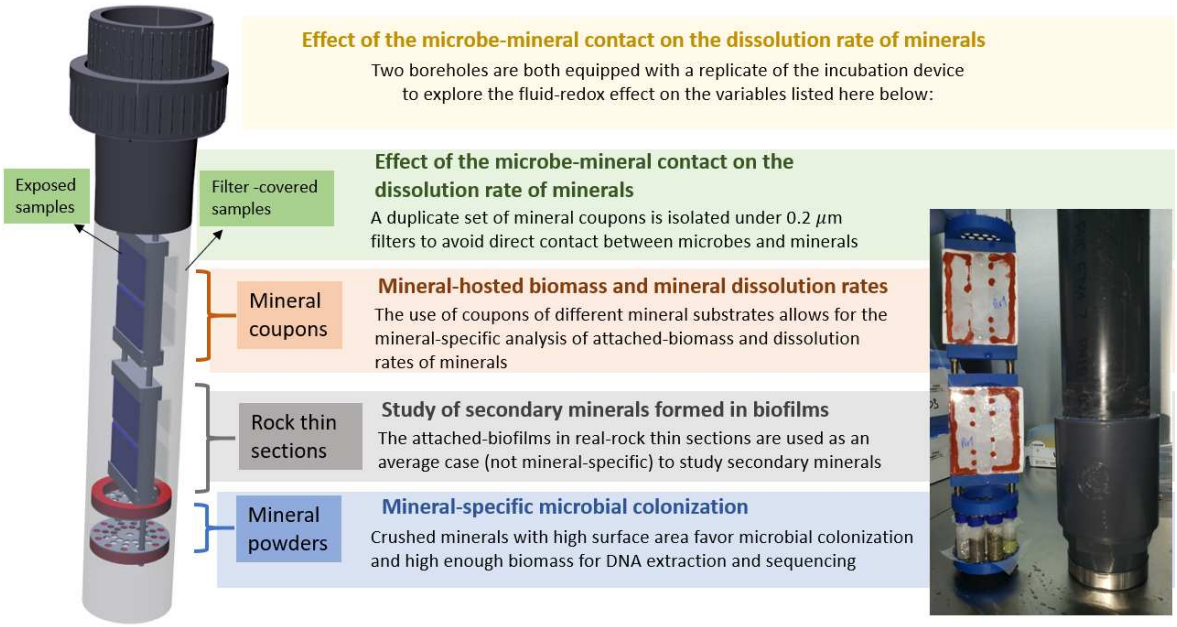

Figure VII.1: **Description of the proof-of-concept passive incubator device.** The left-side image corresponds to a 3D model of the device while the image on the right shows the device with the mineral samples already mounted. This device is used in this chapter to explore the effects of the groundwater redox conditions on different aspects of the microbe-mineral interactions. Incubated mineral coupons include: biotite, pyrite, quartz, olivine and calcite. All minerals except for calcite were also incubated in powder form in the "mineral-powders" compartment. Rock thin sections are polished micaschist samples obtained from a rock-core from borehole B2, from the Ploemeur CZO.

Box VII.2 - The microbe-mineral feedback: a conversation between life and rocks

The overarching theme in this chapter is how the redox state of groundwater, in particular the presence of oxic and anoxic zones, affects the microbe-mineral interactions. Nevertheless, microbe-mineral interactions encompass a broad range of complex processes. Microorganisms can take part in geological processes, and minerals, in turn, can influence microbial activities. **Thus, this chapter is divided into two main parts, each exploring one direction of the microbe-mineral feedback.** In the first part of the chapter, we explore the *mineral-to-microbe* direction. We focus particularly on (1) how the cell abundance (i.e. the biomass) and (2) the taxonomic composition of mineral-attached consortia are impacted by redox conditions and mineral substrates in the subsurface. In the second part of the chapter, we explore the feedback in the opposite way, i.e. the *microbe-to-mineral* direction. In this part, that is presented as perspective, we focus on answering the following questions: (1) Can we quantify a microbe-induced effect on the weathering of minerals under *in-situ* conditions? and (2) What is the chemical and mineralogical composition of secondary minerals formed in *in-situ* mineral-attached biofilms?

1 Effects of minerals on microbes

1.1 Article: "Mineral substrate and fluid-redox conditions control cell density in attached biofilms: *in-situ* incubations in deep groundwater", in prep. for *Geobiology*

Control of mineral substrate and fluid-redox conditions on cell density in attached biofilms: insights from *in-situ* incubations in deep groundwater

Ivan-David Osorio-Leon[1], Bastien Wild[2,3], Camille Bouchez[1], Achim Quaiser[5], Emmanuelle Gerard[4], Bénédicte Menez[4], Alexis Dufresne[5], Tanguy Le Borgne[1]

[1]Univ Rennes – CNRS, Géosciences Rennes - UMR 6118. Rennes, France
[2]Princeton University, USA
[3]University of Grenoble, ISTerre, CNRS, Grenoble, France
[4]Université Paris, Institut de Physique du Globe de Paris, UMR 7154 CNRS, F-75005 Paris, France
[5]Univ Rennes – CNRS, ECOBIO - UMR 6553. Rennes, France

Key Points:

- We developed a low-cost passive device for the *in-situ* incubation of mineral surfaces and sampling of attached microorganisms.
- We show that the mineral substrate exerts a first-order control on cell densities in attached biofilms as more reactive minerals host higher cell densities.
- Fluid-redox conditions play an important role for biotite surfaces only, suggesting a preferential use of the abundant dissolved iron under anoxic conditions

Corresponding author: Ivan-David Osorio-Leon, idosoriole@unal.edu.co

Abstract

The deep continental subsurface sustains most of Earth's microbial life. Recent studies have shown that about 80% of Earth's microbial biomass lives in the deep continental subsurface, mostly in the form of biofilms, with important consequences for biogeochemical processes and element fluxes in the critical zone. However, one of the major uncertainties in those studies comes from cell density estimations that have been obtained from microbial communities filtered from fluids. Little is known about cell densities in microbial biofilms attached to minerals in the subsurface, especially because of difficulties to access and sample those environments. A comprehensive and quantitative view of how the mineral substrate or the lithology affect cell density in biofilms is particularly missing. In this study, we engineered a set of probes to incubate well-characterized mineral samples at key locations of the fractured-bedrock aquifer of the Ploemeur-Guidel critical zone observatory (Brittany, France). We incubated 3 environmentally-relevant mineral substrates with different geochemical compositions (quartz, pyrite and biotite). The samples were incubated *in-situ* during ten months in two 100-meter deep boreholes with redox-contrasted groundwater typical of recharge (oxic) and discharge (anoxic) zones of the aquifer. After incubation, we characterized the morphology and cell density in the mineral-attached biofilms. Our results show that the mineral substrate acts as a primary control as the highest cell densities are found on the most reactive minerals. While inert mineral substrates have an average of $10^4 cell.cm^{-2}$, reactive minerals host between 10^6 and $10^7 cell.cm^{-2}$. The fluid-redox conditions had a major influence on cell densities formed on biotite surfaces but not on pyrite surfaces. We used a thermodynamic model to explain these differences in terms of availability of electron donors/acceptors in the fluid and solid phases. This study provides quantitative and field-relevant information on biofilms attached to minerals which should allow to better constrain biomass estimations as well as reactive transport models for microbe-mediated mineral dissolution.

1 Introduction

The deep continental subsurface, defined as the rocky environment deeper than 8 meters, excluding soil (Whitman et al., 1998), sustains most of Earth's microbial life. Microbial cells in the deep continental subsurface have been assessed by several authors (Whitma et al., 1998; Mcmahon & Parnell, 2014; Magnabosco et al., 2018; Bar-on et al., 2018; Flemming & Wuertz, 2019), and recent estimates range around $3{\times}10^29$ cells, i.e. about 80% of Earth's microbial biomass according to Bar-on et al. (2018). These cells represent a large carbon reservoir in our planet, and they mostly occur in the form of biofilms attached to minerals (Flemming & Wuertz, 2019). They are believed to play a central role on the biogeochemical processes in the subsurface. However, global estimations of the deep microbial biomass bear large uncertainties mainly related to the difficulty to access and study subsurface environments. Some of the main uncertainty factors for biomass estimations have been identified by Bar-on et al. (2018): (1) the correlation between biomass and depth, (2) the total volume of aquifers and how it depends on depth and (3) the ratio of attached to unattached cells. In this work we focus on this latter factor. Indeed, microorganisms in subsurface environments can be found either suspended in the fluid (planktonic cells) or attached to rock surfaces (attached cells) mostly in the form of biofilms (Flemming & Wuertz, 2019). The common approach to estimate the total microbial biomass in the continental subsurface is based on planktonic cell counts which are then extrapolated to the total cells by assuming a *constant* ratio between attached and unattached cells (R_{a-u}) (Whitman et al., 1998; Mcmahon & Parnell, 2014; Magnabosco et al., 2018; Bar-on et al., 2018; Flemming & Wuertz, 2019). R_{a-u} values range between 10 and 10^3 (Kölbel-Boelke et al., 1988; Alfreider et al., 1997; Whitman et al., 1998; Lehman, Roberto, et al., 2001; Griebler et al., 2002) and indicate that attached cells account for, at least, 99% of cells in the continental subsurface (Flemming & Wuertz, 2019). It should nevertheless be noted that models estimating continental subsurface biomass (Whitman et al., 1998; Mcmahon & Parnell, 2014; Magnabosco et al., 2018; Bar-on et al., 2018; Flem-

ming & Wuertz, 2019) usually consider R_{a-u} as a constant. Yet, little is known about the dependence of attached cell densities to environmental factors such as depth, redox conditions or lithology. Moreover, a constant R_{a-u} implies that both planktonic and attached cell populations respond similarly to changes in environmental factors. This implication may not necessarily be accurate since the availability of nutrients and energy sources between fluid and mineral environments leads to contrasted compositions of planktonic and attached microbial communities (Lehman, Roberto, et al., 2001) and a different partitioning of cells between solid and aqueous phases (Ginn et al., 2002).

The attachment of microbial cells to mineral surfaces provides several advantages with respect to planktonic cells: mineral surfaces offer a source of nutrients and a source of energy (Dong et al., 2022), and mineral-attached biofilms provide chemical protection and favorable microenvironments (Liermann et al., 2000; Uroz et al., 2009; Ahmed & Holmström, 2015). Moreover, mineral-attached biofilms are composed of a diversity of extracellular polymeric substances (EPS) which contribute to create a favorable environment for microorganisms denominated as the *mineralosphere* (Uroz et al., 2009; Flemming et al., 2022). The presence of EPS in the biofilm matrix for example contributes to retain exoenzymes and to the sorption or stabilization of nutrients and ions (Grant et al., 2016; Flemming et al., 2022).

Direct enumerations of subsurface prokaryotes in mineral-attached biofilms are scarce because of the difficulty to obtain uncontaminated samples. While numerous studies have investigated the composition and diversity of mineral-attached microbial communities, very few works measured the cell abundance in such biofilms. Virtually all available cell counts on subsurface biofilms have been reported for unconsolidated sediments sampled during drilling campaigns (Kölbel-Boelke et al., 1988; Sinclair & Ghiorse, 1989; Hazen et al., 1991; Lehman, Roberto, et al., 2001) or incubated in boreholes (Alfreider et al., 1997; Griebler et al., 2002). In other geologic environments such as fractured rocks, cell counts have been reported in a laboratory incubation experiment (Lehman, Colwell, & Bala, 2001) or more recently, in *in-situ* incubated surrogate minerals (Casar et al., 2020; Casar, Kruger, & Osburn, 2021). Most of these works used a common approach for enumerating cells which involved resuspending the mineral-attached biofilm by shaking or sonication, followed by counting the resuspended prokaryotes using traditional methods for planktonic cells, such as Acridine Orange direct counts (AODC) [e.g. Lehman, Roberto, et al. (2001)]. This biofilm-destructive approach was necessary because the irregular shape of sediments is not suitable for cell enumeration in a microscope. As a consequence, all the information about the biofilm structure, microbe-mineral interactions and cell distribution in the biofilm was lost. More recently, Casar et al. (2020) and Casar, Kruger, and Osburn (2021) incubated polished mineral coupons which allowed the direct imaging of mineral-attached biofilms by SEM. While SEM is suitted to image mineral-attached biofilms, cell enumerations by this approach can be challenging in multilayer biofilms or when the distinction between biotic and abiotic morphologies can be ambiguous [e.g. Chan et al. (2019)]. Casar et al. (2020) studied the dependence of the number of cells in attached biofilms on the type of mineral substrate. They found that the metabolic relationships between the biofilms and the colonized mineral substrates can promote selective colonization and enhanced cell densities. This finding motivates further investigation to identify how environmental factors affect attached biomass in the continental subsurface.

Here, we assessed the control of two environmental conditions, (1) fluid-redox and (2) lithology, on cell densities in mineral-attached biofilms. We used *in-situ* incubation experiments of surrogate minerals in two redox-contrasted boreholes of the Guidel catchment in the critical zone observatory (CZO) of Ploemeur, France. A detailed description of this site and the geological context is provided in (Osorio-Leon et al., 2023). We developed a new approach, combining confocal microscopy with microtopography analyses, to enumerate prokaryotic cells in multilayer biofilms while preserving and charac-

terizing biofilm structure. We also investigated the composition of attached communities and the thermodynamic potential of putative metabolic reactions to interpret the measured cell densities.

2 Materials and Methods

2.1 Mineral samples preparation

2.1.1 Model minerals

Monocrystal mineral coupons of biotite, pyrite and quartz, provided by Wards Science (USA), were prepared at Princeton University to expose preferential mineralogical phases and eliminate anisotropic effects of the mineral substrate.

2.1.2 Real-rock thin sections

Polished thin sections of micaschist, containing an heterogeneous abundance of minerals were incubated in order to expose a higher surface and facilitate the observation of microbial morphologies in the mineral-attached biofilms. Thin sections were prepared at the University of Rennes by sampling a core from the borehole B2 in the CZO of Ploemeur.

2.1.3 Mineral powders

Mineral samples of biotite and pyrite were crushed using a Boron mortar until a grain size of millimeter size was obtained. Mineral powder samples were incubated in order to expose a high specific surface area allowing for further DNA extraction and sequencing. Additionally, we used glass beads ($\Phi = 1$ mm) as an inert surface control.

2.1.4 Samples sterilization

Once placed in their respective holders, all mineral samples, as well as the incubation device, were washed three times by immersion in 70% ethanol under a laminar flow hood. Next, the samples were washed again three times by immersion in 0.2 μm-filtered *in-situ* groundwater from the incubation boreholes. The samples were finally left immersed in their respective 0.2 μm-filtered *in-situ* groundwater to avoid pressure differences in the device when putting it at depth. The samples were inserted in the incubation device, and the latter was closed in sterile sealed bags prior to incubation in the field.

2.1.5 in-situ incubation

Mineral samples were incubated for ten months by immersion in two redox-contrasted boreholes at the Ploemeur CZO (Psr1 and Psr5, see Table 2 for groundwater details). The incubation devices were opened at both ends to allow for groundwater circulation and they were stabilized at the depth of the main contributing fracture in the borehole as previously determined by (Osorio-Leon et al., 2023), i.e. -45m in the oxic borehole and -95m in the anoxic one. Groundwater in the boreholes were under natural gradient flow during the whole incubation period.

2.2 Samples recovery

2.2.1 Microbial fixation

The incubation device was retrieved from the boreholes on May 2022. Following uptake from groundwater, mineral samples (thin sections and model minerals) were im-

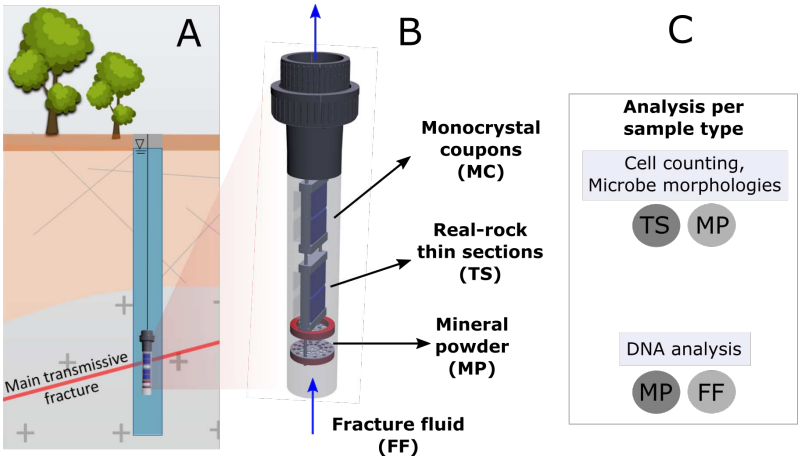

Figure 1. Overview of the *in-situ* incubation experiment. (A): illustration of the incubation setup in the field, showing the incubation device in the water column at the depth corresponding to the main transmissive fracture in a borehole. (B): detail of the passive incubation device used to hold different sample types that were adapted for different analyses, as detailed in (C).

mersed in a fixating solution (50% Ethanol - 50% of Modified Wolfe's Mineral Medium (MWMM) without K_2HPO_4) and stored in an anoxic container (BD GazPack EZ incubation container) that was kept at 4°C for 4h and then stored at -20°C until sample analysis. Powder samples were immediately stored at 4°C during 4h and then treated for DNA extraction at University of Rennes.

2.2.2 Groundwater sampling for hydrochemistry and microbiology

Once the mineral samples were retrieved from the boreholes, groundwater was sampled for hydrochemistry and microbial diversity analyses. Sampling consisted on descending a submersible MP1 pump (Grundfos) until the depth of the dominant fracture in the borehole. Physicochemical parameters in the pump discharge were monitored with a WTW probe. Groundwater was sampled after the monitored parameters were stable. For hydrochemical analysis, groundwater was 0.2 μm-filtered and then acidified at 1%vol/vol using HNO_3 14.6 N. Major and trace cations were quantified by Inductively Coupled Plasma Mass Spectroscopy (Agilent Technologies, 7700x). For microbial diversity analysis, groundwater was filtered using two sampling strategies at the pump outlet : (1) a 0.2 μm pre-filter followed by a Sterivex filter and (2) a single Sterivex filter. In both cases, groundwater was pumped until filtering a volume between 5 to 7 liters.

2.3 Mineral samples analysis

After the incubation time of ten months, the mineral-attached biofilms that colonized the model mineral samples were analyzed by following the workflow in Figure S1. We detail here the associated methods. The images acquired by epifluorence microscopy were processed using the ImageJ software and the cells were counted with the "Analyze Particles" tool.

2.3.1 Cell counting by epifluorescence microscopy (monolayer biofilms)

Cell counting in samples where microorganisms were directly observed in contact with the mineral substrate (i.e. monolayer biofilms) was done by using epifluorescence microscopy. Cells were marked with 10 μM SYTO 9 green-dye (ThermoFisher Scientific). SYTO 9 dye stains DNA and RNA in live and dead gram-negative and gram-positive bacteria. Marked samples were imaged in an Olympus BX51 fluorescence microscope, equipped with a U-MNIB3 blue excitation unit (470-495nm), a 510IF emission filter and a 505 dichromatic mirror. Before any cell staining, samples were tested for autofluorescence using a FITC filter.

2.3.2 Cell counting for samples with 3D-biofilms

Epifluorescence microscopy is well adapted for samples where microorganisms were in direct contact with the mineral substrate (i.e. monolayer colonization). However, for samples where microbial colonization resulted in the formation of thick biofilms, epifluorescence microscopy can lead to underestimate the cell counting by neglecting cells inside the biofilm's volume. In this case, we used a complementary approach combining microtopography measurements and confocal microscopy to determine a volumetric cell density in the biofilms.

Microtopography images of mineral surfaces were acquired before and after the experiment using a white light Vertical Scanning microscope (VSI) equipped with a Mirau objective. The difference between the final and the initial topography of the colonized mineral surfaces allowed to determine the biofilm's volume per surface area of exposed mineral.

In order to measure the volumetric cell density in the biofilm, we first used a Confocal Laser Scanning Microscope (CLSM) (Olympus FV1000) to image SYTO 9-stained cells at different focal planes. The CLSM was equipped with a laser emitting at 488 nm and we collected fluorescence in the 500-600nm range. The vertical displacement between confocal slices was 0.8μm. A 3D reconstruction of biofilms upon the confocal images was built on BiofilmQ (Hartmann et al., 2021), allowing for cells segmentation and volumetric cell density estimation.

We estimated an average volumetric cell density per redox condition based on confocal images (see worflow in Figure S1). We acquired a total of five confocal volumetric-images for the oxic condition and eight for the anoxic condition to ensure statistical significance. Total number of cells were about 15×10^3 in the oxic condition and about 6×10^3 for the anoxic condition.

2.3.3 Imaging of cells and biofilm morphologies

Biofilm and mineral-attached cells were imaged with a Scanning Electron Microscope (SEM) equipped with a Field Emission Gun (FEG). Fixed biofilm samples were dehydrated by gradually replacing water with ethanol with increasing concentration solutions. In order to preserve the mineral samples for microtopography analyses, SEM images were acquired without coating. We used a low accelerating voltage (1.00 kV) and a SESI detector to avoid charging effects.

2.4 Modeling the thermodynamic potential under *in-situ* conditions

To model the energetic potential for microbial metabolisms that is available at the *in-situ* conditions of the Ploemeur CZO, we followed the methods of Osburn et al. (2014). We modeled 19 reactions (see Table 1) coupling electron donors in mineral (biotite, pyrite) or aqueous form (Fe^{2+}, H_2) to the aqueous electron acceptors O_2, NO_3^-, HCO_3^-, SO_4^{2-}.

Table 1. Reactions considered for the thermodynamic model

ID	Reaction	e-/rxn
Pyrite as electron donor		
1	$FeS_2 + 3.5\,O_2 + H_2O \longrightarrow Fe^{2+} + 2\,{SO_4}^{2-} + 2\,H^+$	14
2	$FeS_2 + 7\,{NO_3}^- + H_2O \longrightarrow Fe^{2+} + 2\,{SO_4}^{2-} + 7\,{NO_2}^- + 2\,H^+$	14
3	$FeS_2 + 1.75\,{HCO_3}^- + 2.75\,H_2O \longrightarrow Fe^{2+} + 2\,{SO_4}^{2-} + 1.75\,CH_4 + 0.25\,H^+$	14
Biotite as electron donor		
4	$\text{Biotite} + 0.75\,O_2 + 4\,H^+ \longrightarrow 3\,FeOOH + 3\,SiO_2 + Al^{3+} + K^+ + 1.5\,H_2O$	3
5	$\text{Biotite} + 1.5\,{NO_3}^- + 4\,H^+ \longrightarrow 3\,FeOOH + 3\,SiO_2 + Al^{3+} + K^+ + 1.5\,{NO_2}^- + 1.5\,H_2O$	3
6	$\text{Biotite} + 0.375\,{SO_4}^{2-} + 4.375\,H^+ \longrightarrow 3\,FeOOH + 3\,SiO_2 + Al^{3+} + K^+ + 0.375\,HS^- + 1.5\,H_2O$	3
7	$\text{Biotite} + 0.375\,{HCO_3}^- + 4.375\,H^+ \longrightarrow 3\,FeOOH + 3\,SiO_2 + Al^{3+} + K^+ + 0.375\,CH_4 + 1.125\,H_2O$	3
8	$\text{Biotite} + 0.75\,O_2 + 4\,H^+ \longrightarrow 3\,{FeOOH}_{am} + 3\,SiO_2 + Al^{3+} + K^+ + 1.5\,H_2O$	3
9	$\text{Biotite} + 1.5\,{NO_3}^- + 4\,H^+ \longrightarrow 3\,{FeOOH}_{am} + 3\,SiO_2 + Al^{3+} + K^+ + 1.5\,{NO_2}^- + 1.5\,H_2O$	3
10	$\text{Biotite} + 0.375\,{SO_4}^{2-} + 4.375\,H^+ \longrightarrow 3\,{FeOOH}_{am} + 3\,SiO_2 + Al^{3+} + K^+ + 0.375\,HS^- + 1.5\,H_2O$	3
11	$\text{Biotite} + 0.375\,{HCO_3}^- + 4.375\,H^+ \longrightarrow 3\,{FeOOH}_{am} + 3\,SiO_2 + Al^{3+} + K^+ + 0.375\,CH_4 + 1.125\,H_2O$	3
H_2 as electron donor		
12	$2\,H_2 + O_2 \longrightarrow 2\,H_2O$	4
13	$4\,H_2 + {NO_3}^- + 2\,H^+ \longrightarrow {NH_4}^+ + 3\,H_2O$	8
14	$4\,H_2 + {HCO_3}^- + H^+ \longrightarrow CH_4 + 3\,H_2O$	8
15	$4\,H_2 + {SO_4}^{2-} + H^+ \longrightarrow HS^- + 4\,H_2O$	8
Fe^{2+} as electron donor		
16	$4\,Fe^{2+} + O_2 + 6\,H_2O \longrightarrow 4\,FeOOH + 8\,H^+$	4
17	$8\,Fe^{2+} + {NO_3}^- + 13\,H_2O \longrightarrow {NH_4}^+ + 8\,FeOOH + 14\,H^+$	8
18	$8\,Fe^{2+} + {HCO_3}^- + 13\,H_2O \longrightarrow CH_4 + 8\,FeOOH + 15\,H^+$	8
19	$8\,Fe^{2+} + {SO_4}^{2-} + 12\,H_2O \longrightarrow HS^- + 8\,FeOOH + 15\,H^+$	8

Biotite is assimilated to the annite end-member: $KFe_3Si_3AlO_{10}(OH)_{10}$
FeOOH: goethite, $FeOOH_{am}$: ferrihydrite

First, we computed the Gibbs free energy:

$$\Delta G_r = -RT \ln \frac{K_r}{Q_r} \tag{1}$$

Where ΔG_r is the *in-situ* Gibbs free energy of reaction r, R is the ideal gas constant, T is the absolute temperature, K_r and Q_r are, respectively, the equilibrium constant and activity product for reaction r. The activity product is defined as:

$$Q_r = \prod a_i^{v_i} \tag{2}$$

where a_i and ν_i are, respectively, the activity and the stoichiometric coefficient of species i in reaction r.

The estimated Gibbs free energies are normalized per mole of reaction and per kilogram of fluid to compute the energy density (E_r):

$$E_r = \left| \frac{\Delta G_r}{v_i} \right| a_i \tag{3}$$

According to Osburn et al. (2014), energy densities have shown to better correlate to the environmental conditions and the associated microbial diversity in subsurface environments. Therefore, E_r is used as a more accurate proxy of the expected microbial metabolisms.

3 Results

3.1 Groundwater chemistry

The aqueous composition of groundwater from the two boreholes used for the incubation of the mineral substrates is presented in Table 2. Both boreholes are charac-

terized by near-neutral groundwater, similar contents of total dissolved solids (E.C.) and contrasted redox conditions, as indicated by the oxidizing and reducing redox potential (Eh) in boreholes Psr1 and Psr5, respectively. The difference in the redox states of the boreholes follows contrasted abundances of electron acceptors and donors. Under oxic conditions (borehole Psr1), the most abundant electron acceptor is NO_3^-, followed by SO_4^{2-}, O_2 and HCO_3^-. Under anoxic conditions (borehole Psr5), the most abundant electron acceptor is SO_4^{2-} followed by HCO_3^-, NO_3^- and O_2. On the other hand, the availability of electron donors under oxic conditions is dominated by acetate, while dissolved iron is the most abundant electron donor under anoxic conditions.

Table 2. Aqueous chemistry and physicochemical parameters of groundwater from boreholes Psr1 and Psr5. E.C. indicates Electrical Conductivity and MF Depth indicates the main transmissive fracture in the borehole according with (Osorio-Leon et al., 2023). Data corresponds to groundwater sampled at the end of the incubation experiment. Parameters marked with an * were not measured during the experiment. Instead, we include their average ($\pm 1\sigma$) values for the period 2016-2022 as reported by (Osorio-Leon et al., 2023). Redox classification is defined according to Berg et al. (2022).

		Borehole	
Parameter	Units	Psr1	Psr5
Redox classification		Oxic	Suboxic
MF Depth	[m to ref]	45.0	97.6
Water level	[m to ref]	5.23	1.83
T	[°C]	13.3	15.1
E.C.	[µS.cm^{-1}]	450	533
pH	[-]	6.27	7.06
Eh	[mV]	177	-10.3
N_2	[log M]	-3.12	-2.97
*H_2	[log M]	-7.91	-7.68
*O_2	[log M]	-3.78	-5.60
NO_3^-	[log M]	-3.16	-4.16
SO_4^{2-}	[log M]	-3.54	-3.38
Mn	[log M]	-7.26	-5.16
Fe	[log M]	-7.43	-4.33
[a]CH_3COO^-	[log M]	-4.67	-4.62
[b]HCO_3^-	[log M]	-3.59	-3.41

[a]: CH_3COO^- assimilated from DOC measurement
[b]: HCO_3^- assimilated from DIC measurement

3.2 Demographics of mineral-hosted biofilms

The incubated mineral substrates were colonized by microorganisms in all studied conditions, but the mineral-attached communities formed biofilms with different average thicknesses (dh_{Bf} in Figure 2-A). Globally, the inert controls (quartz samples) were colonized by monolayer biofilms ($dh_{Bf} < 1$ in Figure 2-A) while the more reactive minerals (pyrite and biotite) presented 3D biofilms with average thicknesses ranging between 1 to 10μm. While the fluid-redox condition did not impact the average thickness of quartz and pyrite-hosted biofilms, it had a strong effect in biotite samples. Indeed, under anoxic conditions biotite hosted a monolayer biofilm while under oxic conditions, it hosted the thickest 3D biofilm as shown in Figure 2-A.

The estimated distributions of microbial cell densities on the colonized mineral surfaces (Figure 2-B) appear to show a dependence on the mineral substrate. All mineral samples were colonized by microorganisms, but average cell densities were the lowest in the inert quartz samples (about $10^4 cells.cm^{-2}$) compared to reactive minerals (pyrite and biotite). Indeed, regardless of whether the samples hosted monolayer or 3D biofilms, reactive minerals hosted between 10 to 10^3 times more cells than the inert controls.

A clear difference in cell abundance is observed among the various incubated minerals, indicating that biofilm development is dependent on the mineral substrate. Additionally, for biotite, we note distinct variations in cell abundance across different fluid-redox conditions in which the minerals were incubated. This observation suggests that biofilm formation on certain minerals might also be influenced by fluid chemistry.

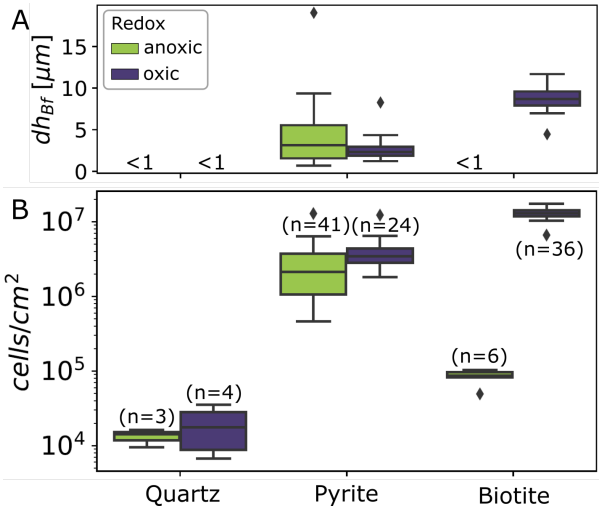

Figure 2. Biofilm thickness and demographics for different mineral substrates and redox conditions. (A): Average biofilm thickness as measured by Vertical Scanning Interferometry, VSI. (B): Cell counts per incubated mineral as determined by epifluorescence microscopy for monolayer biofilms (dh_{Bf}<1 in (A) plot) and by the CLSM+VSI method for 3D-biofilms. The oxic redox condition corresponds to borehole Psr1 while the anoxic one corresponds to borehole Psr5.

3.3 Morphologies and cell-distribution in mineral-attached biofilms

The architecture of mineral-attached biofilms appears to have a stronger dependence on mineral substrate than on fluid-redox conditions. In particular, inert control samples (Quartz) hosted monolayer biofilms at both oxic and anoxic conditions, while reactive minerals (pyrite and biotite) mainly hosted 3D biofilms (Figure 3-A). Only biotite substrates showed a contrast depending on the fluid-redox condition, with a monolayer and 3D biofilm under anoxic and oxic conditions, respectively.

SEM-acquired images of microorganisms colonizing mineral surfaces exhibited different morphologies depending on the redox conditions. Figure 3-B presents the most commonly observed morphologies of microorganisms and extracellular structures. In oxic conditions, the most commonly observed microbial morphologies were cocci and rods, but a wide variety of other microbial shapes, including vibrio, coccobacilli and spirilla were also observed. In anoxic conditions, the most commonly observed morphologies were

coccobacilli, philamentous bacteria and stalk-shaped extracellular structures. No apparent links between mineral substrates or shapes were identified. Extracellular sheat-structures were also commonly observed in the 3D biofilms, at both oxic and anoxic conditions, in biotite and pyrite samples but they were not found in the quartz control. Under anoxic conditions, rod-shaped and filamentous microorganisms as well as sheat and stalk extracellular structures were the most commonly found morphologies. Cocci were only observed in pyrite samples.

Confocal images of 3D biofilms (Figure 3-C) reveal a clear effect of the redox conditions on the cell distribution in the biofilm. While under oxic conditions cells are sparsely distributed in the biofilm, under anoxic conditions cells are organized in colony-like clusters. Filamentous structures with a fluorescence signal weaker than that of cells, that we interpret as EPS, were abundant in confocal images under anoxic conditions (Figure 3-C and Figure S2).

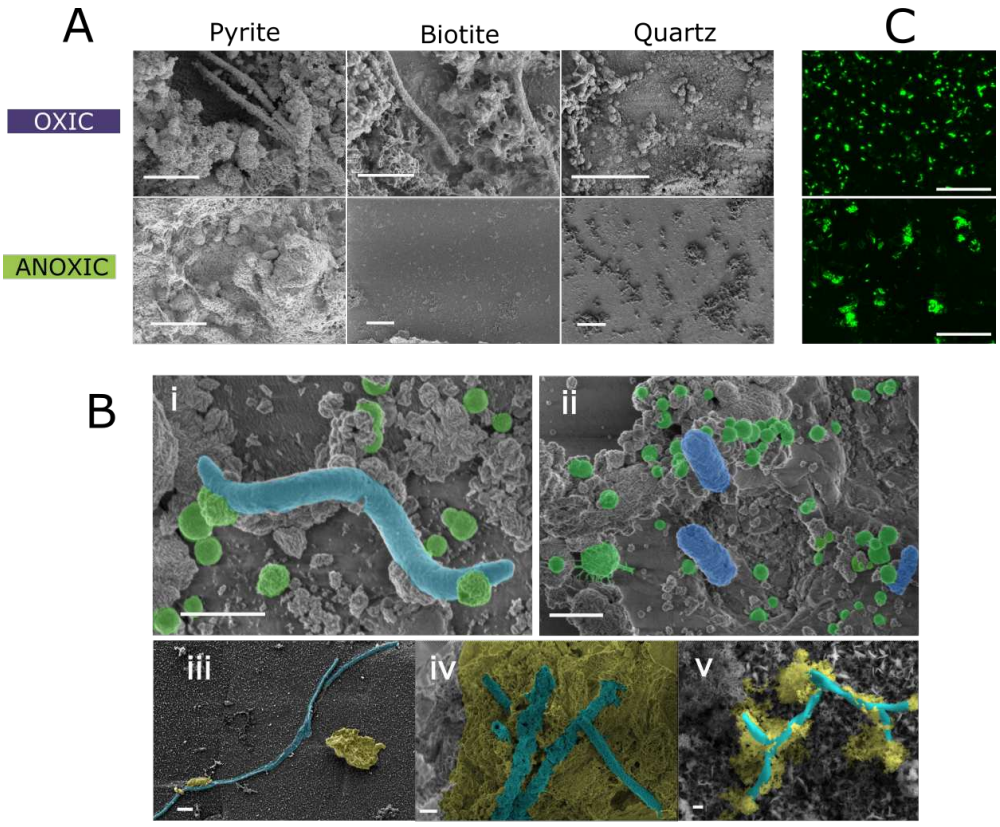

Figure 3. Mozaic of images of mineral-attached biofilms and prokaryotes after ten months of incubation. (A): SEM images of mineral-attached biofilms. Columns show different mineral substrates while rows show different fluid-redox conditions. (B): SEM images of the most commonly found microbial morphologies: spirillum (i), rod-shaped (ii), cocci (i and ii) and filamentous (iii) microorganisms. Extracellular structures such as sheats (iv) and stalks (v) were also observed. (C): Confocal image stacks of cell distribution in olivine biofilms under oxic and anoxic conditions. Scale bars are A): $5\mu m$, B) $1\mu m$ and C) $20\mu m$.

3.4 Thermodynamic potential of geochemical reactions

The contrast in the redox conditions between the two boreholes used to incubate the mineral substrates results in different thermodynamic potentials for the geochemical reactions, as illustrated in Figure 4. Among the 19 modeled putative reactions in Figure 4-A, only 9 are exergonic ($\Delta G_r < 0$). The most exergonic reactions involve O_2 as electron acceptor and pyrite and H_2 as electron donors. To take into account the aqueous composition of the incubation boreholes, we calculated the energy densities for the exergonic reactions as presented in Figure 4-B. A different trend is observed depending on the redox setting, i.e. on the incubation borehole. Under oxic conditions (borehole Psr1), the highest energy densities are related with reactions involving a mineral substrate as electron donor (Biotite and Pyrite) and oxygen or nitrate as electron acceptor. Conversely, under anoxic conditions the highest energy density corresponds to the purely aqueous reaction between Fe^{2+} and O_2.

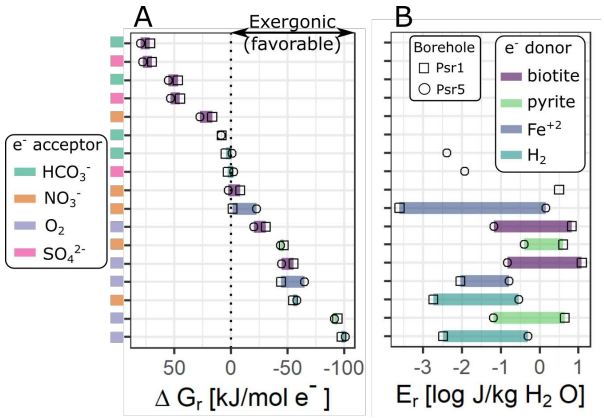

Figure 4. Thermodynamic potential of the *in-situ* metabolic reactions at the Ploemeur CZO. The reactions relating couples of electron donors and acceptors can be found in Table 1. (A): Gibbs free energy (ΔG_r) of the metabolic reactions between electron acceptors (y-axis) and electron donors (color fill). Symbols account for the two studied boreholes. ΔG_r is computed with Equation 1. (B): Energy density (E_r) for the exergonic reactions from (A), computed with Equation 3.

4 Discussion

4.1 Environmental controls on the demographics of mineral-attached biofilms

Our estimated cell densities in the mineral-attached biofilms are comparable to previous measurements in similar experiments. Casar et al. (2020) reported cell densities between 10^5 and 10^7 $cells/cm^2$. Even the inert surfaces like quartz contain high cell densities (about 10^4 $cells/cm^2$), supporting previous estimations which suggested that most of the deep biomass is hosted in the mineral surfaces, e.g. Flemming and Wuertz (2019).

Our findings suggest a strong correlation between biofilm demographics and the mineral substrate. Reactive minerals such as pyrite and biotite hosted between 10 to 10^3 times more cells than the inert quartz substrates (Figure 2-B). The mineral-selective colonization of mineral substrates has been previously suggested in similar incubation experiments (P. C. Bennett et al., 2001; Casar, Kruger, & Osburn, 2021) that found higher

cell concentrations in minerals containing nutrients that are limited in the aqueous phase. Altogether, these results suggest that the lithological context can represent a major control on the mineral-attached biomass in the continental subsurface. Felsic rocks, which have a higher proportion of less reactive minerals such as feldspar and quartz, could hence host less biomass than mafic rocks, that contain a major proportion of reactive Fe-bearing minerals such as biotite of pyrite.

While the fluid-redox conditions exert a weak influence on the mineral-hosted biomass for quartz and pyrite, there was a strong contrast in cell abundances for biotite samples between oxic and anoxic-incubated conditions (Figure 2-B). This phenomenon may be understood by considering the energy densities (E_r), shown in Figure 4-B. Under oxic conditions (borehole Psr1), electron donors are scarce and electron acceptors abundant (see Table 2). This results in a maximum thermodynamic potential in the solid-fluid reactions where the electron donors of mineral substrates offer an energetic advantage (Figure 4-B). On the other hand, under anoxic conditions (borehole Psr5) the abundance of dissolved iron as a readily available electron donor in the aqueous phase overcomes the energetic potential of the solid-fluid reactions (see reaction between Fe^{2+} and NO_3^- in Figure 4-B). In such case, prokaryotes with the capacity to use reduced iron as an electron donor would prefer to use the abundant aqueous Fe^{2+}, resulting in less attached cell densities in Fe-bearing minerals such as biotite. This hypothesis is support by laboratory mineral incubation experiments, which have reported the active attachment and detachment of cells based on the availability of aqueous electron donors (Jones & Bennett, 2017). While biotite provides only the reducing potential of Fe, pyrite contains both reduced iron and sulfur as a sulfide mineral. Even when dissolved iron is present in the fluid phase, we hypothesize that consortia attached to pyrite can leverage sulfur-oxidizing pathways for their growth. The activation of these sulfur-oxidizing pathways under anoxic conditions could thus possibly account for the stable biomass observed in pyrite-attached biofilms.

Finally, we note that the fluid-redox conditions also impacted the physiological state of mineral-attached biofilms. Cell organization within biofilms under oxic and anoxic conditions display important contrasts as shown in Figure 3-C. Cells were sparsely distributed under oxic conditions, while under anoxic conditions cells were concentrated in colony-like clusters. This contrasts suggest a physiological difference between redox conditions. Our confocal images in Figure 3-C and Figure S2 also suggest that biofilms under anoxic conditions qualitatively exhibit a greater presence of EPS.

4.2 Other environmental parameters potentially affecting the demographics of mineral-attached biofilms

In the above sections we have demonstrated that mineral substrate and fluid-redox conditions play a major role on mineral-attached cell densities. Nevertheless, inert samples (quartz) hosted a significant attached-biomass, suggesting that non-chemical effects could also induce differences on the mineral-attached cell densities. The interactions between cells and mineral surfaces rely on electrostatic interactions between negatively-charged cells and surface sites with positive charges (Ginn et al., 2002). Environmental parameters that can potentially modify the net charge of both organic and mineral surfaces can exert a control on the resulting cell densities of mineral-attached biofilms. Low pH environments for instance have the potential to increase the positively-charged sites through the adsorption of hydronium ions (H_3O^+) onto negatively-charged surfaces, such as in the case of quartz. Likewise, ionic strength can result in similar effects by the adsorption of anions or cations in counterionic sites on mineral surfaces (Ginn et al., 2002). Because of coulombic interactions, surfaces with a positive charge have a higher potential to be colonized by negatively-charged cells (P. C. Bennett et al., 2001). We attribute the colonization of the inert controls in our experiment (quartz samples) to these type of electrostatic interactions. Since the incubation boreholes Psr1 and Psr5 are similar in terms

of pH conditions (both boreholes are near-neutral according to Table 2), we do not expect the electrostatic interactions to significantly change between the two fluid-redox conditions.

Finally, an additional environmental parameter that is directly related to the redox compartmentalization in aquifers is surface aging. Several authors have for instance reported the formation of amorphous silica-rich surface layers (ASSLs) at the surface of silicates in acidic and circum-neutral solutions (Daval et al., 2011; Wild et al., 2016). Mineral surfaces in natural settings are indeed usually aged due to the formation of secondary mineral coatings as a result of weathering reactions. Likewise, in oxic environments, the dissolution of iron-bearing minerals and the subsequent oxidation of iron leads to the formation of iron oxyhydroxides (Antoniellini et al., 2017). Under anoxic conditions, the weathering of iron-bearing minerals leads to the formation of clays (Sugimori et al., 2008). These secondary-mineral layers formed in aged minerals can modify the attachment conditions for prokaryotes and then impact the mineral-attached biomass. For instance, iron-oxides have a net positive surface charge that presents a high affinity with prokaryotic cells (Schädler et al., 2009). The effect of these environmental parameters on the deep continental biomass should be assessed in future works.

4.3 Implications of this work

In the above sections we have discussed how environmental parameters impact cell densities in rock-hosted biofilms, in accordance with previous studies (P. C. Bennett et al., 2001; Casar, Momper, et al., 2021). However, the estimation of global biomass neglect subsurface heterogeneity and its impact on rock-hosted biomass. (Whitman et al., 1998; Mcmahon & Parnell, 2014; Bar-on et al., 2018; Magnabosco et al., 2018; Flemming & Wuertz, 2019). In this work we provide evidence, following previous findings (P. C. Bennett et al., 2001; Casar, Momper, et al., 2021), revealing orders-of-magnitude variations on the mineral-attached biomass related to changes in the mineralogy or fluid-redox conditions. We argue that larger data sets are however necessary to better identify large scale trends on the correlation between biomass and environmental factors, which can be included in future global biomass estimations.

4.4 Limits of the study and future work

In our *in-situ* incubation experiments, we measured the mineral-hosted biomass after an incubation time of ten months. Whether the mineral-attached communities were or not at a stationary growth phase is not known in our case. Future work should adapt the experimental setup to allow for sampling of colonized mineral substrates at intermediate times. A correlation between biomass and incubation time at *in-situ* conditions could hence be derived, providing valuable insights on the growth time scales of biomass in the deep continental subsurface. So far, very few estimates of this growth time scales are available. For the continental subsurface, the doubling time of microbial populations has been estimated to take about 10^2 years (Templeton & Caro, 2023). Yet, the incubation of pristine surfaces reported here resulted in the formation of thick mineral-attached biofilms in only ten months. While pristine surfaces are poorly representative of aged surfaces in natural environments, future works estimating growth rates in pristine and aged surfaces could help to establish limit values to *in-situ* microbial growth.

In the above sections, we highlighted the possible impacts that other environmental factors, not assessed in this study, could have in the mineral-hosted biomass, e.g. pH, ionic strength or surface aging. Because of the nature of our *in-situ* incubation setup, the effect of these factors was not isolated in our experiment and therefore, their impact on our biomass estimations should be assessed with future experiments.

5 Conclusions

This study investigated the controls of environmental factors on the mineral-hosted biomass in the continental subsurface. We designed a simple passive device to incubate surrogate minerals in boreholes and developed a new approach for the estimation of cell densities in multi-layer biofilms attached to minerals. We particularly studied the effect of two key environmental parameters, mineral substrate and fluid-redox conditions, that can be related to large scale environmental factors such as the geological context and groundwater residence time, respectively. Our findings highlight the role of the geological context as a first-order control on the mineral-attached biomass, especially due to the presence of electron donors hosted in minerals. Indeed, the reducing potential of minerals can compensate the lack of energy sources in oligotrophic fluids, leading to larger biomass in reactive mineral substrates. On the other hand, the fluid-redox state had an important impact for biotite only, which may be explained based on thermodynamic modeling. Altogether, this work provides novel insights into the influence of environmental parameters on the rock-hosted biomass, which have been so far neglected by global estimations of biomass in the continental subsurface.

6 Open Research

All figures were made using Matplotlib version 3.5.1 (Hunter, 2007), available under the Matplotlib license at `https://matplotlib.org/`. Confocal images were treated by using the freely available BiofilmQ toolkit (Hartmann et al., 2021), while epifluorescence images were processed with the public domain software ImageJ (Schneider et al., 2012). All codes for the processing of vertical scanning interferometry images were built on Python and used the PyVista package (Sullivan & Kaszynski, 2019). The codes are freely available on the GitHub repository: `https://github.com/idosoriole/Osorio-Leon-EnvControls-CellsAttached`.

Acknowledgments

This research was funded, in whole, by the ANR IRONSTONE (ANR-21-CE01-0008) and the PIA3 TERRAFORMA project. A CC-BY public copyright license has been applied by the authors to the present document and will be applied to all subsequent versions up to the Author Accepted Manuscript arising from this submission, in accordance with the grant's open access conditions. We are very grateful to the French networks of hydrogeological sites H+ (https://hplus.ore.fr/en/) and of critical zone observatories OZCAR (https://www.ozcar-ri.org/) for providing access to the Ploemeur CZO. We also thank the geomicrobiology group at IPGP (Paris) for allowing access to epifluorescence, confocal and SEM microscopes, to ISTerre institute (Grenoble) for providing access to the vertical scanning interferometer. We also thank the GeOHeLiS service for their support with groundwater chemistry analysis.

References

Ahmed, E., & Holmström, S. J. M. (2015). Microbe – mineral interactions : The impact of surface attachment on mineral weathering and element selectivity by microorganisms. *Chemical Geology*, *403*, 13–23. doi: 10.1016/j.chemgeo.2015.03.009

Alfreider, A., Krössbacher, M., & Psenner, R. (1997). Groundwater samples do not reflect bacterial densities and activity in subsurface systems. *Water Research*, *31*(4), 832–840. doi: 10.1016/S0043-1354(96)00311-9

Antoniellini, M., Mollema, P., & Del Sole, L. (2017). Application of analytical diffusion models to outcrop observations: Implications for mass transport by fluid flow through fractures. *Water Resources Research*, *53*, 5545–5566. doi:

10.1111/j.1752-1688.1969.tb04897.x

Bar-on, Y. M., Phillips, R., & Milo, R. (2018). The biomass distribution on Earth. *Proceedings of the National Academy of Sciences of the United States of America*, *115*(25), 6506–6511. doi: 10.1073/pnas.1711842115

Berg, J. S., Ahmerkamp, S., Pjevac, P., Hausmann, B., Milucka, J., & Kuypers, M. M. M. (2022, May). How low can they go? Aerobic respiration by microorganisms under apparent anoxia. *FEMS Microbiology Reviews*, *46*(3), fuac006. doi: 10.1093/femsre/fuac006

Casar, C. P., Kruger, B. R., Flynn, T. M., Masterson, A. L., Momper, L. M., & Osburn, M. R. (2020). Mineral-hosted biofilm communities in the continental deep subsurface, Deep Mine Microbial Observatory, SD, USA. *Geobiology*(October 2019), 1–15. doi: 10.1111/gbi.12391

Casar, C. P., Kruger, B. R., & Osburn, M. R. (2021). Rock-Hosted Subsurface Biofilms: Mineral Selectivity Drives Hotspots for Intraterrestrial Life. *Frontiers in Microbiology*, *12*(April), 1–14. doi: 10.3389/fmicb.2021.658988

Casar, C. P., Momper, L. M., Kruger, B. R., & Osburn, M. R. (2021). Iron-Fueled Life in the Continental Subsurface : Deep Mine. *Applied and Environmental Microbiology*, *87*(20).

Chan, M. A., Hinman, N. W., Potter-Mcintyre, S. L., Schubert, K. E., Gillams, R. J., Awramik, S. M., … Cleaves, H. J. (2019). Deciphering Biosignatures in Planetary Contexts. *Astrobiology*, *19*(9), 1075–1102. doi: 10.1089/ast.2018.1903

Daval, D., Sissmann, O., Menguy, N., Saldi, G. D., Guyot, F., Martinez, I., … Hellmann, R. (2011, May). Influence of amorphous silica layer formation on the dissolution rate of olivine at 90°C and elevated pCO2. *Chemical Geology*, *284*(1-2), 193–209. doi: 10.1016/j.chemgeo.2011.02.021

Dong, H., Huang, L., Zeng, Q., & Liu, X. (2022). A critical review of mineral-microbe interaction and coevolution: Mechanisms and applications. *National Science Review*. doi: 10.1093/nsr/nwac128

Flemming, H.-C., van Hullebusch, E. D., Neu, T. R., Nielsen, P. H., Seviour, T., Stoodley, P., … Wuertz, S. (2022, September). The biofilm matrix: Multitasking in a shared space. *Nature Reviews Microbiology*. doi: 10.1038/s41579-022-00791-0

Flemming, H.-C., & Wuertz, S. (2019, April). Bacteria and archaea on Earth and their abundance in biofilms. *Nature Reviews Microbiology*, *17*(4), 247–260. doi: 10.1038/s41579-019-0158-9

Ginn, T. R., Wood, B. D., Nelson, K. E., Scheibe, T. D., Murphy, E. M., & Clement, T. P. (2002, August). Processes in microbial transport in the natural subsurface. *Advances in Water Resources*, *25*(8), 1017–1042. doi: 10.1016/S0309-1708(02)00046-5

Grant, M. R., Tymon, L. S., Helms, G. L., Thomashow, L. S., Kent Keller, C., & Harsh, J. B. (2016). Biofilm adaptation to iron availability in the presence of biotite and consequences for chemical weathering. *Geobiology*, *14*(6), 588–598. doi: 10.1111/gbi.12187

Griebler, C., Mindl, B., Slezak, D., & Geiger-Kaiser, M. (2002). Distribution patterns of attached and suspended bacteria in pristine and contaminated shallow aquifers studied with an in situ sediment exposure microcosm. *Aquatic Microbial Ecology*, *28*(2), 117–129. doi: 10.3354/ame028117

Hartmann, R., Jeckel, H., Jelli, E., Singh, P. K., Vaidya, S., Bayer, M., … Drescher, K. (2021, February). Quantitative image analysis of microbial communities with BiofilmQ [software]. *Nature Microbiology*, *6*(2), 151–156. doi: 10.1038/s41564-020-00817-4

Hazen, T. C., Jiménez, L., López de Victoria, G., & Fliermans, C. B. (1991, December). Comparison of bacteria from deep subsurface sediment and adjacent groundwater. *Microbial Ecology*, *22*(1), 293–304. doi: 10.1007/BF02540231

Hunter, J. D. (2007). Matplotlib: A 2d graphics environment [software]. *Computing in science & engineering*, *9*(03), 90–95.

Jones, A. A., & Bennett, P. C. (2017). Mineral Ecology : Surface Specific Colonization and Geochemical Drivers of Biofilm Accumulation , Composition , and Phylogeny. *Frontiers in Microbiology*, *8*(March), 1–14. doi: 10.3389/fmicb.2017.00491

Kölbel-Boelke, J., Anders, E. M., & Nehrkorn, A. (1988). Microbial communities in the saturated groundwater environment II: Diversity of bacterial communities in a Pleistocene sand aquifer and their in vitro activities. *Microbial Ecology*, *16*(1), 31–48. doi: 10.1007/BF02097403

Lehman, R. M., Colwell, F. S., & Bala, G. A. (2001, June). Attached and Unattached Microbial Communities in a Simulated Basalt Aquifer under Fracture- and Porous-Flow Conditions. *Applied and Environmental Microbiology*, *67*(6), 2799–2809. doi: 10.1128/AEM.67.6.2799-2809.2001

Lehman, R. M., Roberto, F. F., Earley, D., Bruhn, D. F., Brink, S. E., O'Connell, S. P., ... Colwell, F. S. (2001). Attached and Unattached Bacterial Communities in a 120-Meter Corehole in an Acidic, Crystalline Rock Aquifer. *Applied and Environmental Microbiology*, *67*(5), 2095–2106. doi: 10.1128/AEM.67.5.2095-2106.2001

Liermann, L. J., Kalinowski, B. E., Brantley, S. L., & Ferry, J. G. (2000). Role of bacterial siderophores in dissolution of hornblende. *Geochimica et Cosmochimica Acta*, *64*(4), 587–602. doi: 10.1016/S0016-7037(99)00288-4

Magnabosco, C., Lin, L. H., Dong, H., Bomberg, M., Ghiorse, W., Stan-Lotter, H., ... Onstott, T. C. (2018). The biomass and biodiversity of the continental subsurface. *Nature Geoscience*, *11*(10), 707–717. doi: 10.1038/s41561-018-0221-6

Mcmahon, S., & Parnell, J. (2014). Weighing the deep continental biosphere. *FEMS Microbiology Ecology*, *87*(1), 113–120. doi: 10.1111/1574-6941.12196

Osburn, M. R., Larowe, D. E., Momper, L. M., Jan, P., & Amoozegar, M. A. (2014). Chemolithotrophy in the continental deep subsurface : Sanford Underground Research Facility (SURF), USA. *Frontiers in Microbiology*, *5*(November), 1–14. doi: 10.3389/fmicb.2014.00610

Osorio-Leon, I., Bouchez, C., Chatton, E., Lavenant, N., Longuevergne, L., & Le Borgne, T. (2023). Hydrological and geological controls for the depth distribution of dissolved oxygen and iron in silicate catchments.

P. C. Bennett, J. R. Rogers, W. J., & Choi, W. J. (2001, January). Silicates, Silicate Weathering, and Microbial Ecology. *Geomicrobiology Journal*, *18*(1), 3–19. doi: 10.1080/01490450151079734

Schädler, S., Burkhardt, C., Hegler, F., Straub, K. L., Miot, J., Benzerara, K., & Kappler, A. (2009, February). Formation of Cell-Iron-Mineral Aggregates by Phototrophic and Nitrate-Reducing Anaerobic Fe(II)-Oxidizing Bacteria. *Geomicrobiology Journal*, *26*(2), 93–103. doi: 10.1080/01490450802660573

Schneider, C. A., Rasband, W. S., & Eliceiri, K. W. (2012). Nih image to imagej: 25 years of image analysis [software]. *Nature methods*, *9*(7), 671–675.

Sinclair, J., & Ghiorse, W. (1989, January). Distribution of aerobic bacteria, protozoa, algae, and fungi in deep subsurface sediments. *Geomicrobiology Journal*, *7*(1-2), 15–31. doi: 10.1080/01490458909377847

Sugimori, H., Iwatsuki, T., & Murakami, T. (2008, July). Chlorite and biotite weathering, Fe2+-rich corrensite formation, and Fe behavior under low PO2 conditions and their implication for Precambrian weathering. *American Mineralogist*, *93*(7), 1080–1089. doi: 10.2138/am.2008.2663

Sullivan, C. B., & Kaszynski, A. (2019). PyVista: 3d plotting and mesh analysis through a streamlined interface for the visualization toolkit (VTK) [software]. *Journal of Open Source Software*, *4*(37), 1450. Retrieved from `https://doi.org/10.21105/joss.01450` doi: 10.21105/joss.01450

Templeton, A. S., & Caro, T. A. (2023). The Rock-Hosted Biosphere. *Annual Review of Earth and Planetary Sciences*, *51*(1), 493–519. doi: 10.1146/annurev-earth-031920-081957

Uroz, S., Calvaruso, C., Turpault, M. P., & Frey-Klett, P. (2009). Mineral weathering by bacteria: Ecology, actors and mechanisms. *Trends in Microbiology*, *17*(8), 378–387. doi: 10.1016/j.tim.2009.05.004

Whitman, W. B., Coleman, D. C., & Wiebe, W. J. (1998). Prokaryotes: The unseen majority. *Proceedings of the National Academy of Sciences of the United States of America*, *95*(12), 6578–6583. doi: 10.1073/pnas.95.12.6578

Wild, B., Daval, D., Guyot, F., Knauss, K. G., Pollet-villard, M., & Imfeld, G. (2016). pH-dependent control of feldspar dissolution rate by altered surface layers. *Chemical Geology*, *442*, 148–159. doi: 10.1016/j.chemgeo.2016.08.035

1.1.1 Perspectives

Here, we present some experimental improvements identified during this work and that could be considered to improve future experiments on mineral-attached biomass estimations:

1. **Improvements for cell counting and confocal microscopy:** cell counting was conducted by staining cells with a unique fluorescent probe, SYTO 9 green-dye ® (ThermoFisher Scientific). SYTO 9 dye is a non-selective fluorescent probe, i.e. it stains DNA and RNA in live and dead gram-negative and gram-positive bacteria. Estimates of mineral-attached biomass could be improved by making the distinction between viable and non-viable cells by using commercial kits such as the LIVE/DEAD ® Cell Imaging Kit (ThermoFisher Scientific). It is worth noting that the quantity of viable cells in soils and aquatic environments is thought to be less than 10% (Locey; 2010). In the deep subsurface this proportion of viable cells is still to be determined.

2. **Bulk viable-cell biomass:** a complementary approach to the LIVE/DEAD imagery, proposed in the previous point, is the use of PLFA (phospholipid fatty acids) analysis as a proxy of viable microbial biomass. Despite being a bulk analysis without the spatial and morphological information provided by miscroscopy, this complementary approach is a simple and widely used tool to measure viable cell-biomass (Willers et al.; 2015). Notably, it has been shown that PLFA degrade rapidly after cells die and therefore, they are a good proxy of viable cell-biomass (Willers et al.; 2015).

3. **Cell- vs biofilm-biomass:** in this study we focused on the estimation of cell densities in mineral-attached biofilms since this is the proxy used by models estimating the global subsurface microbial biomass [e.g. Bar-on et al. (2018); Magnabosco et al. (2018)]. One of the main goals of these global biomass models is to assess the carbon stock hosted in biomass. However, considering only cells as carbon stocks results in neglecting many other carbon-based molecules that are also present in mineral-attached biofilms (Flemming et al.; 2022). Other than cells, the biofilm matrix comprises a diversity of extracellular polymeric substances (EPS) such as polysaccharides, proteins, amyloids, lipids and extracellular DNA (Flemming et al.; 2022). A more accurate biomass estimation should then consider both cells and organic constituents in the biofilm matrix. Such an approach could be done by combining gravimetric measurements of the whole biofilm [e.g. Jones and Bennett (2017)] and an elemental analysis to estimate the carbon content per total biofilm mass [e.g. Miot et al. (2009b)].

1.2 Microbial community analysis in mineral-attached biofilms

As part of the mineral incubation experiment, a taxonomic analysis was planned but because of analytical problems, the results are only partially available as I write this manuscript. Therefore, the taxonomic analysis that was formerly planned to be included in the above article is presented here as a work in progress. Below we present the methods and results for the sequencing run that was already done and that only delivered sequences for samples belonging to the anoxic incubation experiment (borehole Psr5). Unfortunately, data for the oxic condition is not yet available which prevents us from assessing the effect of the fluid-redox condition. A second sequencing run which will include the data from all the samples is in progress.

1.2.1 Methods for the 16S rRNA amplicon sequencing

We extracted DNA from 20 mineral-powder samples in the anoxic incubation experiment. These samples correspond to replicates of 7 mineral-powder substrates as follows:

1. Glass beads (gl) [n replicates = 3]. This was the inert control used as a proxy of quartz.

2. Biotite (bt) [2]

3. Iron filings (fel) [4]

4. Pyrite (py) [2]
5. Olivine (ol) [3]
6. Fe(0) powder 99% (fep) [3]
7. Labradorite feldspar (fz) [2]

We also extracted DNA from 2 sterivex filters in which we sampled planktonic communities from the incubation borehole Psr5. The purpose of the taxonomic analysis is two-fold: first, to investigate how the community composition changes depending on the environmental conditions (fluid-redox and mineral substrate) and second, to compare the attached conditions with the planktonic communities.

To extract DNA from samples, we used a PowerSoil DNA Isolation Kit. We then amplified the V3-V4 hypervariable region of the 16S rRNA gene by using 341F (CCTACGGGNGGCWGCAG) and 785R (GACTACHVGGGTATCTAATCC) universal primers and prepared sequencing libraries using a LoopSeq 16S Long Read Kit (Loop Genomics ®). The libraries were sent to the ECOGENO service (ECOBIO, Université de Rennes) for sequencing in an Illumina MiSeq instrument.

1.2.2 Preliminary sequencing results under anoxic conditions

DNA extractions were successful in 19 out of the 20 extracted samples (one replicate of the sterivex filters was lost during the extraction process). Quality control of the sequences was done with the FastQC software (version 0.12.1) and the sequence treatment and alignment were done with QIIME 2. The 16s rRNA amplicon sequencing of these samples yielded about 46% of annotation at the genus level.

Figure VII.2-A presents a hierarchical clustering of the samples using the annotated sequences at the genus level. First, we observe that replicates of the same samples are generally grouped in the same clusters, which shows a good reliability of the replicates. For clarity, Figure VII.2-A highlights in color the samples that are treated in detail in the paper draft in Section 1.1, i.e. glass beads (inert control) as proxy of quartz, pyrite, biotite. The fracture fluid (Psr5) is also highlighted for reference. Overall, these samples are well identified in independent clusters. Only one of the control replicates (gl) is mixed among the olivine (ol) and feldspar (fz) cluster that did not show a clear distinction between the latter samples. In Figure VII.2-B we performed a non-metric multidimensional scaling plot in which we highlight the dominant taxa present in the sample sequences. Overall, all dominant taxa represent anaerobic or microaerobic bacteria, which is consistent with the suboxic state of the groundwater in incubation borehole Psr5 (dissolved oxygen concentrations are on average 0.08ppm, see paper draft in Section 1.1). We observe that the MDS2 component makes a clear distinction between the fluid and the mineral-attached taxa.

Dominant taxa in the fracture fluid are the iron oxidizer *Ferriphaselus* and the nitrite-oxidizing *Candidatus Nitrotoga*, both belonging to the *Gallionellaceae* family of bacteria. Bacteria from the *Gallionellaceae* family are commonly found in iron-rich environments like the fracture fluid in the Psr5 borehole (the average Fe^{2+} concentration is about 2.6ppm as reported in Table 2 of the paper-draft, Section 1.1). *Gallionellaceae* in the Guidel site have also been previously reported elsewhere (Bethencourt et al.; 2020). Dominant taxa in the mineral-attached communities are radically different. In pyrite samples, the dominant taxon is the mixotrophic sulfate-reducer *Desulfovibrio* whereas in biotite samples, the dominant taxon is the heterotroph iron-reducer *Geothrix* and in the inert controls (glass beads) the dominant taxon is the autothropic acetate-producer *Acetobacterium*. While *Desulfovibrio* is largely dominant in pyrite samples (about 70% of the reads), it is also present in significant amounts in biotite (10%) and control samples (20%).

1.2.3 Partial conclusion: what do we learn from the sequencing results?

Planktonic and the mineral-attached microbial communities were clearly distinguished in Figure VII.2-b, showing that restricting field sampling to planktonic microorganisms gives a limited view of the microbial diversity in

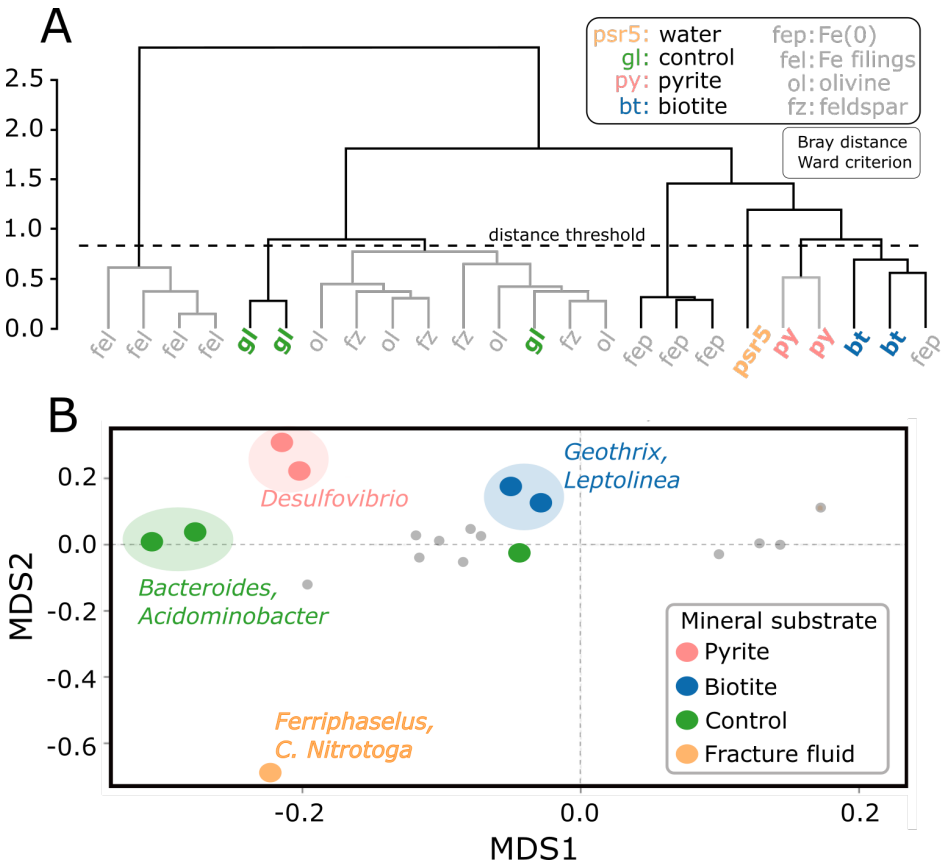

Figure VII.2: **Taxonomy classification of 16s rRNA amplicon sequences at genus level.** A: Hierarchical clustering using bray distance and ward criterion. B: Non-metric multidimensional scaling (NMDS) highlighting the dominant genera per mineral substrate condition. The color legend emphasizes samples corresponding to the incubation fluid (fracture fluid in the borehole Psr5) and the 3 mineral substrates that match those of the article-draft presented in section 1.1. Grey points represent the rest of the samples which are not discussed here.

the subsurface. Interestingly, in the attached-communities the majority taxa correspond to heterotrophic bacteria (Figure VII.2-b), while the planktonic compartment is dominated by autotrophs *Ferriphaselus* and *C. Nitrotoga*. In a similar study, Converse et al. (2015) also found that heterotrophs were dominant in mineral-attached consortia under anoxic conditions, and that iron-reducing (FeRB) and sulfate-reducing (SRB) were the main taxa. **This particularity in the distribution of heterotrophs and autotrophs is worth exploring with more detail since it could provide a better understanding of the primary production in the deep subsurface.** Future experiments providing e a *transient* monitoring of the colonization process, e.g. with time-resolved sampling of replicates, could provide valuable insights on the composition of the biofilm consortium with time.

The dominant taxa in the planktonic communities are associated to oxidizing metabolisms (iron and nitrite), whereas the attached communities are associated to reducing metabolisms (sulfate and iron reduction). This result is somehow unexpected since the microbial consortia colonizing the reactive mineral substrates (pyrite and biotite) do not appear to utilize the energetic potential offered by those minerals, which host both reduced iron and sulfur as potential energy sources. **We hypothesize that this is a consequence of the fluid-redox condition in which dissolved iron is an abundant and ready-to-use electron donor**. Indeed, previous studies have found that the composition of mineral-attached consortia is sensitive to the availability of nutrients and that the adhesion/detachment is an active process [e.g. Ginn et al. (2002) and Jones and Bennett (2017)]. It is worth noting that the thermodynamic modeling presented in Figure 4 (Section 1.1) seems to support our hypothesis. While the maximum values of energy density (E_r) in the oxic condition (borehole Psr1) correspond to metabolic reactions associated to the oxidation of mineral substrates, in the anoxic condition (borehole Psr5) the most energetic reaction is the oxidation of dissolved Fe^{2+} by nitrate. The complete sequencing data set,

including the sequencing data for the oxic condition, will be particularly useful to analyze this hypothesis.

1.2.4 Perspectives

As stated at the beginning of this section, the data presented here is very preliminary because of analytical problems during the sequencing process. A new sequencing run is under process and an in-depth exploitation of the sequencing data will be performed with the complete data set. Some of the perspectives for the exploitation of the complete sequencing data include the comparison between the fracture fluid communities in the two redox-contrasted environments and an analysis, from a microbial ecology standpoint, of the availability of electron donors and acceptors and the putative metabolisms suggested by the annotated taxa.

Box VII.3 - Guiding hypothesis for future sequencing data on mineral-attached biofilms

The fluid-redox condition plays a major role on the taxonomic composition of both planktonic and attached communities. Under reducing conditions, aqueous electron donors such as dissolved iron are easily accessible and there is no special advantage on using the reducing power of minerals. Conversely, under oxic conditions dissolved electron donors are scarce and there is an advantage of using the reducing elements present in the minerals, as suggested by the thermodynamic model. We hypothesize that this will be visible on the sequencing data under oxic conditions.

2 Effects of microbes on minerals

In this section, we present two current works-in-progress, which offer perspectives on the mineral-incubation experiment presented above. In the preceding sections, the primary emphasis was on the study of how mineral substrates impact the mineral-attached microorganisms. We explore here the opposite direction of the microbe-mineral interactions, i.e. how the mineral-attached microbes can have an impact on the colonized minerals and for this we use calcite coupons that were present in the incubation experiment. We use calcite as a model mineral since its dissolution rate fits well with the incubation time of the experiment (10 months), which allows to measure dissolution rates precisely.

In a first part, we explore how the presence of mineral-attached microbes and the fluid-redox conditions can impact the *in-situ* dissolution rate of calcite. Then, in a second part we explore the secondary minerals formed in one of the calcite samples.

2.1 *In-situ* quantification of microbial-induced weathering of calcite

2.1.1 Why studying calcite?

Water-rock interactions play a central role in the fluxes of matter on Earth. By releasing elements in solution, mineral-dissolution reactions control the large-scale availability of nutrients for living organisms as discussed in Chapter IV. Furthermore, dissolution and precipitation reactions of minerals are relevant because they release or immobilize contaminants (Nordstrom; 2011), control the water chemistry in rivers (Floury et al.; 2019) and groundwater (Osorio-Leon et al.; 2023) and ultimately, regulate the carbon cycle and climate (Gaillardet et al.; 1999; Maher and Chamberlain; 2014). Silicate weathering is particularly acknowledged for its role as a global carbon sink that operates over geological timescales (Hartmann et al.; 2009; Maher and Chamberlain; 2014). Unlike silicates, carbonates like calcite do not have a net-sink effect on the carbon cycle as illustrated by the

simplified reactions here below:

Carbonate dissolution in the continents

$$CaCO_{3\,(s)} + CO_{2\,(g)} + H_2O \longrightarrow Ca^{2+} + 2\,HCO_3{}^- \tag{VII.1}$$

Carbonate precipitation in the ocean

$$Ca^{2+} + 2\,HCO_3{}^- \longrightarrow CaCO_{3\,(s)} + CO_{2\,(g)} + H_2O \tag{VII.2}$$

CO_2 is initially captured during calcite dissolution but finally re-emitted during carbonates precipitation in the ocean (Hartmann et al.; 2009). Nonetheless, because of the fast kinetics of the dissolution reaction of calcite, reaction VII.2 is the limiting step in the whole process. Thus, over short timescales (e.g. less than 10^5 years) carbonate dissolution acts as a net CO_2-sink (Daoxian; 1997; Cao et al.; 2012). Furthermore, reactions VII.1 and VII.2 are also relevant in engineered solutions for the geological carbon sequestration (GCS). Overall, the study of the calcite dissolution reaction is particularly relevant for the research on CO_2 budgets in natural or engineered environments.

2.1.2 Why do *in-situ* dissolution rates matter?

Research works interested on assessing the contribution of minerals dissolution as a CO_2-sink commonly use a conventional reactive-transport strategy (e.g, (Molins et al.; 2014, 2020)): first, the kinetic laws governing mineral dissolution reactions are determined experimentally in laboratory tests and second, these experimental kinetic laws are implemented in reactive transport codes. Kinetic laws are generally implemented in reactive transport codes through a semi-empirical rate equation that takes the simplified form [modified from Lasaga (1984, 1998)]:

$$-r = S_M k_M f(T) g(a_i) h(\Delta_r G) \tag{VII.3}$$

where the dissolution rate, r, depends on two type of factors: (1) **intrinsic factors** which are directly related to the nature of the dissolving mineral such as the intrinsic dissolution constant (k_M) or the specific surface area (S_M), and (2) **extrinsic factors** which are related to the environment surrounding the mineral such as fluid temperature, solute concentration or distance to chemical equilibrium through the functions f(T), $g(a)$ and $h(\Delta_r G)$, respectively.

Even if laboratory-based formulations of Equation VII.3 are commonly used in reactive-transport models to describe the dissolution of minerals, there is a general consensus on the fact that laboratory-derived dissolution rates overestimate field weathering rates by up to six orders of magnitude (Pačes; 1983; White and Brantley; 2003; Maher et al.; 2006). One possible explanation for this "lab-field discrepancy" is that laboratory and field-based approaches rely on distinct temporal and spacial scales and may not account for the same processes (Wild et al.; 2019). Laboratory-derived rates are usually measured on pristine minerals, exposing high specific surface areas and under homogeneous-abiotic conditions [e.g. Malmström et al. (1996)]. On the other hand, field-derived rates integrate several additional factors which are not described by Equation VII.3. For instance, minerals in the field are *aged*, meaning that their reactivity may have been changed due to the historic of fluid-mineral interactions they have previously been submitted to. One common such effect is the formation of nanometric coatings of secondary minerals that can reduce their apparent dissolution rate (Nugent et al.; 1998; Daval et al.; 2011; Wild et al.; 2016). Also, the physico-chemical conditions of fluids in the field are non-uniform and change e.g. with groundwater residence time (Maher; 2011). Furthermore, the influence of extrinsic factors such as redox conditions and microbial-induced weathering remain poorly constrained. The quantification of the contribution of microorganisms on mineral dissolution rates remains indeed challenging (Wild et al.; 2019). Even if several microorganisms with weathering capacity have been identified [e.g. Uroz et al. (2022)], there is still not a univocal approach to demonstrate that their presence in the mineral surface implies an active contribution to the dissolution process.

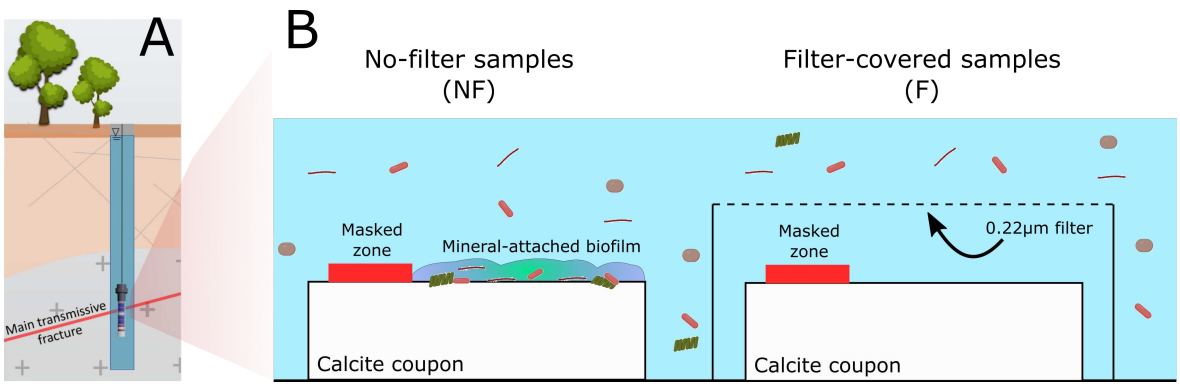

Figure VII.3: **Conceptualization of the experimental setting to measure *in-situ* calcite dissolution rates.** A): Calcite coupons are incubated in two redox-contrasted boreholes in order to study the redox-effect on calcite dissolution rates. B): in every redox condition, two replicates of calcite coupons are incubated under different microbe-mineral contact conditions. Filter-covered samples aim to prevent direct microbial colonization of surfaces while allowing the diffusion of solutes.

Hence, it is widely recognized that laboratory-based dissolution rates of minerals overestimate the field-based estimates. The estimation of local (i.e. non-integrative) weathering rates in the field are needed to obtain field-relevant estimates. Nevertheless, the experimental conditions in the field makes it difficult to disentangle the effects of intrinsic and extrinsic factors on such settings. Therefore, new experimental approaches were recently developed for the measurement of *in-situ* weathering rates (Wild et al.; 2019).

2.1.3 Method used to measure *in-situ* mineral weathering rates

We designed the experimental setup in Figure VII.3 to explicitly quantify the effect of two extrinsic factors on the *in-situ* weathering rate of calcite:

1. **Microbe-induced dissolution of calcite:** to test if attached microorganisms actively contribute to the dissolution of calcite, we compared dissolution rates measured on open surfaces to those measured on replicates of calcite coupons covered with 0.22 μm filters. The latter allowed the solutes exchange but prevented direct contact of microbes with minerals (see Figure VII.3).

2. **Effect of the fluid-redox conditions on the dissolution rate:** to test the effect of redox conditions, we placed two replicates of the mineral incubation setup in two redox contrasted boreholes, Psr1 and Psr5 (see Section 1.1 for details on the boreholes).

We adapted the methodology of Wild et al. (2019) to quantify the dissolution rate of calcite at *in-situ* conditions. The method consists in the estimating of the surface retreat (Δz) of polished calcite coupons exposing the 100 cleavage plane. The surface retreat is then used to compute the weathering rate according with Equation VII.4 (Arvidson et al.; 2003):

$$r = \frac{\Delta z}{\Delta t \times V_m}, \tag{VII.4}$$

where Δt accounts for the incubation time and V_m corresponds to the molar volume of the mineral. For the case of calcite, $V_m = 36.934 cm^3.mol^{-1}$ (Blanc et al.; 2012).

The surface retreat is measured after the incubation experiment as the topographic difference between the dissolved surface and the original topography. To preserve the topographic reference of the original surface, we avoid mineral-fluid contact in some areas by masking the mineral surface with inert silicon glue. The microtopography analyses required to measure surface retreats using the vertical scanning interferometry (VSI) technique already introduced in Section 1.1. Figure VII.4 illustrates the methods using as an example one of the *in-situ* incubated coupons.

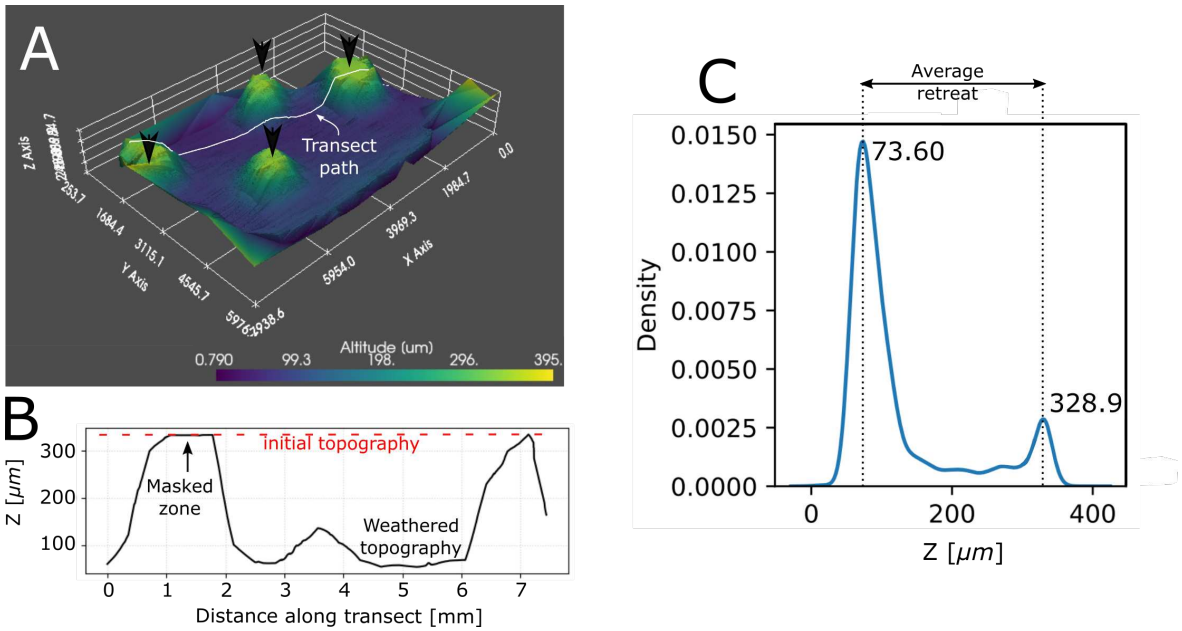

Figure VII.4: **Example of surface retreats in calcite coupons incubated under oxic conditions and exposed to microbe-mineral contact.** (A): VSI image of the weathered surface of calcite coupon after 10 months of *in-situ* incubation. The high topographic areas, indicated with black arrows, correspond to masked surfaces that were preserved from fluid-mineral contact during the incubation experiment. (B): topographic profile on the transect path showed in (A). The surface retreat, i.e. the difference between the initial surface (in red) and the weathered surface (in black), is apparent throughout the surface. (C) Kernel density distribution of the topography from the 3D image in (A). This statistical approach shows a bimodal distribution of elevations corresponding to the topography of initial (masked) and reacted (exposed to the fluid) portions of the mineral surface.

2.1.4 Results of the *in-situ* calcite dissolution experiment

The measured surface retreats associated to the calcite coupons after 10 months of *in-situ* incubation, as well as the associated dissolution rates computed with Equation VII.4 are presented in Figure VII.5-A. Average surface retreats span over several orders of magnitude. Under anoxic conditions the surface retreat ranges from 1 to 10 μm whereas under oxic conditions it ranges from 200 to 400 μm. In all the measured conditions, surface retreats are above the vertical detection limit of the VSI technique which is between 0.5 and 2 nm. The dissolution rates associated with the measured retreats vary from $10^{-6.5}$ to $10^{-8.5} mol.m^{-2}.s^{-1}$. Moreover, dissolution rates are more sensitive to changes in fluid-redox than to the microbe-mineral contact condition. Noteworthy, independently of the microbe-mineral contact condition, the highest dissolution rates are measured under oxic conditions. Samples exposed to direct microbe-mineral contact (NF condition) present systematically higher rates no matter the fluid-redox condition (see Figure VII.5-A).

2.1.5 Comparison with lab-derived dissolution rates

In Figure VII.5-B, our measured dissolution rates are compared against previously reported laboratory-derived rates as a function of fluid pH. Consistent with the previously cited *lab-field* discrepancy, our *in-situ* measurements are generally lower than laboratory estimates, including the reference value used in reactive-transport models, i.e. the R-T reference line in Figure VII.5-B. Laboratory-derived rates, mainly measured on calcite powders in stirred reactors, overestimate our oxic rates by one to two orders of magnitude and anoxic rates by three to four orders of magnitude.

These differences likely highlight effects of transport limitation which are almost eliminated in batch reactors where hydrodynamics (stirring) is designed to enable far-from-equilibrium fluid conditions. Notably, more recent laboratory-derived rates using hydrodynamic conditions that are more relevant to those prevailing

in the field Jordan and Rammensee (1998); Arvidson et al. (2003); Bouissonnié et al. (2018) are consistent with our *in-situ* measurements. As in our field measurements, these works also use microtopography approaches (e.g. AFM or VSI) to measure dissolution rates on pristine calcite crystals. To the best of our knowledge, however, our work provides the first measurements of *in-situ* dissolution rates for pristine calcite crystals. Our setup allows comparing our data with the cleavage specific measurements of recent works such as Arvidson et al. (2003); Bouissonnié et al. (2018); Stigliano et al. (2021). Thus, this new datasets constitutes a reference for the *in-situ* dissolution rates of calcite.

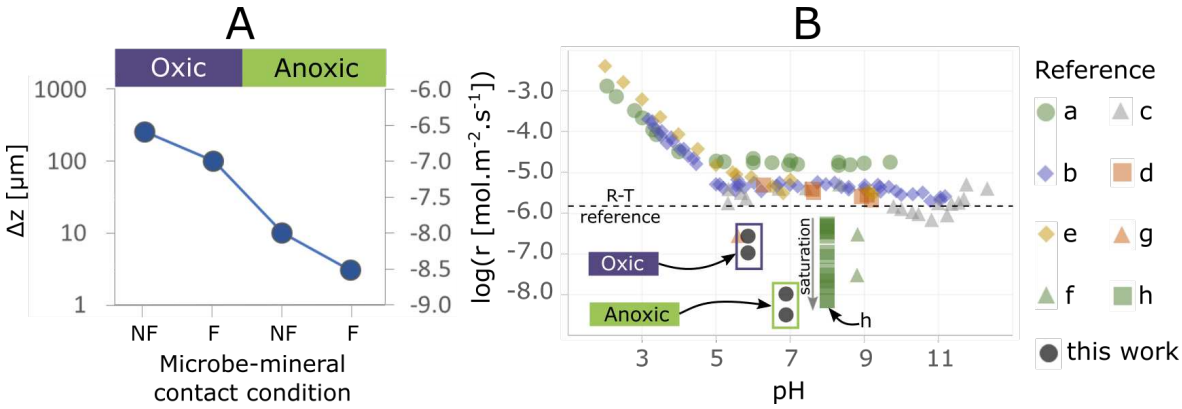

Figure VII.5: **Measured surface retreats and *in-situ* dissolution rates of calcite coupons.** A): Surface retreats (left axis) and dissolution rates (right axis) measured from calcite coupons incubated at *in-situ* conditions for a period of ten months. Oxic and anoxic labels indicate measurements on samples incubated either in Psr1 and Psr5, i.e. the oxic and anoxic boreholes, respectively. The microbe-mineral contact condition in the x-axis indicate whether the sampled was (F): filter-covered to prevent direct contact between microorganisms and minerals or (NF): non-covered by a filter and then exposed to direct microbe-mineral contact. B): comparison of our *in-situ* measured rates with previously reported laboratory-derived rates. The dashed line indicates the reference dissolution rate used in reactive-transport (RT) models, from Palandri and Kharaka (2004). References correspond to a: Sjoberg (1978), b: Busenberg et al. (1986), c: Shiraki et al. (2000), d: Cubillas et al. (2005), e: Plummer et al. (1978), f: Arvidson et al. (2003), g: Jordan and Rammensee (1998), h: Bouissonnié et al. (2018)

2.1.6 Effect of fluid properties

The two incubation boreholes used in this study are differentiated by their redox state (oxic in Psr1 vs anoxic in Psr5) but also by pH and saturation state of the fluid. While both boreholes have a near-neutral pH, Psr1 is slightly more acidic ($pH_{Psr1} = 5.87$) than Psr5 ($pH_{Psr5} = 6.89$). Likewise, the saturation index (SI) for calcite is lower in Psr1 ($\log SI - 3.23$) than in Psr5 ($\log SI = -1.34$). The lower pH and SI in the Psr1 borehole are thus likely responsible for the increased dissolution rates measured in the oxic condition. Nevertheless, it has been reported by several authors that laboratory-derived dissolution rates for calcite are poorly sensitive for $pH > 5$ (see Figure VII.5-A). This suggests that the pH differences in our case might not be a main control, which could rather be related to the saturation state of the fluid. This is supported by the data from Bouissonnié et al. (2018) (green squares in Figure VII.5-A), highlighting the effect of fluid saturation on calcite dissolution rates.

In Chapter IV we showed how groundwater redox conditions evolve, from oxic to anoxic, as a function of residence time and the progression of water-rock reactions. Mineral weathering, and in particular calcite weathering is sensitive to the saturation of the fluid, which is progressively increasing with groundwater residence time because of dissolution reactions. As a consequence, in natural settings a joint evolution of redox conditions along with pH and saturation index, and therefore weathering rate can be expected. The decreasing weathering rates we measured against the evolving fluid-redox in Figure VII.5-A are therefore consistent with previous large-scale observations that reported an anti-correlation between groundwater residence times and weathering rates in the field (Maher; 2011).

To summarize, we probed *in-situ* calcite dissolution rates in two contrasted redox boreholes (oxic vs anoxic). We found that the fluid conditions clearly influence the dissolution rate of calcite. The latter is between one to two orders of magnitude higher in the oxic case, which corresponds to more aggressive conditions (lower pH and fluid saturation). Nonetheless, at the pH ranges studied in this work, calcite dissolution rate has been reported as being of limited sensitivity to pH variations. Thus, we hypothesize that the *redox effect* measured in Figure VII.5-A is mainly due to the saturation state of the fluid.

2.1.7 Effect of microbe-induced dissolution

Figure VII.5-A suggests an effect of the direct microbe-mineral contact condition. Samples that were exposed to the direct microbe-mineral contact (NF in Figure VII.5-A) present systematically higher dissolution rates than samples in which the microbe-mineral contact was prevented (F). Dissolution rates with direct microbe-mineral contact were 2.6 and 3.3 times higher under oxic and anoxic conditions, respectively. Similar effects have been observed in laboratory measurements which reported enhanced dissolution rates when microbes were in direct contact with mineral substrates (Ahmed and Holmström; 2015). Although our results suggest that experimental setup successfully captured a signal of microbe-induced dissolution of calcite, further measurements are necessary to statistically support the differences in the dissolution rates.

We note that the experimental setup used to prevent microbe-mineral contact was not 100% efficient. SEM images of filter-covered samples (F in Figure VII.5-A) evidenced a microbial colonization of the surfaces after the incubation time and the formation of secondary layer at the calcite surface, possibly leading to passivation effects. The characterization of this secondary layer is discussed in further detail in the following Section 2.2. Based on this evidence, we hypothesize that the differences in the measured dissolution rates between F and NF samples could be due to three different effects, or to a combination of them:

1. **Passivation effects:** the secondary layer establishes a transport limitation which partially inhibits the dissolution of calcite, leading to reduced dissolution rates in the filter-covered samples. While passivation layers have been shown to produce reduced dissolution effects in other contexts (Daval et al.; 2011), in our case we only observed a secondary layer in the oxic-F sample. Therefore, this hypothesis should not be enough to explain the reduced NF rates observed at the two contrasted fluid-redox conditions. Moreover, under oxic conditions, the difference between F and NF dissolution rates is of 2.6 compared to 3.3 under anoxic conditions. If the passivation layer had a major impact, one could expect a stronger contrast between F and NF samples under oxic conditions, which is not the case. In this case, the secondary-layer could even have a stimulation effect rather than a passivating one.

2. **Filter degradation:** filters could be degraded at an intermediate time of the incubation period, resulting on a reduced time of microbe-mineral contact. This late colonization reflected in a reduced effect of the microbe-mineral contact in the F-samples. To evaluate the likelihood of this hypothesis, future experiments are needed to evaluate the filters' resistance to degradation.

3. **Colonization by $< 0.22\mu m$ cells:** in our proof-of-concept experimental setup we used $< 0.22\mu m$ filters to prevent microbe-mineral contact since this is the standard pore-size used to capture cells in environmental sampling. However, cells smaller than $< 0.22\mu m$ have been shown to be present in deep aquifers (Wu et al.; 2016). Such small cells could pass through the filters and colonize the samples. In such case, the difference in the dissolution rates could be due to a reduced capacity of the $< 0.22\mu m$ prokaryotes to induce calcite dissolution. We note however that we did not find any evidence of $< 0.22\mu m$ prokaryotes during our SEM inspection on the samples.

2.1.8 Partial conclusion

Box VII.4 - Quantifying the effect of fluid-redox and microbe-mineral contact on *in-situ* calcite dissolution rates

Our incubation device allowed us to estimate dissolution rates under *in-situ* conditions. We measured dissolution rates on calcite coupons under both oxic and anoxic conditions while controlling the microbe-mineral contact. **Our *in-situ* estimates of dissolution rates range from $10^{-6.5}$ to $10^{-8.5} mol.m^{-2}.s^{-1}$.** These field values are below most of the laboratory-derived dissolution rates, highlighting a lab-field discrepancy in calcite dissolution rates. Based on our measurements, **we conclude that the fluid-redox condition exerts an indirect control, with oxic conditions leading to higher dissolution rates.** Our hypothesis is that oxic groundwater is related to a small water transit-time and therefore, to a lower fluid-saturation. The microbe-mineral contact conditions in our experiment indicate a systematic enhancement of dissolution rates when direct contact is allowed. **Dissolution rates with direct microbe-mineral contact were 2.6 and 3.3 times higher under oxic and anoxic conditions, respectively.** Our measurements are yet not conclusive regarding the microbe-mineral contact effect, as the filter-covered samples, which were intended to mitigate this effect, were not completely efficient.

2.1.9 Perspectives

Future experiments, including replicates with shorter incubation times, should help to elucidate the effects of the microbe-mineral contact. These experiments should also include tests on the resistance of filters to long-term incubation times and the sequencing of mineral-attached communities to investigate the presence of $< 0.22 \mu m$ cells which have been reported in similar environments (Wu et al.; 2016).

While this work was focused on calcite coupons because their dissolution rates facilitate the measurement of surface retreats in an incubation time frame of 10 months, similar measurements could be done on other mineral substrates. In this experiment, we attempted, without success, to measure surface retreats in biotite and pyrite coupons. The use of longer incubation times could allow overcoming this issue. Additionally, complementary approaches could also be used to measure the weathering rates of these mineral substrates. Instead of producing a surface retreat, weathering may proceed through the progression of a weathering front inside the volume of the material, especially for redox-sensitive minerals such as biotite and pyrite. In that case, FIB-TEM approaches can constitute a particularly suited alternative, as successfully used in (Bonneville et al.; 2009, 2011), where weathering profiles in biotite coupons were quantified with a nm-scale resolution.

2.2 Characterization of secondary minerals in attached biofilms

In the first part of this chapter, the discussion was centered on the organic fraction of mineral-attached biofilms, i.e. on microbial biomass (cells and EPS) that form the biofilm matrix. In this section, we explore the inorganic fraction of these biofilms through the study of the secondary minerals that were commonly observed either encrusting or surrounding prokaryotic cells (see Figure in chapter's Appendix). It is widely recognized that microbes can induce and influence the formation of minerals as a consequence of their metabolic activity (Li et al.; 2013). Biological induced mineralization (BIM) and biological influenced mineralization (BIFM) commonly lead to the precipitation of secondary minerals that deposit externally to cells or in the periplasm of gram-negative bacteria (Schädler et al.; 2009; Miot et al.; 2009a). To the best of our knowledge, the mineralogical composition of in-situ mineral-attached biofilms has not yet been studied. Thus, the samples collected during our *in-situ* incubations offer a valuable opportunity to explore the mineralogical composition of biofilms. Here, we briefly present a mineralogical survey performed on the secondary crust formed on the filter-covered calcite coupons incubated under oxic conditions.

2.2.1 Chemical composition of the secondary layer formed on calcite

The filter-covered calcite coupon, incubated under oxic conditions, revealed the formation of a secondary crust covering the entire surface of the mineral (Figure VII.6-A). We sampled the crust and applied a gold-coating to analyze its chemical composition by SEM-EDS. The average chemical composition (see Figure VII.6-C) shows that the crust is mainly composed of Fe and O, but there are also accessory elements such as C, Ca, Cl, Si, Al, Na and N. The chemical maps of the accessory elements, not shown here, indicate an homogeneous chemical composition of this crust. Nonetheless, the composite elemental map of Fe and O (Figure VII.6-D) indicates an heterogeneous O/Fe ratio within the crust.

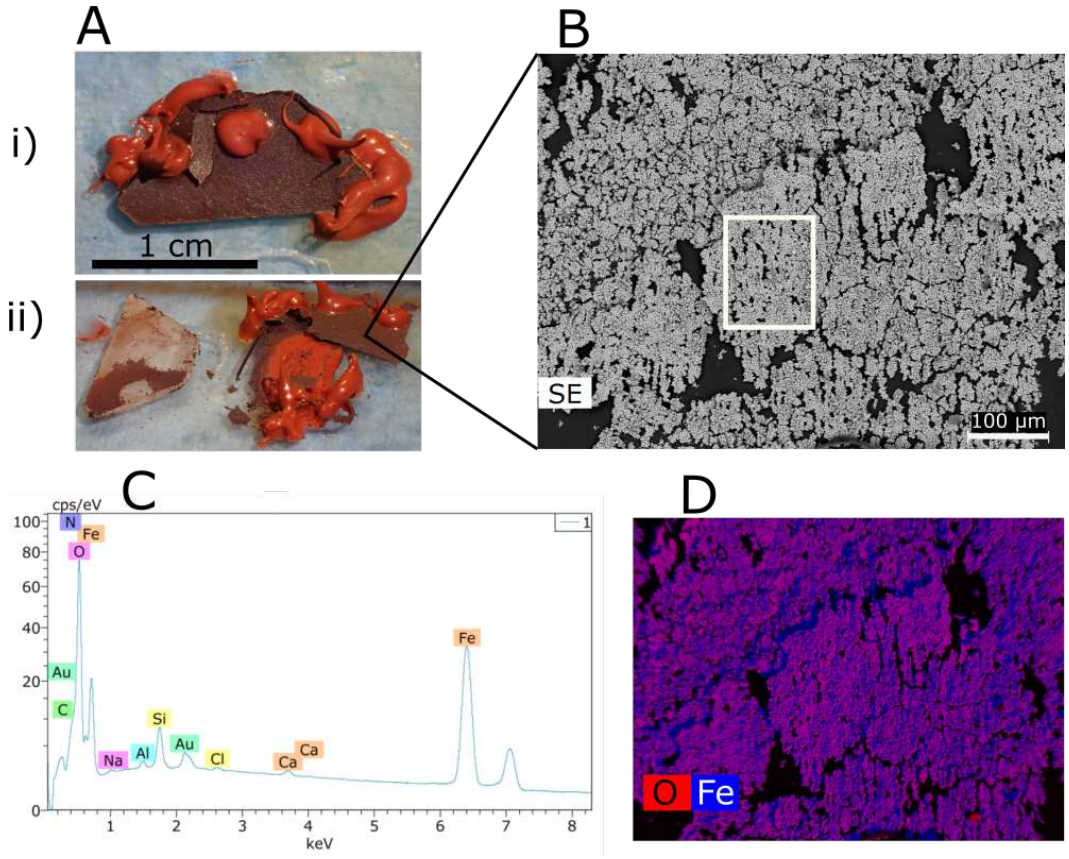

Figure VII.6: **Chemical composition of the secondary crust formed on filter-covered calcite incubated under oxic conditions.** A): Macroscopic image of the secondary minerals formed on calcite coupons showing that (i) the secondary minerals covered the entire surface of the coupon and (ii) the weathered calcite surface as exposed after detaching the compact crust. B): SEM image of the crust. C): average chemical analysis of the region indicated with the white rectangle in B. D): elemental map showing the O and Fe distributions from image in C.

2.2.2 Mineralogy of the secondary crust

Despite the homogeneous chemical composition of the crust, its optical aspect reveals three dominant colors in the crust, which indicates a mineralogical heterogeneity. As shown in Figure VII.7-A, the crust is composed by yellow (Y), white (W) and red (R) crystals. We analyzed the mineralogy of the secondary crust with an InVia® Raman spectrometer (Renishaw, UK) equipped with a 514nm laser and coupled to an Olympus FV1000® (Olympus, Japan) confocal microscope. To interpret the Raman spectra, we used the database of the RRUFF® project as a reference, as well as some internal standards from the geomicrobiology team at IPGP in Paris.

Figure VII.7-B presents three spectra acquired on the yellow crystals. The presence of peaks around 220, 290, 400, 605 and 1312 cm^{-1} allows the identification of this mineral as Hematite crystals as they fairly match with Hematite standards (not shown here). On the other hand, the Raman spectra corresponding to the red and

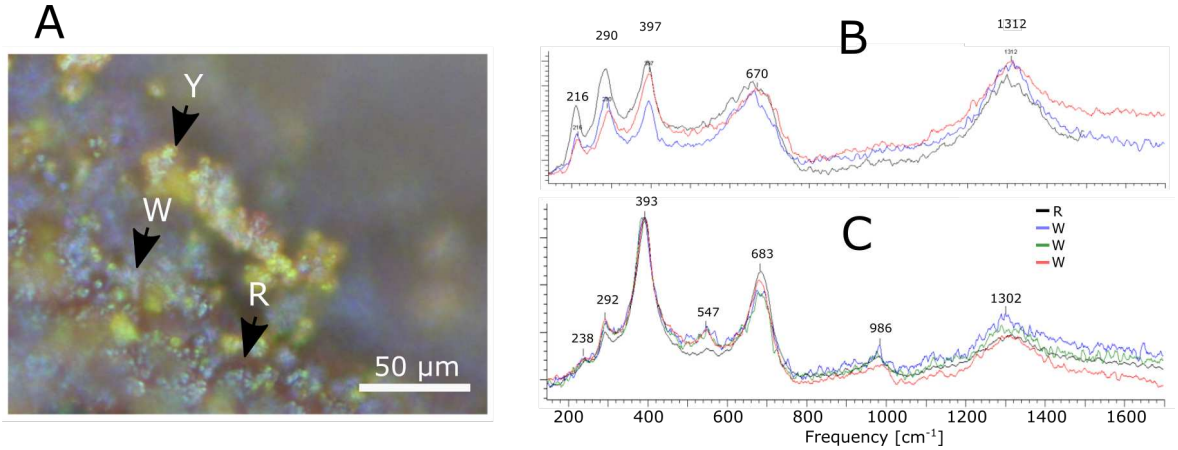

Figure VII.7: **Raman spectra acquired on the secondary crust formed on calcite.** A): optical aspect of the crust showing the presence of yellow (Y), white (W) and red (R) crystals as indicated by the arrow tips. B): Raman spectra of the Y crystals. C) Raman spectra of the R and W crystals. Spectra are the result of 10 runs of 10s with a power of 0.25 mW.

white crystals are very similar (see Figure VII.7-C). The high intensity of the peaks at 393 and 683 cm^{-1} as well as the presence of the peaks at 547 and 986 indicate that these spectra primarily correspond to goethite crystals. Furthermore, the presence of peaks at 290 and 1302 cm^{-1} also suggests the presence of Hematite, yet in a less dominant proportion than goethite as indicated by the intensity of the peaks. We interpret the differences in color as due to the presence of different proportions of hematite in the crust.

To summarize, the secondary crust formed on the incubated calcite coupons consists of crystals in three distinct colors: yellow, white, and red. Raman spectra acquired from these crystals indicate that the yellow crystals are identified as hematite. On the other hand, both white and red crystals predominantly exhibit characteristics of goethite, albeit with varying proportions of hematite. This variation in hematite content is likely responsible for the observed differences in color. Furthermore, the fluctuations in goethite and hematite proportions within the secondary crust align with the heterogeneous distribution of O/Fe ratios shown in Figure VII.6-D. While both goethite and hematite are Fe(III) oxyhydroxides, the presence of water in goethite (FeOOH) results in a distinct O/Fe ratio compared to hematite (Fe_2O_3).

2.2.3 Biomineralizations and micrometric structure of the secondary crust of calcite coupons

We inspected the structure of the secondary crust formed on the filter-covered calcite sample incubated under oxic conditions. SEM acquired images in Figure VII.8-A reveal a globular structure of the minerals in this crust. The micrometric globules result from the aggregation of iron oxide nanocrystals (goethite and hematite as seen in the above section) which are packed into exopolymeric substances (EPS) as shown by the light-blue arrows in Figure VII.8. Moreover, prokaryotic cells are intimately related to the nanocrystal aggregates as shown by the different degrees of encrusting of cells in Figures VII.8-B and C. These images suggest that organic surfaces, i.e. EPS layers and prokaryotic cells, serve as nucleation points for the crystallisation of iron oxyhydroxides. Similar nucleation effects in which the presence of organic substances promotes the formation of iron oxyhydroxides while controlling their size, shape and density, have been reported previously (Pédrot et al.; 2011). Furthermore, Pédrot et al. (2011) found that the presence of organic molecules (in their case, humic substances) influenced the hydrolyzation degree of the formed iron oxyhydroxides. We hypothesize that the influence of organic substances on the crystallization processes of iron oxyhydroxides may explain the observed mineralogical heterogeneities in the Raman analyses in Section 2.2.2.

Finally, the high degree of mineralization of the prokaryotic cells in Figures VII.8-B and C, and the association with hematite and goethite minerals have close similarities with previously reported encrusting observations in cultures of the anaerobic iron-oxidizer (FeOB) *Acidovorax* sp. (Li et al.; 2013; Kappler et al.;

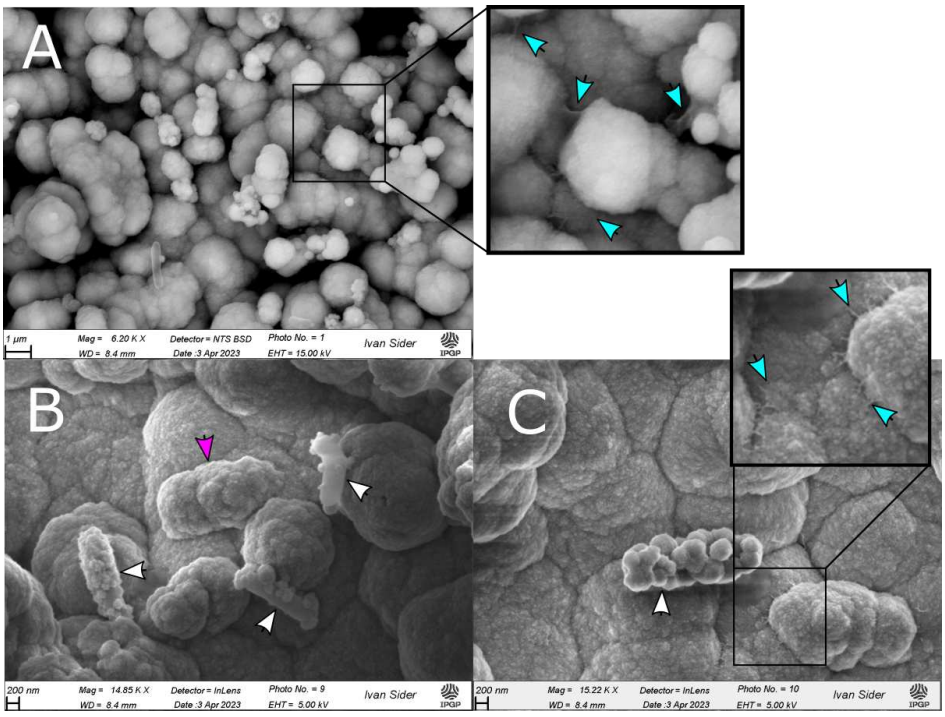

Figure VII.8: **SEM images of biomineralizations in the secondary crust formed on calcite coupons.** A): Backscattered-electron images showing the globular structure of the crust at a micrometer level. The enlarged zones in A and C reveal that the micrometric grains result from the aggregation of fine nanocrystals packed into exopolymers (EPS), indicated by light-blue arrows. B and C are secondary-electron images showing different levels of encrusting of prokaryotic cells, indicated by white arrows. Purple arrow in B likely indicates a bacteriomorph at an advanced level of encrusting. Organic surfaces such as prokaryotic cells and EPS serve as nucleation points for the crystallization of iron oxyhydroxides.

2005). Since the calcite coupon was incubated under oxic conditions, the only way for FeOB to be responsible for the observed mineralizations is that a dissolved oxygen gradient formed at the vicinity of the mineral. Several studies have indeed shown that FeOB thrive preferentially in microaerobic or anoxic environments (Kappler et al.; 2021, 2005). Nevertheless, we estimate that the formation of a low-oxygen microenvironment in the vicinity of the calcite surface is not a likely explanation. The differences in the secondary minerals that formed in oxic or anoxic-incubated samples are in fact apparent (orange crusts under oxic conditions and black crusts under anoxic conditions, see Figure in chapter's Appendix). If an anoxic microenvironment were to develop near the oxic-incubated samples, it would be expected to result in similar black crusts as those observed in the anoxic-incubated samples. Instead, we consider that the biomineralizations observed in the secondary crust are enhanced by the abundant inorganic carbon that is available from the dissolution of calcite. Further analysis of microbial community composition is however necessary to gain a better understanding of the potential metabolisms that may have been involved in the formation of the secondary crust.

2.2.4 Fluid-redox as a control on the mineralogical composition of the secondary crust

In the above section, Figure VII.8 presented evidence of the intimate link between the surface-attached biofilm and the formation of mineral concretions in the calcite mineralosphere under oxic conditions. Surprisingly, even if calcite ($CaCO_3$) is not an iron-bearing mineral, the secondary crust covering the mineral is rich in iron oxyhydroxides. Moreover, the fluid in the incubation environment (borehole Psr1) has very low concentrations of dissolved iron (about 10^{-3}ppm) according to Table 2 in Section 1.1. We attribute the massive presence of iron oxides in this crust to two environmental factors:

1. **The presence of iron-bearing minerals in the bedrock and in the surrounding minerals in the experimental setup:** while calcite coupons are not Fe-bearing minerals, the experimental setup hosted

iron-bearing minerals such as biotite, pyrite and to a lesser extent forsteritic olivine. Moreover, the surrounding bedrock (micaschist) also hosts biotite as previously shown in Chapter III. Therefore, these different mineral substrates are possible sources for the iron that precipitated in the secondary crust of calcite coupons.

2. **The fluid-redox conditions favor the oxidation but also the replenishment of dissolved iron:** according to Table 2 in Section 1.1, borehole Psr1 has a high oxic state (the average dissolved oxygen concentration is 5.3ppm). While these oxic conditions favor the fast oxidation of dissolved Fe^{2+}, this environmental setting also favors high dissolution rates of iron-bearing minerals (Osorio-Leon et al.; 2023). Remarkably, the numerical model presented in Chapter IV showed that even if dissolved Fe^{2+} concentrations are below detection limits, there is an active dissolution of iron-bearing minerals promoted by the oxic conditions. The formation of massive iron oxyhydroxide concretions in the secondary crust of calcite coupons likely indicates that the half-life of dissolved iron is enough to be transported in the aquifer from Fe-bearing to neighboring minerals.

2.2.5 Partial conclusion

The characterization of the minerals composing the secondary crust that formed on filter-covered calcite coupons, incubated under oxic conditions, revealed a massive presence of iron oxyhydroxides. The crust is characterized by a micrometric globular texture, mainly composed of goethite and hematite nanocrystals that nucleate on organic surfaces such as EPS and prokaryotic cells. We attribute the abundant presence of Fe-oxyhydroxides to the fluid-redox conditions that favor the dissolution of the neighboring Fe-bearing minerals and the oxidation of dissolved iron.

2.2.6 Perspectives

Here, we present some perspectives to follow the work on the mineralogy of secondary minerals:

1. **Microbial communities associated to the secondary crust:** Unlike the mineral-attached communities on other mineral substrates such as biotite and pyrite (presented in Section 1.1), in the calcite coupons we do not observe a diversity of prokaryotic cell morphologies. The secondary crust of calcite appears indeed to host only a singular type of rod-shaped prokaryotes. The characterization of the microorganisms associated to this crust by molecular biology methods (e.g. 16S rRNA sequencing) could provide insights on the composition and also on the putative metabolisms associated to the secondary minerals.

2. **Mineralogy of the secondary minerals in other mineral substrates and fluid-redox conditions:** in this study we only focused on the characterization of the secondary minerals on calcite coupons under oxic conditions. However, similar analyses could be conducted on the secondary minerals that formed on the other mineral substrates incubated during the experiment (e.g. biotite, pyrite, quartz, olivine). A better characterization of the mineralogy and the chemical composition of the secondary minerals can provide valuable insights on the putative metabolisms taking place in the mineralosphere. Ultimately, a better knowledge of how secondary minerals are sensitive to environmental conditions such as host-mineral substrate, fluid-redox conditions or the indigeneous microbial communities could contribute to other fields of the geomicrobiology such as bacteria fossilization or the formation of biosignatures.

3 Chapter conclusion

This chapter presented the outcomes of a long term field experiment for studying the effects of environmental factors in aquifers on microbe-mineral interactions. The focus of this chapter was mineral-attached communities, occupying a unique ecological niche known as the *mineralosphere* (Uroz et al.; 2015), which is responsible for

hosting at least 99% of the microbial biomass in the continental subsurface. Despite its significant biomass contribution, this mineral-attached biosphere remains poorly understood due to challenges associated with sampling.

This chapter suggests some decisive methodological advancements to overcome sampling limitations, with the development of a proof-of-concept device designed for the *in-situ* incubation of surrogate minerals within boreholes. This device enables the controlled sampling of mineral-attached communities, which are usually challenging to access, using boreholes as incubation media. Its efficiency in sampling mineral-attached microbial communities was confirmed by an *in-situ* incubation experiment over 10 months. Furthermore, we developed a systematic workflow for estimating various key parameters of microbe-mineral interactions, which can be applied to future studies addressing related questions. These advances have inspired the development at a broader scale of similar field setups to be deployed in different field observatories in the PIA3 project TerraForma (https://terra-forma.cnrs.fr).

From a general perspective, our study is one of the few works that quantitatively assessed the effects of environmental conditions on microbe-mineral interactions under *in-situ* conditions. In the first part of the chapter, we showed that the redox conditions can impact the energy availability in the subsurface environment. As a consequence, minerals bearing energy sources (electron donors) were shown to host denser cell populations. The sensitivity of attached microbial communities to oxic/anoxic conditions was evidenced for biotite surfaces but not for other tested minerals. We related this observation to distinct biogeochemical reactions, as derived from thermodynamic modeling. Sequencing data using 16S rRNA amplicon from samples incubated under anoxic conditions further showed that the composition of attached communities was clearly different from the planktonic consortium, and was also affected by the mineral substrate.

In the second part of the chapter, we assessed the effect of (1) the fluid conditions and (2) the microbe-mineral contact on the dissolution rate of minerals. Using calcite as a reference mineral, we quantified *in-situ* calcite dissolution rates for the first time. Our results indicated a clear correlation between oxic conditions and significantly higher mineral dissolution rates, typically one to two orders of magnitude higher than under anoxic conditions. Moreover, we quantified the effect of the microbe-induced dissolution of calcite leading to dissolution rates two to three times faster than in the case when the microbe-mineral contact was prevented. Finally, a mineralogical survey done in a secondary crust formed on calcite, revealed an intimate link between mineralization and mineral-attached biofilms. The chemical composition of this secondary crust, rich in iron oxyhydroxides, is closely related to the fluid-redox conditions.

Collectively, the findings presented in this chapter offer complementary evidence that highlights the significant influence of fluid-redox conditions on various aspects of microbe-mineral interactions within the subsurface. The transport of dissolved oxygen in the continental subsurface, investigated in previous chapters, can thus impact not only the weathering of rocks, but also the biomass and the functional traits of mineral-attached consortia. Consequently, I argue that it is important that reactive-transport models and subsurface biomass models account for the redox compartmentalization of the subsurface. This consideration is essential as it can potentially impact fundamental variables within these models, such as mineral dissolution rates and cell densities.

4 Take-home messages

Redox effects on microbe-mineral interactions

1. We designed and successfully tested a passive device for the *in-situ* incubation of surrogate minerals in order to study the mineral-attached microbial communities. We also developed a workflow allowing the measurement of key parameters related to different aspects of microbe-mineral interactions.
2. **Effects of *minerals on microbes*:**
   (a) The mineral substrate exerts a primary control over the mineral-attached biomass, while the fluid-redox condition affect the biomass attached to specific minerals. Minerals bearing electron donors host significantly more attached biomass than inert minerals.
   (b) The composition of the mineral-attached consortia is generally differentiated from the planktonic one, and also depends on the mineral substrate as deduced from 16S rRNA amplicon sequencing. The effect of fluid-redox conditions on community composition is a work-in-progress.
3. **Effects of *microbes on minerals*:**
   (a) For the first time, we measured *in-situ* dissolution rates of calcite in the deep subsurface. Fluid-redox conditions exert a significant control on these rates, with dissolution occurring between one to two orders of magnitude faster under oxic conditions. Additionally, direct microbe-mineral contact further enhances calcite dissolution rates by approximately two to three times.
   (b) The mineralogical analysis of a secondary crust revealed that the fluid-redox conditions are a first order control on the secondary minerals. The crust structure, formed of microcrystalline iron oxyhydroxides, is intimately related to organic compounds in mineral-attached biofilms.

5 Chapter acknowledgments

I want to expressly thank my exceptional collaborator, Bastien Wild. Without his help, the work that fueled this chapter would never have been accomplished. Bastien inspired the experimental approach with his original work on rock-weathering and supported my work all along this experiment. Thank you very much Bastien! I also want to thank the different collaborators of the ANR project IronStone for their support at the different stages of this experiment:

- Nicolas Lavenant for his valuable help with the design and construction of the incubation device.
- Achim Quaiser for his support with molecular biology analyses. Thank you very much for always being there during the long-time effort these analyses implied!
- The members of the geomicrobiology group from IPGP institute in Paris (Emmanuelle Gerard, Hélène Bouquerel, Bénédicte Menez and Stephan Borenztajn). Their support throughout the entire microscopic workflow (confocal, Raman, epifluorescence and SEM-EDS methods) was decisive during my numerous visits to Paris. Thanks very much to you all!
- Last but not least, Alexis Dufresne, Tanguy Le Borgne and Camille Bouchez for their supervision, advice and support throughout the whole project.

Finally, I want to thank the PIA3 project TERRAFORMA for providing funding for this research and adding value to the passive incubator design.

Bibliography

Ahmed, E. and Holmström, S. J. M. (2015). Microbe – mineral interactions : The impact of surface attachment on mineral weathering and element selectivity by microorganisms. *Chemical Geology*, 403:13–23.

Alfreider, A., Krössbacher, M., and Psenner, R. (1997). Groundwater samples do not reflect bacterial densities and activity in subsurface systems. *Water Research*, 31(4):832–840.

Anantharaman, K., Brown, C. T., Hug, L. A., Sharon, I., Castelle, C. J., Probst, A. J., Thomas, B. C., Singh, A., Wilkins, M. J., Karaoz, U., Brodie, E. L., Williams, K. H., Hubbard, S. S., and Banfield, J. F. (2016). Thousands of microbial genomes shed light on interconnected biogeochemical processes in an aquifer system. *Nature Communications*, 7:1–11.

Arvidson, R. S., Ertan, I. E., Amonette, J. E., and Luttge, A. (2003). Variation in calcite dissolution rates:. *Geochimica et Cosmochimica Acta*, 67(9):1623–1634.

Balkwill, D. L. (1989). Numbers, diversity, and morphological characteristics of aerobic, chemoheterotrophic bacteria in deep subsurface sediments from a site in South Carolina. *Geomicrobiology Journal*, 7(1-2):33–52.

Bar-on, Y. M., Phillips, R., and Milo, R. (2018). The biomass distribution on Earth. *Proceedings of the National Academy of Sciences of the United States of America*, 115(25):6506–6511.

Bethencourt, L., Bochet, O., Farasin, J., Aquilina, L., Borgne, T. L., Quaiser, A., Biget, M., Michon-Coudouel, S., Labasque, T., and Dufresne, A. (2020). Genome reconstruction reveals distinct assemblages of Gallionellaceae in surface and subsurface redox transition zones. *FEMS Microbiology Ecology*, 96(5).

Blanc, P., Lassin, A., Piantone, P., Azaroual, M., Jacquemet, N., Fabbri, A., and Gaucher, E. C. (2012). Thermoddem: A geochemical database focused on low temperature water/rock interactions and waste materials. *Applied Geochemistry*, 27(10):2107–2116.

Bonneville, S., Morgan, D. J., Schmalenberger, A., Bray, A., Brown, A., Banwart, S. A., and Benning, L. G. (2011). Tree-mycorrhiza symbiosis accelerate mineral weathering: Evidences from nanometer-scale elemental fluxes at the hypha–mineral interface. *Geochimica et Cosmochimica Acta*, 75(22):6988–7005.

Bonneville, S., Smits, M. M., Brown, A., Harrington, J., Leake, J. R., Brydson, R., and Benning, L. G. (2009). Plant-driven fungal weathering: Early stages of mineral alteration at the nanometer scale. *Geology*, 37(7):615–618.

Bouissonnié, A., Daval, D., Marinoni, M., and Ackerer, P. (2018). From mixed flow reactor to column experiments and modeling: Upscaling of calcite dissolution rate. *Chemical Geology*, 487:63–75.

Busenberg, E., Plummer, L., and Mumpton, F. (1986). A comparative study of the dissolution and crystal growth kinetics of calcite and aragonite. *Studies in diagenesis*, 1578:139–168.

Cao, J., Yuan, D., Groves, C., Huang, F., Yang, H., and Lu, Q. (2012). Carbon Fluxes and Sinks: The Consumption of Atmospheric and Soil CO_2 by Carbonate Rock Dissolution. *Acta Geologica Sinica - English Edition*, 86(4):963–972.

Casar, C. P., Kruger, B. R., Flynn, T. M., Masterson, A. L., Momper, L. M., and Osburn, M. R. (2020). Mineral-hosted biofilm communities in the continental deep subsurface, Deep Mine Microbial Observatory, SD, USA. *Geobiology*, (October 2019):1–15.

Converse, B. J., McKinley, J. P., Resch, C. T., and Roden, E. E. (2015). Microbial mineral colonization across a subsurface redox transition zone. *Frontiers in Microbiology*, 6.

Cubillas, P., Köhler, S., Prieto, M., Chaïrat, C., and Oelkers, E. H. (2005). Experimental determination of the dissolution rates of calcite, aragonite, and bivalves. *Chemical Geology*, 216(1-2):59–77.

Daoxian, Y. (1997). Sensitivity of karst process to environmental change along the PEP II transect. *Quaternary International*, 37:105–113.

Daval, D., Sissmann, O., Menguy, N., Saldi, G. D., Guyot, F., Martinez, I., Corvisier, J., Garcia, B., Machouk, I., Knauss, K. G., and Hellmann, R. (2011). Influence of amorphous silica layer formation on the dissolution rate of olivine at 90°C and elevated pCO2. *Chemical Geology*, 284(1-2):193–209.

Flemming, H.-C., van Hullebusch, E. D., Neu, T. R., Nielsen, P. H., Seviour, T., Stoodley, P., Wingender, J., and Wuertz, S. (2022). The biofilm matrix: Multitasking in a shared space. *Nature Reviews Microbiology*.

Flemming, H.-C. and Wuertz, S. (2019). Bacteria and archaea on Earth and their abundance in biofilms. *Nature Reviews Microbiology*, 17(4):247–260.

Floury, P., Gaillardet, J., Tallec, G., Ansart, P., Bouchez, J., Louvat, P., and Gorge, C. (2019). Chemical weathering and CO 2 consumption rate in a multilayered-aquifer dominated watershed under intensive farming: The Orgeval Critical Zone Observatory, France. *Hydrological Processes*, 33(2):195–213.

Flynn, T. M., Sanford, R. A., Santo Domingo, J. W., Ashbolt, N. J., Levine, A. D., and Bethke, C. M. (2012). The active bacterial community in a pristine confined aquifer. *Water Resources Research*, 48(9).

Gaillardet, J., Dupré, B., Louvat, P., and Allègre, C. J. (1999). Global silicate weathering and CO2 consumption rates deduced from the chemistry of large rivers. *Chemical Geology*, 159(1):3–30.

Ginn, T. R., Wood, B. D., Nelson, K. E., Scheibe, T. D., Murphy, E. M., and Clement, T. P. (2002). Processes in microbial transport in the natural subsurface. *Advances in Water Resources*, 25(8):1017–1042.

Griebler, C., Mindl, B., Slezak, D., and Geiger-Kaiser, M. (2002). Distribution patterns of attached and suspended bacteria in pristine and contaminated shallow aquifers studied with an in situ sediment exposure microcosm. *Aquatic Microbial Ecology*, 28(2):117–129.

Hartmann, J., Jansen, N., Dürr, H. H., Kempe, S., and Köhler, P. (2009). Global CO2-consumption by chemical weathering: What is the contribution of highly active weathering regions? *Global and Planetary Change*, 69(4):185–194.

Hazen, T. C., Jiménez, L., López de Victoria, G., and Fliermans, C. B. (1991). Comparison of bacteria from deep subsurface sediment and adjacent groundwater. *Microbial Ecology*, 22(1):293–304.

Jones, A. A. and Bennett, P. C. (2017). Mineral Ecology : Surface Specific Colonization and Geochemical Drivers of Biofilm Accumulation , Composition , and Phylogeny. *Frontiers in Microbiology*, 8(March):1–14.

Jordan, G. and Rammensee, W. (1998). Dissolution rates of calcite (1014) obtained by scanning force microscopy: Microtopography-based dissolution kinetics on surfaces with anisotropic step velocities. *Geochimica et Cosmochimica Acta*, 62(6):941–947.

Kappler, A., Bryce, C., Mansor, M., Lueder, U., Byrne, J. M., and Swanner, E. D. (2021). An evolving view on biogeochemical cycling of iron. *Nature Reviews Microbiology*, 19(6):360–374.

Kappler, A., Schink, B., and Newman, D. K. (2005). Fe (iii) mineral formation and cell encrustation by the nitrate-dependent fe (ii)-oxidizer strain bofen1. *Geobiology*, 3(4):235–245.

Kölbel-Boelke, J., Anders, E. M., and Nehrkorn, A. (1988). Microbial communities in the saturated groundwater environment II: Diversity of bacterial communities in a Pleistocene sand aquifer and their in vitro activities. *Microbial Ecology*, 16(1):31–48.

Lasaga, A. C. (1984). Chemical kinetics of water-rock interactions. *Journal of Geophysical Research: Solid Earth*, 89(B6):4009–4025.

Lasaga, A. C. (1998). *Kinetic Theory in the Earth Sciences:*. Princeton University Press.

Lehman, R. M., Colwell, F. S., and Bala, G. A. (2001a). Attached and Unattached Microbial Communities in a Simulated Basalt Aquifer under Fracture- and Porous-Flow Conditions. *Applied and Environmental Microbiology*, 67(6):2799–2809.

Lehman, R. M., Roberto, F. F., Earley, D., Bruhn, D. F., Brink, S. E., O'Connell, S. P., Delwiche, M. E., and Colwell, F. S. (2001b). Attached and Unattached Bacterial Communities in a 120-Meter Corehole in an Acidic, Crystalline Rock Aquifer. *Applied and Environmental Microbiology*, 67(5):2095–2106.

Li, J., Benzerara, K., Bernard, S., and Beyssac, O. (2013). The link between biomineralization and fossilization of bacteria: Insights from field and experimental studies. *Chemical Geology*, 359:49–69.

Locey, K. J. (2010). Synthesizing traditional biogeography with microbial ecology: the importance of dormancy.

Magnabosco, C., Lin, L. H., Dong, H., Bomberg, M., Ghiorse, W., Stan-Lotter, H., Pedersen, K., Kieft, T. L., van Heerden, E., and Onstott, T. C. (2018). The biomass and biodiversity of the continental subsurface. *Nature Geoscience*, 11(10):707–717.

Maher, K. (2011). The role of fluid residence time and topographic scales in determining chemical fluxes from landscapes. *Earth and Planetary Science Letters*, 312(1):48–58.

Maher, K. and Chamberlain, C. P. (2014). Hydrologic Regulation of Chemical Weathering and the Geologic Carbon Cycle. *Science*, 343(6178):1502–1504.

Maher, K., Steefel, C. I., DePaolo, D. J., and Viani, B. E. (2006). The mineral dissolution rate conundrum: Insights from reactive transport modeling of U isotopes and pore fluid chemistry in marine sediments. *Geochimica et Cosmochimica Acta*, 70(2):337–363.

Malmström, M., Banwart, S., Lewenhagen, J., Duro, L., and Bruno, J. (1996). The dissolution of biotite and chlorite at 25 ºC in the near-neutral pH region. *Journal of Contaminant Hydrology*, 21:201–213.

Miot, J., Benzerara, K., Morin, G., Kappler, A., Bernard, S., Obst, M., Férard, C., Skouri-Panet, F., Guigner, J.-M., Posth, N., Galvez, M., Brown, G. E., and Guyot, F. (2009a). Iron biomineralization by anaerobic neutrophilic iron-oxidizing bacteria. *Geochimica et Cosmochimica Acta*, 73(3):696–711.

Miot, J., Benzerara, K., Obst, M., Kappler, A., Hegler, F., Schädler, S., Bouchez, C., Guyot, F., and Morin, G. (2009b). Extracellular Iron Biomineralization by Photoautotrophic Iron-Oxidizing Bacteria. *Applied and Environmental Microbiology*, 75(17):5586–5591.

Molins, S., Soulaine, C., Prasianakis, N. I., Abbasi, A., Poncet, P., Ladd, A. J., Starchenko, V., Roman, S., Trebotich, D., Tchelepi, H. A., and Steefel, C. I. (2020). Simulation of mineral dissolution at the pore scale with evolving fluid-solid interfaces: Review of approaches and benchmark problem set. *Computational Geosciences*.

Molins, S., Trebotich, D., Yang, L., Ajo-Franklin, J. B., Ligocki, T. J., Shen, C., and Steefel, C. I. (2014). Pore-Scale Controls on Calcite Dissolution Rates from Flow-through Laboratory and Numerical Experiments. *Environmental Science & Technology*, 48(13):7453–7460.

Nordstrom, D. K. (2011). Hydrogeochemical processes governing the origin, transport and fate of major and trace elements from mine wastes and mineralized rock to surface waters. *Applied Geochemistry*, 26(11):1777–1791.

Nugent, M. A., Brantley, S. L., Pantano, C. G., and Maurice, P. A. (1998). The influence of natural mineral coatings on feldspar weathering. *Nature*, 395(6702):588–591.

Nuppunen-Puputti, M., Kietäväinen, R., Raulio, M., Soro, A., Purkamo, L., Kukkonen, I., and Bomberg, M. (2022). Epilithic Microbial Community Functionality in Deep Oligotrophic Continental Bedrock. *Frontiers in Microbiology*, 13.

Osorio-Leon, I., Bouchez, C., Chatton, E., Lavenant, N., Longuevergne, L., and Le Borgne, T. (2023). Hydrological and geological controls for the depth distribution of dissolved oxygen and iron in silicate catchments.

Overholt, W. A., Trumbore, S., Xu, X., Bornemann, T. L. V., Probst, A. J., Krüger, M., Herrmann, M., Thamdrup, B., Bristow, L. A., Taubert, M., Schwab, V. F., Hölzer, M., Marz, M., and Küsel, K. (2022). Carbon fixation rates in groundwater similar to those in oligotrophic marine systems.

Pačes, T. (1983). Rate constants of dissolution derived from the measurements of mass balance in hydrological catchments. *Geochimica et Cosmochimica Acta*, 47(11):1855–1863.

Palandri, J. and Kharaka, Y. (2004). A Compilation of Rate Parameters of Water-Mineral Interaction Kinetics. Technical report.

Pédrot, M., Boudec, A. L., Davranche, M., Dia, A., and Henin, O. (2011). How does organic matter constrain the nature, size and availability of Fe nanoparticles for biological reduction? *Journal of Colloid and Interface Science*, 359(1):75–85.

Plummer, L. N., Wigley, T. M. L., and Parkhurst, D. L. (1978). The kinetics of calcite dissolution in CO2 -water systems at 5 degrees to 60 degrees C and 0.0 to 1.0 atm CO2. *American Journal of Science*, 278(2):179–216.

Reardon, C. L., Cummings, D. E., Petzke, L. M., Kinsall, B. L., Watson, D. B., Peyton, B. M., and Geesey, G. G. (2004). Composition and Diversity of Microbial Communities Recovered from Surrogate Minerals Incubated in an Acidic Uranium-Contaminated Aquifer. *Applied and Environmental Microbiology*, 70(10):6037–6046.

Schädler, S., Burkhardt, C., Hegler, F., Straub, K. L., Miot, J., Benzerara, K., and Kappler, A. (2009). Formation of Cell-Iron-Mineral Aggregates by Phototrophic and Nitrate-Reducing Anaerobic Fe(II)-Oxidizing Bacteria. *Geomicrobiology Journal*, 26(2):93–103.

Shiraki, R., Rock, P. A., and Casey, W. H. (2000). Dissolution kinetics of calcite in 0.1 m nacl solution at room temperature: an atomic force microscopic (afm) study. *Aquatic Geochemistry*, 6:87–108.

Sinclair, J. and Ghiorse, W. (1989). Distribution of aerobic bacteria, protozoa, algae, and fungi in deep subsurface sediments. *Geomicrobiology Journal*, 7(1-2):15–31.

Sjoberg, E. (1978). Kinetics and mechanism of calcite dissolution in aqueous solutions at low temperature temperatures. *Stockholm Contrib. Geol.*, 32:1–92.

Stigliano, L., Siena, M., Ackerer, P., Guadagnini, A., and Daval, D. (2021). Statistical Description of Calcite Surface Roughness Resulting from Dissolution at Close-to-Equilibrium Conditions. *ACS Earth and Space Chemistry*, 5(11):3115–3129.

Uroz, S., Kelly, L. C., Turpault, M. P., Lepleux, C., and Frey-Klett, P. (2015). The Mineralosphere Concept: Mineralogical Control of the Distribution and Function of Mineral-associated Bacterial Communities. *Trends in Microbiology*, 23(12):751–762.

Uroz, S., Picard, L., and Turpault, M.-P. (2022). Recent progress in understanding the ecology and molecular genetics of soil mineral weathering bacteria. *Trends in Microbiology*, 30(9):882–897.

White, A. F. and Brantley, S. L. (2003). The effect of time on the weathering of silicate minerals: Why do weathering rates differ in the laboratory and field? *Chemical Geology*, 202(3-4):479–506.

Whitman, W. B., Coleman, D. C., and Wiebe, W. J. (1998). Prokaryotes: The unseen majority. *Proceedings of the National Academy of Sciences of the United States of America*, 95(12):6578–6583.

Wild, B., Daval, D., Beaulieu, E., Pierret, M. C., Viville, D., and Imfeld, G. (2019). In-situ dissolution rates of silicate minerals and associated bacterial communities in the critical zone (Strengbach catchment, France). *Geochimica et Cosmochimica Acta*, 249:95–120.

Wild, B., Daval, D., Guyot, F., Knauss, K. G., Pollet-villard, M., and Imfeld, G. (2016). pH-dependent control of feldspar dissolution rate by altered surface layers. *Chemical Geology*, 442:148–159.

Willers, C., Jansen Van Rensburg, P., and Claassens, S. (2015). Phospholipid fatty acid profiling of microbial communities-a review of interpretations and recent applications. *Journal of Applied Microbiology*, 119(5):1207–1218.

Wu, X., Holmfeldt, K., Hubalek, V., Lundin, D., Åström, M., Bertilsson, S., and Dopson, M. (2016). Microbial metagenomes from three aquifers in the Fennoscandian shield terrestrial deep biosphere reveal metabolic partitioning among populations. *ISME Journal*, 10(5):1192–1203.

VIII. GENERAL CONCLUSION

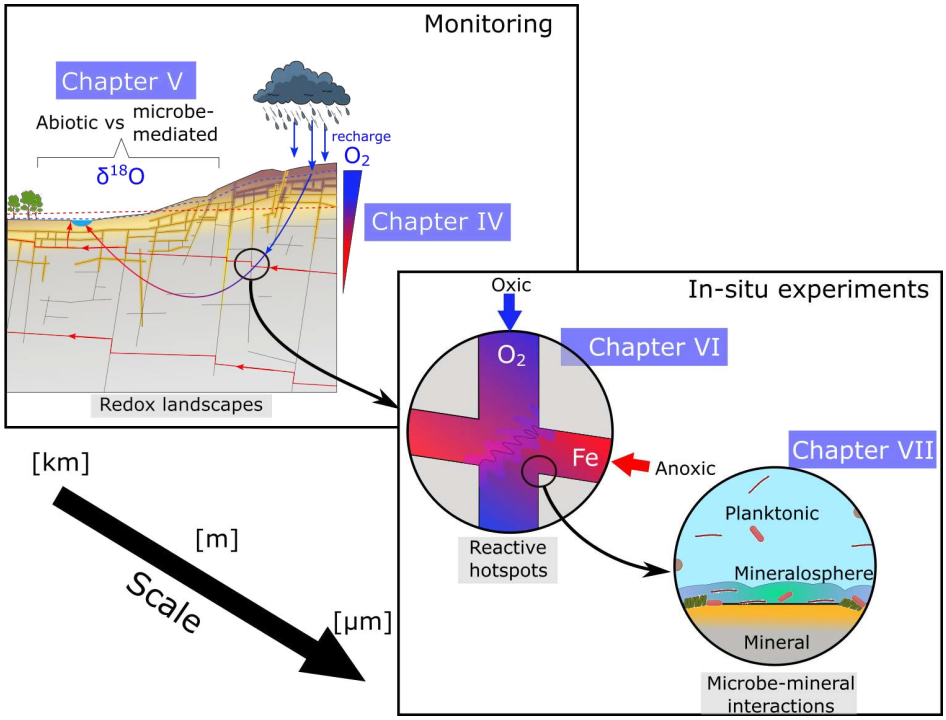

Contents

1 Exploring the deep oxic hydrosphere

This PhD thesis presented an interdisciplinary and multiscale study to conceptualize and disentangle some aspects of the complex interplay between groundwater flow, reactive processes and microbial dynamics taking place in the underground as part of the critical zone (Brantley et al.; 2007; Singha and Navarre-Sitchler; 2022). The main particularity of the deep continental biosphere is its primary energy source: it is isolated from sunlight-powered surface environments and therefore, life in dark subsurface environments relies on chemical energy sources, i.e. on redox reactions (Edwards et al.; 2012). Redox reactions depend on the availability of electron donors and acceptors. In this study we focused on the study of dissolved oxygen (DO) as a key element in redox-powered systems. DO is an essential component of rock-weathering reactions (Kim et al.; 2017) and its concentration in groundwater determines which kind of metabolisms can operate in subsurface ecosystems, e.g. aerobic vs anaerobic (Ehrlich et al.; 2015).

Several works have reported the occurrence of deep oxic groundwater (Winograd and Robertson; 1982) and fast transport of oxic groundwater in fractures (Bochet et al.; 2020). This challenges the current view of subsurface environments as inertial systems which are independent of surface dynamics and cycles driven by the sun (LaRowe and Amend; 2019). However, the extent to which DO reaches and impacts life and biogeochemical processes in deep subsurface environments is not well understood. Addressing this challenge is the overarching motivation of this work. **The general objective of this dissertations was to conceptualize the factors that control the occurrence of a *deep oxic hydrosphere* in modern groundwater systems and develop *in-situ* approaches to characterize and quantify how oxic/anoxic environments affect rock weathering reactions and the activity of the deep subsurface biosphere.**

To investigate the factors that control the transport of DO to the subsurface and the resulting impacts on weathering reactions and the deep biosphere, we focused on fractured-bedrock environments. These systems are characterized by preferential flow paths, which favor the occurrence of deep oxic groundwater. We considered iron oxidation reaction by oxygen as a model reaction as iron is the foremost electron donor in Earth's crust (Wedepohl; 1995) and it is related to both microbial activity (Kappler et al.; 2021) and rock weathering processes (Buss et al.; 2008). Our research strategy was based on *in-situ* monitoring and experimental approaches at different scales that were conducted in the Ploemeur critical zone observatory (CZO). It included two main parts:

1. **Catchment-scale studies** to identify the patterns of DO distributions with depth and space, and conceptualize the mechanisms that control the observations in the field of a deep oxic hydrosphere.

2. ***In-situ* experiments at smaller scales** to assess and quantify the impacts of the deep oxic hydrosphere on subsurface microbial processes and weathering reactions.

2 A bridge from surface to subsurface environments

This dissertation challenges the general view of deep subsurface environments as an inertial system that follows geological processes and timescales, independently of surface dynamics and cycles (LaRowe and Amend; 2019). Through field-based observations of groundwater and the development of a conceptual framework to quantify the occurrence of O_2, we have established that a significant portion of the deep continental subsurface, extending to several hundred meters in depth depending on hydrological and geological settings, is potentially affected by the transport of oxic water from the Earth's surface. As a consequence, the redox-powered metabolisms of ecosystems that inhabit the deep oxic hydrosphere are linked to the hydrologic connections that transport DO from the surface (Figure VIII.1).

The deep oxic hydrosphere is a dynamic component of subsurface environments, where DO can either enhance or inhibit aerobic and anaerobic metabolisms, respectively. While subsurface ecosystems are commonly considered as oligotrophic and with slow rates of biomass production (Templeton and Caro; 2023), our reactive

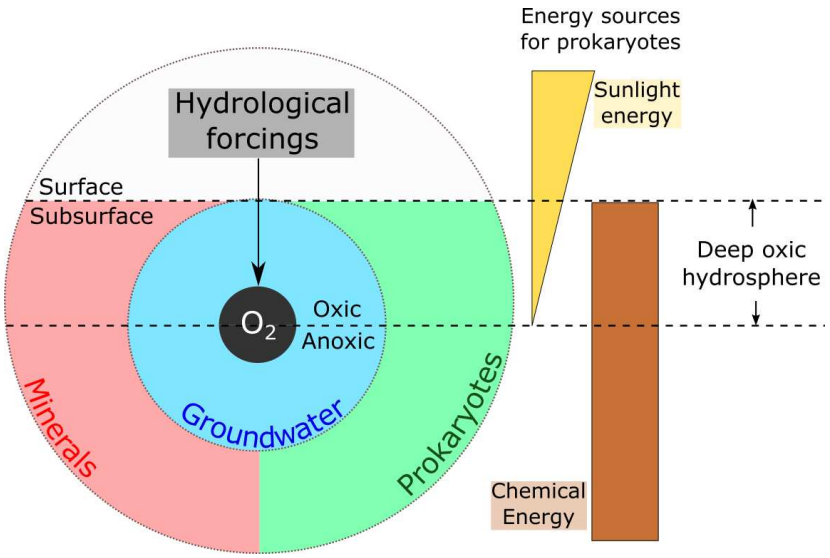

Figure VIII.1: **Conceptual view of the deep oxic hydrosphere and its interactions with minerals and life.** O_2, a product of sunlight-powered photosynthesis, is transported by hydrological forcings to the deep oxic hydrosphere, where it reacts with mineral-hosted electron acceptors in redox reactions that can be mediated by prokaryotes. O_2 is the electron acceptor that offers the highest redox potential for these redox reactions, and links the activity of prokaryotes in the deep oxic hydrosphere to surface processes.

tracer test experiments provided new observations questioning this paradigm (Chapter VI). We demonstrated that the redox fluctuations induced by the fast recharge of oxic groundwater can indeed stimulate deep ecosystems by providing a highly energetic electron acceptor such as O_2. Within a maximum time frame of eight hours, we observed that planktonic biomass doubled in number following the O_2 arrival, thus showing a remarkably fast physiological response of the subsurface environment to a hydrological perturbation. While groundwater environments have been recently shown to exhibit important carbon fixation rates, comparable to oligotrophic marine systems (Overholt et al.; 2022), our results indicate that this biomass production could be highly dynamic and respond to hydrologic forcings from the surface.

Mineral-attached micro-organisms likely represent the majority of the subsurface biomass (Flemming and Wuertz; 2019), but little is known about their dynamics. As planktonic prokaryotes show a strong response to redox changes, we can assume that mineral-attached microorganisms could also be sensitive to redox changes. We targeted this question through a mineral incubation experiment (Chapter VII). By performing two incubation experiments in redox-contrasted and deep groundwater environments, we quantified the mineral-attached biomass that colonized both reactive and inert mineral surfaces. Our results showed that, overall, the amount of mineral-attached biomass is more sensitive to the mineral substrate than the fluid redox conditions, highlighting an important control of the geological context on the mineral-attached biomass.

To summarize, the *in-situ* experimental study of both planktonic and mineral-attached microbial communities through the tracer test and the mineral incubation experiments -chapters VI and VII, respectively- showed that fluid redox conditions have a strong impact on the planktonic microorganisms while the mineral-attached biomass are more sensitive to the mineralogical composition of the rocks. This difference could be related to energetic limitations due to the availability of electron donors and acceptors. Oxic groundwater is commonly related to low residence times and low saturation states of the fluid, while anoxic groundwater usually corresponds to longer residence times and higher saturation states. This means that at oxic conditions, groundwater is usually limited by the availability of aqueous electron donors while they are abundant at anoxic conditions, resulting in contrasted fluid-redox potentials for planktonic prokaryotes. Mineral substrates provide a very large reservoir of electron donors on which mineral-attached prokaryotes grow, they are thus not sensitive to fluid redox potentials. These results are consistent with previous incubations experiments in laboratory settings (Jones and Bennett; 2017). It is worth noting, however, that in our incubation experiments pristine minerals

were used, while minerals in natural settings are "aged" (Daval et al.; 2011; Wild et al.; 2016), i.e. they are covered by secondary minerals that can impose additional constraints to the accessibility to the solid-supported electron donors.

3 How deep is the deep oxic hydrosphere?

Using the Ploemeur CZO as a case study, in Chapter IV we have provided evidence for the presence of deep oxic groundwater extending to depths of up to 400 meters. We developed a conceptual and modeling framework to quantitatively characterize how the depth of the deep oxic hydrosphere in fractured rocks depends on the balance between advective recharge of surface oxic-water and rock-weathering reactions that consume DO through the oxidation of Fe(II). Our modeling framework thus fills the knowledge gap that existed on the reactive transport of DO in modern deep groundwater systems, characterized by short groundwater residence times at which the timescales of both reactive and transport processes are comparable. We showed that the DO depth-distribution can be described by two synthetic dimensionless numbers, Damkhöler (Da) and a new Lithological number (Λ), that capture both hydrological (transport) and geological (reactive) controlling processes. Our conceptual framework thus provides an analytical tool to interpret and predict the presence of dissolved O_2 in deep groundwater environments, e.g. Winograd and Robertson (1982) and further confirms the presence of O_2 at depth that has been inferred by palaeohydrological studies on weathering fronts, e.g. Fletcher et al. (2006). Overall, this study supports the existence of a deep oxic hydrosphere reaching up to several hundred meters depth, depending on the specific hydrological and geological contexts.

4 Biotic and abiotic processes in the deep oxic hydrosphere

Whether redox reactions consuming dissolved O_2 occur through biotic or abiotic mechanisms in subsurface environments is not well constrained. For the oxidation of iron by DO, microaerobic conditions seem favorable to the microbe-mediated reaction while higher DO concentrations favor abiotic mechanisms (Druschel et al.; 2008; Emerson et al.; 2010; Eggerichs et al.; 2014; Maisch et al.; 2019). However, these observations are derived from laboratory cultures which are not necessarily representative of the *in-situ* activity of microbial consortia. Which conditions favor abiotic or biotic mechanisms of DO consumption in the deep oxic hydrosphere? To answer to this question, in Chapter V we presented a study in which we studied, for the first time, the isotopic fractionation of DO in deep subsurface environments. Our results are remarkably consistent with the microaerobic range deduced from laboratory cultures. Indeed, at DO concentrations above the microaerobic range, DO isotope fractionations were dominated by physical processes and did not exhibit the $\delta^{18}O$ enrichment expected from microbial activity. Conversely, at microaerobic DO concentrations the $\delta^{18}O$ trend presented an enrichment of +7.2 ‰that was consistent with the activity of iron oxidizing bacteria (FeOB). Our DO isotope investigation thus showed that the microbe-mediated iron oxidation by oxygen is restricted to a specific microaerobic range. These results open new research opportunities to constrain a DO-dependant biomass in the continental subsurface and to quantify the biotic contribution on iron oxidation in the subsurface.

5 *In-situ* approaches: characterizing deep oxic biogeochemical processes and highlighting lab-field discrepancies

We developed novel *in-situ* approaches in order to describe and quantify *in situ* biogeochemical processes occurring in subsurface environments. However, the field-derived results were sometimes different from laboratory-derived parameters, highlighting potential lab-field discrepancies. Such kind of differences between laboratory- and field-derived results have been a longstanding issue in mineral dissolution studies, where

laboratory conditions -usually more extreme and poorly representative of natural settings- result in dissolution rates which exceed field estimations by several orders of magnitude (Maher et al.; 2006).

In our work we evidenced different types of discrepancies with respect to laboratory-derived parameters:

- "Negative" lab-field discrepancies (field < lab):

  1. **Isotopic fractionation measurements:** in Chapter V we used the isotopic composition of DO to unravel abiotic and biotic processes at catchment scale. By fitting an isotope-fractionation model to the isotopic composition of DO during microbe-mediated iron oxidation, we determined an effective fractionation factor that is between 0.4 and 8 ‰ weaker than laboratory results (Oba and Poulson; 2009; Pati et al.; 2016). Based on previous studies, we attributed this lab-field discrepancy to the possible effects of velocity fields and dispersive mixing that can affect isotopic ratios (Johnson and DePaolo; 1994; Druhan and Maher; 2017) or to different isotopic fractionations of microbial consortia compared to isolated cultures.
  2. **Mineral dissolution rates:** in Chapter V we measured for the first time *in-situ* cleavage-specific dissolution rates for calcite coupons. Our measurements resulted in dissolution rates 1 to 3 orders of magnitude lower than classical rates derived in stirred reactors. However, our *in-situ* rates were remarkably consistent with more recent cleavage-specific measurements that used hydrodynamic conditions which are more relevant to those prevailing in the field (Jordan and Rammensee; 1998; Arvidson et al.; 2003; Bouissonnié et al.; 2018). This latter studies emphasizes the importance of selecting appropriated experimental conditions in laboratory settings in order to measure parameters which can be transposed to field conditions.
  3. **O_2 consumption rates:** in Chapter VI we measured for the first time the *in-situ* consumption rate of dissolved oxygen in a fracture's fluid dominated by dissolved iron. We determined second-order rate constants which are 2 orders of magnitude lower than the expected rate constants for the aqueous reaction between O_2 and Fe but which are comparable to rates for the heterogeneous reaction between O_2 and structural-Fe from minerals. Our *in-situ* rates highlight that the effective rate of DO consumption is subject to lab-field discrepancies.

- "Positive" lab-field discrepancies (lab < field):

  – **Microbial biomass production in a hotspot:** in Chapter VI observed a two-fold increase in the extracted DNA of an FeOB-dominated microbial hotspot in a time frame between 3 to 8 hours. This fast response of the microbial consortia to a redox perturbation is faster than growth rates reported for FeOB isolates in laboratory cultures, ranging between 8 to 13 hours (Emerson and Moyer; 1997). We note however that our results are not conclusive to say that the DNA increase observed during the experiment is directly related to cell division and biomass production. Indeed, we consider that the enhanced redox-conditions during mixing processes in the subsurface can induce the active detachment of mineral-attached prokaryotes, which would result in the fast increased of planktonic DNA that we measured. This observations emphasize the necessity of a better understanding of the mineral-attached biomass and its potential to take part in biogeochemical processes which are only considered as planktonic-driven.

Most of the *in-situ* measurements reported in this study are unique in their respective disciplines and provide reference values that can serve as guide for future laboratory measurements or field-relevant models.

Bibliography

Arvidson, R. S., Ertan, I. E., Amonette, J. E. and Luttge, A. (2003). Variation in calcite dissolution rates:, *Geochimica et Cosmochimica Acta* **67**(9): 1623–1634.

Bochet, O., Bethencourt, L., Dufresne, A., Farasin, J., Pédrot, M., Labasque, T., Chatton, E., Lavenant, N., Petton, C., Abbott, B. W., Aquilina, L. and Le Borgne, T. (2020). Iron-oxidizer hotspots formed by intermittent oxic–anoxic fluid mixing in fractured rocks, *Nature Geoscience* **13**(2): 149–155.

Bouissonnié, A., Daval, D., Marinoni, M. and Ackerer, P. (2018). From mixed flow reactor to column experiments and modeling: Upscaling of calcite dissolution rate, *Chemical Geology* **487**: 63–75.

Brantley, S. L., Goldhaber, M. B. and Vala Ragnarsdottir, K. (2007). Crossing disciplines and scales to understand the critical zone, *Elements* **3**(5): 307–314.

Buss, H. L., Sak, P. B., Webb, S. M. and Brantley, S. L. (2008). Weathering of the Rio Blanco quartz diorite , Luquillo Mountains , Puerto Rico : Coupling oxidation , dissolution , and fracturing, *Geochimica et Cosmochimica Acta* **72**: 4488–4507.

Daval, D., Sissmann, O., Menguy, N., Saldi, G. D., Guyot, F., Martinez, I., Corvisier, J., Garcia, B., Machouk, I., Knauss, K. G. and Hellmann, R. (2011). Influence of amorphous silica layer formation on the dissolution rate of olivine at 90°C and elevated pCO2, *Chemical Geology* **284**(1-2): 193–209.

Druhan, J. and Maher, K. (2017). The influence of mixing on stable isotope ratios in porous media: A revised Rayleigh model, *Water Resources Research* **53**: 1101–1124.

Druschel, G. K., Emerson, D., Sutka, R., Suchecki, P. and Luther, G. W. (2008). Low-oxygen and chemical kinetic constraints on the geochemical niche of neutrophilic iron(II) oxidizing microorganisms, *Geochimica et Cosmochimica Acta* **72**(14): 3358–3370.

Edwards, K. J., Becker, K. and Colwell, F. (2012). The Deep, Dark Energy Biosphere: Intraterrestrial Life on Earth, *Annual Review of Earth and Planetary Sciences* **40**(1): 551–568.

Eggerichs, T., Opel, O., Otte, T. and Ruck, W. (2014). Interdependencies between Biotic and Abiotic Ferrous Iron Oxidation and Influence of pH, Oxygen and Ferric Iron Deposits, *Geomicrobiology Journal* **31**(6): 461–472.

Ehrlich, H. L., Newman, D. K. and Kappler, A. (eds) (2015). *Ehrlich's Geomicrobiology*, 0 edn, CRC Press.

Emerson, D., Fleming, E. J. and McBeth, J. M. (2010). Iron-Oxidizing Bacteria: An Environmental and Genomic Perspective, *Annual Review of Microbiology* **64**(1): 561–583.

Emerson, D. and Moyer, C. (1997). Isolation and Characterization of Novel Iron-Oxidizing Bacteria That Grow at Circumneutral pH, *Applied and Environmental Microbiology* **63**(12): 4784–4792.

Flemming, H.-C. and Wuertz, S. (2019). Bacteria and archaea on Earth and their abundance in biofilms, *Nature Reviews Microbiology* **17**(4): 247–260.

Fletcher, R. C., Buss, H. L. and Brantley, S. L. (2006). A spheroidal weathering model coupling porewater chemistry to soil thicknesses during steady-state denudation, *Earth and Planetary Science Letters* **244**(1-2): 444–457.

Johnson, T. M. and DePaolo, D. J. (1994). Interpretation of isotopic data in groundwater-rock systems: Model development and application to Sr isotope data from Yucca Mountain, *Water Resources Research* **30**(5): 1571–1587.

Jones, A. A. and Bennett, P. C. (2017). Mineral Ecology : Surface Specific Colonization and Geochemical Drivers of Biofilm Accumulation , Composition , and Phylogeny, *Frontiers in Microbiology* **8**(March): 1–14.

Jordan, G. and Rammensee, W. (1998). Dissolution rates of calcite (1014) obtained by scanning force microscopy: Microtopography-based dissolution kinetics on surfaces with anisotropic step velocities, *Geochimica et Cosmochimica Acta* **62**(6): 941–947.

Kappler, A., Bryce, C., Mansor, M., Lueder, U., Byrne, J. M. and Swanner, E. D. (2021). An evolving view on biogeochemical cycling of iron, *Nature Reviews Microbiology* **19**(6): 360–374.

Kim, H., Stinchcomb, G. and Brantley, S. L. (2017). Feedbacks among O2 and CO2 in deep soil gas , oxidation of ferrous minerals , and fractures : A hypothesis for steady-state regolith thickness, *Earth and Planetary Science Letters* **460**: 29–40.

LaRowe, D. and Amend, J. (2019). *Energy Limits for Life in the Subsurface*, Vol. 3.

Maher, K., Steefel, C. I., DePaolo, D. J. and Viani, B. E. (2006). The mineral dissolution rate conundrum: Insights from reactive transport modeling of U isotopes and pore fluid chemistry in marine sediments, *Geochimica et Cosmochimica Acta* **70**(2): 337–363.

Maisch, M., Lueder, U., Laufer, K., Scholze, C., Kappler, A. and Schmidt, C. (2019). Contribution of Microaerophilic Iron(II)-Oxidizers to Iron(III) Mineral Formation, *Environmental Science and Technology* **53**(14): 8197–8204.

Oba, Y. and Poulson, S. R. (2009). Oxygen isotope fractionation of dissolved oxygen during reduction by ferrous iron, *Geochimica et Cosmochimica Acta* **73**(1): 13–24.

Overholt, W. A., Trumbore, S., Xu, X., Bornemann, T. L. V., Probst, A. J., Krüger, M., Herrmann, M., Thamdrup, B., Bristow, L. A., Taubert, M., Schwab, V. F., Hölzer, M., Marz, M. and Küsel, K. (2022). Carbon fixation rates in groundwater similar to those in oligotrophic marine systems.

Pati, S. G., Bolotin, J., Brennwald, M. S., Kohler, H.-p. E., Werner, R. A. and Hofstetter, T. B. (2016). Measurement of oxygen isotope ratios (18 O / 16 O) of aqueous O 2 in small samples by gas chromatography / isotope ratio mass spectrometry, *Rapid Communications in Mass Spectroscopy* **30**: 684–690.

Singha, K. and Navarre-Sitchler, A. (2022). The Importance of Groundwater in Critical Zone Science, *Groundwater* **60**(1): 27–34.

Templeton, A. S. and Caro, T. A. (2023). The Rock-Hosted Biosphere, *Annual Review of Earth and Planetary Sciences* **51**(1): 493–519.

Wedepohl, K. (1995). The composition of the continental crust, *Geochimica et Cosmochimica Acta* **59**(7): 1217–1232.

Wild, B., Daval, D., Guyot, F., Knauss, K. G., Pollet-villard, M. and Imfeld, G. (2016). pH-dependent control of feldspar dissolution rate by altered surface layers, *Chemical Geology* **442**: 148–159.

Winograd, Isaac. and Robertson, F. (1982). Deep Oxygenated Ground Water : Anomaly or Common Occurrence?, *Science* **216**(4551): 1227–1230.

APPENDIX CHAPTER 3: SUPPLEMENTARY INFORMATIONS

1 Average chemical composition of minerals

Table A-1: **Average chemical composition of minerals as determined by SEM-EDS (Scanning Electron Microscope - Energy Dispersive Spectrometer)**. Column "n" indicates the number of crystals analyzed. Column "Rock" indicates the rock sample, either granite (Grnt) or micaschist (Scht). Abbreviation in the "Mineral" column correspond to biotite (Bt), chlorite (Chl), albite (Alb), K-feldspar (KF), quartz (Qz), muscovite (Ms)

Rock	Mineral	n	Al [Wt%]	Ca [Wt%]	Fe [Wt%]	K [Wt%]	Mg [Wt%]	Si [Wt%]	Ti [Wt%]	Na [Wt%]	O [Wt%]
Grnt	Bt	2	7.98		12.99	6.28	1.04	27.09	0.85	0.34	43.44
Scht	Bt	30	9.59	0.01	10.75	7.64	4.84	21.07	1.53	0.04	44.53
Grnt	Chl	12	8.57		21.82		1.95	21.29	0.09		45.12
Grnt	Alb	6	13.61			1.19		32.51		7.38	44.90
Grnt	KF	3	10.84			10.26		31.13		0.79	46.50
Scht	KF	5	9.15			11.77		31.77	0.21	1.04	46.19
Grnt	Ms	3	15.60		2.58	7.89	0.42	26.19	0.39	0.99	46.66

2 Compilation of bulk chemical compositions for granite (Grnt) and micaschist (Msch) from the CZO of Ploemeur.

Table A-2: Compilation of bulk chemical compositions for granite (Grnt) and micaschist (Msch) from the CZO of Ploemeur, as mesured on crushed-rock powders. Data source references: (1) (Touchard; 1999), (2) Anne-Cathering Pierson-Wickman personal communication, (3) this work.

Data Source	Sample ID	Type	lithology	Analysis	SiO2 %	Al2O3 %	Fe2O3 %	MnO %	MgO %	CaO %	Na2O %	K2O %	TiO2 %	P2O5 %	SO3 %	PF %	Total %
1	**F34 (56-57m)**	cutting	**Grnt**	ICP-MS	73.5	14.2	0.98	0.01	0.17	0.63	3.46	4.71	0.16	0.26		0.50	98.55
1	**F34 (83m)**	cutting	**Grnt**	ICP-MS	74.0	15.2	0.49	0.01	0.10	0.42	4.11	4.31	0.11	0.25		0.80	99.79
1	**F35 (93-94m)**	cutting	**Grnt**	ICP-MS	73.7	14.7	0.39	0.01	0.00	0.27	4.34	4.66	0.02	0.20		0.49	98.79
1	**F35 (104-105m)**	cutting	**Grnt**	ICP-MS	74.3	15.0	0.27	0.02	0.00	0.28	5.81	2.95	0.00	0.32		0.46	99.36
1	**F36 (54-55m)**	cutting	**Grnt**	ICP-MS	73.4	14.4	0.34	0.01	0.00	0.29	3.16	6.49	0.01	0.22		0.82	99.13
1	**F36 (61-62m)**	cutting	**Grnt**	ICP-MS	74.7	14.1	0.44	0.04	0.00	0.31	5.03	3.31	0.03	0.25		0.45	98.66
3	**B2 C22#12a**	core	**Grnt**	ICP-MS	73.9	14.3	0.77	0.02	0.15	0.44	3.96	4.19	0.08	0.27		0.91	99.01
3	**B2 C22#12a**	core	**Grnt**	XRF	75.1	14.3	0.87	0.00	0.20	0.52	4.56	3.92	0.07	0.34	0.032		99.95
2	**D2 C1-10**	core	**Grnt**	ICP-MS	72.0	14.9	0.89	0.01	0.20	0.47	3.60	4.89	0.12	0.27		1.15	98.43
2	**D2 C2-7**	core	**Grnt**	ICP-MS	74.0	14.7	0.89	0.02	0.19	0.48	3.61	4.55	0.12	0.28		1.14	99.97
2	**D2 C4-7**	core	**Grnt**	ICP-MS	73.0	15.2	0.84	0.02	0.18	0.43	3.96	4.62	0.10	0.26		1.06	99.61
2	**B1 C13-8**	core	**Grnt**	ICP-MS	72.7	14.9	1.17	0.04	0.20	0.51	3.45	4.60	0.11	0.36		1.54	99.65
2	**B1 C17-8**	core	**Grnt**	ICP-MS	72.6	15.0	0.74	0.02	0.17	0.52	3.94	4.43	0.10	0.29		1.31	99.12
2	**D2 C4-10**	core	**Grnt**	ICP-MS	72.5	14.8	0.80	0.02	0.20	0.50	3.84	4.42	0.11	0.27		1.61	99.04
1	**F34 (87-88m)**	cutting	**Msch**	ICP-MS	71.0	15.4	3.67	0.05	1.14	0.46	1.09	4.18	0.61	0.14		1.72	99.44
1	**F34 (101-102m)**	cutting	**Msch**	ICP-MS	68.6	16.0	3.05	0.05	1.31	0.72	1.23	5.93	0.47	0.15		1.47	98.98
1	**F35 (69-70m)**	cutting	**Msch**	ICP-MS	73.6	12.2	3.64	0.05	1.45	0.88	2.10	2.81	0.57	0.15		1.24	98.67
1	**F35 (131-132m)**	cutting	**Msch**	ICP-MS	61.0	18.2	6.11	0.10	2.71	1.20	2.55	3.96	0.82	0.17		2.02	98.84
1	**F36 (39-40m)**	cutting	**Msch**	ICP-MS	72.5	14.3	3.34	0.03	0.96	0.30	2.38	2.94	0.56	0.10		1.70	99.06
1	**F36 (69-70m)**	cutting	**Msch**	ICP-MS	64.7	16.6	6.08	0.08	2.57	0.92	2.12	3.94	0.68	0.15		1.14	98.96
3	**B2 C6#4**	core	**Msch**	ICP-MS	69.1	15.4	3.03	0.03	0.91	1.17	2.41	5.20	0.47	0.20		1.69	99.66
3	**B2 C6#4**	core	**Msch**	XRF	70.5	15.5	3.16	0.02	0.86	1.26	2.68	4.80	0.51	0.21	0.211		99.73
2	**B1 C2-5**	core	**Msch**	ICP-MS	71.2	15.3	1.60	0.01	0.52	0.06	0.20	8.03	0.59	0.08		2.18	99.77
2	**B1 C5-23**	core	**Msch**	ICP-MS	71.2	14.9	2.63	0.03	0.80	0.96	2.45	5.04	0.40	0.19		1.46	100.07
2	**B1 C9-20**	core	**Msch**	ICP-MS	68.3	14.9	3.11	0.02	0.98	0.39	2.36	6.21	0.43	0.17		1.94	98.89
2	**SC39**	core	**Msch**	ICP-MS	59.6	15.6	3.77	0.20	2.90	0.80	0.30	2.01	0.08	0.19		14.20	99.65

Bibliography

Touchard, F. (1999). *Caractérisation Hydrogéologique d'un Aquifère de Socle Fracturé : Site de Ploemeur (Morbihan).*, PhD thesis, Université de Rennes 1.

APPENDIX CHAPTER 4: SUPPLEMENTARY INFORMATIONS

1 Supplementary Information for the article "Hydrological and geological controls for the depth evolution of dissolved oxygen and iron in silicate catchments"

Supporting Information for

Hydrological and geological controls for the depth distribution of dissolved oxygen and iron in silicate catchments

Ivan Osorio-Leon[1], Camille Bouchez[1], Eliot Chatton[1], Nicolas Lavenant[1], Laurent Longuevergne[1], Tanguy Le Borgne[1]

[1]Univ Rennes – CNRS, Géosciences Rennes - UMR 6118. Rennes, France

Table of contents

Corresponding author: Ivan-David Osorio-Leon, idosoriole@unal.edu.co

Corresponding author: Camille Bouchez, camille.bouchez@univ-rennes1.fr

Table S1. Aqueous initial condition for the base case simulation with the numerical model. Chemical composition of the water used as initial condition in the base case simulation of the fully resolved reactive transport simulations. The aqueous composition corresponds to average values (n=10) in the period 2016-2022 for the borehole psr1 from the CZO of Ploemeur (Brittany, France). The pH value has been set to 7.0 for the numerical simulation.

Temperature [ºC]	16	
pH	7.0	
	Concentrations	[mol/kg]
$O_2(aq)$		2.6×10^{-4}
Cl^-		2.0×10^{-3}
SO_4^{2-}		2.9×10^{-4}
Na^+		2.1×10^{-3}
Mg^{2+}		5.5×10^{-4}
Al^{3+}		3.5×10^{-8}
H_4SiO_4		4.8×10^{-4}
K^+		9.6×10^{-5}
Ca^{2+}		2.6×10^{-4}
Fe^{2+}		0.0
Fe^{3+}		2.6×10^{-7}
$CO_2(aq)$		4.5×10^{-4}

Table S2. Mineralogical initial condition in the numerical simulations. Φ_j stands for Mineral volume fraction. *TST* indicates that both dissolution and precipitation can occur. k_{kin} are kinetic constants in SI units for both mineral dissolution and aqueous reactions. K_{sp} are the solubility product constants. Kinetic and thermodynamic parameters come from the database files of the Thermoddem project (Blanc et al., 2012) and from Palandri and Kharaka (2004). For the aqueous reaction, the kinetic constant comes from Singer and Stumm (1970).

Mineral	Structural formula	Φ_j	Kin. law	$log_{10}k_{kin}$	$log_{10}K_{sp}$
Primary minerals					
Quartz	SiO_2	0.445	TST	-13.19	-4.000
K-Feldspar	$KAlSi_3O_8$	0.297	TST	-12.41	-0.275
Biotite	$K(Mg_2Fe^{II})(Si_3Al)O_{10}(OH)_2$	0.099	TST	-12.55	41.10
Muscovite	$KAl_2(AlSi_3O_{10})(OH)_2$	0.149	TST	-13.55	13.58
Secondary minerals					
Chlorite	$(Mg_3Fe_2^{II}Al)(Si_3Al)O_{10}(OH)_8$	1×10^{-5}	TST	-12.52	47.60
Kaolinite	$Al_2Si_2O_5(OH)_4$	0.000	TST	-13.18	6.810
Goethite	$Fe^{III}OOH$	0.000	TST	-7.94	-0.600
Aqueous kinetics					
$4Fe^{2+} + O_2 + 4H^+ \rightarrow 4Fe^{3+} + 2H_2O$			Aqueous	-5.969	[-]

Figure S1. Mineral stability diagram built on the K-feldspar system. Points represent boreholes from the recharge and discharge zones of the Guidel and Kermadoye catchments. See plot's legend for details. The majority of the boreholes, independently of the catchment, plot in the kaolinite domain.

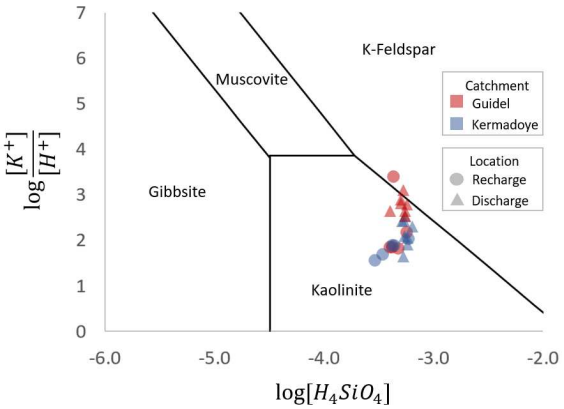

Text S1. Methods for field measurements of dissolved iron

Major and trace cations were quantified by Inductively Coupled Plasma Mass Spectroscopy (Agilent Technologies, 7700x) in pre-acidified and 0.2 μm-filtered samples. Uncertainties were between 2 to 5%. Groundwater sampling consisted on descending a submersible MP1 pump (Grundfos) until the depth of the dominant fracture in the borehole. Physicochemical parameters in the pump discharge were monitored with a WTW probe. Groundwater was sampled after the monitored parameters were stable.

Text S2. Methods for field measurements of dissolved oxygen

Multiparameter borehole logs under ambient conditions (dissolved oxygen and temperature) acquired since 2003, available in the database of the French network of hydrogeological research sites (`https://doi.org/10.26169/hplus.ploemeur_field_data_dissolved_oxygen_and_iron_landscapes`), were used as base for exploring the physicochemical parameters with depth. This dataset was completed with two additional field campaigns in order to validate the historical data. Multiparameter borehole logs in ambient conditions were acquired at two different times of the hydrologic year: high groundwater level's season (late fall 2022) and low level's season (late spring 2021) using an Idronaut Ocean Seven multiparameter probe. The instrument was calibrated following the manufacturer's specifications.

Figure S2. Calibration plot for DO field measurements. In order to validate the accuracy of the DO probe used for the borehole logs (Text S2), we crosschecked the probe-based measurements with DO analyses by gas chromatography (GC) in the same samples. Following the same pumping protocol described in Text S1, groundwater samples were collected in glass bottles, isolated from atmosphere, stored at 4ºC, and analyzed after head-space extraction by GC with a thermal conductivity detector (μGC/TCD) in the 24h after sampling, following the method of (Sugisaki Taki, 1987). Analytical precision is under 5%.

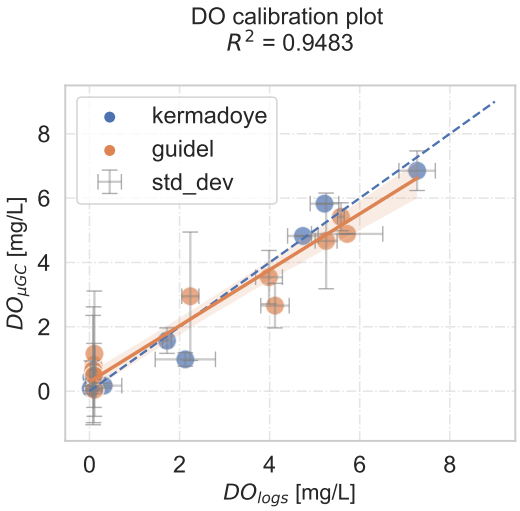

Text S3. The $Depth_{proxy}$ methodology for fractured media

Since fracture networks are highly heterogeneous features (Le Borgne et al., 2006), one cannot directly rely the depth of an intersected fracture in a borehole with the representative depth of origin of the circulating fluid (Chatelier et al., 2011). For instance, at the site scale, normal faults dipping of about 70º (Ruelleu et al., 2010) will globally favor subvertical circulations. At a more restricted scale, a fracture analysis in a borehole from the Guidel catchment (Bochet et al., 2020) has shown that fracture's dip can vary from 20 to 80º.

Following this, we have used the methodology developed by Chatelier et al. (2011) in which we use groundwater temperature as a proxy of its depth of origin, i.e. the depth at which the fluid was in thermal equilibrium with the host rock (called here $Depth_{proxy}$). Hence, the $Depth_{proxy}$ was calculated as:

$$Depth_{proxy} = \frac{T - T_{rech}}{G_G}$$

T corresponds to groundwater temperature as measured from borehole logs at the depth of the sampled fracture ($Depth_{physical}$), T_{rech} corresponds to the average recharge temperature of the Ploemeur site, that is 12.2 ºC, as deduced from the average temperature in the weather station, and G_G corresponds to the Geothermal Gradient. For the Ploemeur site, G_G has been estimated at 0.013 $°C.m^{-1}$ after Klepikova et al. (2011) and Pouladi et al. (2021). If the $Depth_{proxy}$ and the $Depth_{physical}$ are equal, it means that the fracture is close to horizontal. If the $Depth_{proxy}$ is higher than the $Depth_{physical}$, it means that the fracture is tilted and that flows are oriented upward. As shown in Figure S3, This methodology is consistent as most of the samples located in the recharge zone are characterized by downward flows (lower $Depth_{proxy}$), while samples in the discharge zone are characterized by upward flows (higher $Depth_{proxy}$). Also consistently, we observe a linear positive-correlation between groundwater temperature and apparent age data (not shown in this work) showing that higher $Depth_{proxy}$ values reflect longer flow path lengths. Since $Depth_{proxy}$ is a function of two site-specific parameters (T_{rech} and G_G), the accuracy of the $Depth_{proxy}$ estimates depends on how good those two parameters can be constrained. This is discussed in Text S4.

Figure S3. Groundwater temperature and depth in the CZO of Ploemeur. (A) temperature profiles measured on the sites. The geothermal gradient is determined from profiles that are not perturbed by vertical borehole flows (Klepikova et al., 2011). (B) Comparison between $Depth_{physical}$ (the physical depth at which a fracture is sampled) and $Depth_{proxy}$ (the depth the fluid in the fracture should come from in order to have reached its temperature by thermal equilibrium with the host-rock).

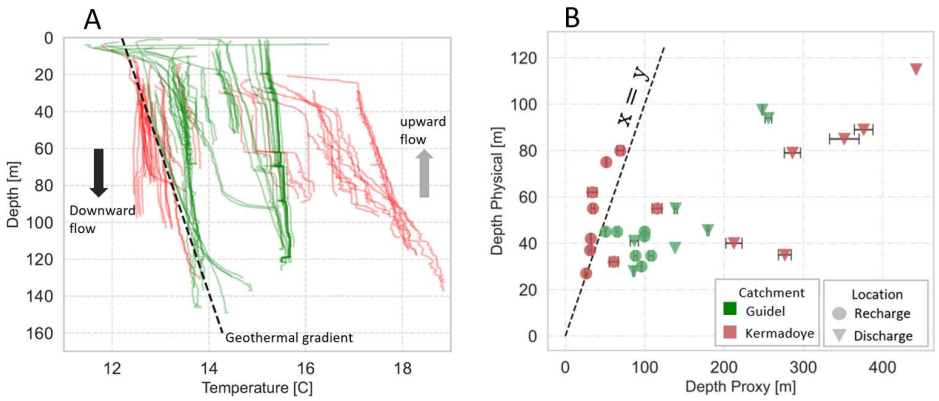

Text S4. Sensitivity of $Depth_{proxy}$ estimates

$Depth_{proxy}$ depends on two site-dependent parameters, i.e. the average recharge temperature (T_{rech}) and the Geothermal Gradient (G_G). Both parameters are mostly invariant at short timescales and are not easily measurable. As a result, uncertainties around their value come from measurements rather than seasonality or natural disturbances. The CZO of Ploemeur is a well-studied site and both T_{rech} and G_G are well constrained, allowing to reduce incertitude's around their value. The average value for T_{rech} has been estimated to be 12.2±0.41 $°C$ as deduced from temperature time-series (from 2002 to 2018) recorded at the weather station in the Ploemeur CZO. On the other hand, previous works suggest that the G_G of the Ploemeur site ranges between 0.016 and 0.013 $°C.m^{-1}$ (Pouladi et al., 2021; Klepikova et al., 2011) and for this work we considered the most recent estimate of 0.013 $°C.m^{-1}$ after Pouladi et al. (2021).

It is important to notice that the estimated $Depth_{proxy}$ is highly sensitive to both parameters and it can thus directly impact the estimated depth of the oxygenated zone in the aquifer. For instance, if one considers the borehole with the highest temperature (and thus the deepest $Depth_{proxy}$) from Figure 7 (from main text), and by combining the uncertainties of T_{rech} and G_G , the maximum depth in which oxygen has been detected in this study can oscillate between 333 m and 473 m below surface.

Figure S4. Effect of vertical velocity on the predicted iron concentrations at oxic concentrations. For a same Damköhler number, the variations in the apparent vertical velocity impact the iron concentrations at oxic conditions according to Equation 20 in main text. Predicted concentrations are restricted to low values because they are limited by the fast oxidation of iron by oxygen. Note that the predicted values are close to or below the detection limit of ICPMS analysis, that usually is close to 10^{-4} ppm. This makes difficult to constrain the apparent vertical velocity by using the iron concentration data, yet it is theoretically possible if analytical methods for iron are sensible enough.

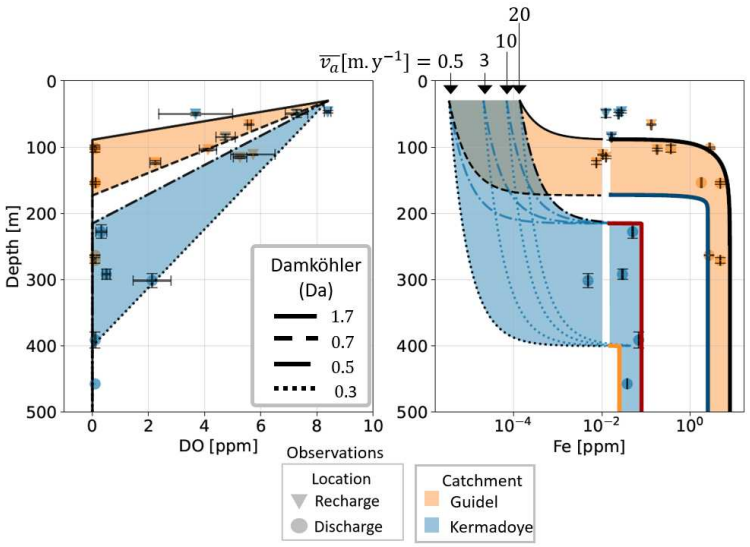

Text S5. Use of rainwater as initial condition for water chemical composition in the fully resolved numerical model.

The model presented in the main manuscript uses as initial condition for water chemistry a typical composition of groundwater from a recharge zone, in order to focus on reactive processes occurring in groundwater and to set aside unsaturated zone reactive processes. Although, it is interesting to evaluate the sensitivity of our model to the initial concentrations. We thus changed the input water composition into a dilute rainwater composition such as measured on the study site, with an initial pH of 5.9 and compared the results with the simulation using recharge water as initial condition in Figure S5.

First, we observe that changing the initial condition of the water has no significant effects in the oxygen and iron profiles. Only a small increase in the anoxic iron concentration is observed because the saturation levels of minerals are slightly different. However the discrepancy is small and predicted values are in the same order of magnitude. More importantly, the shape of both iron and oxygen profiles remains the same, meaning that the analytical model captures well the co-evolution of O_2 and Fe^{2+} in groundwater. Since recharge zone groundwater can be seen as an 'evolved' rainwater that has interacted with soil and regolith, one could expect that using rainwater as input in our model should converge to the recharge groundwater composition by interaction with the minerals. However, as shown by Figure S5 it is not exactly the case. While K and Mg concentrations reach the initial levels of recharge water in a range going from 50 to 100 years, the rainfall model never reaches the initial values for SiO_2. This discrepancy is expected since our model does not take into account a soil compartment where the mineralogy and the biogeochemical processes are different from those in the fractures. Therefore, since the oxygen and iron profiles are not affected by the change in the initial water composition, using an initial composition of a recharge water in order to focus on groundwater reactive processes and to limit the complexity of including a soil compartment, is an approximation that simplifies the model without introducing significant bias in the purpose of the model.

Figure S5. Use of rainwater as initial condition for water chemical composition in the fully resolved numerical model. The recharge zone scenario uses the average composition of a borehole in the recharge zone while the 'rainwater' scenario uses the average rainwater composition of the study site. We equated the initial oxygen concentrations between the two simulation scenarios in order to make them comparable.

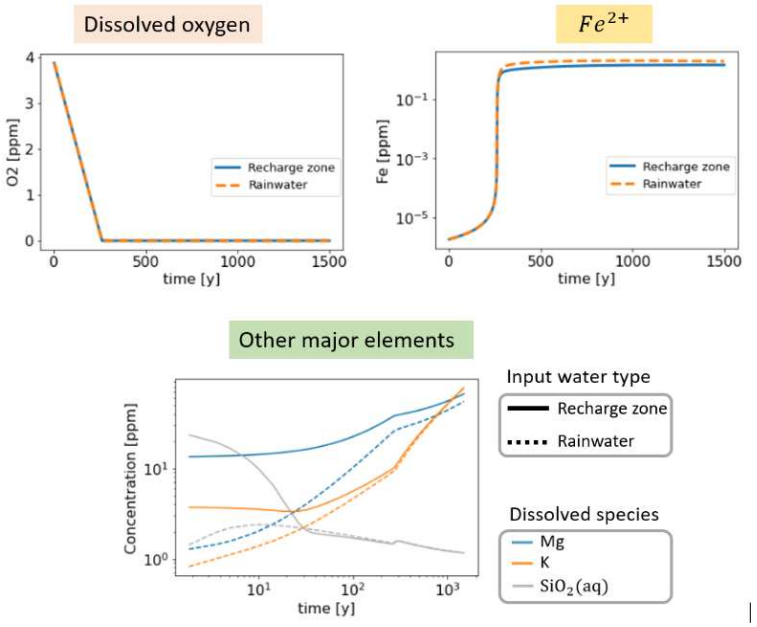

Text S6. Simulations with non-silicate secondary Fe-bearing minerals. In the main manuscript we show the importance of the secondary Fe-bearing minerals as regulators of the iron concentrations at anoxic conditions. If the secondary phase is not present in the simulations, the dissolved iron concentration at anoxic conditions would reach high concentrations (>100 mg/L) which are far above environmental levels. Here, we test if the mineralogical nature of the secondary mineral phase is a condition for the model to work.

For that purpose, besides chlorite (a silicate), we include siderite (a carbonate) in the simulations to test if the behavior of the oxygen and iron profiles are affected by the nature of the dominant secondary mineral (Figure S6). We specified the volume fractions of both minerals to control which of the two is the dominant secondary mineral phase.

Globally, the shape of both DO and Fe remain the same when compared with the Control Case (see Figure S6). We note however two effects that were not observed in the Chlorite case. Under oxic conditions, siderite dissolves while chlorite does not, because the kinetic constant of siderite dissolution is 3 orders of magnitude higher than chlorite. The dissolution of siderite implies an additional source of iron at oxic conditions (siderite + biotite), which enhances the reducing capacity and depletes oxygen more rapidly. Since the analytical model only considers one iron source, we observe a shift in consumption time between the analytical and numerical models when siderite is present. While deviations between the model and the analytical solution are observed when another Fe(II) bearing mineral is added, the behavior of the DO-Fe system remains similar. The reduced analytical solution could thus be adapted to different mineral assemblages without a significant increase in complexity.

Figure S6. Simulations with non-silicate secondary Fe-bearing minerals. The figure illustrates the effect of the change in the nature of the secondary Fe-bearing mineral phase in the fully resolved numerical simulations. The difference between the Chlorite case (upper plots) and the Siderite case (lower plots) stands on the mineral volume fractions that allow to neglect the effect of one of the two minerals. See Text S6 for details.

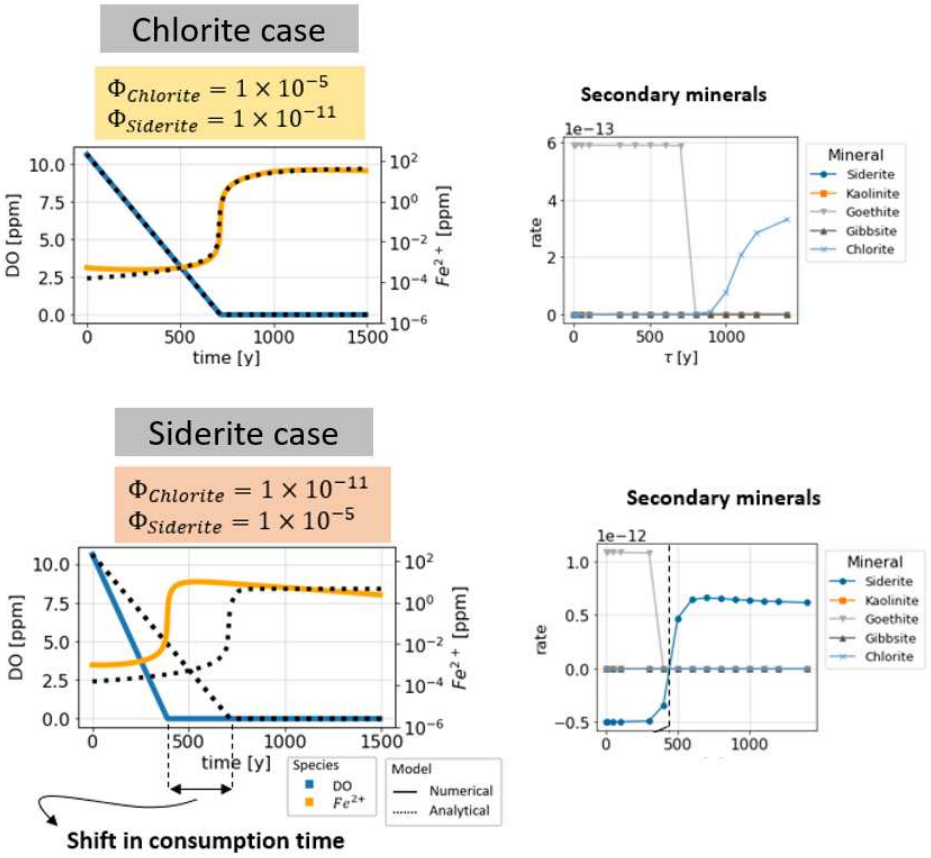

Supporting References S1.

Blanc, P., Lassin, A., Piantone, P., Azaroual, M., Jacquemet, N., Fabbri, A., Gaucher, E. C. (2012). Thermoddem: A geochemical database focused on low temperature water/rock interactions and waste materials. Applied Geochemistry, 27 (10), 2107–2116. doi: 10.1016/j.apgeochem.2012.06.002

Klepikova, M. V., Le Borgne, T., Bour, O., Davy, P. (2011). A methodology for using borehole temperature-depth profiles under ambient, single and cross-borehole pumping conditions to estimate fracture hydraulic properties. Journal of Hydrology, 407 (1-4), 145–152. doi: 10.1016/j.jhydrol.2011.07.018

Le Borgne, T., Paillet, F., Bour, O., Caudal, J. P. (2006). Cross-borehole flowmeter tests for transient heads in heterogeneous aquifers. Ground Water ,44 (3), 444–452. doi: 10.1111/j.1745-6584.2005.00150.x

Pouladi, B., Bour, O., Longuevergne, L., de La Bernardie, J., Simon, N. (2021). Modelling borehole flows from Distributed Temperature Sensing data to monitor groundwater dynamics in fractured media. Journal of Hydrology, 598 (November 2020). doi: 10.1016/j.jhydrol.2021.126450

Sugisaki, R., Taki, K. (1987). Simplified analyses in of He, natural Ne, waters and Ar dissolved. Geochemical Journal, 21, 23–27. doi: 10.2343/geochemj.21.23

APPENDIX CHAPTER 6: SUPPLEMENTARY INFORMATIONS

1 Isolation pumping tests for the isolated fractures

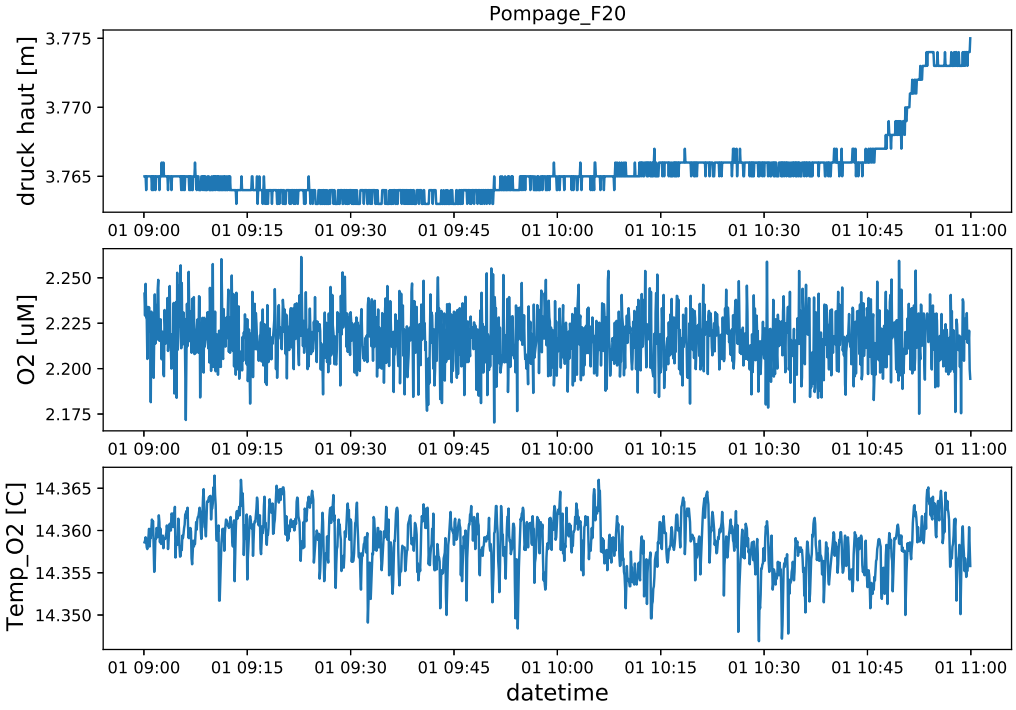

Figure A-2: Isolation pumping tests in the fracture at 20 m deep, borehole Pz26.

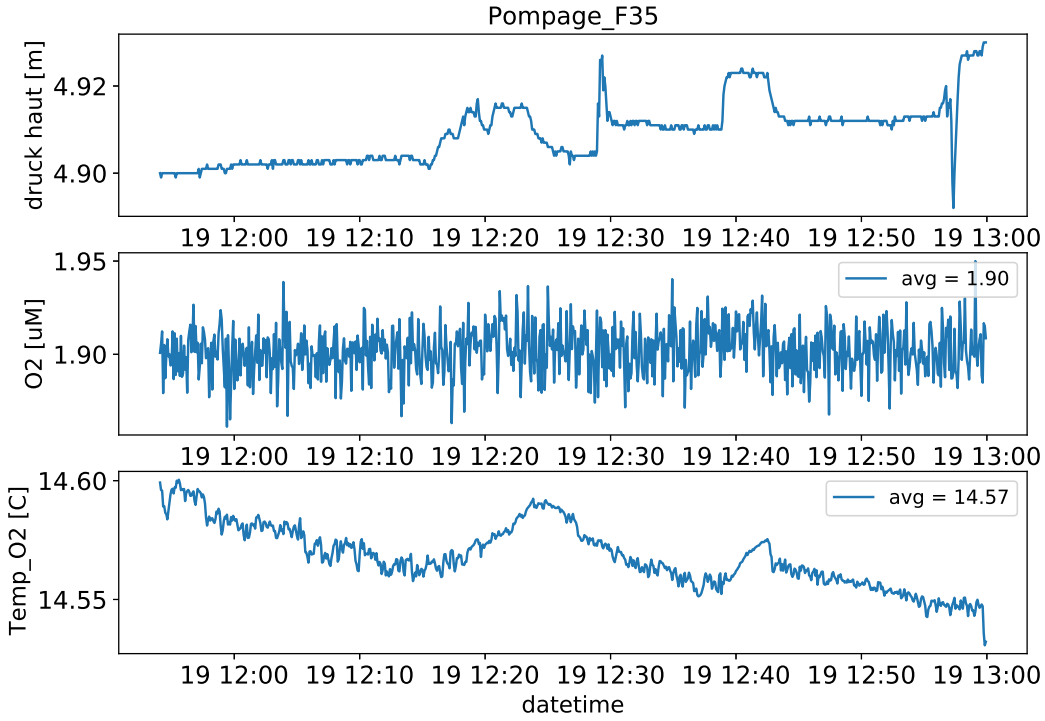

Figure A-3: Isolation pumping tests in the fracture at 35 m deep, borehole Pz26.

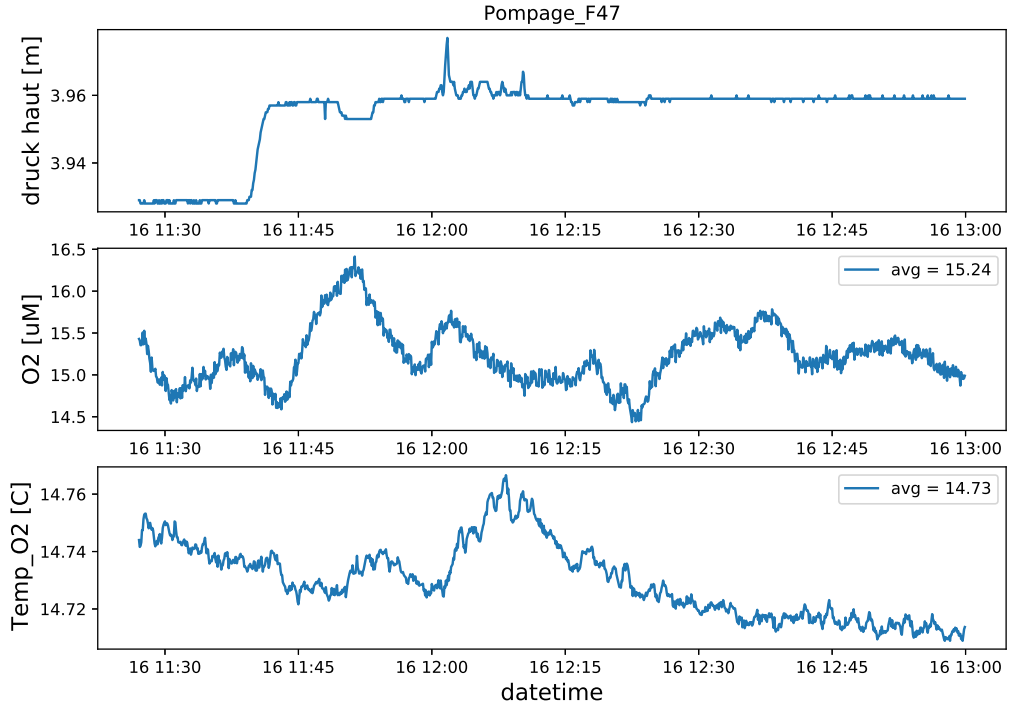

Figure A-4: Isolation pumping tests in the fracture at 47 m deep, borehole Pz26.

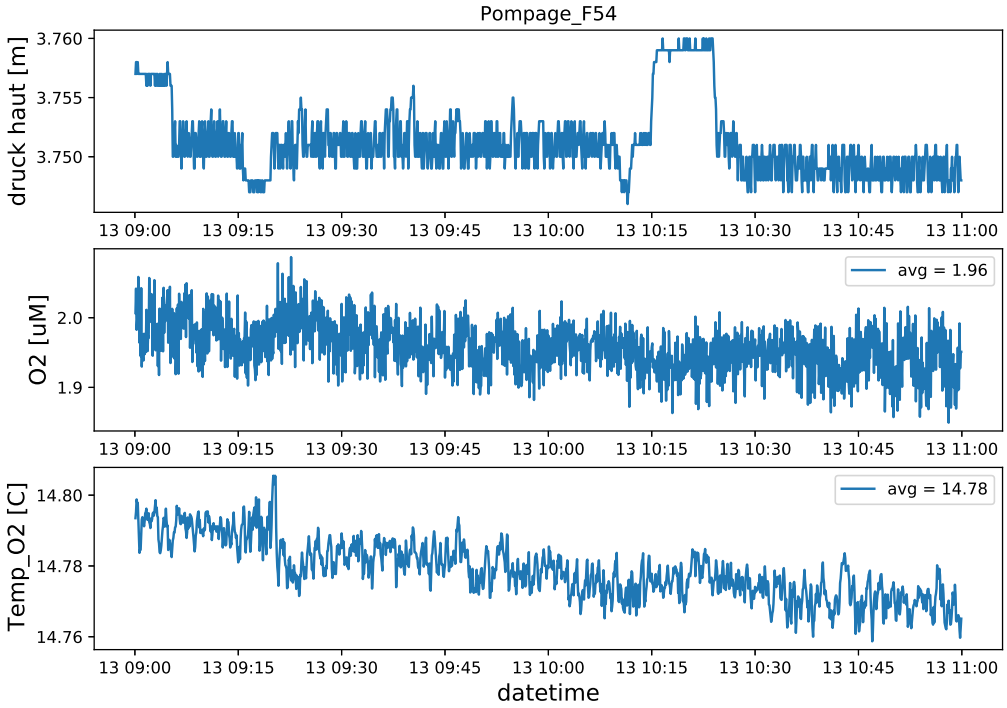

Figure A-5: Isolation pumping tests in the fracture at 54 m deep, borehole Pz26.

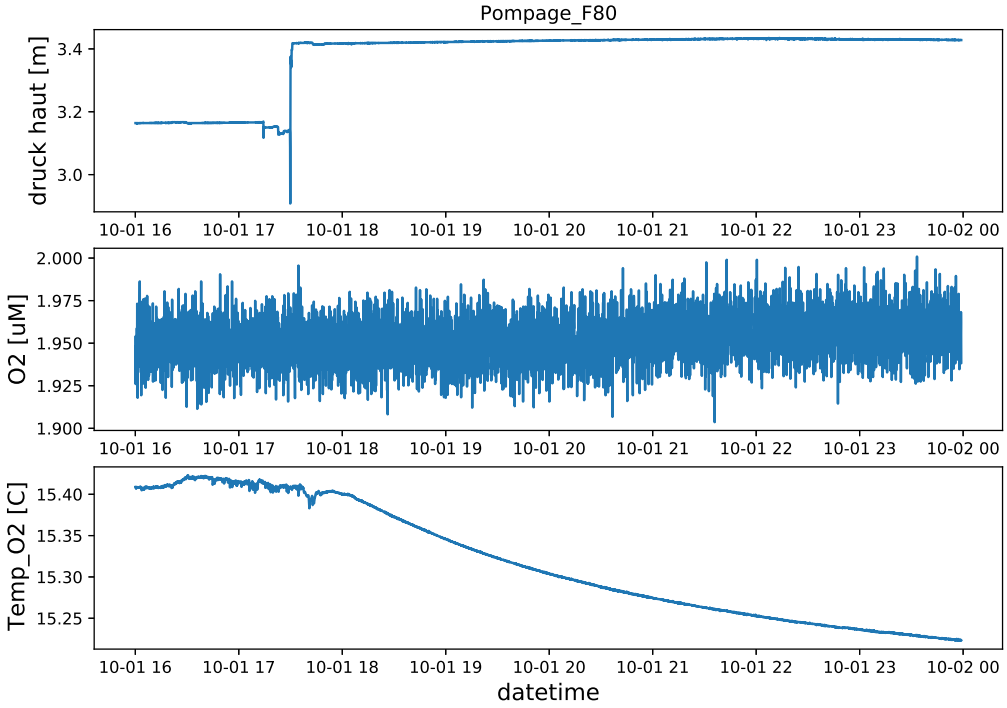

Figure A-6: Isolation pumping tests in the fracture at 80 m deep, borehole Pz26.

2 Conservative tracer concentration during the incubation phase.

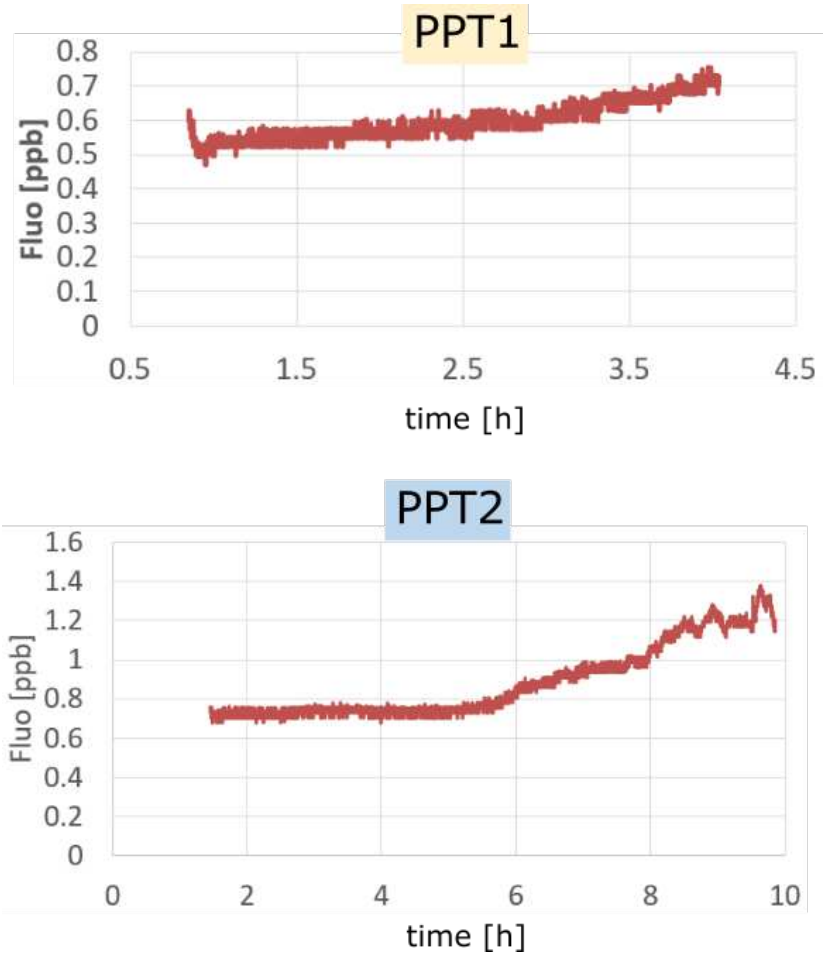

Figure A-7: Conservative tracer concentration during the incubation phase.

APPENDIX CHAPTER 7: SUPPLEMENTARY INFORMATIONS

1 Images of secondary minerals

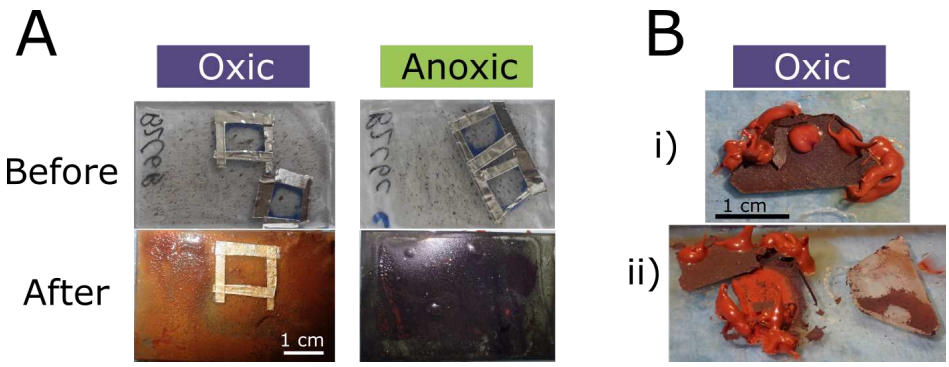

Figure A-8: **Macroscopic aspect of mineralizations obtained at contrasted redox conditions and the particular case of calcite.** A): average crusts formed on oxic and anoxic-incubated samples. B): the secondary crust formed on the filter-covered oxic-incubated calcite coupon showing a distinctive aspect.

2 Images of biomineralizations

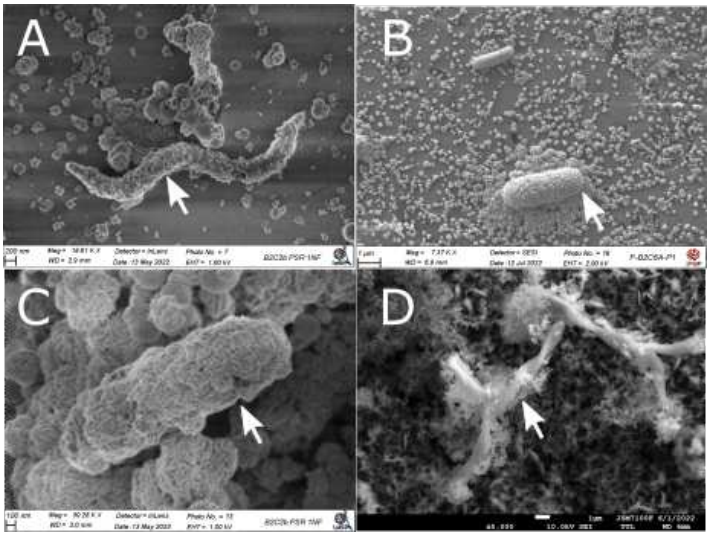

Figure A-9: **Examples of biomineralizations observed in the mineral-incubation experiment.** White arrows in subfigures A, B and C indicate examples of prokaryotic cells with surface encrusting, whereas in subfigure D the arrow shows an example of stalks, which are typical extracellular structures formed by *Gallionella*. The formation of secondary minerals is likely produced by BIM/BIFM biomineralizations.

3 Supplementary Information for the paper draft "Mineral substrate and fluid-redox conditions control cell density in attached biofilms: *in-situ* incubations in deep groundwater"

Supporting Information for

Mineral substrate and fluid redox conditions control cell density in attached biofilms: in-situ incubations in deep groundwater

Ivan-David Osorio-Leon[1], Bastien Wild[2,3], Camille Bouchez[1], Achim Quaiser[5], Emanuelle Gerard[4], Bénédicte Menez[4], Alexis Dufresne[5], Tanguy Le Borgne[1]

[1]Univ Rennes – CNRS, Géosciences Rennes - UMR 6118. Rennes, France
[2]Princeton University, USA
[3]University of Grenoble, ISTerre, CNRS, Grenoble, France
[4]Université Paris, Institut de Physique du Globe de Paris, UMR 7154 CNRS, F-75005 Paris, France
[5]Univ Rennes – CNRS, ECOBIO - UMR 6553. Rennes, France

Table of contents

Corresponding author: Ivan-David Osorio-Leon, idosoriole@unal.edu.co

Figure S1. Workflow for the characterization of mineral-attached biofilms.

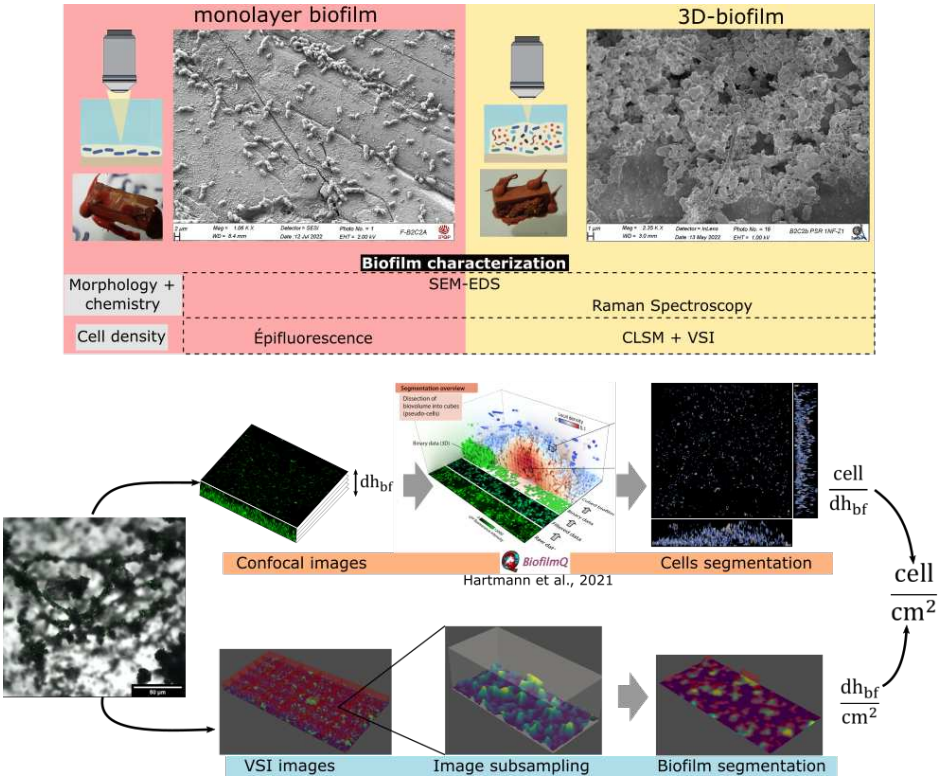

Figure S2. Mozaic of confocal images of mineral-attached biofilms at oxic and anoxic conditions. Scale bars correspond to $20\mu m$.

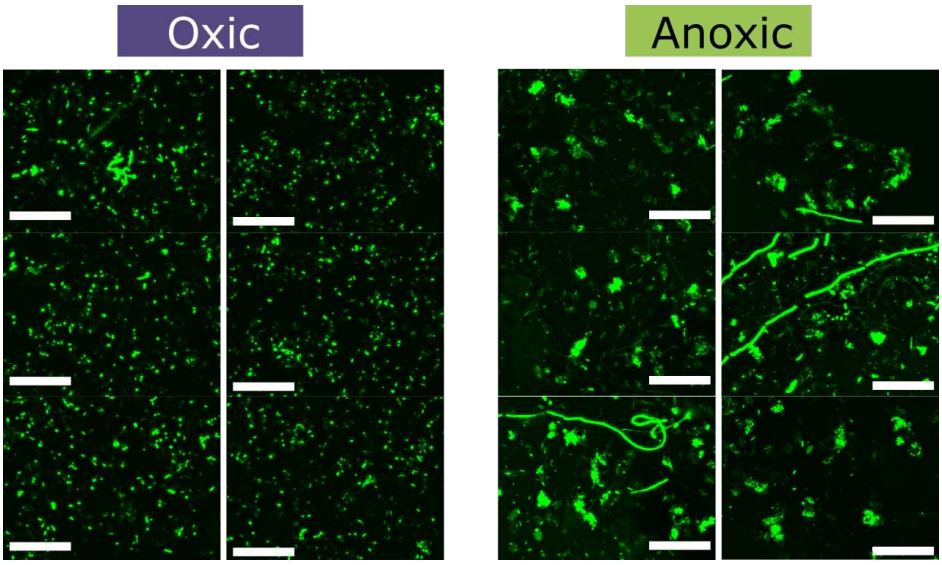

Figure S3. Elemental composition of biofilms as acquired by SEM-EDS analyses

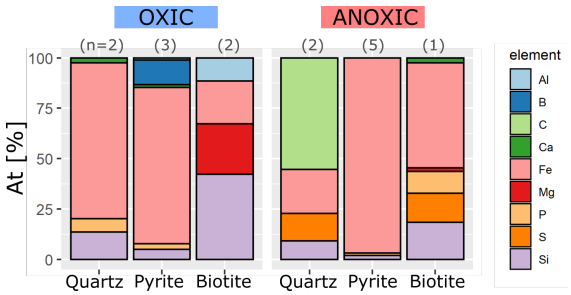

Figure S1. Average elemental percent composition of biofilms as measured by SEM-EDS analyses. The compositions are presented as a function of mineral substrate and fluid redox condition. Globally, biofilms are mainly composed by Fe but the proportion of accessory elements changes depending on the different redox and mineral substrate conditions.

APPENDIX 5: RÉSUMÉ ÉTENDU POUR DES LECTEURS FRANCOPHONES (OVERVIEW FOR FRENCH READERS)

This research work was, in whole, hosted, funded and developed in French institutions. This is why this section is dedicated to French readers.

1 Introduction

La *Zone Critique* (ZC) (NRC; 2001), qui va de la limite supérieure de la canopée jusqu'à la "base des systèmes d'eaux souterraines actives" (Anderson et al.; 2008), est la fine couche de notre planète dans laquelle le cycle de l'eau transporte de l'énergie et des solutés essentiels au fonctionnement des écosystèmes, à la survie de toutes les formes de vie et à l'évolution des paysages (Brantley et al.; 2007; Singha and Navarre-Sitchler; 2022). L'énergie solaire est la principale source d'énergie qui soutient la vie à la surface terrestre grâce à la photosynthèse, et alimente le cycle de l'eau qui connecte les flux d'énergie et de matière entre les continents et les océans.

En revanche, la subsurface continentale est un compartiment particulier de la ZC, moins étudié que les environnements de surface car l'accès y est moins direct, et avec un fonctionnement particulier car les écosystèmes souterrains ne peuvent pas être alimentés par l'énergie solaire (Singha and Navarre-Sitchler; 2022). Cette "Zone Critique souterraine" abrite des écosystèmes "sombres" qui sont en effet principalement alimentés par une énergie chimique provenant de sources inorganiques (Edwards et al.; 2012), telles que les minéraux des roches. Par leur interaction avec les eaux souterraines, ces minéraux fournissent des nutriments aux microorganismes et soutiennent la "biosphère profonde" (Edwards et al.; 2012). De plus, certains auteurs suggèrent que la majorité de la biomasse microbienne sur notre planète réside dans l'espace poreux des roches de la subsurface continentale (Whitman et al.; 1998; Edwards et al.; 2012; Bar-on et al.; 2018). **Cependant, on sait peu dans quelle mesure la Zone Critique souterraine interagit avec son homologue de surface. L'environnement de la subsurface continentale profonde est-il isolé des flux dynamiques d'énergie et de matière provenant de la surface de la Terre ?**

Les travaux présentés dans cette thèse se déroulent dans ce compartiment souterrain particulier où les interactions entre la vie, l'eau et les minéraux sont encore mal comprises. Pour étudier la connexion entre les environnements de surface et la subsurface, nous utilisons le dyoxygène dissous (OD) comme élément clé. En effet, l'OD est l'accepteur d'électrons offrant le plus grand potentiel pour les réactions redox qui soutiennent

les écosystèmes profonds. De plus, l'OD conditionne les processus cataboliques des microorganismes de la subsurface : il détermine à quel point les métabolismes aérobies (qui dépendent de l'O_2 en tant qu'accepteur d'électrons) ou les anaérobies (qui utilisent d'autres accepteurs d'électrons que l'O_2) deviennent dominants.

1.1 Les aquifères cristallins : un cas d'étude remarquable

Dans une étude à grande échelle portant sur les principaux aquifères des États-Unis, McMahon et al. (2011) et DeSimone et al. (2014) ont montré que les eaux souterraines sont plus susceptibles d'être oxiques dans certains contextes géologiques que dans d'autres. La Figure A-10 montre que les aquifères de roches fracturées sont généralement plus oxygénés que les environnements poreux par exemple. Cependant, les mécanismes expliquant les teneurs plus élevées en O_2 dissous et les conséquences des eaux souterraines oxiques sur les processus réactifs en subsurface sont largement inconnus.

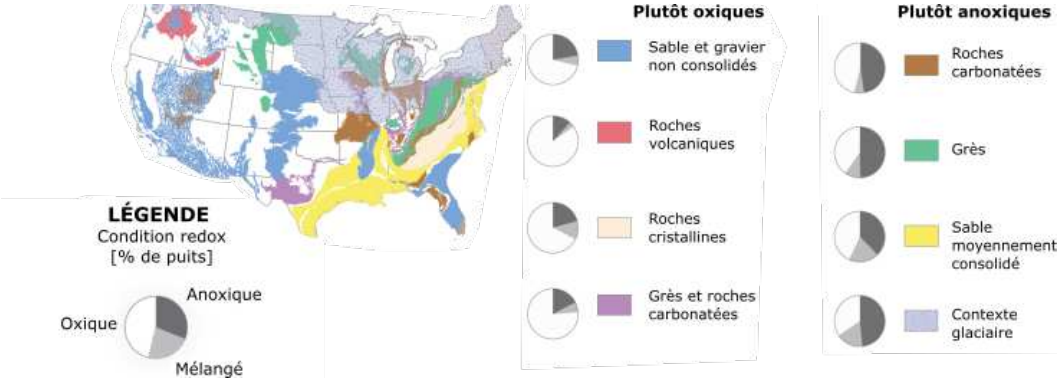

Figure A-10: **Carte d'état rédox des principaux aquifères des États-Unis.** État rédox dans les principaux aquifères des États-Unis, distingués par lithologie. Les données correspondent aux mesures dans les puits domestiques de certains aquifères régionaux sélectionnés. Image modifiée de DeSimone et al. (2014).

Nous avons identifié les roches fracturées comme un environnement géologique où la faible teneur en carbone organique les rend propices à la présence d'eaux souterraines oxiques. **Cela fait des roches fracturées un bon cas d'étude pour explorer les effets de l'O_2 sur les processus biogéochimiques en subsurface. De plus, cette étude se concentre sur le cas particulier des roches cristallines (ignées et métamorphiques) qui représentent plus de 30 % des roches exposées à la surface continentale.** L'O_2 dissous peut participer à diverses réactions aqueuses dans lesquelles il peut oxyder les donneurs d'électrons dans des réactions rédox médiées par des micro-organismes. Parmi les différents donneurs d'électrons, le fer ferreux est le plus courant et abondant dans la croûte terrestre (Wedepohl; 1995). Il joue un rôle critique dans les processus biogéochimiques en subsurface où il fait partie des réactions abiotiques ou médiées par les microorganismes (voir Figure A-11). **Par conséquent, cette étude se concentre particulièrement sur l'interaction entre l'oxygène dissous (O_2) et le fer ferreux en subsurface.**

2 Lacunes de connaissance

L'observation d'eaux oxiques dans la subsurface (e.g. Figure A-10) a remis en question l'idée prédominante selon laquelle les aquifères étaient exclusivement des environnements anoxiques et a soulevé la question de savoir si les eaux souterraines oxiques sont "une occurrence courante ou une anomalie" (Winograd and Robertson; 1982). L'O_2 dissous a été identifié comme une variable biogéochimique clé de la subsurface continentale. De plus, nous avons identifié les aquifères de roche fracturée comme des environnements favorables à la présence d'eaux souterraines oxiques dans la subsurface continentale, et donc comme un bon cas d'étude pour explorer : (1) les mécanismes permettant à l'OD de persister dans la subsurface et (2) les implications de la présence d'eaux souterraines oxiques sur les processus biogéochimiques dans la subsurface continentale.

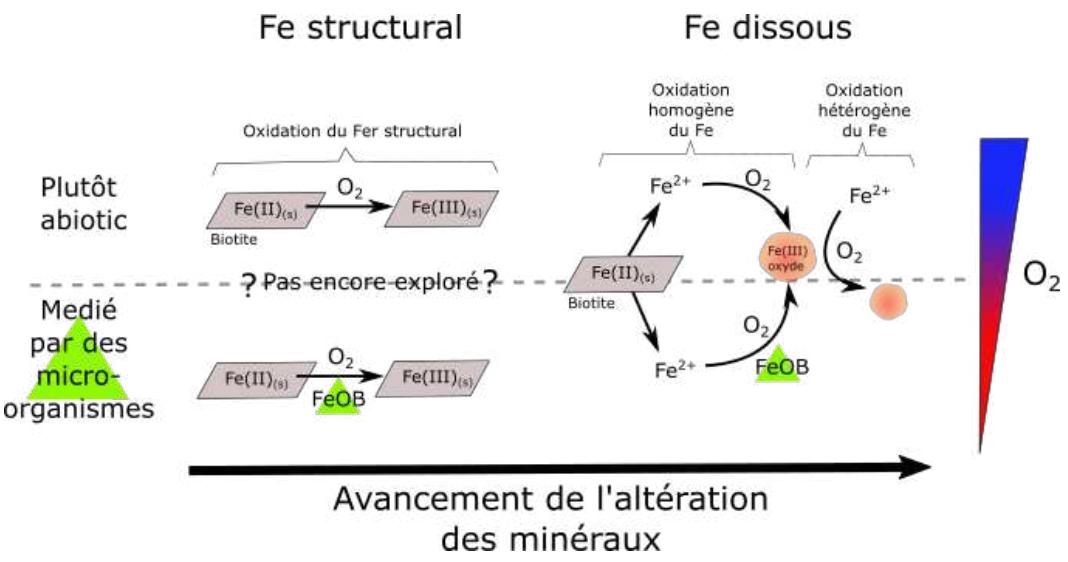

Figure A-11: **Réseau de processus réactifs liant les cycles du fer et de l'O_2 dans les eaux souterraines.** Les bactéries oxydantes du fer (FeOB) sont impliquées dans des processus médiés par les micro-organismes qui sont favorisés par de faibles concentrations d'OD (dites *micro-aérobies*). Alors que plusieurs études (Druschel et al.; 2008; Eggerichs et al.; 2014; Maisch et al.; 2019) ont démontré l'effet micro-aérobie dans les réactions aqueuses, son impact sur les réactions impliquant le Fe-structural, i.e. du Fe faisant partie de la structure des minéraux, reste inexploré.

Des eaux souterraines oxiques ont été recensées dans certains aquifères de roche fracturée [e.g. Bucher et al. (2009); Bochet et al. (2020); Ruff et al. (2023)], **mais il manque encore une étude systématique de la distribution de l'OD dans la subsurface et les facteurs qui contrôlent la profondeur de l'*hydrosphère oxique profonde***. Néanmoins, des avancées significatives sur la conceptualisation du transport et de la réactivité de l'OD dans les milieux cristallins ont été faites par des approches indirectes tels que de la modélisation [e.g. Trinchero et al. (2019)] ou des études minéralogiques et conceptuels sur les fronts d'altération dans des massifs cristallins [e.g. Kim et al. (2017) ou Hampl et al. (2022)]. Ces études ont notamment mis en évidence le rôle de facteurs géologiques tels que la présence de fractures et le contexte lithologique [e.g. Kim et al. (2017); Trinchero et al. (2019)] sur la profondeur à laquelle l'OD peut persister dans la subsurface. Cependant, ces avancées conceptuelles sur le problème du transport réactif de l'OD dans la subsurface continentale ont essentiellement porté sur des processus pertinents à des échelles de temps géologiques, dans lesquels les modèles font des fortes hypothèses tels que négliger la cinétique des réactions eaux-roche ou la contribution des réactions médiées par les micro-organismes. En fait, **il manque encore un cadre conceptuel pour décrire comment les interfaces oxic-anoxiques sont contrôlées dans les systèmes d'eaux souterraines modernes**. À ces courtes échelles de temps, l'écoulement rapide dans des chemins préférentiels, lors des évènements de pluie peut favoriser le transport d'eaux oxiques en profondeur (Bochet et al.; 2020), favorisant ainsi des réactions redox dépendantes de l'OD. Dans ce contexte, le transport-réactif de l'OD doit être conceptualisé pour tenir compte des échelles de temps du transport avec les échelles de temps des réactions eau-roches et des réactions médiées par les micro-organismes. En effet, le rôle de l'O_2 dans les réactions biologiques et chimiques se produisant en subsurface a été jusqu'à présent quasiment inexploré.

On comprend encore mal dans quelle mesure les conditions redox des eaux souterraines (i.e. conditions oxiques vs anoxiques) affectent les taux et les flux des processus biogéochimiques dans la subsurface continentale profonde tels que les réactions d'altération des roches et l'activité des micro-organismes (planctoniques et attachés aux minéraux).

Box .1 - Objectif global de cette thèse

Conceptualiser les facteurs qui contrôlent la présence et la profondeur de l'*hydrosphère oxique profonde* dans les systèmes modernes d'eaux souterraines et développer des approches *in situ* pour caractériser et quantifier comment les environnements oxiques/anoxiques affectent les réactions d'altération des roches et l'activité de la biosphère souterraine profonde.

Questions de recherche

Q1. **Profondeur de l'hydrosphère oxique :** à quelle profondeur les eaux souterraines oxiques peuvent-elles persister dans la subsurface continentale et quels processus contrôlent leur transport et leur réactivité ?

Q2. **Impacts de l'O_2 dissous sur les processus biotiques et abiotiques :** comment différencier la contribution de l'OD dans les processus biotiques et abiotiques dans la subsurface continentale profonde et comment les tracer dans des environnements hétérogènes ?

Q3. **Dynamique des conditions redox dans la subsurface :** comment les processus biogéochimiques sont-ils impactés lorsque le transport des eaux souterraines oxiques modifie les conditions redox dans la subsurface ?

Q4. **Interactions entre microorganismes et minéraux dans des conditions redox contrastées :** comment les interactions entre les microorganismes et les minéraux sont-elles affectées par l'existence d'environnements redox contrastés dans la subsurface continentale ?

3 Présentation des chapitres

Dans la Figure A-12, nous présentons l'organisation générale du présent travail, ainsi que les questions associées et les échelles étudiées. Cette thèse est composée de deux parties majeures. Dans une première partie, composée des chapitres III à V, nous abordons les questions Q1 et Q2 par le biais d'approches d'*observation* et de *modélisation* pour identifier les principaux contrôles de l'état rédox de la subsurface à l'échelle du bassin versant (Figure A-12-A). Ensuite, dans une deuxième partie composée des chapitres VI et VII, nous abordons les questions Q3 et Q4 pour explorer les conséquences des variations de l'état redox des eaux souterraines sur les processus biogéochimiques. Nous utilisons pour cela des approches expérimentales *in-situ* à des échelles plus petites (Figure A-12-B et C). Pour étudier les processus *in-situ*, nous développons de nouveaux outils qui nous permettent de dissocier les variables clés au sein de la complexité des environnements naturels.

Pour construire notre recherche, nous exploitons les capacités de l'Observatoire de la Zone Critique (OZC) de Ploemeur (Bretagne, France). Cet OZC, présenté en détail dans le chapitre III, est composé de deux bassins versants, Guidel et Kermadoye, dans lesquels plus de quarante forages offrent un accès à la zone saturée dans un aquifère de roche fracturée. De plus, la proximité de ces deux bassins versants et leurs contextes lithologiques et hydrogéologiques contrastés offrent une opportunité remarquable pour dissocier l'influence des facteurs géologiques et hydrologiques sur l'état redox de la subsurface continentale.

3.1 Comment délimiter l'hydrosphère oxique profonde dans les roches fracturées ? (Chapitre IV)

Dans ce chapitre, nous présentons un cadre conceptuel pour définir le problème de transport réactif de l'OD dans les roches silicatées riches en fer (Figure A-12-A). À partir de ce cadre conceptuel, nous dérivons des solutions

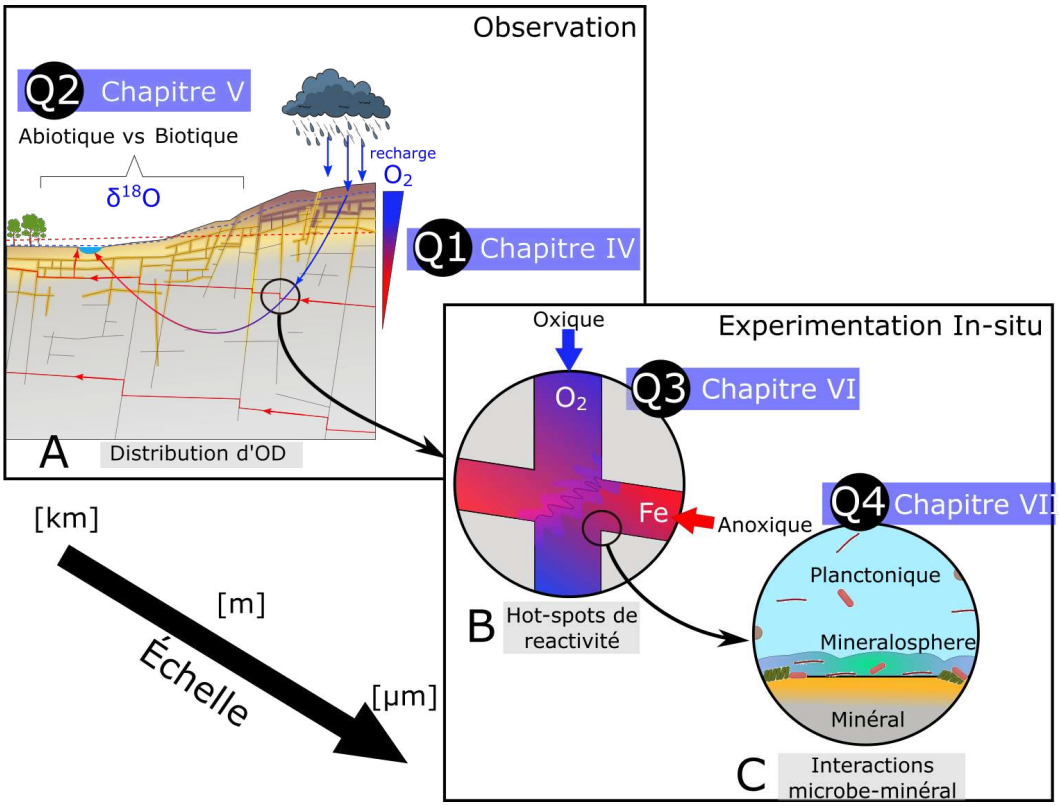

Figure A-12: **Stratégie de recherche adoptée dans ce travail.** Les questions directrices (Q) et leurs chapitres associés sont classés en deux approches de recherche : *observation* et *expérimences in-situ*. **A) :** Les trajectoires d'écoulement des eaux souterraines avec des concentrations en OD décroissantes sont représentées dans une vue à l'échelle d'un bassin versant. Les distributions de l'OD sont hétérogènes et dépendent de l'équilibre entre le transport d'OD depuis la surface et sa consommation par des réactions biogéochimiques en subsurface (Q1). La consommation d'OD en subsurface par des processus abiotiques et médiés par les micro-organismes peut entraîner un fractionnement des isotopes de l'OD (Q2). **B) :** L'intersection des trajectoires d'écoulement avec des eaux souterraines à redox contrasté crée des *hot-spots* réactifs intermittents en subsurface, qui dépendent du transport d'OD depuis la surface. Les conditions redox changeantes pendant les *hot-spots* réactifs sont des environnements potentiellement favorables aux procaryotes de la subsurface (Q3). **C) :** Les procaryotes de la subsurface, à la fois planctoniques et attachés aux minéraux, dépendent des potentiels redox pour prospérer et sont potentiellement affectés par des conditions redox compartimentées ou changeantes en subsurface (Q4).

analytiques pour décrire les distributions en profondeur de l'O_2 dissous et du fer dans les systèmes aquifères modernes. Nous validons les hypothèses sous-jacentes du modèle analytique avec un modèle numérique qui aborde en détail les interactions eau-roche.

Par ce modèle analytique, nous montrons notamment que dans des conditions oxiques, la concentration d'OD décroît linéairement avec le temps de transit en suivant une pente qui dépend du contexte lithologique et de la vitesse d'advection dans les fractures. Dans ce régime oxique, la concentration de Fe dissous est limitée par la cinétique d'oxydation aqueuse qui est plus rapide que la cinétique de dissolution des minéraux. À la transition oxique-anoxique, l'OD est épuisé et la concentration de Fe dissous montre une augmentation rapide et non-linéaire jusqu'à atteindre une concentration de régime pseudo-permanent. Nous montrons que cette concentration est contrôlée par l'abondance relative entre minéraux primaires et secondaires porteurs de Fer. Cette dynamique qui définit le transport réactif de l'OD et du Fe à l'échelle du bassin versant est caractérisée par deux nombres adimensionnels : le nombre de Damköhler (Da) et un nouveau nombre Lithologique (Λ). Nous montrons que l'étude conjoint du Fe et de l'OD permet de contraindre complètement le problème de transport-réactif décrivant leurs distributions en profondeur.

Notre modèle analytique validé est finalement appliqué à l'étude de site de l'OZC de Ploemeur. Le modèle permet de reproduire avec succès les différentes distributions en profondeur de l'O_2 et du Fer dans les bassins

versants de Guidel et Kermadoye. En effet, nous présentons un relevé systématique des concentrations en O_2 et Fe dissous dans ce site d'étude et montrons que l'interface oxique-anoxique se trouve à des profondeurs entre 150 et 300 mètres dans les bassins versants de Guidel et de Kermadoye, respectivement. Les différences dans la profondeur de la transition oxique-anoxique et dans la concentration en régime pseudo-permanent de Fe^{2+} sont modélisées avec succès et expliquées par des différences dans Da et Λ. En somme, ces résultats montrent qu'une portion non négligeable de la subsurface est potentiellement influencée par des processus biogeochimiques aérobies qui sont sensibles au transport d'O_2 depuis la surface. On propose d'appeler cette portion de la subsurface *l'hydrosphere oxique profonde*.

3.2 Les isotopes stables de l'oxygène dissous comme traceurs des processus biotiques et abiotiques dans la subsurface (Chapitre V)

Dans le chapitre V, nous utilisons la composition isotopique de l'O_2 dissous pour décrypter les voies réactives incluant l'OD en subsurface (Figure A-12-A). Ce travail constitue la première mesure systématique des isotopes stables de l'OD dans les environnements profonds de la subsurface. En couplant ces informations isotopiques avec une caractérisation hydrogéochimique approfondie du bassin versant de Guidel, incluant le temps de résidence de l'eau souterraine, la structure des trajectoires d'écoulement et la distribution redox dans l'aquifère, nous identifions les zones du bassin où les concentrations d'OD sont dominées soit par des processus physiques, soit par des processus médiés par les micro-organismes.

Pour cette étude, nous avons échantillonné huit piézomètres situés dans les zones de recharge et de décharge de Guidel, avec des profondeurs allant de 60 à 150 mètres sous la surface. Les concentrations d'OD diminuent avec le temps de résidence de l'eau tandis que sa composition isotopique ($\delta^{18}O_{OD}$) montre deux tendances différentes en fonction des concentrations d'OD. Dans les puits de la zone de recharge, les concentrations d'OD diminuent de 10 à 1,6 mg/L et les valeurs de $\delta^{18}O_{OD}$ diminuent de 24,8 à 18,1 ‰. Cette diminution inattendue de ^{18}O dans l'OD n'est pas susceptible d'être due à des processus réactifs qui sont connus pour produire un effet d'enrichissement, c'est-à-dire une augmentation des valeurs de $\delta^{18}O_{OD}$. Nous émettons donc l'hypothèse qu'elle est induite par le mélange des fluides des fractures avec l'eau de l'aquifère non confiné dans le compartiment du régolithe. Cette dernière est isotopiquement appauvrie en raison de la diffusion plus rapide du ^{16}O à l'interface de la nappe et la zone non-saturée. Dans les puits de la zone de décharge, les concentrations d'OD diminuent de 1,6 à 0,04 mg/L, tandis que les valeurs de $\delta^{18}O_{OD}$ montrent une augmentation nette de 18,1 à 25,3 ‰. Nous montrons que cette diminution de la concentration d'OD, accompagnée de l'augmentation du $\delta^{18}O_{OD}$, sont cohérentes avec une réaction qui fractionne positivement l'OD dans la phase dissoute restante, c'est-à-dire que l'OD restant est progressivement enrichi en ^{18}O. De plus, la coïncidence de ces tendances avec la gamme microaérobie, qui favorise l'activité des bactéries oxydantes du Fe, indique fortement l'activité microbienne dans cette part de l'aquifère. En employant des modèles de fractionnement isotopique à l'échelle du bassin versant nous estimons un facteur d'enrichissement *in-situ* (ε = -6.9 ‰) correspondant à cette activité microbienne. Cependant, cette estimation d'ε, calibrée sur les données de terrain, est significativement plus basse que des estimations faites lors d'expériences en laboratoire pour un contexte similaire (Oba and Poulson; 2009; Pati et al.; 2016). Nous attribuons cette divergence entre les estimations de laboratoire et de terrain à des effets de transport provoqués par l'hétérogénéité des milieux fracturés. Ces résultats fournissent donc de nouvelles perspectives sur l'utilisation potentielle de la composition isotopique de l'OD pour différencier et élucider les voies réactives de la consommation d'OD dans les environnements souterrains.

Dans les chapitres VI et VII, des approches expérimentales *in-situ* sont menées pour explorer les effets que l'état redox (oxique vs anoxique) de l'eau souterraine a sur les processus biogéochimiques, en particulier sur la biomasse microbienne, à la fois planctonique et attachée aux minéraux, et sur les taux d'altération des minéraux.

3.3 L'hydrosphère oxique profonde en tant que système dynamique (Chapitre VI)

Dans ce chapitre, nous présentons une première expérience sur le terrain utilisant un dispositif spécialement conçu, l'obturateur, qui correspond à une chambre d'échantillonnage encadrée par deux boudins gonflables. Cet obturateur permet d'isoler une fracture réductrice dans un forage pour y reproduire un événement de recharge d'eaux souterraines oxiques. Cette approche est particulièrement précieuse pour étudier des événements qui sont difficiles à observer dans des conditions naturelles sur le terrain. En effet, le transport d'eau souterraine oxygénée dans la subsurface peut résulter de contraintes hydrologiques telles que de grands événements de recharge, qui sont difficiles à prédire. En réalisant deux tests réactifs et séquentiels de type "Push-Pull", nous introduisons une perturbation redox dans une fracture réductrice. Chacun de ces deux tests de traçage entraîne la création d'un hot-spot de réactivité biogéochimique dominé par l'oxydation du fer par l'oxygène et une activité conséquente des communautés microbiennes planctoniques dominées par les bactéries oxydantes du fer (FeOB). Nous déterminons les taux de réaction *in-situ* pour la réaction d'oxydation du fer par l'OD, mettant en évidence que les taux *in-situ* sont inférieurs aux mesures en laboratoire. De plus, les rapports stœchiométriques entre le Fe et l'OD démontrent que des mécanismes autres que la consommation de fer sont susceptibles de consommer l'OD dans la subsurface, tels que les métabolismes hétérotrophes potentiels qui peuvent être déclenchés par l'activité des FeOB. De manière surprenante, la réponse du système biogéochimique de la fracture isolée est rapide par rapport aux taux de croissance connus en laboratoire pour les FeOB. De plus, nos mesures révèlent également que les fluctuations redox dans la subsurface entraînent un changement des conditions biogéochimiques du système de la fracture qui persiste après les expériences, résultant en un nouvel état permanent. En somme, l'étude présentée dans ce chapitre remette en question la vision de la subsurface continentale comme un environnement inertiel où l'activité microbienne est faible et lente. Nos résultats suggèrent que les contraintes hydrologiques entraînant des fluctuations redox des eaux souterraines fournissent un stimulus dynamique avec le potentiel d'amplifier l'activité biogéochimique dans la subsurface continentale.

3.4 Interactions microbes-minéraux dans des conditions redox contrastées (Chapitre VII)

Ce chapitre présente les résultats d'une expérience de terrain à long terme visant à les effets des conditions redox sur les communautés attachées aux minéraux et leurs effets réciproques sur l'altération des minéraux (Figure A-12-C). L'accent de ce chapitre est mis sur les communautés attachées aux minéraux, occupant une niche écologique unique connue sous le nom de *minéralosphère* (Uroz et al.; 2015), responsable de l'accueil d'au moins 99 % de la biomasse microbienne dans la subsurface continentale. Malgré sa contribution significative en biomasse, cette biosphère attachée aux minéraux reste mal comprise en raison des défis liés à l'échantillonnage.

Ce chapitre présente des avancées méthodologiques décisives pour surmonter les limitations de l'échantillonnage, avec le développement d'un dispositif de test conçu pour l'incubation *in-situ* de minéraux dans les forages. Ce dispositif permet l'échantillonnage contrôlé des communautés de micro-organismes attachés aux minéraux, qui sont généralement difficiles à accéder, en utilisant les forages comme milieux d'incubation. Son efficacité dans l'échantillonnage des communautés microbiennes attachées aux minéraux a été confirmée par une expérience d'incubation *in-situ* sur 10 mois. De plus, nous avons développé une méthodologie pour estimer divers paramètres clés des interactions entre les microbes et les minéraux, qui peut être appliqué à de futures études abordant des questions connexes. Ces avancées ont inspiré le développement à plus grande échelle de configurations de terrain similaires à déployer dans différents observatoires de terrain dans le cadre du projet PIA3 TerraForma (https://terra-forma.cnrs.fr).

D'un point de vue général, l'étude présentée dans ce chapitre est l'une des rares à évaluer quantitativement les effets des conditions environnementales sur les interactions entre les microbes et les minéraux dans des conditions *in-situ*. Dans la première partie du chapitre, nous montrons que les conditions redox peuvent

avoir un impact sur la disponibilité d'énergie dans l'environnement de la subsurface. Ainsi, nous démontrons que les minéraux riches en donneurs d'électrons hébergent des populations cellulaires plus denses. Nous mettons en évidence la sensibilité des communautés microbiennes attachées aux conditions oxiques/anoxiques pour les surfaces de biotite, mais pas pour d'autres minéraux testés. Nous relions cette observation à des réactions biogéochimiques distinctes, en accord des résultats de modélisation thermodynamique. Les données de séquençage du gène ARNr 16S sur les échantillons incubés dans des conditions anoxiques montrent également que la composition des communautés attachées est clairement différente du consortium planctonique et est également affectée par le substrat minéral.

Dans la deuxième partie du chapitre, nous évaluons l'effet (1) de l'état redox du fluide et (2) du contact microbe-minéral sur la vitesse de dissolution des minéraux. En utilisant la calcite comme minéral de référence, nous quantifions pour la première fois le taux de dissolution *in-situ* de la calcite. Nos résultats indiquent une corrélation claire entre les conditions oxiques et des taux de dissolution minérale significativement plus élevés, généralement d'un à deux ordres de grandeur supérieurs à ceux observés dans des conditions anoxiques. Nous attribuons cet effet redox à la corrélation entre les conditions oxiques et les eaux récentes, qui présentent des degrés de saturation plus faibles, favorisant ainsi la dissolution des minéraux. De plus, nous quantifions l'effet de la dissolution de la calcite induite par les microbes, conduisant à des taux de dissolution deux à trois fois plus rapides que lorsque le contact microbe-minéral est empêché. Enfin, une étude minéralogique réalisée sur une croûte secondaire formée sur la calcite révèle un lien étroit entre la minéralisation et les biofilms attachés aux minéraux. La composition chimique de cette croûte secondaire, riche en oxyhydroxydes de fer, est étroitement liée aux conditions redox du fluide.

Dans l'ensemble, les résultats présentés dans ce chapitre apportent des preuves complémentaires mettant en évidence l'influence significative des conditions redox de la subsurface sur divers aspects des interactions entre les microbes et les minéraux. Le transport d'O_2 dissous dans la subsurface continentale, étudié dans les chapitres précédents, peut donc avoir un impact non seulement sur la dissolution des roches, mais aussi sur la biomasse et les caractéristiques fonctionnelles des consortiums attachés aux minéraux. Par conséquent, nous préconisons qu'il est important que les modèles de transport réactif et les modèles de biomasse de subsurface tiennent compte de la compartimentation redox de la subsurface. Cette considération est essentielle car elle peut potentiellement avoir un impact sur des variables fondamentales au sein de ces modèles, telles que les taux de dissolution des minéraux et les densités cellulaires.

4 Conclusion

4.1 Un pont des environnements de surface aux environnements souterrains

Cette thèse remet en question la vision générale de la subsurface continentale profonde en tant que système inerte qui suit les processus et les échelles de temps géologiques, indépendamment des dynamiques et des cycles de surface (LaRowe and Amend; 2019). Grâce à des observations sur le terrain et au développement d'un cadre conceptuel pour quantifier la présence d'O_2 dans les eaux souterraines, nous avons établi qu'une partie significative de la subsurface continentale profonde, s'étendant sur plusieurs centaines de mètres de profondeur en fonction des paramètres hydrologiques et géologiques, est potentiellement affectée par le transport d'eau oxique depuis la surface de la Terre. Par conséquent, les métabolismes alimentés par le potentiel rédox dans les écosystèmes de l'hydrosphère oxique profonde sont liés aux connexions hydrologiques qui transportent l'O_2 depuis la surface (Figure A-13).

L'hydrosphère oxique profonde est un composant dynamique des environnements souterrains, où l'O_2 dissous peut soit favoriser, soit inhiber les métabolismes aérobies et anaérobies, respectivement. Alors que les écosystèmes souterrains sont généralement considérés comme oligotrophes et ayant des taux de production de biomasse lents (Templeton and Caro; 2023), nos expériences de traçage réactif ont fourni de nouvelles observations remettant en question ce paradigme (Chapitre VI). Nous avons démontré que les fluctuations redox

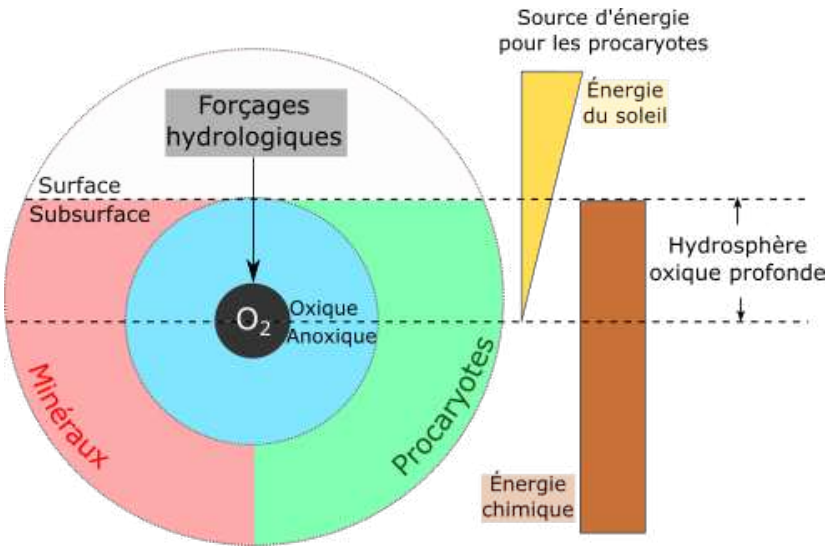

Figure A-13: **Vue conceptuelle de l'hydrosphère oxique profonde et de ses interactions avec les minéraux et la vie.** L'O_2, produit de la photosynthèse alimentée par la lumière du soleil, est transporté par des forcages hydrologiques vers l'hydrosphère oxique profonde, où il réagit avec les accepteurs d'électrons des minéraux lors de réactions redox pouvant être médiées par les procaryotes. L'O_2 est l'accepteur d'électrons offrant le potentiel redox le plus élevé pour ces réactions redox, et relie l'activité des procaryotes dans l'hydrosphère oxique profonde aux processus de surface.

induites par la recharge rapide des eaux souterraines oxiques peuvent en effet stimuler les écosystèmes profonds en fournissant un accepteur d'électrons hautement énergétique tel que l'O_2. Dans un délai maximal de huit heures, nous avons observé que la biomasse planctonique doublait en nombre suite à l'arrivée de l'O_2, montrant ainsi une réponse physiologique remarquablement rapide de l'environnement souterrain à une perturbation hydrologique. Alors que les environnements souterrains ont récemment montré des taux importants de fixation du carbone, comparables à ceux des systèmes marins oligotrophes (Overholt et al.; 2022), nos résultats indiquent que cette production de biomasse pourrait être très dynamique et réagir aux contraintes hydrologiques de la surface.

Les micro-organismes attachés aux minéraux représentent probablement la majorité de la biomasse souterraine (Flemming and Wuertz; 2019), mais on en sait peu sur leur dynamique. Tout comme les procaryotes planctoniques montrent une forte réponse aux changements redox, on peut supposer que les microorganismes attachés aux minéraux pourraient également être sensibles aux changements redox. Nous avons abordé cette question par le biais d'une expérience d'incubation des minéraux (Chapitre VII). En réalisant deux expériences d'incubation dans des environnements d'eaux souterraines profondes, contrastées du point de vue redox, nous avons quantifié la biomasse attachée, tant sur des minéraux inertes comme des minéraux réactifs (i.e. portant de nutriments). Nos résultats ont montré que, dans l'ensemble, la quantité de biomasse attachée aux minéraux est plus sensible au substrat minéral qu'aux conditions redox du fluide, mettant en évidence un contrôle important du contexte géologique sur la biomasse attachée aux minéraux.

Pour résumer, l'étude expérimentale *in situ* des communautés microbiennes planctoniques et attachées aux minéraux à travers les expériences de traçage et d'incubation des minéraux a montré que les conditions redox du fluide ont un impact fort sur les microorganismes planctoniques tandis que la biomasse attachée aux minéraux est plus sensible à la composition minérale des roches. Cette différence pourrait être liée à des limitations énergétiques dues à la disponibilité des donneurs et accepteurs d'électrons. Les eaux souterraines oxiques sont généralement associées à de faibles temps de résidence et de faibles états de saturation du fluide, tandis que les eaux souterraines anoxiques correspondent généralement à des temps de résidence plus longs et à des états de saturation plus élevés. Cela signifie qu'en conditions oxiques, les eaux souterraines sont généralement limitées par la disponibilité de donneurs d'électrons aqueux, tandis qu'ils sont abondants en conditions anoxiques,

entraînant des potentiels redox de fluide contrastés pour les procaryotes planctoniques. Les substrats minéraux constituant un réservoir majeur de donneurs d'électrons sur lesquels les procaryotes attachés aux minéraux se développent, ils ne sont donc pas sensibles aux potentiels redox du fluide. Ces résultats sont cohérents avec des expériences d'incubation précédentes en laboratoire (Jones and Bennett; 2017).

4.2 À quelle profondeur se trouve l'hydrosphère oxique profonde ?

Dans le cadre de l'étude du OZC de Ploemeur, au Chapitre IV, nous avons apporté des preuves de la présence d'eaux souterraines oxiques profondes s'étendant jusqu'à des profondeurs allant jusqu'à 400 mètres. Nous avons développé un cadre conceptuel et de modélisation pour caractériser quantitativement comment la profondeur de l'hydrosphère oxique profonde dans les roches fracturées dépend de l'équilibre entre la recharge advective en eau oxygénée de surface et les réactions de altération des roches qui consomment l'O_2 dissous par l'oxydation du Fe(II). Notre cadre de modélisation comble ainsi la lacune de connaissances qui existait sur le transport réactif de l'OD dans les systèmes modernes d'eaux souterraines profondes, caractérisés par de courts temps de résidence au cours desquels les échelles de temps des processus réactifs et de transport sont comparables. Nous avons montré que la distribution de l'OD avec la profondeur peut être décrite par deux nombres adimensionnels synthétiques, le nombre de Damkhöler (Da) et un nouveau nombre lithologique (Λ), qui capturent à la fois les processus hydrologiques (transport) et géologiques (réactifs). Notre cadre conceptuel fournit donc un outil analytique pour interpréter et prédire la présence d'oxygène dissous dans les environnements d'eaux souterraines profondes [e.g. Winograd and Robertson (1982)], et confirme davantage la présence d'O_2 en profondeur, comme cela a été déduit par des études paléohydrologiques sur les fronts d'altération, par exemple Fletcher et al. (2006). Dans l'ensemble, cette étude confirme l'existence d'une hydrosphère oxique profonde s'étendant jusqu'à plusieurs centaines de mètres de profondeur, en fonction des contextes hydrologiques et géologiques spécifiques.

4.3 Processus biotiques et abiotiques dans l'hydrosphère oxique profonde

Il n'est pas bien déterminé si les réactions redox consommant l'O_2 dissous se produisent par des mécanismes biotiques ou abiotiques dans les environnements souterrains. Pour l'oxydation du fer par l'OD, des conditions microaérobies semblent favorables à la réaction médiée par les micro-organismes, tandis que des concentrations plus élevées d'OD favorisent les mécanismes abiotiques (Druschel et al.; 2008; Emerson et al.; 2010; Eggerichs et al.; 2014; Maisch et al.; 2019). Cependant, ces observations sont issues de cultures en laboratoire qui ne sont pas nécessairement représentatives de l'activité *in-situ* des consortiums microbiens. Quelles conditions favorisent les mécanismes abiotiques ou biotiques de consommation de l'OD dans l'hydrosphère oxique profonde ? Pour répondre à cette question, nous avons présenté une étude (Chapitre V) dans laquelle nous avons étudié, pour la première fois, la fractionnement isotopique de l'OD dans les environnements souterrains profonds. Nos résultats sont remarquablement cohérents avec la plage microaérobie déduite des cultures en laboratoire. En effet, à des concentrations d'OD supérieures à la plage microaérobie, les fractionnements isotopiques de l'OD étaient dominés par des processus physiques et ne présentaient pas l'enrichissement $\delta^{18}O$ attendu de l'activité microbienne. En revanche, à des concentrations microaérobies, la tendance $\delta^{18}O$ présentait une augmentation de +7,2 ‰, en accord avec l'activité des bactéries oxydantes du fer (FeOB). Notre investigation isotopique de l'OD a donc confirmé que l'oxydation du fer par l'oxygène, médiée par les micro-organismes, est limitée à une plage microaérobie spécifique. Ces résultats ouvrent de nouvelles opportunités de recherche pour contraindre une biomasse dépendante de l'O_2 dans la subsurface continentale et quantifier la contribution biotique à l'oxydation du fer en subsurface.

Bibliography

Anderson, S. P., Bales, R. C. and Duffy, J. (2008). Critical Zone Observatories : Building a network to advance interdisciplinary study of Earth surface processes, *Mineralogical Magazine* **72**(1): 7–10.

Bar-on, Y. M., Phillips, R. and Milo, R. (2018). The biomass distribution on Earth, *Proceedings of the National Academy of Sciences of the United States of America* **115**(25): 6506–6511.

Bochet, O., Bethencourt, L., Dufresne, A., Farasin, J., Pédrot, M., Labasque, T., Chatton, E., Lavenant, N., Petton, C., Abbott, B. W., Aquilina, L. and Le Borgne, T. (2020). Iron-oxidizer hotspots formed by intermittent oxic–anoxic fluid mixing in fractured rocks, *Nature Geoscience* **13**(2): 149–155.

Brantley, S. L., Goldhaber, M. B. and Vala Ragnarsdottir, K. (2007). Crossing disciplines and scales to understand the critical zone, *Elements* **3**(5): 307–314.

Bucher, K., Zhu, Y. and Stober, I. (2009). Groundwater in fractured crystalline rocks, the Clara mine, Black Forest (Germany), *International Journal of Earth Sciences* **98**(7): 1727–1739.

DeSimone, L., Mcmahon, P. B. and Rosen, M. (2014). The quality of our Nation's waters - Water quality in Principal Aquifers of the United States, 1991-2010, *Technical report*, U.S. Geological Survey Circular 1360.

Druschel, G. K., Emerson, D., Sutka, R., Suchecki, P. and Luther, G. W. (2008). Low-oxygen and chemical kinetic constraints on the geochemical niche of neutrophilic iron(II) oxidizing microorganisms, *Geochimica et Cosmochimica Acta* **72**(14): 3358–3370.

Edwards, K. J., Becker, K. and Colwell, F. (2012). The Deep, Dark Energy Biosphere: Intraterrestrial Life on Earth, *Annual Review of Earth and Planetary Sciences* **40**(1): 551–568.

Eggerichs, T., Opel, O., Otte, T. and Ruck, W. (2014). Interdependencies between Biotic and Abiotic Ferrous Iron Oxidation and Influence of pH, Oxygen and Ferric Iron Deposits, *Geomicrobiology Journal* **31**(6): 461–472.

Emerson, D., Fleming, E. J. and McBeth, J. M. (2010). Iron-Oxidizing Bacteria: An Environmental and Genomic Perspective, *Annual Review of Microbiology* **64**(1): 561–583.

Flemming, H.-C. and Wuertz, S. (2019). Bacteria and archaea on Earth and their abundance in biofilms, *Nature Reviews Microbiology* **17**(4): 247–260.

Fletcher, R. C., Buss, H. L. and Brantley, S. L. (2006). A spheroidal weathering model coupling porewater chemistry to soil thicknesses during steady-state denudation, *Earth and Planetary Science Letters* **244**(1-2): 444–457.

Hampl, F. J., Schiperski, F., Byrne, J. M., Schwerdhelm, C., Kappler, A., Bryce, C., von Blanckenburg, F. and Neumann, T. (2022). The role of iron-bearing minerals for the deep weathering of a hydrothermally altered plutonic rock in semi-arid climate (Chilean Coastal Cordillera), *Chemical Geology* **604**: 120922.

Jones, A. A. and Bennett, P. C. (2017). Mineral Ecology : Surface Specific Colonization and Geochemical Drivers of Biofilm Accumulation , Composition , and Phylogeny, *Frontiers in Microbiology* **8**(March): 1–14.

Kim, H., Stinchcomb, G. and Brantley, S. L. (2017). Feedbacks among O2 and CO2 in deep soil gas , oxidation of ferrous minerals , and fractures : A hypothesis for steady-state regolith thickness, *Earth and Planetary Science Letters* **460**: 29–40.

LaRowe, D. and Amend, J. (2019). *Energy Limits for Life in the Subsurface*, Vol. 3.

Maisch, M., Lueder, U., Laufer, K., Scholze, C., Kappler, A. and Schmidt, C. (2019). Contribution of Microaerophilic Iron(II)-Oxidizers to Iron(III) Mineral Formation, *Environmental Science and Technology* **53**(14): 8197–8204.

McMahon, P. B., Plummer, L. N., Böhlke, J. K., Shapiro, S. D. and Hinkle, S. R. (2011). A comparison of recharge rates in aquifers of the United States based on groundwater-age data, *Hydrogeology Journal* **19**(4): 779–800.

NRC (2001). *Basic Research Opportunities in Earth Science*.

Oba, Y. and Poulson, S. R. (2009). Oxygen isotope fractionation of dissolved oxygen during reduction by ferrous iron, *Geochimica et Cosmochimica Acta* **73**(1): 13–24.

Overholt, W. A., Trumbore, S., Xu, X., Bornemann, T. L. V., Probst, A. J., Krüger, M., Herrmann, M., Thamdrup, B., Bristow, L. A., Taubert, M., Schwab, V. F., Hölzer, M., Marz, M. and Küsel, K. (2022). Carbon fixation rates in groundwater similar to those in oligotrophic marine systems.

Pati, S. G., Bolotin, J., Brennwald, M. S., Kohler, H.-p. E., Werner, R. A. and Hofstetter, T. B. (2016). Measurement of oxygen isotope ratios (18 O / 16 O) of aqueous O 2 in small samples by gas chromatography / isotope ratio mass spectrometry, *Rapid Communications in Mass Spectroscopy* **30**: 684–690.

Ruff, S. E., Humez, P., de Angelis, I. H., Diao, M., Nightingale, M., Cho, S., Connors, L., Kuloyo, O. O., Seltzer, A., Bowman, S., Wankel, S. D., McClain, C. N., Mayer, B. and Strous, M. (2023). Hydrogen and dark oxygen drive microbial productivity in diverse groundwater ecosystems, *Nature Communications* **14**(1): 3194.

Singha, K. and Navarre-Sitchler, A. (2022). The Importance of Groundwater in Critical Zone Science, *Groundwater* **60**(1): 27–34.

Templeton, A. S. and Caro, T. A. (2023). The Rock-Hosted Biosphere, *Annual Review of Earth and Planetary Sciences* **51**(1): 493–519.

Trinchero, P., Sidborn, M., Puigdomenech, I., Svensson, U., Ebrahimi, H., Molinero, J., Gylling, B., Bosbach, D. and Deissmann, G. (2019). Transport of oxygen into granitic rocks: Role of physical and mineralogical heterogeneity, *Journal of Contaminant Hydrology* **220**(November 2018): 108–118.

Uroz, S., Kelly, L. C., Turpault, M. P., Lepleux, C. and Frey-Klett, P. (2015). The Mineralosphere Concept: Mineralogical Control of the Distribution and Function of Mineral-associated Bacterial Communities, *Trends in Microbiology* **23**(12): 751–762.

Wedepohl, K. (1995). The composition of the continental crust, *Geochimica et Cosmochimica Acta* **59**(7): 1217–1232.

Whitman, W. B., Coleman, D. C. and Wiebe, W. J. (1998). Prokaryotes: The unseen majority, *Proceedings of the National Academy of Sciences of the United States of America* **95**(12): 6578–6583.

Winograd, Isaac. and Robertson, F. (1982). Deep Oxygenated Ground Water : Anomaly or Common Occurrence?, *Science* **216**(4551): 1227–1230.

COLLEGE ECOLOGIE
DOCTORAL GEOSCIENCES
BRETAGNE AGRONOMIE ALIMENTATION

Université de Rennes

Titre : Dynamiques oxiques-anoxiques dans la subsurface continentale : prédiction et contrôle sur l'altération des roches et la biomasse profonde

Mot clés : Zone Critique ; Biosphère profonde ; Transport Réactif ; Eaux souterraines ; Altération des roches ; Oxygène dissous

Résumé : Les réactions redox impliquant l'oxygène dissous (OD) sont les plus énergétiques et offrent une source majeure d'énergie pour la biosphère profonde. La capacité des milieux fracturés à transporter rapidement des eaux oxygénées de la surface vers la profondeur permet le maintien d'une hydrosphère oxique profonde (HOP) jusqu'à présent négligée. Cette thèse porte donc sur l'origine, la dynamique et les conséquences de cette HOP. Dans un premier temps, nous établissons un cadre conceptuel pour identifier les facteurs qui contrôlent le transport réactif de l'OD à l'échelle d'un bassin versant. Nous développons un modèle d'interactions eau-roche afin de prédire la profondeur de l'HOP. Ce modèle est ensuite utilisé pour expliquer l'occurrence d'une HOP dans les premiers 300 mètres de profondeur de l'Observatoire de la Zone Critique de Ploemeur. Nous étudions le $\delta^{18}O$ de l'OD au sein de l'HOP afin d'identifier la distribution des processus biotiques et abiotiques qui contrôlent la réactivité de l'OD dans le bassin versant. Dans un deuxième temps, nous développons deux expériences *in-situ* pour explorer les conséquences de l'HOP sur le fonctionnement biogéochimique de la subsurface. Grâce à un test de traçage réactif à l'OD et une expérience d'incubation de minéraux, nous démontrons, respectivement, la réponse de la biomasse planctonique et de celle attachée aux minéraux aux dynamiques oxiques-anoxiques de la subsurface. Ces travaux mettent en lumière une HOP dans laquelle les processus biogéochimiques souterrains sont sensibles aux dynamiques hydrologiques de surface impliquant le transport de l'OD, remettant ainsi en question le paradigme de la biosphère profonde en tant que système inertiel et anoxique.

Title: Oxic-anoxic dynamics in the continental subsurface: prediction and control of rock weathering and deep biomass

Keywords: Critical Zone; Deep biosphere; Reactive transport; Groundwater; Rock weathering, Dissolved oxygen

Abstract: Redox reactions involving dissolved oxygen (DO) are the most energetic and provide a major source of energy for the deep biosphere. The ability of fractured rocks to rapidly transport oxygenated waters from the surface to depth allows for the existence of a deep oxic hydrosphere (DOH), which has been historically neglected. This thesis focuses on the origin, dynamics, and consequences of this DOH. First, we establish a conceptual framework to identify the factors controlling the reactive transport of DO at the watershed scale. We develop a water-rock interaction model to predict the depth of the DOH. This model is used to explain the occurrence of a DOH within the first 300 meters of the aquifer in the Critical Zone Observatory of Ploemeur. We investigate the $\delta^{18}O$ of DO within the DOH to identify the distribution of biotic and abiotic processes that control the reactivity of DO in the watershed. Second, we conduct two in-situ experiments to explore the consequences of the DOH on the biogeochemical functioning of the subsurface. A reactive DO tracer test and a mineral incubation experiment are developed to study the response of, respectively, the planktonic and mineral-attached biomass to oxic and anoxic dynamics in the subsurface. This work highlights a DOH in which subsurface biogeochemical processes are sensitive to surface hydrological dynamics involving the transport of DO, thus challenging the paradigm of the deep biosphere as an inertial and anoxic system.